Mechanisms of strain localisation in the lithosphere

Katherine Elizabeth Willis

Submitted in accordance with the requirements for the degree of Doctor of Philosophy

The University of Leeds

School of Earth and Environment

September 2019

The candidate confirms that the work submitted is their own, except where work which has formed part of jointly authored publications has been included. The contribution of the candidate and the other authors to this work has been explicitly indicated below. The candidate confirms that appropriate credit has been given within the thesis where reference has been made to the work of others.

The work in Chapter Three and Four of the thesis has appeared in publication as follows: Tectonophysics, volume 764 (5), August 2019, Katy Willis, Gregory A. Houseman, Lynn Evans, Tim Wright, Andrew Hooper.

I was responsible for design and implementation of the experiments, code and script development for quantifying the results, and background literature search for the introduction and supporting geophysical data.

The contribution of the other authors was modification of the finite element code *basil* to refine the recalculation of the finite element mesh (remesh command), and include the recovery component to strain-weakening and temperature dependence of the strain-weakening parameter; support in developing the MatLab code for calculating fugacity and change in strain-weakening parameter with depth.

Acknowledgements

This work was supported by Natural Environment Research Council (NERC) grant "Looking Inside Continents from Space (NE/K010867/1). COMET is the NERC Centre for the Observation and Modelling of Earthquakes, Volcanoes and Tectonics.

With grateful thanks to Greg Houseman and Lynn Evans for their work on refining the *basil* code for this project. This includes developing the remesh command, extending the application to represent plate rotations on a sphere, adding the strain recovery and T_{ref} modification and making adjustments to deal with any bugs that occurred.

With thanks to Greg Houseman for the support in developing the MatLab code for calculating fugacity and strain-weakening parameter changes with depth.

With heartfelt thanks to the following people.
James Shaw, my ever wonderful husband, who supported me through this journey. It would not have happened without you.
Greg Houseman, my primary supervisor, for his boundless kindness and patience.
Cerridwen, for inspiration, thirst for knowledge and tenacity. And that moment by Llyn Tegid where you told me to get my life in order.
My family for encouragement, tips on navigating academia, distractions relating to gardening, trees, history research and beer, for smiles and laughs, and for dealing with abstract maths enquiries. They know which bits apply to them, it was all important.
My good friends Russell, Rachel, Imogen, Tamara, Lizzie, Badger, Joanna, Gail. Your support was invaluable, it would have been a lonely time without you.

The Hartley Avenue gang. Mushi Cat, because the rats and dead squirrel are funny in hindsight. Andy, for providing a wonderful home for me in Leeds. Levi and Layla, for reminding me sanity is sometimes over-rated.

To all those in IGT who have helped me. Tim Wright and Andy Hooper (my secondary supervisors), my fellow PhD students (especially those whom I shared an office with) and to all those who attended coffee breaks.

Abstract

This thesis examines the development of shear-zone localisation in the continental lithosphere. I use non-Newtonian, viscous models to examine the controls on strain localisation with depth and on the development of horizontal shear-zones in regions away from strength contrasts. I show how the vertical extent of strain localisation is principally controlled by lithology and geothermal gradient, and how the horizontal extent of localisation is a consequence of strain-weakening and the geometry of strength contrasts.

I explore how strain localisation develops from an initial isolated weak inclusion. The progress of strain localisation follows a power-law growth that is strongly non-linear. When applied to the rheological laws for common lithospheric minerals, the temperature and stress-dependence provide a direct means of predicting the depth below which localisation does not occur. I apply the calculations to four major continental strike-slip zones and find observations from seismic data agree with the calculations. Localisation to the base of the lithosphere is not supported by the calculations or the geophysical data.

I use a model configured to resemble the India-Asia convergence that includes an isolated weak region within the Tibetan Plateau area and, in selected experiments, strong regions representing the Tarim and Sichuan Basins. I rotate a strong India region into a weaker Asia and observe the evolving strain. Shear zones develop adjacent and propagate outwards from the weak region. Where the Basins are present then high strain- rate zones develop adjacent to them and the overall distribution of strain within

the model is altered. A high strain-weakening component enables shear-zones to localise. Micro-plate models assume the pre-existence of such high strain regions but I show how a continuum model can initiate and grow localised deformation within a region of generally diffuse deformation.

Table of Contents

Figure Index

Table Index

Abbreviations used

β	Recovery parameter
Γ	Strain-weakening parameter
Δ	Radius of circle on a sphere
$\dot{\varepsilon}$	Strain rate
η_{eff}	Effective viscosity
Θ	Second invariant of the deviatoric stress $\left(\Theta^2 = \tau_{ij}\,\tau_{ij}\right)$
θ	Colatitude
θ'	Latitude
κ	Thermal diffusivity
λ	Thermal conductivity
ρ	Density
σ	Total stress
$\bar{\sigma}$	average stress
τ	Deviatoric stress
Φ	Rate of shear-heating
φ	Longitude
A	Pre-exponent constant
Ar	Argand number
A^{res}	Residual Helmholtz energy
ATF	Altyn-Tagh Fault
B	Strength parameter
Cp	Heat capacity
D	Thermal anomaly parameter
d	Locking depth
$\dot{E}$	Second invariant of the strain-rate $\sqrt{\dot{\varepsilon}_{ij}\,\dot{\varepsilon}_{ij}}$
e	Lithosphere surface
f_{H20}	Water fugacity
g	Gravitational acceleration
GF	Ganzi Fault
HFT	Himalayan Frontal Thrust
h	Crustal thickness
HFZ	Haiyuan Fault Zone
InSAR	Interferometric synthetic aperture radar
k	Thermal wave-number
KF	Kunlunn Fault
KKF	Karakorum Fault

L	Lithosphere thickness
LAB	Lithosphere-asthenosphere boundary
LMT	Longmen Shan Thrust
m	Grain size exponent
n	Strain exponent (stress to a power of strain rate)
NAFZ	North Anatolian Fault Zone
NNAF	Northern branch of the North Anatolian Fault
P	Pressure
p	shear-zone growth exponent
Q	Activation energy
q	Inferred fault mechanism parameter
R	Gas constant
r	Fugacity exponent
S	Final entropy of a system
s	Grain size
$\dot{s}$	Plate movement rate
SAFOD	San Andreas Fault Observatory at Depth
SAFZ	San Andreas Fault Zone
T	Temperature
t	Time
T_{ref}	Reference temperature
U	Internal energy of a system
u	Horizontal velocity
V	Activation volume
V_p	P-wave velocity
V_s	S-wave velocity
XXF	Xianshuihe-Xiaojiang Fault
$x_{i/j}$	Displacement in x or y direction

1 Motivation for study

1.1 Establishing the context: deformation at plate boundaries

Plate tectonic theory show that Earth's surface is covered in a number of rigid lithospheric plates that move over the interior asthenosphere. A key assumption is that plates transmit stress without internal deformation, any deformation being limited to narrow regions at plate boundaries. This boundary deformation is observed through tectonic and magmatic activity. All lithospheric plates are moving across the Earth's surface, and the relative motion between two plates can be described by Euler's fixed point theorem (McKenzie and Parker, 1967). Here the motion of any rigid body on the surface of a sphere can be described as a rotation around a pole, the latter referred to as an Euler pole.

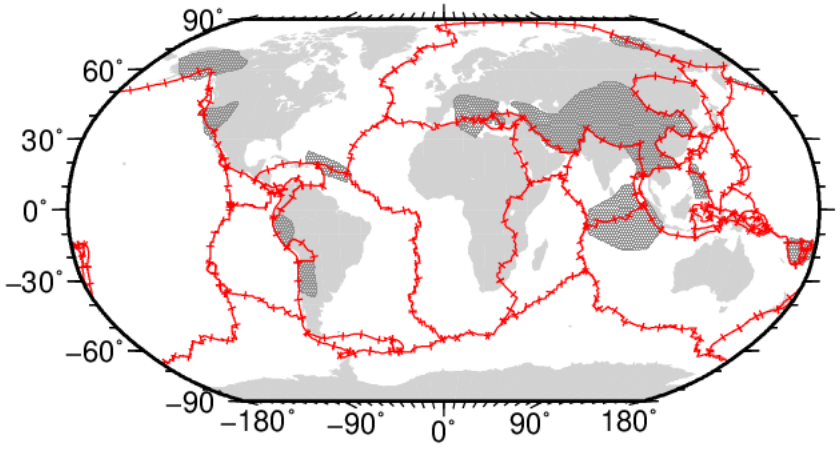

Figure 1.1: Global plate boundaries (red). Grey hashed areas indicate regions where deformation is not localised at the plate boundary but accommodated over a large region. Data after Bird (2003).

The principal that lithospheric plates are rigid and deform only at the margins applies to ~ 85% of Earth's surface (Fig. 1.1). Plate closure calculations based solely on a rigid plate assumption do not balance, and require some level of internal deformation (e.g. DeMets et al., 2010; Minster and Jordan, 1978). Geodetic data from continental regions provide quantitative evidence that a significant amount of plate motion is accommodated away from the plate boundary. Here, and at other diffuse plate boundaries, evidence for far-reaching deformation can be seen through scattered seismicity, orogenic activity and large scale (> 100 km) shear-zones and faults (England, 1987; Gordon, 1998; Molnar, 1988; Wang-Ping and Grimison, 1989).

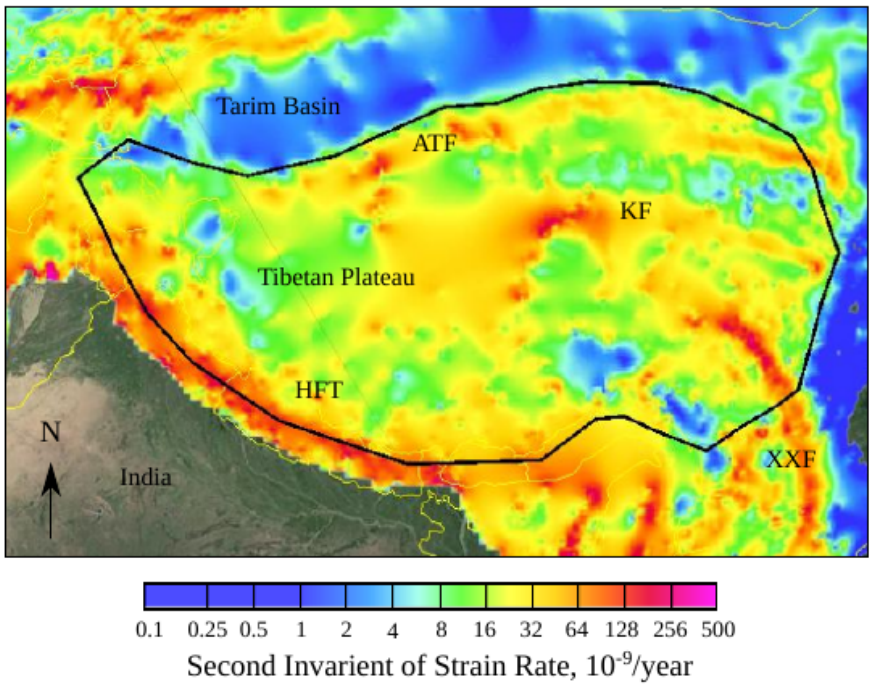

Figure 1.2: Second invariant of the surface strain-rate tensor from the Global Strain-rate Model 2 (Kreemer et al., 2014) projected onto a Google Earth view of the Tibetan Plateau (outlined by black line). Curvilinear regions of high strain-rate indicate major shear zones: ATF, Altyn-Tagh fault; HFT, Himalayan Frontal Thrust; KF, Kunlun fault; XXF, Xianshuihe-Xiaojiang fault.

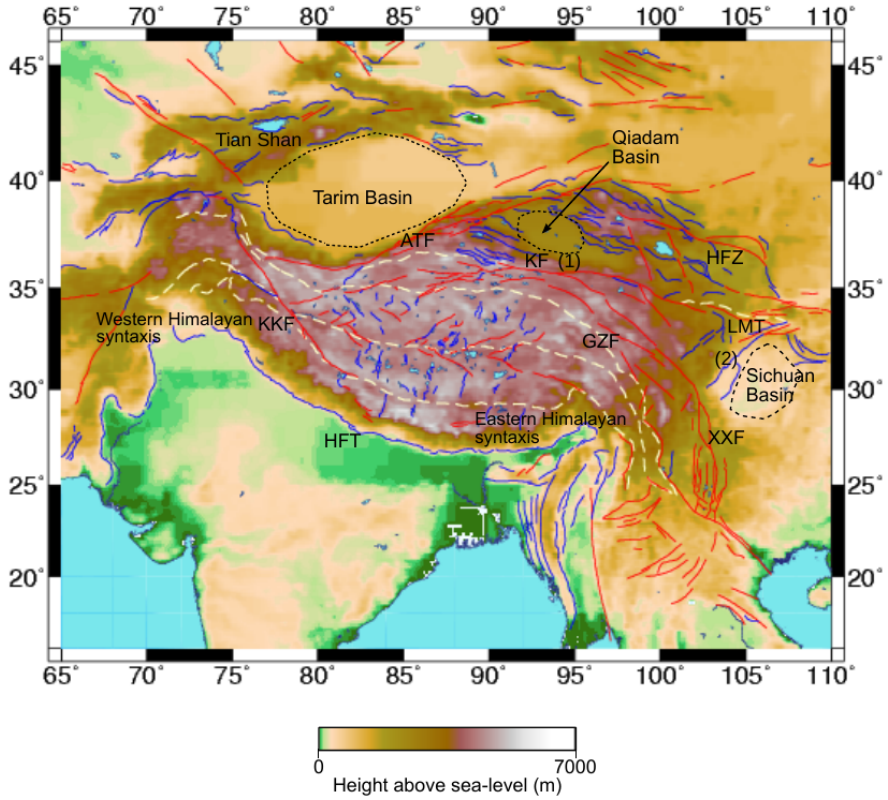

Figure 1.3: Topographical map of India and Tibet showing faults and suture zones. Strike-slip faults, red; normal and thrust faults, blue; suture zones, white dashed. Key faults labelled. ATF, Altyn-Tagh fault; GZF, Ganzi fault; HFT, Himalayan Frontal Thrust; HFZ, Haiyuan fault zone; KF, Kunlun fault; KKF, Karakorum fault; LMT, Longmen Shan Thrust; XXF, Xiangshuihe-Xiaojiang fault. Kunlun orogen (1) and Longmen Shan orogen (2). Topography data from Amante and Eakins (2009). Fault data after Styron and Okoronkwo (2010); Taylor and Yin (2009).

Diffuse deformation distant from plate boundaries can be seen in oceanic and continental tectonic environments. For example, ongoing deformation across the central Andes is partly driven by the subduction of the oceanic Nazca plate beneath the South American plate and partly by the bouyancy forces from the high elevation of the central Andes (Dalmayrac and Molnar, 1981). Seismic activity is recorded at the western

margin and in the continental interior, at a distance > 300 km from the plate boundary. A second example of diffuse deformation is found between the Australian and Indian plates, originally considered as a single plate, but now recognised as two plates separated by a region of intraplate deformation within the Indian Ocean. The historic occurrence of large (M > 7.0) earthquakes within the Indian Ocean (Stein and Okal, 1978) led to the proposal that Australia and India were two plates (Wiens et al., 1985). Plate-closure calculations showed an improved model to data fit when allowing for a diffuse plate boundary between the Central Indian Ridge and Sumatra Trench rather than assuming a single Indian-Australian plate (DeMets et al., 2010; Gordon et al., 1990). Thirdly, the boundary between the Nubia (Africa) and Somali plates is an example of diffuse deformation at a divergent plate booundary. These plates are separated by the Ethopian Rift, but geodetic observations, (e.g. Stamps et al., 2008) and plate closure models (Chu and Gordon, 1999; Horner-Johnson et al., 2007) support a region of broad deformation that extends south through the continent and offshore.

These examples show how diffuse deformation at plate boundaries occurs in a range of tectonic settings but this thesis is motivated by the India-Asia boundary, one of the largest continental regions of diffuse deformation. The Global Strain Model of Kreemer et al. (2014) compiled from horizontal geodetic velocities shows that deformation between the India and Asia plates is accommodated across the Tibetan Plateau and Tian Shan, at least 1,200 km north from the India boundary (Fig. 1.2). The initiation and ongoing deformation is driven by the northward motion of the Indian plate relative to the Eurasian plate. Contact between the India and Eurasian continental shelf occurred around 50 Ma (Meng et al., 2012). Deformation is accommodated on orogens (e.g. the Himalaya and Kunlun) and a number of large scale (> 100 km) shear zones such as the

Altyn Tagh, Karakoram-Jiali and Xianshuihe-Xiaojiang fault systems (Fig. 1.3). The shear zones (regions of localised high strain-rate) are separated by areas of relatively low-strain rate (Fig. 1.2). Why is strain unequally distributed across the Tibetan Plateau and what causes such deformation to localise in some regions and form shear zones?

1.2 Rheology and strength of the lithosphere and fault zones

The long term strength of the lithosphere can be measured by the maximum supported stress, itself a function of pressure, temperature and lithology. In the continental upper crust faults limit the strength, consistent with the empirically derived linear frictional law, normally referred to as Byerlee's law (Byerlee, 1978). Byerlee's law can be used for pressures over 1 GPa and temperatures up to 500 °C (Brace and Kohlstedt, 1980), and with increasing pressure (depth) the strength increases. However with increasing temperature (depth) thermally activated creep processes reduce viscous strength, and thus lithosphere strength is also temperature limited and geothermal gradient an important consideration (Goetze and Evans, 1979). This change with depth from a frictional to viscous controlled regime is sometimes called the brittle-ductile transition, and coincides with the maximum strength (Fig. 1.4). In addition the general change from a dominantly felsic to mafic lithology with lithosphere depth influences lithosphere strength, as mafic rocks have a higher viscosity at a given temperature.

Lithosphere strength-depth profiles can be constructed by extrapolating experimentally derived constitutive flow-laws. That laboratory conditions cannot fully replicate changes in stress and temperature with depth, nor replicate the long term strain-rates, is

an inherent limitation with this approach. While the upper crust the strength is limited by fractures and faults with increasing pressure and temperature viscous strength decreases and on long time scales the lower lithosphere deforms viscously. A general creep law for silicates may be represented by:

$$\dot{\varepsilon} = A\,\sigma^{n} f_{H_2O}^{r} s^{-m} \exp\left(\frac{-(Q+PV)}{RT}\right) \qquad \text{Eq. (1.1)}$$

where $\dot{\varepsilon}$ is strain rate, σ the stress, *n* is the power-law stress exponent, *Q* and *V* are the activation energy and volume respectively, *T* is the temperature in Kelvin, *P* is pressure, *R* is the universal gas constant, *s* is the grain size, f_{H20} is the fugacity of water, *r* and *m* are experimentally determined indices and *A* is an empirical constant determined by experiment. The values of *A*, *m*, *n* and *r* vary depending on the mineralogy and the deformation mechanism. At low stress or high temperature, diffusion creep dominates, *n* is ~ 1 and *m* > ~ 1. At greater stress or lower temperature *n* > ~ 3 and *m* is generally thought to be about zero, so that there is no grain-size sensitivity.

Using estimates of the elastic thickness (T_e), a measure of flexural rigidity, Burov and Diament (1995) determined that in addition to to the thermal structure, lithosphere strength was controlled by the decoupling the crust and mantle, and the bending stresses arising from plate loading. Differences between the rheological properties of the upper crust, lower crust and upper mantle can permit a weak lower crust, which allows the crust and mantle to decouple. This has been termed the jelly sandwich model. The occurrence of earthquakes in the upper crust and upper mantle has also been used to infer these regions are strong, and the absence of seismic activity in the lower crust as an indication that it is weak (e.g. Chen and Molnar, 1983).

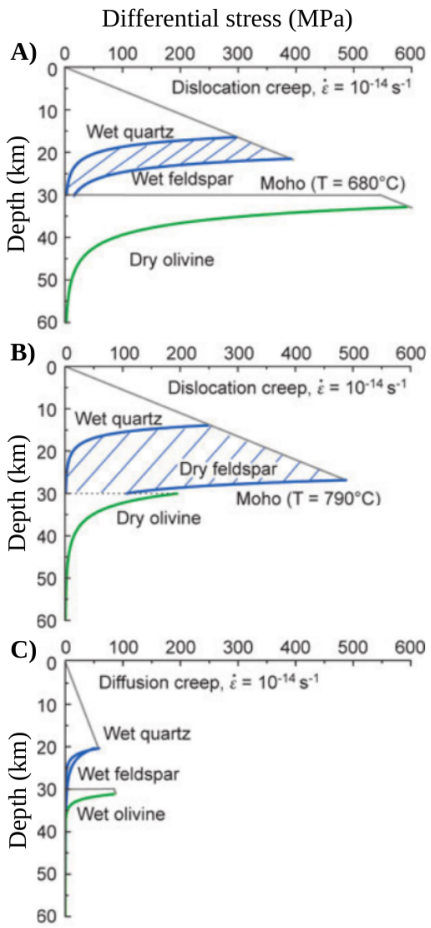

Figure 1.4: Modelled strength profiles of the continental lithosphere after Burgmann and Dresen (2008). Frictional strength initially increases in the upper-crust with depth (following Byerlee's law). Presence of fluids can increase pore-fluid pressure and reduce strength, as seen for lower crust feldspar in A and B. A) Jelly-sandwich model, characterised by a weak lower crust and stronger mantle; B) Crème brûlée model, where the mantle is weak (here a result of an increased geotherm, but presence of water would further reduce the strength of olivine); c) Banana split model (Burgmann and Dresen, 2008) in which weak shear zones extend through the depth of the lithosphere and control the overall strength of the lithosphere.

With increased data availability and improvement in analytic techniques Maggi et al. (2000a, b) concluded that continental lithosphere earthquakes are confined to the crust. This led Jackson (2002) to propose an alternative to the jelly sandwich model, where a strong upper lithosphere overlays a weaker lower lithosphere, commonly termed the crème-brûlée model.

The experimentally derived flow laws show that the presence of water can strongly influence the strength profile (see Fig. 1.4). In the continent fluid sources can include metasomatic fluids, or originate from subduction processes. Strength profiles for the jelly-sandwich model can be fulfilled by allowing for a wet lower-crust and a dry upper mantle, and for the crème-brûlée model by allowing for wet upper mantle and either a dry or wet lower crust.

Alternatively the strength of the lithosphere may be limited by major shear zones. Faults within the upper crust are frictionally very weak (e.g. Zoback et al., 1987), and at depth shear zones in the viscous regime can potentially localise through a number of strain-weakening mechanisms (see section 1.5).

Dislocation models, which consider a rectangular fault within an elastic half-space, can be used to model interseismic deformation near faults (e.g. Okada, 1992). Here, the brittle crust deforms elastically in response to the far field plate displacement rate and ductile deformation at depth. In the seismic cycle model of Savage (1983) subduction zone faults are locked in the shallow crust, with the slip deficit recovered during earthquakes. Below the locked section the fault is assumed to slip at the far-field deformation rate. Using relevant geodetic data, this approach has been used to model

slip-rates across faults (e.g. Elliott et al., 2008; Hussain et al., 2016; Zhang et al., 2007). This mathematical model acts as a proxy for shear zone width, which increases non-linearly with depth (e.g. Vauchez et al., 1998).

1.3 Overview of modelling deformation of the Tibetan Plateau

1.3.1 Approaches to modelling Tibet deformation

Two end member models have been invoked to explain the deformation field in the collision zone. The first is the micro-plate or block model, that assumes that the lithosphere is pre-divided into a number of smaller rigid blocks. In common with large scale plate tectonics, deformation occurs primarily on the edge of the blocks. Such micro-plate models use kinematic data - velocity data of surface movement obtained through morphological offsets along shear zones or geodetically derived estimates through the use of GPS or InSAR. Micro-plate boundaries are identified as the regions where the highest strain rates occur, i.e. where the fault zones are weaker than the adjacent crust. This approach uses the velocity field to describe deformation, and has been adopted by Avouac and Tapponnier (1993); Chen et al. (2004); Meade (2007); Thatcher (2009). Globally the sum of all proposed micro-plate surface areas is smaller than that of any major plate.

The second modelling approach is the continuum model. Here, the long term deformation of the continental lithosphere can be modelled by assuming continuous viscous flow that follows a power-law rheology (England and McKenzie, 1982). In section 1.3.3 I discuss a range of published analogue and numerical models of the India-

Asia convergence. However, in this thesis I choose to focus on the thin viscous sheet model developed by England & McKenzie (1982) and the application using the finite element method developed by Houseman & England (1986), see section 1.3.4. Here it is assumed deformation is controlled by the viscous lower crust and upper mantle, and faults in the upper crust follow the viscous deformation field. The thin sheet approximation assumes vertical gradients of horizontal velocity are negligible, allowing stress to be integrated with depth, and that the strength properties of the lithosphere are averaged with depth so that the resistance to deformation is defined by a depth-averaged effective viscosity (Sonder and England, 1986).

England & Houseman (1986) applied thin viscous sheet models to the India-Asia continental collision. The governing equations are presented in Chapter Two but can be summarised as follows. Flow within the thin sheet is driven by external boundary forces and interior forces from gradients in crustal thickness; it is dependent on the stress exponent, (where $n = 1$ for Newtonian rheology and $n > 1$ for a power-law rheology), and the ratio of stress from the crustal thickness differences and the stress required to deform the layer at a required strain-rate (the Argand number, *Ar*). Such models allow for a self-consistent determination of stress and strain-rate fields. They require a choice of boundary conditions and the extent to which the crustal thickness gradients contribute towards deformation, together with the relative lithosphere rheology and lateral variation thereof.

1.3.2 Overview of Tibet micro-plate models

Initial micro-plate models used geologically derived estimates of shortening and slip-rates across major fault zones to derive a velocity field. Avouac and Tapponnier (1993) divide Central Asia into four blocks (Siberia, Tarim, Tibet, India-Asia) separated by the Himalyan and Tian Shan thrust zones and the Altyn-Tagh and Karakorum strike-slip faults. Using a geologically derived velocity field they calculate the best fit Euler-vectors to describe the motion of the blocks, and propose that movement along the block boundaries accounts for most of the convergence between India and Western Siberia. With increasing geodetic data coverage over the Tibetan Plateau, Tian Shan and

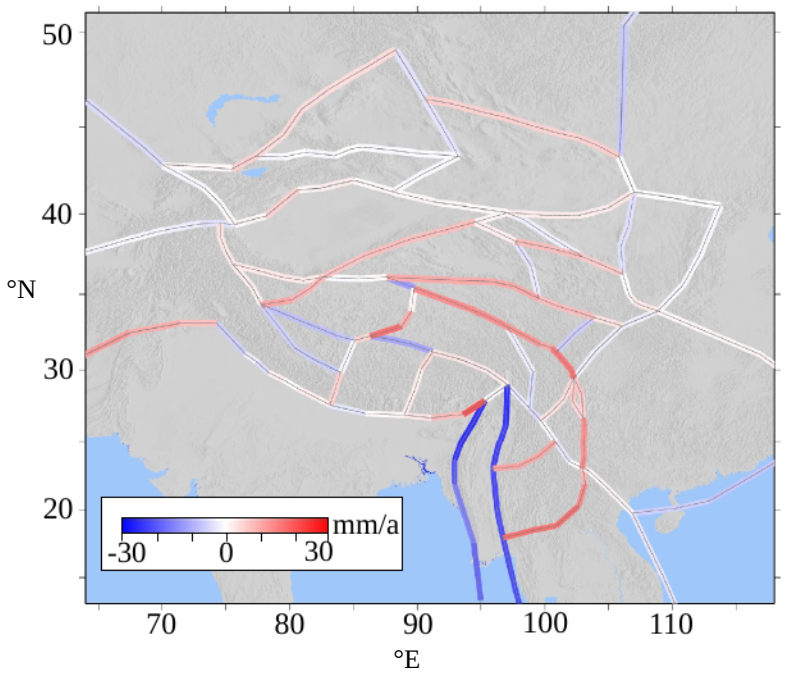

Figure 1.5: Kinematic model from Wang et al. (2017) showing division of Tibet, Tian Shan and western China into blocks. The colour shows estimates of slip-rate along each boundary, positive values indicate left lateral motion.

western China, alongside the major faults, an increasing number of minor faults (those with relatively low slip-rates and along-strike distance) are used to define the micro-plate boundaries (e.g. Fig. 1.5). Consequently the number of proposed micro-plates has increased in order to fit the geodetic data (Fig. 1.6). For example, Meade (2007) combined geological and geodetic measurements to divide the greater Tibetan Plateau region into 17 blocks bound by faults. Meade (2007) predicted faults in the south-east region, with no observed data supporting their existence, but found inclusion resulted in a better fit between the modelled and observed velocity field.

The block model of Avouac and Tapponnier (1993) requires a low number of faults to exhibit high slip-rates and thus accommodate block interior velocities. Increasing the number of blocks may account for deformation within larger blocks, but minor faults, although more numerous, accommodate an order of magnitude less deformation (Cowgill et al., 2009; Peltzer and Saucier, 1996) and do not show the concentration of earthquakes and volcanoes observed at major plate boundaries. Block models may therefore over-estimate the scale and rate of deformation along the minor faults (Cowgill et al., 2009). Micro-plate models may permit internal deformation, where multiple smaller faults with relatively low slip-rate compared to the major boundary faults (Chen et al., 2004; Langstaff and Meade, 2013), but in doing so approach the concept of a continuum model.

Deformation controlled by rigid blocks predicts high velocity gradients across the boundaries. The Tibetan Plateau has shortening rate an order of magnitude greater than the blocks surrounding it (Zhang et al., 2004) and velocity gradients generally are not concentrated into narrow zones, but occur over distances > 400 km, inconsistent with

elastic strain produced by slip on faults or localised shear zones (Fig. 1.7). Geodetic and geological observed slip rates of ~ 10 mm.yr^{-1} across major faults, e.g. the Altyn Tagh, Karakorum and Kunlun (Fig. 1.3), are around half that of the ~ 20 to 30 mm.yr^{-1} (e.g. Tapponnier et al., 2001) required by block models (Zhang et al., 2004).

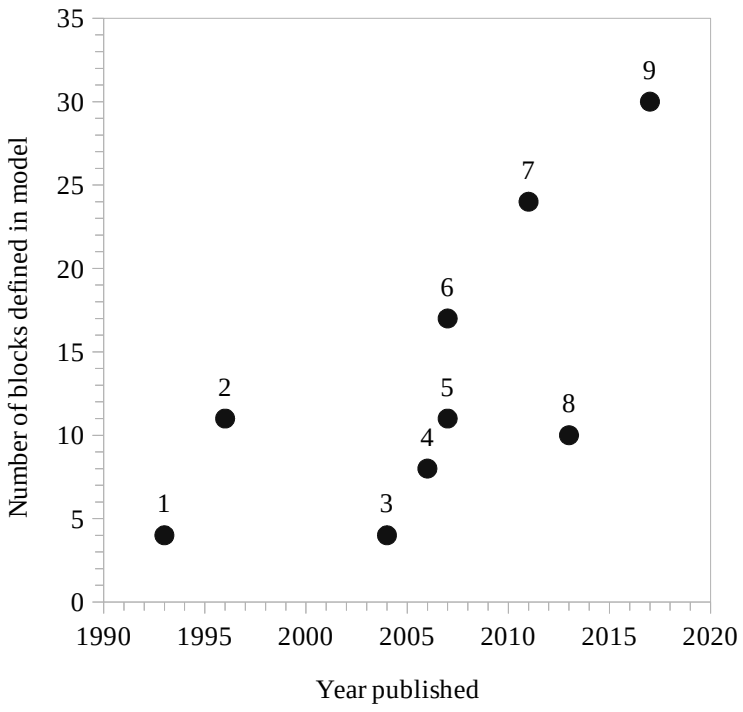

Figure 1.6: Kinematic models of deformation of Tibet and central Asia divides the region into a number of blocks bound by faults. GPS station coverage has increased from 45 (Chen et al., 2004) to 1854 (Wang et al., 2017) and corresponds to a general increase in the number of blocks. Models by Chen et al. (2004) and Langstraff & Meade (2013) permit deformation within the blocks. 1, Avouac and Tapponnier (1993); 2, Peltzer and Saucier (1996); 3, Chen et al. (2004); 4, Calais et al. (2006); 5, Thatcher (2009); 6, Meade (2007); 7, Loveless and Meade (2011); 8, Langstaff and Meade (2013); 9, Wang et al. (2017) (shown in Fig. 1.5).

Micro-plate models assume that the rigid behaviour of the faulted crust is representative of the bulk rheological behaviour of the lithosphere. They offer no explanation on the

origin of faults defining the mico-plate boundaries. The contrast between the gradational change in geodetic velocities observed across Tibet (e.g. Wang et al., 2019; Wang and Wright, 2012) and the strain-rate maps constrained by geodetic data and plate boundaries (Kreemer et al., 2014) raises questions on how important localised strain is in accommodating deformation.

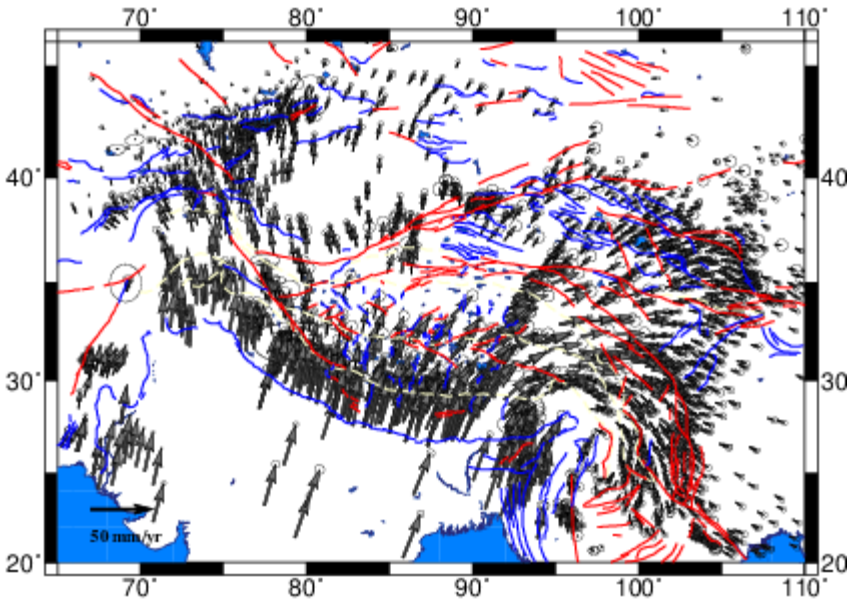

Figure 1.7: Fault location overlaying scaled geodetic derived velocities, reference frame Eurasia where the ellipse marks the 95% confidence level. Coloured lines represent: strike-slip faults, red; normal and thrust faults, blue; suture zones, white dashed. Fault data after Styron and Okoronkwo (2010) and Taylor and Yin (2009); geodetic data after Zheng et al. (2017).

1.3.3 Overview of Tibet continuum models

Numerical and analogue models are used to explore the parameters that can result in replicating, generally to a first order, observations of present day process, for example topography and surface velocities. Earthquake (e.g. Jackson, 2002) and gravity (e.g.

McKenzie and Fairhead, 1997) data indicate the India continental lithosphere is relatively strong. Therefore models typically assign a relatively high viscosity to the Indian continental lithosphere in comparison to the Asian continental lithosphere. Low elevation and relief suggest the Tarim and Sichuan Basins undergo less deformation than the surrounding regions. The Sichuan Basin is stationary within a China reference frame (Shen et al., 2005) while GPS data suggest the Tarim Basin is rotating as a block clockwise relative to a stable Eurasia (Taylor and Yin, 2009). Therefore the Tarim and Sichuan Basins, where included, are also assigned a higher viscosity than the surrounding Asian lithosphere.

The contribution of Tibetan crustal flow processes to deformation in south-east Tibet was examined by Copley and McKenzie (2007). Their model used a vertically averaged but laterally varying viscosity, stress-free upper surfaces and, following McKenzie et al. (2000), a deformable base layer to maintain isostatic equilibrium. The Sichuan Basin and Eastern Syntaxis were represented as a rigid walls. Deformation was driven by topographical gradients and a zero velocity condition was applied to the external boundaries. Comparison of observed and modelled surface velocities suggests a viscosity below southern Tibet of ~ 10^{20} Pa.s and between the Sichuan Basin and the Eastern Syntaxis ~ 10^{22} Pa.s. Copley and McKenzie (2007) further propose a rigid crustal base beneath southern Tibet (likely supported by the India lithosphere) and a stress-free base, i.e. deformable, between the Sichuan Basin and the Eastern Syntaxis.

The regional morphology of Tibet may be explained by flow in a weak lower crust, numerically modelled as a Newtonian viscous fluid in a channel with fixed, rigid boundaries (Clark et al., 2005). Here unidirectional, parabolic channel flow is driven by

horizontal pressure gradients associated with topographical gradients. An overlaying elastic layer deforms in response to the pressures arising from channel flow, and this layer deforms continuously. The stresses are proportionally related to the mean velocity and viscosity of the channel fluid and have an inverse square relationship to the channel thickness. Clark et al. (2005) found that pressure gradients around a rigid object in the channel, representative of the Sichuan Basin could explain the topography of eastern Tibet.

The influence of crustal heterogeneities on uplift and surface deformation in Tibet was examined by Cook and Royden (2008). Using a three-dimensional continuum model with a Newtonian viscous crust, their model incorporates two horizontal layers, representing the upper and low crust. For each layer the viscosity is invariant with depth but can be varied laterally. Boundary conditions impose a zero horizontal shear stress at the top, vertical gradients in stress as proportional to the topographical gradient, and a horizontal velocity on the base of the model. Isostatic equilibrium is assumed, and the crustal thickness evolves in response to the imposed basal velocity and the vertical stress gradients arising from the developing topography. Cook and Royden (2008) showed how a strong crust resists shortening and promotes a steep plateau margin, whereas a weak crust is subject to rapid uplift and produces a gently sloped plateau margin. By including a strong Tarim and Sichuan basin, and a weak south-eastern corner of Tibet, Cook and Royden (2008) were able to replicate the Tibetan Plateau morphology and the present day surface around the eastern syntaxis. The weakened south-eastern region may also promote east-west extension across the Plateau.

Lechmann et al. (2014) considered how mechanical layering of the lithosphere and the strength of the lower-crust influenced surface velocities, strain-rates and stress fields in the India-Asia convergence zone. Their three-dimensional numerical model is laterally divided into regions representing the India oceanic lithosphere, India continental lithosphere and Asian continental lithosphere. Each region has four horizontal layers, representing the upper and lower crust, and upper and lower lithospheric mantle. Rigid Tarim and Sichuan Basins are included, as are weak zones representing the Quetta-Chaman and Sagaing strike-slip faults. A viscous only rheology is used throughout, where viscosity is assigned a temperature (depth) dependence and for simplicity variations due to strain-rate are ignored. To assess the influence of topographical gradients on deformation then initially only gravitational potential energy is used as a driving force. Here, the bottom layer of the model is subject to a free slip condition (zero normal velocity, zero tangential stress) and the top later to a free surface condition (zero normal stress). In a second set of experiments a velocity is applied to the southern boundary, causing the Indian continent to indent Asia.

Experimental results found the reasonable variations in crustal density causes little difference in the surface velocity and stress fields. Varying the Indian lower crust viscosity by three orders of magnitude also had limited impact on surface velocity, leading Lechmann et al. (2014) to suggest that measured surface velocity alone is insufficient to constrain deformation at depth or the extent to which the crust and mantle lithosphere are coupled. The viscosity of weak zones, representative of large-scale strike-slip faults, strongly influenced the horizontal velocities. Where vertical stresses are high, they will override the horizontal forces that originate from an indenting India.

Schellart et al. (2019) used an analogue model to explore deformation in Asia arising from the India-Asia convergence. They found extension forces, arising from subduction rollback on the West Pacific and Sundaland margins, could explain east-west extension in Tibet and eastward continental extrusion, dependent on the rate of convergence of India. The approach is supported by evidence of Eocene-Oligocene continental extensional deformation and strike-slip faulting around the Western Pacific rim.

1.3.4 Overview of Tibet thin viscous sheet models

Thin viscous sheet models representing the India-Asia convergence, where a strong region indents a weaker one, show when shortening occurs, both strike-slip and crustal thickening occur (England and McKenzie, 1982; Houseman and England, 1986). The thin-sheet formulation provides a quantitative method of determining the balance between these two modes of deformation and how that balance evolves as a plateau of thick crust is formed in front of the collision boundary.

Plane strain models enforce convergence to be accommodated by extrusion (Tapponnier et al., 1982; Vilotte et al., 1984) and provide no information on the contribution of crustal thickening to the deformation. For a thin viscous sheet approach under a plane stress condition where only the boundary forces contribute to deformation, gradients in crustal thickness still occur in response to spatial gradients of strain. Increasing the ratio of stress from the crustal thickness differences to the stress required to deform the layer at a required strain-rate ($Ar > 0$), means the gradients of crustal thickness increasingly contribute to the deformation and the maximum crustal thickness gradient supported by the sheet decreases. For $Ar = 1$ or 3 in a region subject to bulk shortening the gradients

in crustal thickness become sufficiently high that a local extensional regime results (England and McKenzie, 1982). For $Ar \geq 3$ deformation in the brittle layer changes from thrust fault to strike-slip fault dominated (Houseman and England, 1986). For an averaged lithosphere rheology where $n = 3$ or 10 and $Ar = 0$ to 10 shortening from the India-Asia convergence is accommodated by a ratio of crustal thickening and lateral extrusion at a minimum 3:1 (Houseman and England, 1993). The transition of the Tibetan Plateau from a purely shortening regime to one with an extensional component occurred ~ 8 Ma (Molnar et al., 1993). (England and Houseman, 1989) show this could be explained by convective thinning, replacement of a cold lower lithosphere by hot asthenosphere, represented by increasing *Ar* once a critical lithosphere thickness is obtained.

With no lateral variations in strength or topography, the thin viscous sheet subjected to stress will show a velocity field that smoothly decays away from a stress concentration on the boundary. Lateral variations in strength influence the deformation field (England and Houseman, 1985) and strong regions may transmit stress to weaker regions (Neil and Houseman, 1997). The inclusion of a region stronger than the background, analogous to the Tarim Basin in a model of the India-Asia collision, concentrates deformation at the boundary within the weaker region (Dayem et al., 2009; England and Houseman, 1985; Neil and Houseman, 1997). Elevation and total strain remain relatively low in the stronger Basin region and crustal thickness (and hence elevation) increase around it, with strike-slip deformation developing when the boundary is oblique to the convergence direction (England and Houseman, 1985). A strong Tarim Basin can transfer stress north of the Basin, with the resultant crustal thickening forming the Tian Shan range (Fig. 1.3) (Neil and Houseman, 1997). Here an improved

match between modelled and observed crustal thickness occurs when the Tian Shan is made weaker than the surrounding region and a strong Tarim Basin is retained.

The India-Asia convergence model of Dayem et al. (2009) also contained a strong region representing the Tarim Basin. With increasing time a high strain region formed along the southern boundary of the strong basin. Dayem et al. (2009) found that increasing n and decreasing Ar narrowed the width of the shear zone. However, for the strain to sufficiently localise to a width comparable to the present day Altyn Tagh Fault (Fig. 1.3) within the time-frame of the convergence then $n >> 10$ was required, assuming a low-temperature plasticity deformation law (Evans and Goetze, 1979). Localisation occurred for $n \sim 10$ when a strain-dependent weakening component was included, such as a temperature increase due to shear heating.

The thin viscous sheet model depth averages the strength properties of the lithosphere. The development of linear high strain-rate regions represent the averaged properties of a lithosphere-scale shear zone. Such shear-zones are typically depicted as a localised fault plane in the upper lithosphere above a ductile shear-zone whose width increases with depth in the mid to lower lithosphere (e.g. Burgmann and Dresen, 2008; Moore and Parsons, 2015; Vauchez et al., 1998).

1.4 Numerical approach to modelling continental collision zones

Numerical models of tectonic processes enable exploration of the parameters that may control the observed velocity, strain-rates and stress-fields and, importantly, can identify

implausible scenarios. They contain equations relating to continuity (conservation of mass), motion (conservation of momentum, the Navier-Stokes equations) and temperature (conservation of energy). Different approaches are used to approximate the solution of these differential equations. The finite element method can be used for continental collision problems (e.g. England and McKenzie, 1982; Garthwaite and Houseman, 2011; Houseman and England, 1986; Lechmann et al., 2014), and details of this approach are given in sections 2.3 and 2.4.

Numerical models will differ in the assumptions and simplifications they make. Parameters can be constrained within ranges inferred from geophysical observations, but will still retain a degree of uncertainty. Lateral and depth variations in viscosity, temperature and relative strength have to be considered. Boundary conditions may stipulate zero or set a traction at the base of the model, a free or sticky air at the top of the model, and an imposed or zero velocity or traction condition at the edges. These boundary conditions may be fixed or time-dependent. The later requires assumptions about when and where the boundary conditions change, which may be inferred from paleo-magnetic studies. Deformation may be subject to a plane strain or plane stress condition, and the constitutive equations may stipulate elastic, viscous, visco-plastic or visco-elastic behaviour. The inclusion or absence of erosional processes and instantaneous or time dependent isostasy are also considered.

A numerical model can use a two-dimensional (2D) (e.g. Houseman & England, 1986) or three-dimensional (3D) (e.g. Cook and Royden, 2008; Lechmann et al., 2014) framework. A 3D model can allow for both lateral and depth variations, for example in rheology and constitutive laws, and also include interactions between horizontal layers

(e.g. Lechmann et al., 2014). The results can provide depth dependent information alongside horizontally varying deformation. They are computationally expensive in comparison to 2D models.

A 2D model can consider the lithosphere as a vertical slice, or as horizontal layer where depth properties are averaged. Vertical slices are used where depth dependent properties are essential, such as modelling subduction slabs or rift settings. For example, the 2D vertical section used by Jourdon et al. (2019) examines how rift maturity influences orogenic processes in convergence zones. This model allows different rheological flow laws to be set for the upper crust, lower crust, mantle lithosphere and asthenosphere. Brittle deformation in the upper lithosphere is represented through the Drucker–Prager yield criterion, which determines if failure or continuous deformation occurs in the upper crust. In a series of experiments Jourdon et al. (2019) subjected a region representing a vertical lithosphere section to extension to replicate rift processes, before inverting to simulate convergence processes. The vertical section shows the development of dip and depth extent of such shear zones, along with thrusting and folding which would not be apparent in a 2D horizontal model.

2D horizontal sections are used where lateral variations in rheology and boundary conditions are important, such as continental convergence processes. These models may provide information on surface velocities and the lateral variation in strain-rates, stress field and topography. Throughout this thesis I use the 2D horizontal thin viscous sheet model (formulation presented in Chapter Two) in order to explore controls on strain-rates and topography and compare to present day data.

My approach will use the thin viscous sheet approximation, initially developed by Bird and Piper (1980), England and McKenzie (1982) and Houseman and England (1986). The three-dimensional properties of the lithosphere are reduced to two-dimensions (thin sheet) by assuming the horizontal gradient of the vertical components is approximately zero, allowing stress to be integrated with depth (see sections 2.3.2). The averaged vertical strength of the continental lithosphere can be approximated by a power-law relationship, with a stress exponent *n*, and a strength parameter, the Argand number (Ar) (Sonder and England, 1986). This is the equivalent of the brittle regime deforming under Byerlee's Law and the ductile regime under steady-state creep (see section 1.2) under long term geological strain-rates. However, in averaging the vertical stress and strain-rate it assumes rheological behaviour is non-linear at the top of the lithosphere, and near linear at the base, in contrast to the behaviour suggested by laboratory derived experimental flow laws (section 1.2). The values of *n* and *Ar* depend on the geothermal gradient, Moho temperature and the stress regime in the upper crust. The value of *n* increases with the proportion of brittle behaviour. Thus a representative stress-strain rheology is used even where the upper crust layer is faulted. However, the depth averaged behaviour means discontinuities limited to the upper crust are not explicitly shown on the horizontal section.

In allowing changes in crustal thickness, the horizontal stresses arising from gradients of crustal thickness can be included in the force balance equations. The ratio of the contribution of crustal thickness to the stress required to deform the sheet at the given strain-rates can be adjusted. This allows for variations in effective viscosity that would arise from variations in lithosphere age and temperature.

Comparison of the two-dimensional thin viscous sheet approximation with three-dimensional solutions of a problem representing continental convergence, found the former model provided a good first order estimate of deformation away from the indenter (Garthwaite and Houseman, 2011). The thin viscous sheet model overestimates vertical strain rates where horizontal strain rates are large, such as at an indenter corner. This is because, in contrast to the 3D model, the thin viscous sheet model ignores vertical shear tractions and assumes horizontal gradients of strain rate are invariant with depth. These errors are reduced where the width of an indenter is much greater than the assumed layer thickness, as for the case of the India-Asia convergence.

The thin viscous sheet model permits systematic exploration of the parameters that control shear zone formation. Relevant factors include lithological heterogeneity, the relative importance of diffusion (Newtonian) and dislocation (power-law) creep mechanisms, and the inclusion of strain-weakening and recovery. The numerical models are calculated in the finite element program, *basil*. While a two-dimensional approach averages the influence of lower crustal flow that can be shown in a three-dimensional power-law viscous models (e.g. Lechmann et al., 2014) they have the advantage of being computationally inexpensive. Model outcomes may be potentially applied in more complex 3D models where changing depth properties may be an important control on the deformation process.

1.5 Strain-weakening: natural observations, experiment results and numerical implementation

Localisation of strain may be enhanced by strain-rate weakening in regions where stress differences vary. For the non-Newtonian constitutive laws that typically describe creep deformation of silicates (Hirth and Kohlstedt, 1995; Karato, 1984; Karato et al., 1986; Kohlstedt and Goetze, 1974) effective viscosity is reduced where the concentration of intra-crystalline dislocations is increased in response to greater stress differences. However, the degree of localisation evident in lithospheric-scale shear zones is not explained simply by power-law materials with typical stress versus strain-rate exponents of $n \sim 3$ (Dayem et al., 2009). A strain-weakening process is also required to explain the formation of lithospheric shear zones like the Altyn Tagh, the San Andreas and the North Anatolian. Lithospheric-scale strain-weakening mechanisms based on shear heating (Brun and Cobbold, 1980; Burg and Schmalholz, 2008; Leloup et al., 1999; Regenauer-Lieb et al., 2015; Thielmann and Kaus, 2012), fabric development (e.g. Montési, 2013), grain size sensitive creep (e.g. Precigout and Gueydan, 2009; Warren and Hirth, 2006), and partial melting (e.g. Nabelek et al., 2010; Tommasi et al., 1995) have been proposed. Independent of scale, localisation requires a weakening feedback mechanism that can depend on one or more variables, including changes in temperature and grain-size (Montési and Zuber, 2002). For any weakening mechanism, spatial variations in the work done by deformation cause variations in the strength of the material and thereby promote localisation of deformation.

The extent to which field observations support a thermal strain-weakening mechanism is debatable as geological examples of shear-zone metamorphism can be attributed to

either shear-heating or alternative heat sources, such as hot fluids (see Platt, 2015). Laboratory experiments, show that under a brittle deformation regime shear-heating can increase the temperature by 100 °C (Ben-Zion and Sammis, 2013) but the validity of extrapolating these results to greater depths is questionable. Thielmann and Kaus (2012) showed how shear heating could facilitate the formation of a lithospheric-scale shear zone. In some situations shear heating may be sufficient to cause partial melting and extreme strain localisation (Nicolas et al., 1977; Regenauer-Lieb et al., 2015).

Numerical models using shear heating take the conservation of energy equation as applied to an ideal shear-zone, where temperature variations occur only normal to the boundaries and the specific heat (C) and conductivity (k) are assumed constant. This allows the temperature change ($\partial T/\partial t$) to be simply described as:

$C\frac{\partial T}{\partial t}=k\frac{\partial^2 T}{\partial y^2}+\dot{e}$ (Brun and Cobbold, 1980)	Eq. (1.2)

where $\partial^2T/\partial y^2$ is the heat lost and $\dot{e}$ is the rate of energy dissipated per unit volume. For numerical models that include strain-weakening through shear heating $\dot{e}$ can be given by:

$\dot{e}=\tau_{ij}\dot{\varepsilon}$	Eq. (1.3)

where τ is the deviatoric stress and here $\dot{\varepsilon}$ represents either the viscous strain-rate or the plastic and viscous strain-rate (e.g. Burg and Schmalholz, 2008; Kaus and Podladchikov, 2006; Thielmann and Kaus, 2012). By implementing a temperature dependent viscosity (η), such as that used by Burg and Schmalholz (2008):

$\eta = A^{-1/n} \dot{\varepsilon}^{\frac{1}{n}-1} \exp\left(\frac{Q}{nRT}\right)$	Eq. (1.4)

where $\dot{\varepsilon}$ is the strain-rate, *A* is an experimentally derived empirical constant, *n* the power-law creep exponent, *Q* the activation energy and *R* the universal gas constant, then under a constant stress condition a temperature increase, and consequential viscosity reduction, increases the local strain-rate.

Laboratory experiments and numerical models also support localisation through grain size changes. Braun et al. (1999) demonstrate transient localisation at constant temperature, provided that the grain size sensitivity is highly non-linear, but found grain growth may inhibit localisation. However, grain growth through recrystallisation may be impeded by Zener pinning (Bercovici and Ricard, 2012), a process that influences the movement of grain boundaries in poly-phase materials. Grain size analysis of quartz mylonites suggest the presence of graphite inhibits grain growth, thus promote grain boundary sliding over dislocation creep (Krabbendam et al., 2003). Similarly, experiments of deforming feldspar aggregates in the dislocation creep regime show recrystallisation to a smaller grain size during deformation, which would result in weakening (Tullis and Yund, 1985).

Numerical models use experimentally derived flow laws for dislocation and diffusion creep, the later of which has a grain size dependence (e.g. Braun et al., 1999; Montési and Hirth, 2003; Precigout and Gueydan, 2009). Numerical experiments by Gardner et al. (2017) show that inclusion of a feedback mechanism, representative of a transfer from a dislocation creep to diffusion creep (or grain boundary sliding) regime, allows

strain to localised on to interconnected weak layers. Braun et al. (1999) assume that dislocation and grain-size sensitive creep operate independently and that effective viscosity is a combination of these processes. Grain-size changes are proportional to the strain-rate and constrained by the equilibrium grain-size value for a given stress. Grain growth may be included, where grain-size-sensitive creep is the dominant mechanism, by modifying the rate of grain-size change equation to include a temperature component. Kameyama et al. (1997) included a Newtonian viscosity, with a temperature and grain size dependence, and a non-Newtonian, with a temperature and shear-stress dependence but independent of grain size.

Geological observations and laboratory experiments show deformation in mineral aggregate is preferentially accommodated on weak minerals (e.g. Holyoke and Tullis, 2006a) which interconnect and form localised zones (e.g. Holyoke and Tullis, 2006b). Weak mineral phases may be pre-existing or arise through deformation induced mineral reactions (e.g. serpentinised olivine, Escartín et al., 2001; Reinen et al., 1991). These reactions may in turn may enhance strain localisation through the release of fluids (Holyoke and Tullis, 2006b). Mid-crustal (8 to 15 km) samples from high strain regions of the the Great Glen Fault Zone (Scotland) show localised deformation on interconnected cataclastic shear zones (Stewart et al., 2000). Calculations suggest that large-scale localisation, capable of forming plate boundaries, requires the interconnection of weak mineral phases that have a high-strength contrast between the surrounding minerals (Montési, 2013). Although Montési (2013) calculate that interconnected weak layers formed parallel to the direction of shear have the potential to localise strain, no numerical analysis of how development from separated to interconnected weak phases in relation to deformation is provided.

Ultimately numerical models are limited by the extrapolation of experimentally derived rheological laws. Laboratory conditions cannot replicate slow geological strain-rates, the heterogeneity of the lithosphere and the high pressures and temperatures of the lower lithosphere.

Thin viscous sheet models typically lack the self-consistent formation of shear zones as seen in the strain-rate map of Kreemer et al. (2014), hence the need to modify the model to incorporate a strain localisation mechanism. This thesis follows Dayem et al. (2009) by including a strain localisation mechanism in the model. Here I choose to focus on how shear-heating influences strain localisation. I acknowledge that other localisation mechanisms, such as grain-size changes (e.g. Precigout et al., 2007), fabric development (e.g. Dell'Angelo and Tullis, 1996; Montési, 2013), change to weaker mineral phases (e.g. Urai and Feenstra, 2001), or hydrolytic weakening (e.g. Karato, 2006; Selway, 2013) may also initiate and/or sustain strain localisation.

1.6 Aims of this thesis

1.6.1 Questions arising regarding lithosphere shear-zone formation

The micro-plate model approach does not predict the formation of shear-zones, but uses their existence to explain kinematic data, and fails to explain the extent of strain-rate variation seen across the Tibetan Plateau. Thin viscous sheet models of the India-Asia convergence have shown how deformation can localise adjacent to a strong region but not how shear zones might develop across the Tibetan Plateau. Can models be

developed that permit localised deformation within a general diffuse deformation field? Is it possible to quantify the relative contributions of localised versus diffuse deformation in a region like the Tibetan Plateau?

Large-scale lateral variations in rheology of continental lithosphere arise through orogenesis, pluton emplacement, thermal evolution and other geological processes (Cloetingh et al., 2010). I found no prior work that exclusively examined the role of weak regions in shear zone formation in thin viscous sheet models, or how the presence of weak regions influenced deformation within the Tibetan Plateau. Thin viscous sheet models of the India-Asia convergence that include lateral strength contrasts have focused on the inclusion of a strong region representing the Tarim Basin (e.g. Dayem et al., 2009; Neil and Houseman, 1997). The Sichuan Basin (Fig. 1.3) is a relatively undeformed strong region ~ 230,000 km^2 (Fig. 1.2) on the east boundary of the Tibetan Plateau and has yet to be included in thin viscous sheet models. The abrupt decrease in GPS velocities from the Tibetan Plateau to the Sichuan Basin infers a Basin influence on deformation in the south-eastern Plateau (Shen et al., 2005). The associated deformation may, through shear-zone linkage, enable deformation across the Plateau.

The addition of a strain-dependent weakening component in the formulation can be represented by reducing the average strength of the lithosphere in proportion to the work done in deforming it (Dayem et al., 2009). The weakening can represent a physical process such as temperature increase due to shear-heating, producing a reduction in viscosity. Dayem et al. (2009) presented calculations in which the strain-dependent weakening remains active throughout deformation, implying a continual temperature rise. In practice the rate of temperature increase would slow due to thermal

conduction and, assuming a constant strain-rate, eventually reaches equilibrium (e.g. Kaus & Podladchikov, 2006).

Whether the lithosphere deforms as a continuum or as a series of blocks, brittle upper crustal deformation can be observed by the presence of faults. It has been suggested that the long-term continental lithospheric strength is controlled by the relative weakness of plate boundaries and major fault zones (e.g. Burgmann and Dresen, 2008), which infers such fault zones remain relatively localised through the lower crust and upper mantle. What controls the maximum lithosphere depth that supports a localised shear-zone?

1.6.2 Principal questions addressed in this thesis

This thesis will examine four principal questions.

1. Using a thin viscous sheet approach, how does a low-viscosity region influence the temporal and spatial strain distribution?
2. How may I quantify the process of strain-localisation in thin viscous sheet models of lithospheric deformation?
3. What is the maximum depth to which strain localisation is supported in the lithosphere?
4. For a thin viscous sheet model of the India-Asia convergence what controls strain localisation across the Tibetan Plateau and how does is affect the overall deformation field?

1.7 Synopsis of the research design and method

I use the finite element program *basil*, for which the governing equations are described in Chapter Two, to deform plane-stress, viscous models. These contain a temperature-dependent rheological law for which the material weakens as a result of work done by shear converted to heat. The impact of thermal diffusion is represented approximately.

In Chapter Three, as an initial exploration of how a weak region influences strain distribution, I set a rectangular region embed with small circular inclusion whose strength is less than that of the surrounding area. I vary the initial rheological parameters, *n*, initial strength of the weak region, the strain-weakening and diffusion components, and I subject the region to simple-shear. In this model I measure the temporal and spatial development of strain localisation in the horizontal plane and determine the minimum strain-weakening required for localisation to occur.

The same criteria for horizontal localisation are used to determine the depth-extent to which shear-zones in the lithosphere remain relatively localised. Chapter Four and Five apply the results from Chapter Three to the rheological laws for common lithospheric minerals, quartz, plagioclase and olivine, and the combination of temperature and stress-dependence provide a means of predicting the maximum depth to which a shear-zone can be considered localised. I compare these predicted localisation depths from the numerical model with the seismic interpretations of four major continental strike-slip faults.

The sixth chapter shows the development of a thin viscous sheet model that represents approximately the evolution of the India-Asia convergence from onset of collision (~ 47 Ma) to the present day. I set a strong India and Tarim Basin and Sichuan Basin regions within a weaker Asia region, with the co-ordinates projected on to a spherical shell. When India is restored to the present day position I compare the results with the present day topography, velocity and strain-rate across the Tibetan Plateau.

In Chapter Seven I look at what is required to develop strain localisation across the Tibetan Plateau. Based on the model developed in Chapter Six I add a weak seed within the Tibetan Plateau and vary the strain-weakening component. I observe spatial and temporal changes in strain-rates, and determine the minimum strain-weakening that is required to sustain strain localisation across the Tibetan Plateau on the time scale of interest.

These results are than summarised in Chapter Eight and compared to the questions that I raised in section 1.6.2 I discuss the limitations of this study and identify areas for future work.

1.8 Significance of this study

This thesis makes a contribution to understanding localisation processes when using a numerical model that treats the lithosphere as a viscous continuum. The simple-shear box models (Chapter Three) are the first numerical models using a thin viscous sheet approach to show how a weak seed influences strain-localisation and to incorporate a

strain-weakening recovery mechanism. Based on the results from the simple-shear box model and published rheological parameters I provide a means to predict the maximum depth to which a thermal localisation mechanism can be supported in the lithosphere (Chapter Four and Five). The India-Asia model I develop (Chapter Six) is the first study to use the *basil* time dependent spherical shell calculations and to show how strain can localise across the Tibetan Plateau in addition to localisation adjacent to strong regions (Chapter Seven).

The reader should bear in mind that the study is based on a two-dimensional thin viscous sheet approximation. For exploring the horizontal extent of localisation (Chapters Three and Seven) the rheological parameters are invariant with depth. It is beyond the scope of this study to use time-dependent three-dimensional models that may include basal shear stress (e.g. Medvedev and Podladchikov, 1999) or the complexities of lower crustal flow, as suggested for the Tibetan Plateau (e.g. Royden et al., 1997). Where the vertical extent of localisation is investigated (Chapter Four and Five), rather than attempt to encompass the entire range of published rheological flow laws applicable to continental lithosphere I choose flow laws applicable to my simplified lithology of successive layers dominated by quartz, plagioclase and olivine.

2 Method: the thin viscous sheet model

2.1 Overview of method

Large scale deformation of the continents is reasonably well explained by simplified models in which the lithosphere behaves as a thin viscous sheet that responds to plate boundary stresses and internal variation of gravitational forces (e.g. England et al., 2016; England and Molnar, 2005). By averaging over the thickness of the lithosphere, such models can disregard the apparent localisation of deformation associated with faults in the uppermost crust and localised shear zones that may be present at deeper levels. Block or micro-plate models (Chapter One) assume deformation is accommodated along pre-existing large scale faults that border a pre-divided rigid lithosphere (e.g. Avouac and Tapponnier, 1993; Thatcher, 2009). The boundary faults are identified by morphological offsets along shear zones or geodetically derived estimates through the use of GPS or InSAR. This thesis explains how the localisation process within a continuum deformation model might account for the kind of boundaries that are identified in block-type models.

My approach will use the thin viscous sheet approximation, initially developed by Bird and Piper (1980), England and McKenzie (1982) and Houseman and England (1986). The three-dimensional properties of the lithosphere are reduced to two-dimensions (thin sheet) by assuming the horizontal gradient of the vertical components is approximately zero, allowing stress to be integrated with depth (see sections 2.2.2, 2.3.2). The thin viscous sheet model permits systematic exploration of the parameters that control shear zone formation. Relevant factors include lithological heterogeneity, the relative importance of diffusion (Newtonian) and dislocation (power-law) creep mechanisms,

and the inclusion of strain-weakening and recovery. The numerical models are calculated in the finite element program, *basil*. While a two-dimensional approach averages the influence of lower crustal flow that can be shown in a three-dimensional power-law viscous models (Lechmann et al., 2011) they have the advantage of being computationally inexpensive.

I initially explore how strain localisation develops from an initial isolated weak inclusion, assuming a thermally activated creep mechanism and heating by viscous strain (Chapter Three). I use a 2D plane-stress numerical model where deformation is driven by external boundary conditions and subject to a frame-invariant constitutive law (section 2.2.3). The process of strain-weakening is required for (e.g. Burg and Schmalholz, 2008) or enhances (e.g. Dayem et al., 2009) strain localisation. Here I modify work dependent strain-weakening equations developed by Dayem et al. (2009) to allow a strain-weakening viscosity to evolve with time under the influence of shear heating and thermal diffusion (section 2.2.4). Using results from these experiments and applying rheological laws for common lithospheric minerals and depth-dependent properties of the lithosphere I calculate maximum depths to which localised strain can be supported in the lithosphere (Chapter Four, Five).

I model the India-Asia convergence, where deformation across the Tibetan Plateau (~ 2,500,000 km^2) is accommodated by large scale (> 100 km) shear-zones interspersed by regions of diffuse deformation (see section 1.1). I use this to show how a continuum model can localise strain across the Tibet Plateau. In this model the vertical properties of the lithosphere are averaged and gradients of topography influence deformation (section 2.3.2). The model boundaries are projected onto a spherical shell and the

indenting boundary (Himalayan Front) defined by a rotation about an Euler pole (section 2.3.3).

2.2 Method for simple-shear box model

2.2.1 Purpose of simple-shear box model

As an inital study of how physical parameters, such as strain exponent or relative strength contrast, influence strain-distribution across a deforming region I examine deformation under simple-shear and plane-stress conditions of a region that contains a single, initially circular, heterogeneity (Fig. 2.1). Using 2D numerical experiments I look at how this weak seed in an otherwise homogenous region influences temporal and spatial strain development. Deformation associated with circular heterogeneity has been previously studied by others (e.g. Grujic and Mancktelow, 1998; Kaus and Podladchikov, 2006; Mandal et al., 2004) but here I consider a simple-shear regime, rather than pure-shear.

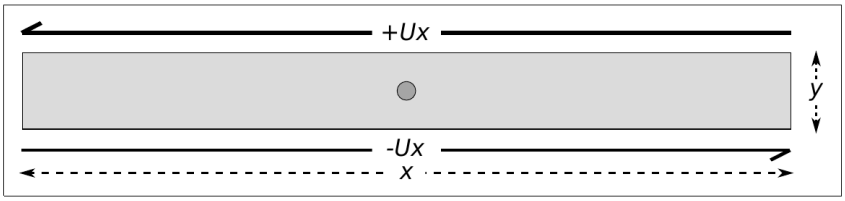

Figure 2.1: The model domain is a rectangular region of length 80r and width 8r in the (x, y) plane with a circular inclusion of radius r *= 1 located centrally. The external boundary conditions ideally should be far enough from the inclusion that they do not affect the inhomogeneous part of the strain field in the locality of the inclusion.*

This 2D model may be seen as a horizontal layer in the lithosphere at constant depth in a strike-slip environment. By considering how temperature, pressure and mineralogy within the lithosphere affect a shear localisation parameter, I then estimate whether thermally activated shear localisation at any given depth in the lithosphere should be expected (Chapter Four, Five).

2.2.2 The thin viscous sheet approximation for a 2D model

The thin viscous sheet approximation describes a continuum approach to lithospheric deformation, and treats the lithosphere as a viscous fluid. For stress equilibrium in 3D, the stress balance can be stated in Cartesian coordinates (*x*,*y*,*z*) by balancing the divergence of stress (σ) and the body force which depends on density (ρ) and gravitational acceleration (g) assumed to act in the *z* direction:

$$\nabla \cdot \sigma_{ij} = \begin{bmatrix} \frac{\partial \sigma_{xx}}{dx} + \frac{\partial \sigma_{xy}}{dy} + \frac{\partial \sigma_{xz}}{dz} \\ \frac{\partial \sigma_{yx}}{dx} + \frac{\partial \sigma_{yy}}{dy} + \frac{\partial \sigma_{yz}}{dz} \\ \frac{\partial \sigma_{zx}}{dx} + \frac{\partial \sigma_{zy}}{dy} + \frac{\partial \sigma_{zz}}{dz} \end{bmatrix} = -\rho g \begin{bmatrix} 0 \\ 0 \\ 1 \end{bmatrix} = -\rho g \underline{\hat{z}} \qquad \text{Eq. (2.1)}$$

The total stress component (σ_{ij}) is the sum of pressure (P) and deviatoric stress (τ_{ij}):

$$\sigma_{ij} = P\delta_{ij} + \tau_{ij} \qquad \text{Eq. (2.2)}$$

The thin sheet approximation assumes that vertical tractions on vertical planes can be neglected, strain-rates are independent of depth and the stress balance is integrated vertically, allowing the three-dimensional problem of lithospheric deformation to be reduced to two-dimensions. The average stress ($\bar{\sigma}$) is obtained by integration of Eq. (2.1) with respect to depth (*z*) between a depth L and the surface. For the x and y

(horizontal) directions it is assumed the shear stresses acting on the upper and lower surfaces of the viscous sheet are negligible, and the horizontal stress balance is then:

For the x-direction: $$\frac{\partial \bar{\sigma}_{xx}}{\partial x}+\frac{\partial \bar{\sigma}_{xy}}{\partial y}+\left(\left(\sigma_{xz}\right)^{top}-\left(\sigma_{xz}\right)^{bottom}\right) =\frac{\partial \bar{\sigma}_{xx}}{\partial x}+\frac{\partial \bar{\sigma}_{xy}}{\partial y}=0$$ Eq. (2.3a)

and similarly for the y-direction: $$\frac{\partial \bar{\sigma}_{yx}}{\partial x}+\frac{\partial \bar{\sigma}_{yy}}{\partial y}=0$$ Eq. (2.3b)

For the shear box calculations, which represent a horizontal slice of the lithosphere, I ignore vertical stress and assume that $\partial \sigma_{zz}=0$. Using Eq. (2.2), Eqs. (2.3a) and (2.3b) can be rewritten in terms of deviatoric stress:

For the x-direction: $$\frac{\partial \bar{\tau}_{xx}}{\partial x}+\frac{\partial \bar{\tau}_{yx}}{\partial y}=0$$ Eq. (2.4a)

and for the y-direction $$\frac{\partial \bar{\tau}_{xy}}{\partial x}+\frac{\partial \bar{\tau}_{yy}}{\partial y}=0$$ Eq. (2.4b)

2.2.3 Constitutive law for deformation

A general creep law for silicates may be represented, e.g. Hirth and Kohlstedt (2013), by:

$$\dot{\varepsilon}=A\,\sigma^{n}\left(f_{H_2O}\right)^{r}s^{-m}\exp\left(\frac{-\left(Q+PV\right)}{RT}\right)$$ Eq. (2.5)

where $\dot{\varepsilon}$ is strain rate, , n is the power-law creep exponent, Q and V are the activation energy and volume respectively, T is the temperature in Kelvin, P is pressure, R is the universal gas constant, s is the grain size, f_{H20} is the fugacity of water, r and m are experimentally determined indices and A is an empirical constant determined by

experiment. At low stress or high temperature, diffusion creep dominates, *n* is ~ 1 and *m* > ~ 1. At greater stress or lower temperature *n* > ~ 3 and *m* is generally thought to be about zero, so that there is no grain-size sensitivity. Eq. (2.5) may be written in the frame invariant form that relates tensors of deviatoric stress and strain-rate:

$$\dot{\varepsilon}_{ij} = A\,\Theta^{n-1}\,\tau_{ij}\,f_{H_2O}^{r}\,s^{-m}\exp\left(\frac{-(Q+PV)}{RT}\right) \qquad \text{Eq. (2.6)}$$

where τ is deviatoric stress, Θ is the second invariant of the deviatoric stress,

$$\left(\Theta^2 = \tau_{ij}\,\tau_{ij}\right)$$

Symmetry of the stress and strain tensors results in only six independent variables. In relating the results of uniaxial experiments to three-dimensional constitutive laws the principal stresses can be defined as:

$$\sigma_1 = \sigma \qquad \sigma_2 = 0 \qquad \sigma_3 = 0 \qquad \text{Eq. (2.7)}$$

the components of deviatoric stress to be expressed as:

$$\tau_1 = \frac{2\sigma}{3} \qquad \tau_2 = -\frac{\sigma}{3} \qquad \tau_3 = -\frac{\sigma}{3} \qquad \text{Eq. (2.8)}$$

and where the second invariant of the deviatoric stress is defined as:

$$\Theta^2 = \tau_{ij}\,\tau_{ij} \quad \text{therefore} \qquad \text{Eq. (2.9)}$$

$$\Theta^2 = \left(\left(\frac{2}{3}\right)^2 + \left(\frac{-1}{3}\right)^2 + \left(\frac{-1}{3}\right)^2\right) \quad \text{and}$$

$$\Theta = \sigma\sqrt{2/3}$$

And for:

$$\dot{\varepsilon}_{ij}=\frac{1}{2}\left(\frac{\partial u_i}{\partial x_j}+\frac{\partial u_j}{\partial x_i}\right) \qquad \text{Eq. (2.10)}$$

the corresponding principal strain-rates are:

$$\dot{\varepsilon}_1=\dot{\varepsilon} \quad \dot{\varepsilon}_2=-\frac{\dot{\varepsilon}}{2} \quad \dot{\varepsilon}_3=-\frac{\dot{\varepsilon}}{2} \qquad \text{Eq. (2.11)}$$

Substituting the first principal components from Eq. (2.8) and (2.11) into (2.6) and re-arranging to give:

$$\dot{\varepsilon}_{ij}=A_1\left(\frac{2}{3}\right)^{(n+1)/2}\sigma^n f_{H_2O}^r s^{-m}\exp\left(\frac{-(Q+PV)}{RT}\right) \qquad \text{Eq. (2.12)}$$

Comparison with Eq. (2.5) gives:

$$A=A_1\left(\frac{2}{3}\right)^{(n+1)/2} \qquad \text{Eq. (2.13)}$$

This allows the viscous deformation law described by Eq. (2.12) to be inverted and re-written using a strength coefficient B that includes the dependence on temperature, grain-size, fugacity, pressure, and the stress invariant Θ given in Eq. (2.6) is replaced by the strain-rate invariant $\dot{E}$:

$$\tau_{ij}=B\dot{E}^{(1-n)/n}\dot{\varepsilon}_{ij} \quad \text{where} \quad \dot{E}=\sqrt{\dot{\varepsilon}_{ij}\dot{\varepsilon}_{ij}} \qquad \text{Eq. (2.14)}$$

$$\text{and} \quad \dot{\varepsilon}_{ij}=\frac{1}{2}\left(\frac{\partial u_i}{\partial x_j}+\frac{\partial u_j}{\partial x_i}\right)$$

$$B=\left(\frac{2}{3}\right)^{(n+1)/2n}A^{-1/n}f_{H_2O}^{-r/n}\exp\left(\frac{Q+PV}{nRT}\right)s^{m/n} \qquad \text{Eq. (2.15)}$$

The numerical factor in Eq. (2.12) and (2.15) arises because *A* is typically defined in the experimental rock physics community as the proportionality constant between strain-

rate and applied stress in a uniaxial deformation apparatus, whereas a frame-invariant numerical formulation requires that the experimental equation is rewritten in terms of the second invariant of strain-rate. Thus the thin viscous sheet responds to stress in accordance with a frame-invariant constitutive law (Eq. 2.14) where deviatoric stress is proportional to strain-rate and strain-rate varies as the n^{th} power of stress.

From Eq. (2.14) a strain-rate dependent effective viscosity (η) can be defined as:

$$\eta_{eff} = \frac{B}{2}\dot{E}^{(1-n)/n} \qquad \text{Eq. (2.16)}$$

The power-law dependence of strain-rate on stress implies that under constant stress difference, with, e.g. $n = 3$, doubling B will cause strain rate to decrease by a factor of 8. In section 2.2.4 I consider a model for strain-weakening in which B is modified in the course of a calculation, dependent on the history of viscous strain.

2.2.4 Strain-weakening in the simple-shear box model

The process of strain-localisation appears to be an essential characteristic of large scale earth deformation (e.g. Burg and Schmalholz, 2008; Gueydan et al., 2014). In order to explore how strain localisation may develop naturally in a viscous continuum deformation model, as described in the preceding sections, I here include a mechanism that represents strain-weakening by implementing in the *basil* program a process that adjustments the viscous coefficient B as deformation occurs.

For strain-weakening dependent on work done (damage based) the rate of reduction of the viscosity coefficient B can be assumed to be proportional to the work done by

viscous strain within the medium. Following the approach of Dayem et al. (2009) the effect is formulated using a strain-weakening parameter Γ which may be estimated for a specific physical model or simply treated as an unknown constant to be determined empirically.

Here I consider shear heating, which arises from the conversion of mechanical work to heat. If the mechanical work is entirely dissipated, and deformation is rapid compared to thermal diffusion, the rate of temperature change ($\partial T/\partial$t) for density ρ and heat capacity C_p is determined by:

$$\rho C_p \frac{\partial T}{\partial t} = \sum_{ij} \dot{\varepsilon}_{ij} \tau_{ij} = B \dot{E}^{(n+1)/n} \qquad \text{Eq. (2.17)}$$

Where the rheological factor B has a temperature dependence, defined by (Eq. 2.15), differentiation gives the rate of change of B with temperature:

$$\frac{1}{B}\frac{dB}{dt} = \frac{-(Q+PV)}{nRT^2}\frac{dT}{dt} \qquad \text{Eq. (2.18)}$$

Assuming all the work dissipated by viscous deformation is converted into heat and locally retained on the time-scale of interest, then following Dayem et al. (2009) substituting Eq. (2.17) into Eq. (2.18) obtains:

$$\frac{1}{B}\frac{dB}{dt} = \frac{-(Q+PV)}{nRT^2}\frac{1}{\rho C_p} B \dot{E}^{(1+n)/n} \qquad \text{Eq. (2.19)}$$

And allowing:

$$\Gamma = \left(\frac{Q+PV}{nRT^2}\right)\left(\frac{1}{\rho C_p}\right) \qquad \text{Eq. (2.20)}$$

then Eq. (2.19) can be written as:

$$\frac{1}{B}\frac{dB}{dt} = -\Gamma B \dot{E}^{(1+n)/n} \qquad \text{Eq. (2.21)}$$

where Γ represents a strain-weakening parameter.

Shear heating arises from the conversion of mechanical work to heat. If the mechanical work is entirely dissipated, and deformation is rapid compared to thermal diffusion, the rate of temperature change ($\partial T/\partial t$) is determined by conservation of energy.

Defining a thermal anomaly parameter D, which represents the time-integrated work per unit volume and is proportional to the local increase in temperature if diffusion of heat is neglected:

$$D = \int_0^t B \dot{E}^{(1+n)/n} dt \qquad \text{Eq. (2.22)}$$

Allows Eq. (2.21) to be rewritten as:

$$\frac{1}{B}\frac{dB}{dt} = -\Gamma \frac{dD}{dt} \qquad \text{Eq. (2.23)}$$

Thus the rate of change of B relates to the rate of work done, via the value of Γ. The simple-shear box model (Fig. 2.1) can apply to a horizontal layer at a given depth (temperature). Eq. (2.20) shows a temperature dependence of Γ. Under a shear-heating regime the value of Γ will evolve, as it is a function of T and hence B, therefore I modify the equations as follows.

I consider plane-stress deformation at constant depth in the lithosphere, and therefore can assume the pre-exponent value (A), water-fugacity (f_{H2O}) and grain-size (s) are constant. For simplification I also assume that activation energy and volume (Q, V), pressure (P), grain size and strain exponents (m, n), density (ρ) and heat capacity (C_p) from Eqs. (2.15) and (2.20) are constant (G) and only T changes, and rewrite Eq. (2.15) as:

$$\ln\left(\frac{B}{G}\right)=\frac{Q+PV}{nRT} \qquad \text{Eq. (2.24)}$$

Squaring both sides of Eq. (2.24) and comparing to Eq. (2.20) allows me to eliminate T and obtain an expression for Γ in terms of B:

$$\left[\ln\left(\frac{B}{G}\right)\right]^2=\left(\frac{Q+PV}{nRT}\right)^2 \qquad \text{Eq. (2.25)}$$
$$=\left(\frac{Q+PV}{nRT^2}\right)\left(\frac{Q+PV}{nR}\right)=\Gamma\rho C_p\left(\frac{Q+PV}{nR}\right)$$

And re-arranging Eq. (2.25) gives:

$$\Gamma=\left[\ln\left(\frac{B}{G}\right)\right]^2\frac{1}{\rho C_p}\left(\frac{nR}{Q+PV}\right) \qquad \text{Eq. (2.26)}$$

Substituting Eq. (2.26) into Eq. (2.23) gives:

$$\frac{dB}{B}=\frac{-1}{\rho C_p}\left(\frac{nR}{Q+PV}\right)\left[\ln\left(\frac{B}{G}\right)\right]^2 D \qquad \text{Eq. (2.27)}$$

And defining for convenience in the following manipulation:

$$H=\frac{1}{\rho C_p}\left(\frac{nR}{Q+PV}\right) \qquad \text{Eq. (2.28)}$$

then Eq. (2.27) can be rearranged as:

$$\int_{B_0}^{B_1}\left[\ln\left(\frac{B}{G}\right)\right]^{-2}\frac{dB}{B}=-HD \qquad \text{Eq. (2.29)}$$

Solving the integral in Eq. (2.29) gives:

$$k=\ln\left(\frac{B}{G}\right) \qquad dk=\frac{dB}{B} \qquad \text{Eq. (2.30)}$$

$$\int_{k_0}^{k1} k^{-2}\,dk=\int_{k_0}^{k_1}\frac{dk}{k^2}=-\left[\frac{1}{k}\right]_{k0}^{k1}$$

$$=\frac{1}{k_0}-\frac{1}{k_1}$$

$$=\ln\left(\frac{B_0}{G}\right)^{-1}-\ln\left(\frac{B_1}{G}\right)^{-1}$$

$$=\frac{\ln B_1-\ln B_0}{\ln\left(\frac{B_1}{G}\right)\ln\left(\frac{B_0}{G}\right)}$$

Allowing Eq. (2.32) to be written as:

$$\int_{B_0}^{B_1}\left[\ln\left(\frac{B}{G}\right)\right]^{-2}\frac{dB}{B}=\frac{\ln B_1-\ln B_0}{\ln\left(\frac{B_1}{G}\right)\ln\left(\frac{B_0}{G}\right)}=-HD \qquad \text{Eq. (2.31)}$$

Therefore:

$$\ln B_1-\ln B_0=-HD\ln\left(\frac{B_1}{G}\right)\ln\left(\frac{B_0}{G}\right) \qquad \text{Eq. (2.32)}$$

Re-arranging Eq. (2.26) to give:

$$\ln\left(\frac{B_0}{G}\right)=\sqrt{\Gamma_0}\sqrt{\rho C_p\left(\frac{Q+PV}{nR}\right)} \qquad \text{Eq. (2.33a)}$$

$$\ln\left(\frac{B_1}{G}\right)=\sqrt{\Gamma_1}\sqrt{\rho C_p\left(\frac{Q+PV}{nR}\right)} \qquad \text{Eq. (2.33b)}$$

and substituting Eq. (2.33a and b) into Eq. (2.32):

$$\ln B_1 - \ln B_0 = -\sqrt{\Gamma_1}\sqrt{\rho C_p\left(\frac{Q+PV}{nR}\right)}\sqrt{\Gamma_0}\sqrt{\rho C_p\left(\frac{Q+PV}{nR}\right)}HD \qquad \text{Eq. (2.34)}$$

and using (Eq. 2.28) for *H*:

$$\ln\left(\frac{B_1}{B_0}\right) = -\sqrt{(\Gamma_1\Gamma_0)}\left(\rho C_p\left(\frac{Q+PV}{nR}\right)\right)\left(\frac{1}{\rho C_p}\frac{nR}{Q+PV}\right)D \qquad \text{Eq. (2.35)}$$

I then obtain:

$$\ln\left(\frac{B_1}{B_0}\right) = -\sqrt{(\Gamma_1\Gamma_0)}\,D \qquad \text{Eq. (2.36)}$$

where B_0 and Γ_0 are the intial local strength coefficient and corresponding value of Γ, and B_1 and Γ_1 are the corresponding values after the deformation that produces the integrated work $D(t)$.

To measure the evolution of B I require Γ_0 and at a spatial point measured I need a time dependent effective value of Γ. Eq. (2.36) can be rewritten as:

$$\ln B_1 = \ln B_0 - \Gamma_{eff}\,D \quad \text{where} \qquad \text{Eq. (2.37)}$$
$$\Gamma_{eff} = \sqrt{\Gamma_1\Gamma_0} = \Gamma_0\sqrt{\frac{\Gamma_1}{\Gamma_0}}$$

And using Eq. (2.33a and b) I obtain:

$$\Gamma_{eff} = \Gamma_0 \frac{\ln\left(\frac{B_1}{G}\right) / \sqrt{\rho C_p \left(\frac{Q+PV}{nR}\right)}}{\ln\left(\frac{B_0}{G}\right) / \sqrt{\rho C_p \left(\frac{Q+PV}{nR}\right)}} = \Gamma_0 \left(\frac{\ln(B_1/G)}{\ln(B_0/G)}\right) \quad \text{Eq. (2.38)}$$

Subsitiuting Eq. (2.38) into Eq. (2.37):

$$\ln B_1 = \ln B_0 - \Gamma_0 \left(\frac{\ln(B_1/G)}{\ln(B_0/G)}\right) D \quad \text{or} \quad \text{Eq. (2.39)}$$

$$\ln B_1 (\ln(B_0/G)) = \ln B_0 (\ln(B_0/G)) - \Gamma_0 D \left(\ln(B_1/G)\right)$$

G represents constants in time, Eq. (2.24). Using the initial temperature T_0, normalised by the other quantities in the Arrhenius term:

$$T_{ref} = \left(\frac{nRT_0}{Q+PV}\right) \quad \text{Eq. (2.40)}$$

allowing Eq. (2.24) to be written as:

$$\ln G = \ln B_0 - \frac{1}{T_{ref}} \quad \text{Eq. (2.41)}$$

Substituting Eq. (2.41) into Eq. (2.39) I obtain:

$$\ln B_1 \left(lnB_0 - lnB_0 + 1/T_{ref}\right) = \ln B_0 \left(lnB_0 - lnB_0 + 1/T_{ref}\right) - \Gamma_0 D \left(lnB_1 - \ln B_0 + 1/T_{ref}\right) \quad \text{Eq. (2.42)}$$

which can be simplified and rearranged to give:

$$\begin{aligned}&\ln B_1(1/T_{ref}) \\ &= \ln B_0(1/T_{ref}) - \Gamma_0 D\left(lnB_1 - \ln B_0 + 1/T_{ref}\right) \\ &= \ln B_0(1/T_{ref}) - \Gamma_0 D\, lnB_1 + \Gamma_0 D \ln B_0 - \left((\Gamma_0 D)/T_{ref}\right)\end{aligned} \qquad \text{Eq. (2.43)}$$

$$\ln B_1\left(\frac{1}{T_{ref}} + \Gamma_0 D\right) = \frac{\ln B_0}{T_{ref}} + \Gamma_0 D\, lnB_0 + \frac{\Gamma_0 D}{T_{ref}}$$

$$\begin{aligned}\ln B_1 &= \frac{(\ln B_0)(1/T_{ref}) + (\Gamma_0 D)(1/T_{ref})(\ln B_0 T_{ref} - 1)}{(1/T_{ref})(1 + \Gamma_0 D T_{ref})} \\ &= \frac{\ln B_0 + \Gamma_0 D(\ln B_0 T_{ref} - 1)}{1 + T_{ref}\Gamma_0 D}\end{aligned}$$

which for the local strength coefficient at any time *t*:

$$\ln B(t) = \frac{\left[\ln B_0 + \left(T_{ref} \ln B_0 - 1\right)\Gamma_0 D(t)\right]}{\left[1 + T_{ref}\Gamma_0 D(t)\right]} \qquad \text{Eq. (2.44)}$$

Although the focus here is on the thermal weakening model for strain localisation, a similar approach could be used for modelling of possible localisation mechanisms based on development of mineral fabric and grain size changes.

2.2.5 Recovery processes in the simple-shear box model

For $\Gamma_0 > 0$ Eq. (2.44) implies that *B* decreases indefinitely as the medium is progressively deformed. In practice it is expected that *B* for the deforming medium will approach a stable value. Local thermal anomalies can be attenuated by diffusion, for example Kaus and Podladchikov (2006) showed that a thermal weakening mechanism may be suppressed by the effect of diffusive cooling. Here I modify the numerical integration of Eq. (2.22) by including an additional term to represent approximately the effect of diffusion of heat away from a shear zone.

A consistent treatment of the thermal energy balance (with typical simplifying assumptions) for a thermal anomaly which varies rapidly in a horizontal direction (perpendicular to the hypothetical shear zone), and is relatively constant in the other two directions follows from the relevant diffusion equation:

$$\rho C_p \frac{\partial T}{\partial t} = -\lambda \frac{\partial^2 T}{\partial x^2} + \Phi \qquad \text{Eq. (2.45)}$$

where Φ is the rate of shear heating and λ is thermal conductivity. When conductivity is assumed negligible ($\lambda = 0$) we use:

$$\rho C_p \frac{\partial T}{\partial t} = \Phi = \dot{\varepsilon}_{ij} \tau_{ij} \qquad \text{Eq. (2.46)}$$

and the thermal anomaly ΔT relative to an original background temperature (assumed constant) is simply proportional to the work done by viscous deformation:

$$\Delta T = \frac{D}{\rho C_p} \qquad \text{Eq. (2.47)}$$

where D is defined by Eq. (2.22). This temperature anomaly must also satisfy Eq. (2.45) above, so the effect of thermal diffusion can be represented in this model by treating D as a proxy for the local temperature anomaly:

$$\frac{\partial D}{\partial t} = -\kappa \frac{\partial^2 D}{\partial x^2} + \Phi \qquad \text{Eq. (2.48)}$$

Where the thermal diffusivity, κ, is related to thermal conductivity (λ) by:

$$\kappa = \frac{\lambda}{\rho C_p} \qquad \text{Eq. (2.49)}$$

If D has a harmonic disturbance of heat with a characteristic wave number k in the x direction, in a uniform medium of diffusivity κ (Turcotte and Schubert, 2014):

$$D = D_0 \cos(kx) \qquad \text{Eq. (2.50)}$$

$$\frac{d^2 D}{dx^2} = -k \frac{d}{dx}\left(D_0 \sin(kx)\right)$$
$$= -k^2 D_0 \cos(kx)$$
$$= -k^2 D$$

where D is the integrated work done, taken as a temperature anomaly proxy, then:

$$\frac{\partial D}{\partial t} = -\kappa k^2 D + \Phi \qquad \text{Eq. (2.51)}$$

Substituting Eq. (2.46) into Eq. (2.51) and defining a decay constant (β):

$$\beta = \kappa k^2 \qquad \text{Eq. (2.52)}$$

Thus Eq. (2.22) can be modified to attenuate the rate of change of D:

$$\frac{dD}{dt} = B \dot{E}^{(1+n)/n} - \beta D \qquad \text{Eq. (2.53)}$$

Low thermal conductivity of most crustal lithologies renders conductive heat loss significant only for very low geological strain-rates. This study assumes geological strain-rates are sufficiently rapid that viscous heating exceeds conductive heat loss. The presence of fluids permits significant heat removal through diffusion or advection, and may be represented through application of the recovery mechanism ($\beta > 0$). For $\beta = 0$ fluids may be absent from the deforming region. Alternatively, fluids may be present and either flow is restricted, inhibiting advection, or the occupy a relatively low volume, limiting the effectiveness of heat removal through diffusion. Consequently heat remains within the deforming region.

Application of this recovery mechanism (Eq. 2.53) assumes a constant proportion of heat loss through time relative to the *D*. Changes in fluid supply are not accounted for. The decay constant, β, does not allow accurate representation of a more complex thermal disturbance, in which a range of wavelengths may be present and changing with time. It does allow a qualitative examination of thermal diffusion in this problem for a range of plausible β values.

2.2.6 Scaling parameters for basil calculations

Calculations within *basil* are dimensionless through self-consistent scaling parameters. Based on a reference background strain-rate of the physical variables are non-dimensionalised as follows:

$$\dot{\varepsilon}=(\dot{\varepsilon}_0)\dot{\varepsilon}';\quad B=H_0B';\quad \tau=H_0(\dot{\varepsilon}_0)^{1/n}\tau' \qquad \text{Eq. (2.54)}$$
$$D=H_0(\dot{\varepsilon}_0)^{1/n}D'$$

where non-dimensional values are primed and H_0 is a physical scale factor for the viscosity coefficient:

$$H_0=\left(\frac{2}{3}\right)^{(n+1)/2n}\left[Af_{H_2O}^{r}s^{-m}\right]^{-1/n}\exp\left(\frac{Q+P_0V}{nRT_0}\right) \qquad \text{Eq. (2.55)}$$

where T_0 and P_0 are the reference temperature and pressure at the depth that correspond to the plane of the calculation. Hence, for consistency with Eqs. (2.21) and (2.20):

$$\Gamma_0'=\Gamma_0H_0(\dot{\varepsilon}_0)^{1/n} \qquad \text{Eq. (2.56)}$$
$$=\left(\frac{2}{3}\right)^{(n+1)/2n}\left(\frac{Q+P_0V}{\rho C_pnRT_0^2}\right)\left[A^{-1}s^{m}f_{H_2O}^{-r}\dot{\varepsilon}_0\right]^{1/n}\exp\left(\frac{Q+P_0V}{nRT_0}\right)$$

The diffusion parameter β is rendered dimensionless after division by the scaling constant for strain-rate.

2.2.7 Localisation with depth

Using results from the simple-shear box model I will evaluate the minimum initial dimensionless strain-weakening parameter (Γ_0') required for strain localisation within a feasible geological time. Here the box model represents a horizontal slice of the lithosphere, where the temperature, pressure, and water fugacity will vary with depth. From Eq. (2.56) using experimentally derived rheological parameters for A, Q, V, n and m and estimates of background strain rate, temperature, pressure, and water fugacity the dimensionless value Γ_0' can be evaluated with lithospheric depth (Chapter Four). The rheological parameters will depend on the lithology and so I assume dominant lithologies of quartz in the upper crust, plagioclase in the lower crust, and olivine in the mantle lithosphere.

The temperature dependence in Eq. (2.56) causes Γ_0' to decrease with increasing lithosphere depth. I identify the depth at which Γ_0' reaches the minimum value required for strain-localisation and below this I infer a thermal activated strain-weakening mechanism cannot support strain-localisation.

2.3 Method for India-Asia model

2.3.1 Purpose of India-Asia model

The ongoing India-Asia convergence, the onset of which occured ~ 50 Ma, has resulted in deformation across the Tibet region (~ 2,500,00 km^2). The presence of relatively undeformed regions, e.g. the Tarim and Sichuan Basins, provides a geological basis for incorporating such strong regions into models of the India-Asia convergence. These regions can provide the strength contrasts required for heterogeneous deformation (section 1.3.4).

I use a model configured to represent the India-Asia convergence from onset of collision (~ 50 Ma) to the present day to examine how strain localisation occur across the Tibetan Plateau (Chapter Six, Seven). I follow previous work (e.g. Dayem et al., 2009; England and Houseman, 1985; Vilotte et al., 1984) and include a strong Tarim Basin, but also add a strong Sichuan Basin. In exploring the development of a heteregenous strain distribution away from the relatively strong Tarim and Sichuan Basins I include in some experiments a weaker region within the Tibetan Plateau area.

I use the thin viscous sheet approximation, where gradients of horizontal velocity are invariant with depth. The co-ordinates for India and Asia are projected onto a spherical shell, and India rotates around a prescribed Euler pole into a stationary Asia.

2.3.2 The thin viscous sheet approximation: buoyancy forces

For the India-Asia model I follow on from the thin viscous sheet approximation presented in section 2.2.2, but allow for stress arising from gradients of topography

(buoyancy forces). Assuming the vertical traction on vertical planes are negligible, so isostatic balance is maintained, then the stress balance in the z-direction:

$$\frac{\partial \sigma_{zz}}{\partial z} = -\rho g \qquad \text{Eq. (2.57)}$$

where σ_{zz} is a measure of the integrated weight of the overlying column beneath an upper surface at $z = e$.

$$\sigma_{zz} = -\int_{e}^{z} \rho g \, dz' \qquad \text{Eq. (2.58)}$$

and the depth-averaged vertical stress is shown to be equivalent to the average gravitational potential energy of the column of lithosphere by:

$$\begin{aligned} \bar{\sigma}_{zz} &= -\frac{1}{L-e}\int_{e}^{L}\left[\int_{e}^{z} \rho g \, dz'\right] dz \\ &= -\frac{1}{L-e}\int_{e}^{L} \rho g (L-z)\, dz \end{aligned} \qquad \text{Eq. (2.59)}$$

where L is the lithosphere thickness, e is the lithosphere surface height (expressed as a negative value) and z is the vertical measurement. As e is relatively small it can be effectively ignored for calculating $\bar{\sigma}_{zz}$, and hence the vertical stress can be simply divided by a lithospheric column thickness of L. It is assumed that isostasy is maintained during deformation in order to evaluate e for a simplified lithospheric structure of constant density crust over constant density mantle.

Using Eq. (2.2) and (2.57), Eqs. (2.3a) and (2.3b) can be rewritten in terms of deviatoric stress:

For the x-direction: $$\frac{\partial \bar{\tau}_{xx}}{\partial x}+\frac{\partial \bar{\tau}_{yx}}{\partial y}=-\left(\frac{\partial \bar{\sigma}_{zz}}{\partial x}+\frac{\partial \bar{\tau}_{zz}}{\partial x}\right)$$ Eq. (2.60a)

and for the y-direction $$\frac{\partial \bar{\tau}_{xy}}{\partial x}+\frac{\partial \bar{\tau}_{yy}}{\partial y}=-\left(\frac{\partial \bar{\sigma}_{zz}}{\partial y}+\frac{\partial \bar{\tau}_{zz}}{\partial y}\right)$$ Eq. (2.60b)

The thin viscous sheet approximation reduces the 3-dimensional properties of the lithosphere to 2-dimensions. Vertical columns in the layer can be changed in thickness, moved or sheared horizontally. The rate of change of crustal thickness depends on the horizontal divergence of the calculated velocity field:

$$\frac{1}{h}\frac{\partial h}{\partial t}=-\nabla . u=-\left(\frac{\partial u}{\partial x}+\frac{\partial v}{\partial y}\right)$$ Eq. (2.61)

where h is the crustal thickness, horizontal co-ordinates (x, y) and u and v are the velocity in x and y directions.

Vertical strain produces crustal thickness variations which modify the distribution of gravitational potential energy within the layer. Regions of increased gravitational potential energy drive a deformation field that causes thickened lithosphere to spread horizontally. The vertical stress balance is given by Eq. (2.58).

For simplicity I assume a two-layer model of the lithosphere with constant density crust (initial thickness h_0) over constant density mantle. In the thin viscous sheet formulation the integral of the vertical stress from the surface of the earth ($z = e$) to the base of the lithosphere ($z = L$) must be evaluated in order to substitute for the pressure in Eq (2.2):

$$\bar{\sigma}_{zz}=\frac{1}{L}\int_{e}^{L}\sigma_{zz}\,dz \quad \text{or} \quad \bar{P}=\frac{1}{L}\int_{e}^{L}P\,dz \qquad \text{Eq. (2.62)}$$

From substitution of Eq. (2.58) into Eq. (2.62) the depth averaged gravitational potential energy is given as:

$$\frac{GPE}{L}=\bar{\sigma}_{zz}=\frac{1}{L}\int_{e}^{L}\int_{e}^{z}\rho g\,dz'\,dz \qquad \text{Eq. (2.63)}$$

Therefore there are two types of force that act on the thin viscous sheet. Firstly, the boundary forces that result in a primary viscous stress field and secondly, the crustal thickness variations that generate gravitational forces. The ratio of these forces under a boundary-driven strain rate strain rate of order U_0/L is given by the Argand number (Ar) (England and McKenzie, 1982; Houseman and England, 1986):

$$Ar=\frac{g\,L\,p_c(1-(\rho_c/\rho_m))}{B_0(U_0/L)^{1/n}}=\frac{P(L)}{\tau(\dot{\epsilon}_0)} \qquad \text{Eq. (2.64)}$$

where ρ_c and ρ_m are crustal and mantle density respectively, L the thickness of the lithosphere, B_0 the initial averaged strength coefficient, $P(L)$ is the scale factor for excess pressure from differences in crust thickness and $\tau(\dot{\epsilon}_0)$ is the viscous stress required to deform the material at a characteristic strain rate of U_0/L :

$$\dot{\varepsilon}_0=\frac{U_0}{L} \qquad \text{Eq. (2.65)}$$

For a small Ar value then deformation is dominated by the boundary conditions. If Ar is large, then topography contrasts will not be supported by the effective viscosity. Therefore for a constant value of B there are two parameters that control the flow, the

strain-exponent (*n*), which dictates the strain-rate and stress dependency, and the Argand number (*Ar*), which relates to the effective viscosity of the medium.

2.3.3 Application to a spherical shell

The Cartesian thin viscous sheet method has been adapted to a thin viscous spherical shell, and applied to instantaneous deformation problems (England et al., 2016; Gordon and Houseman, 2015; Walters et al., 2017). Using a sinusoidal equal area projection of the spherical coordinates (latitude and longitude), the stress balance in the horizontal directions is solved and the solution may be readily compared with actual geography. This makes a spherical shell approach appropriate for the India-Asia model (Chapter Six, Seven). The program *basil* has been further amended so that the relative motion of the indenting boundary (Himalayan Front) is defined by a small circle rotation about an Euler pole, necessitating that the velocity components are re-set at each time level in the integration.

The body forces (dependent on density and gravity) are still assumed to act solely in the vertical direction, and the divergence of the stress tensor is equal and opposite to the body force which depends on density (ρ) and gravitational acceleration (g) (Eq. 2.1). The horizontal displacement rates remain invariant with depth, in this case the radial coordinate. Thus for spherical coordinates the depth-averaged deviatoric stress components (τ_{ij}) are:

$$\frac{2}{r}\frac{\partial \bar{\tau}_{\theta\theta}}{\partial \theta}+\frac{1}{r}\frac{\partial \bar{\tau}_{\varphi\varphi}}{\partial \theta}+\frac{1}{r\sin\theta}\frac{\partial \bar{\tau}_{\theta\varphi}}{\partial \varphi}+\frac{\cot\theta}{r}\left(\bar{\tau}_{\theta\theta}-\bar{\tau}_{\varphi\varphi}\right)=-\frac{1}{r}\frac{\partial \bar{\sigma}_{rr}}{\partial \theta} \qquad \text{Eq. (2.66)}$$

$$\frac{1}{r}\frac{\partial \bar{\tau}_{\theta\varphi}}{\partial \theta}+\frac{2}{r\sin\theta}\frac{\partial \bar{\tau}_{\theta\theta}}{\partial \varphi}+\frac{1}{r\sin\theta}\frac{\partial \bar{\tau}_{\varphi\varphi}}{\partial \varphi}+2\frac{\cot\theta}{r}\bar{\tau}_{\theta\varphi}=-\frac{1}{r\sin\theta}\frac{\partial \bar{\sigma}_{rr}}{\partial \varphi} \qquad \text{Eq. (2.67)}$$

where θ and φ are the colatitude and longitude in radians, r is the radial coordinate, and σ_{rr} is the depth-averaged radial stress component that relates to the gravitational potential energy.

The Cartesian and spherical shell use the same constiutive law that relates deviatoric stress to strain rate (Eq. 2.14a). For a spherical shell approach the relationship between the horizontal velocity components (u_θ, u_φ) and strain-rates is adapted from the Cartersian approach (Eq. 2.14c) and is given by:

$$\dot{\varepsilon}_{\theta\theta} = \frac{1}{r}\frac{\partial u_\theta}{\partial \theta} \qquad \text{Eq. (2.68)}$$

$$\dot{\varepsilon}_{\varphi\varphi} = \frac{1}{r\sin\theta}\frac{\partial u_\varphi}{\partial \varphi} + \frac{u_\theta}{r}\cot\theta$$

$$\dot{\varepsilon}_{\theta\varphi} = \frac{1}{2}\left(\frac{1}{r\sin\theta}\frac{\partial u_\theta}{\partial \varphi} + \frac{1}{r}\frac{\partial u_\theta}{\partial \theta} - \frac{u_\varphi}{r}\cot\theta\right)$$

The spherical co-ordinates (in radians) are projected onto a Cartesian plane using a sinusoidal equal area projection. Scaling using the radius of the sphere, the averaged radius of Earth, 6371 km, the dimensionless co-ordinates are:

$$y = \theta; \qquad x = (\varphi - \varphi_0)\sin\theta \qquad \text{Eq. (2.69)}$$

where φ_0 is the central longitude of the projection.

In *basil* boundary conditions defined using an Euler pole use a rotation rate (ω_0) expressed in radians per unit time, derived from a dimensional rotation rate in deg.Ma^{-1} (Ω):

$$t\,\Omega\,\frac{\pi}{180} = \omega_0 \qquad \text{Eq. (2.70)}$$

where t is time in Ma. By setting t to specified time interval the value can be calculated so that the required rotation of the boundary is complete at $t' = 1$.

2.3.4 Strain-weakening and recovery in the India-Asia model

Continuum models representing the India-Asia convergence have shown that a strain-weakening component enhances strain localisation (Dayem et al., 2009). I follow from my simple-shear box model and include a strain-weakening component that represents shear heating from the conversion of mechanical work to heat (Eq. 2.20).

In section 2.2.4 I showed how under a shear-heating regime the temperature dependence of Γ means it evolves with time. The evolution is reduced to a single parameter, T_{ref}, that assumes only the temperature changes and the pre-exponent value (A), water-fugacity (f_{H2O}), grain-size (s), activation energy and volume (Q, V), pressure (P), grain size and strain exponents (m, n), density (ρ) and heat capacity (C_p) from Eqs. (2.15) and (2.20) are constant. Where a horizontal slice of the lithosphere is considered, as with the simple-shear box model (section 2.2), the constants are chosen from experimentally derived rheological parameters that are appropriate for a given lithosphere depth. For my India-Asia model I consider the depth averaged rheology of the lithosphere. Rather than attempt to average the constants to derive representative values I simplify the calculations and allow Γ to remain constant through time, $T_{ref} = 0$. (Eq. 2.40).

To further simplify I ignore thermal diffusion and set $\beta = 0$. For thermally activated strain localisation in the India-Asia model the thermal weakening now represents the minimum shear-heating required. In practice the heating is attenuated by diffusion, and a higher proportion of shear-heated is required.

2.4 Finite element method

The *basil* model uses the finite element method (FEM) to resolve stress arising from applied boundary conditions and gravitional potential energy arising from changes in the sheet thickness. The region within a prescribed boundary is discritised, forming a mesh comprised of triangular elements. The velocity field (u,v) within each element is represented by a quadratic dependence on horizontal coordinates (x,y) that can be represented by:

$$u(x,y)=\sum_{i=1}^{6} U_i N_i(x,y); \quad v(x,y)=\sum_{i=1}^{6} V_i N_i(x,y) \qquad \text{Eq. (2.71)}$$

where U_i and V_i are the values of the respective velocity component on each of six nodal points (vertices and midpoints of sides) of the triangle and N_i is the continuous quadratic function which is 1 at node i and 0 at the other 5 nodes. To solve for the unknowns $\{U_i, V_i\}$ a set of simultaneous equations is formed by subsituting deviatoric stress, strain rate and velocity into Eq. (2.60), multipling by N_i for each node i, and integrating over the 2D spatial domain (see Appendix B, Houseman and England, 1986). This procedure is known as the Galerkin approximation and allow the partial differentials to be converted to a discrete problem. Every external boundary segment requires specification of x- and y-component velocity or traction.

The implementation of the method in the program *basil* permits magnitude and direction of the boundary velocity or traction to vary along the boundary. The viscosity coefficient *B* may be a functon of location (*x*,*y*) and is specified a priori, though it may be modified in the course of the calculation according to a strain-weakening or healing mechanism decribed in sections 2.2.4 and 2.2.5.

The program *basil* uses a Lagrangian formulation in which physical properties, such as viscosity coefficient or crustal thickness, are moved horizontally with the deforming fluid. Assuming that crustal volume is conserved (no erosion, sedimentation, or phase changes) the velocity field may produce thickening or thinning of the crust:

$$\dot{\varepsilon}_{zz} = \frac{1}{h}\frac{\partial h}{\partial t} = -\left(\frac{\partial u}{\partial x} + \frac{\partial v}{\partial y}\right) \qquad \text{Eq. (2.72)}$$

where h is the crustal thickness.

In finite strain calculations the displacement of the nodes at each time step is calculated using the velocity field:

$$X_i = X_i + U_i \Delta t\,; \quad Y_i = Y_i + V_i \Delta t \qquad \text{Eq. (2.73)}$$

where a two-step predictor corrector method uses an estimate of (U_i, V_i) obtained by averaging the current velocity field and that estimated for a provisional solution at the next time-level using the forward difference as written here. Similarly the crustal thickness distribution, advected on the nodes, is updated using the same velocity field:

$$\ln h_i(t) = \ln h_i - \left(\frac{\partial u}{\partial x} + \frac{\partial v}{\partial y}\right)_i \Delta t \qquad \text{Eq. (2.74)}$$

Derived quantities like strain rate and deviatoric stress are obtained at any time using the velocity field for that time level and the definitions of Eq. (2.14).

The *basil* program employs a Lagrangian formulation in which the finite element nodes that carry properties such as viscosity coefficient are advected with the computed velocity field as the material is deformed. Depending on the distribution and rate of strain, this approach can result in progressive distortion of the finite element mesh that eventually causes the calculation to stop. To counter this problem a remesh process can be invoked to create a new triangular mesh within the current deformed material boundaries and to interpolate the current material properties onto the new mesh before the calculation is continued. The remesh process is triggered at any time step in the calculations where element distortion results in either of the following two conditions. Either the distance between any two nodes falls below a prescribed minimum, or the triangular element distortion exceeds a prescribed limit defined by the sum of the angle cosines. The remesh command used in this study preserves external and internal boundaries and the boundary conditions. Properties (velocity, sheet thickness) across the domains are interpolated on to the new mesh.

2.5 Numerical tests

I check for correct implementation of the boundary velocity conditions in the finite element *basil*. Using a rectangular region of initial uniform viscosity I set an x- and y-velocity condition on one boundary (*Ux, Uy*) and track the x- and y-displacement as

calculated by *basil* (Fig. 2.2). I find the displacement with time (x, y) is identical to independent calculations (Eq. 2.75):

$$x, y = \frac{Ux, Uy}{t} \qquad \text{Eq. (2.75)}$$

A description and the results of a test of the implication of Eq. (2.44), evolution of the strength parameter B with time, is presented in section 3.2.

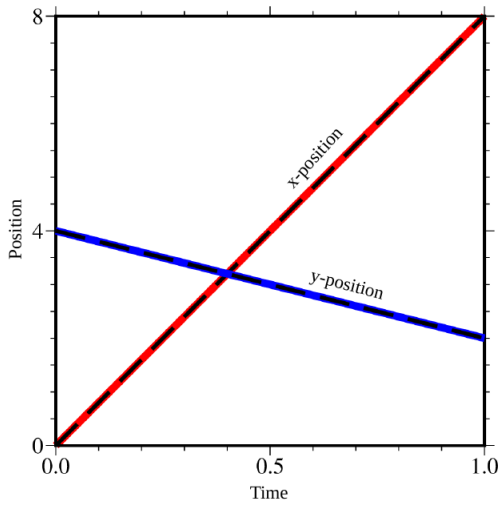

Figure 2.2: The x (red) and y (blue) boundary displacement with time for a homogeneous rectangular region. Black dashed lines show the independent calculations for the displacement. Displacement is the same for n *= 1 or 3, and for* $\Gamma_0' = 0$ *or 0.5.* $T_{ref} = 0$ *for all experiments.*

To determine if discretisation of the simple-shear box model (section 2.2) is adequately resolved I use the initial geometry given in Fig. 2.1, set $\Lambda = 0.5$, $n = 3$, $\Gamma_0' = 0.5$ and $T_{ref} = 0$, and repeat the calculation varying the number of elements. I test for a finite element size of 0.1, 0.5, 0.7, 1.0, 1.5, 2.0 (relative values) for which the number of elements is 15254, 3192, 2306, 1685, 1184 and 949. At $t' = 0$ and 1, I measure the second-invariant of the strain-rate ($\dot{E}$) along a profile that crosses the weak inclusion (Fig. 2.3a) and

compare the results. At $t' = 0$, prior to any integration, $\dot{E}$ is near identical for all results, but the viscosity boundary is better resolved with increasing mesh resolution. At $t' = 1$ the change in $\dot{E}$ is broadly similar for all tested element sizes, but with increasing resolution the noise is reduced. The same test is carried out for the India-Asia model and these results are presented in section 7.3.

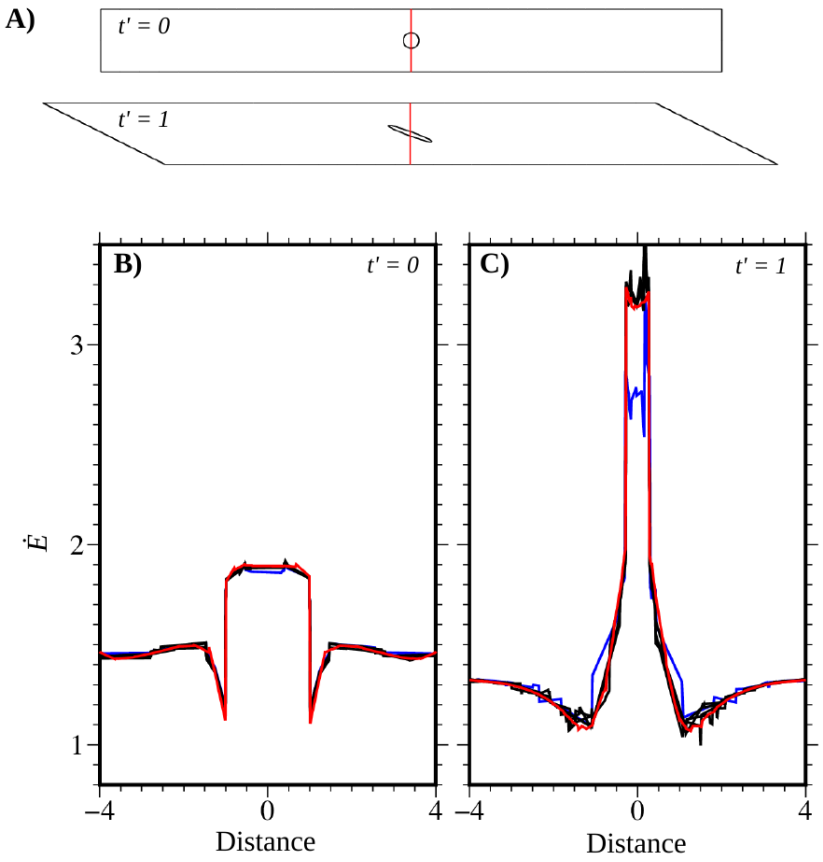

Figure 2.3: a) Location of profile along which AH is measured at t′ *= 0 and 1; b & c)* Ė *for varying grid resolutions (see text) where the finite element size is 2 (blue), 0.1 (red) and the remaining (0.5, 0.7, 1.0, 1.5) are show similar values and are shown in black, at b)* t′ *= 0 and c)* t′ *= 1. With increasing mesh resolution the boundary at the viscosity change is better resolved.*

2.6 Summary of methods used

Throughout this thesis I use the thin viscous sheet approximation that treats the lithosphere as a viscous fluid, and is implemented in the finite element program, *basil*. This approach assumes gradients of horizontal velocity and strength properties are invariant with depth. The deviatoric stress is proportional to strain-rate, where strain-rate varies as the n^{th} power of stress.

I use a 2D plane stress model to examine how strain localisation develops from a weak inclusion. The model allows for shear-heating, where the local strength properties to change in relation to the work done. I implement a simplified thermal diffusion, that assumes heat loss is perpendicular to a shear-zone. Using results from this model and from rheological laws derived from experimental data I calculate the maximum depth to which a thermally activated localisation can be supported.

Using a model configured to represent the India-Asia convergence I look at how strain localisation can develop across the Tibetan Plateau. Here the thin viscous sheet approximation allows for stress arising from gradients of topography (buoyancy forces). The model co-ordinates are defined on a spherical shell and the indenting boundary is defined by a rotation about an Euler pole. I allow for shear-heating, but simplify and ignore thermal diffusion.

Table 2.1: Notation used in the equations

β	Recovery parameter	f_{H20}	Water fugacity
Γ	Strain-weakening parameter	g	Gravitational acceleration
$\dot{\varepsilon}$	Strain rate	h	Crustal thickness
η_{eff}	Effective viscosity	k	Thermal wave-number
Θ	Second invariant of the deviatoric stress $\left(\Theta^2 = \tau_{ij}\,\tau_{ij}\right)$	L	Lithosphere depth
κ	Thermal diffusivity	m	Grain size exponent
λ	Thermal conductivity	n	Strain exponent (stress to a power of strain rate)
ρ	Density	P	Pressure
σ	Total stress	Q	Activation energy
$\bar{\sigma}$	average stress	R	Gas constant
τ	Deviatoric stress	r	Fugacity exponent
Φ	Rate of shear-heating	s	Grain size
A	Pre-exponent constant	T	Temperature
Ar	Argand number	t	Time
B	Strength parameter	T_{ref}	Reference temperature
Cp	Heat capacity	u	Horizontal velocity
D	Thermal anomally parameter	V	Activation volume
$\dot{E}$	Second invarient of the strain-rate $\sqrt{\dot{\varepsilon}_{ij}\,\dot{\varepsilon}_{ij}}$	$x_{i/j}$	Displacement in x or y direction
e	Lithosphere surface		

3 Localisation development under simple-shear

3.1 Influence of heterogeneity and strain-weakening on strain localisation

Large-scale lateral variations in rheology of continental lithosphere arise through orogenesis, pluton emplacement, thermal evolution and other geological processes (Cloetingh et al., 2010). Variations in age, composition, crustal or lithosphere thickness, temperature, pore fluid pressure, or mechanical anisotropy all can influence the resistance to lithospheric-scale deformation. Analogue (Keep, 2000) and numerical (England and Houseman, 1985; Tommasi et al., 1995) models show how high- or low-viscosity domains within the deforming continental lithosphere can influence the strain distribution arising from plate boundary forces. Strain typically localises near domain boundaries between regions of different effective viscosity (Vauchez et al., 2012, 1998). Sustained deformation in this situation can create lithospheric-scale shear zones, such as the Altyn Tagh fault of Central Asia (Dayem et al., 2009) or the Borborema shear zone in Brazil (Tommasi et al., 1995; Tommasi and Vauchez, 1997). Under a convergent strain field, orogenic belts such as those bordering the Tarim Basin may develop (Calignano et al., 2015a). Localisation of deformation is enhanced when the resistance to deformation decreases with strain or strain-rate and Gueydan et al. (2014) argue that progressive strain localisation is a precursor to the formation of tectonic plate boundaries.

Under convergent or divergent strain fields it is clear that weak layers within a vertically stratified lithosphere play an essential role in localising deformation and allowing movement on faults and shear zones that sole into a ductile crustal layer (e.g. Beaumont et al., 2000). Analogue and numerical models of lithospheric deformation (e.g. Brun,

2002; Calignano et al., 2015b; Munteanu et al., 2013; Sokoutis et al., 2005; Willingshofer et al., 2005) have provided essential insights into how a faulted upper crustal layer interacts with ductile deformation at depth. Although some studies have focussed on the process of strain localisation in transpressional or transtensional environments (e.g. Cerca et al., 2004; Corti et al., 2002; Le Pourhiet et al., 2012) the simpler case of strike-slip deformation has attracted less attention, perhaps because orogenic belts and extensional basins are more commonly encountered. In this chapter I focus on how strain may localise in the strike-slip environment.

Strain distribution in viscous or visco-plastic flow models is generally controlled by the background stress field imposed at the boundaries of the domain, but the geometrical shape and alignment of anomalous inclusions can promote the formation of shear zones whether the inclusion is relatively weak (Mandal et al., 2004) or strong (Misra and Mandal, 2007). Shear zones originating from multiple anomalous domains can propagate and amalgamate under sustained strain (Grujic and Mancktelow, 1998; Mandal et al., 2004; Misra and Mandal, 2007). Analogue experiments by Misra et al. (2015) show that increasing temperature inhibits localisation as plastic strain is enabled across the deforming medium, while increasing pressure promotes localisation.

Localisation of strain may be enhanced by strain-rate weakening in regions where stress differences vary. For the non-Newtonian constitutive laws that typically describe creep deformation of silicates (Hirth and Kohlstedt, 1995; Karato, 1984; Karato et al., 1986; Kohlstedt and Goetze, 1974) effective viscosity is reduced where the concentration of intra-crystalline dislocations is increased in response to greater stress differences. However, the degree of localisation evident in lithospheric-scale shear zones is not

explained simply by power-law materials with typical stress versus strain-rate exponents of $n \sim 3$ (Dayem et al., 2009). A strain-weakening process is also required to explain the formation of lithospheric shear zones like the Altyn Tagh, the San Andreas and the North Anatolian. Lithospheric-scale strain-weakening mechanisms based on shear heating (Brun and Cobbold, 1980; Burg and Schmalholz, 2008; Leloup et al., 1999; Regenauer-Lieb et al., 2015; Thielmann and Kaus, 2012), fabric development (e.g. Montési, 2013), grain size sensitive creep (e.g. Precigout and Gueydan, 2009; Warren and Hirth, 2006), and partial melting (e.g. Nabelek et al., 2010; Tommasi et al., 1995) have been proposed. Independent of scale, localisation requires a weakening feedback mechanism that can depend on one or more variables,including changes in temperature and grain-size (Montési and Zuber, 2002) . For any weakening mechanism, spatial variations in the work done by deformation cause variations in the strength of the material and thereby promote localisation of deformation. Thielmann and Kaus (2012) showed that shear heating can facilitate the formation of a lithospheric-scale shear zone. Burg and Schmalholz (2008) showed how buckling of the lithosphere in a convergent environment gives way to localisation of deformation on thrust planes. In some situations shear heating may be sufficient to cause partial melting and extreme strain localisation (Nicolas et al., 1977; Regenauer-Lieb et al., 2015). However, localisation through shear-heating may be suppressed for temperatures greater than some threshold dependent on specific lithology (Montési and Zuber, 2002). Here I focus on the thermal weakening model for strain localisation, but acknowledge that a similar approach could be used for modelling of possible localisation mechanisms based on development of mineral fabric and grain size.

I use 2D numerical experiments to demonstrate how strain can localise around a weak seed in a lithospheric environment which would otherwise undergo homogeneous simple-shear. I follow Grujic and Mancktelow (1998); Kaus and Podladchikov (2006); Mandal et al. (2004) in examining how a weak seed influences strain distribution, but here consider a simple-shear deformation field, rather than pure-shear. Following the method detailed in Chapter Two (and outlined in section 3.2) I use a simplified continuum model with a generalised strain-weakening rheological law based on temperature-activated dislocation creep in silicates to represent a thermal weakening mechanism. The work done by viscous strain causes a weakening dependent on the integrated work. When stress is relatively homogeneous, weakening is most effective in regions of greatest strain rate, thus promoting a feedback mechanism that leads to progressive strain localisation.

3.2 Configuration of simple-shear box model experiments

For the calculations, in which all parameters are dimensionless, I follow the method given in section 2.2 and here present an overview. The strain-rate varies as the n^{th} power of stress scaled by a depth-averaged lithospheric strength coefficient, B, that includes the dependence on temperature, grain-size, fugacity, pressure, and rheological parameters for a specific mineral (Eq. 2.14, 2.15). Following Dayem et al. (2009) I assume that all the work dissipated by viscous deformation is converted into heat and locally retained on the time-scale of interest. The change in B due to temperature change can be described using the integrated work done (Eq. 2.21), and a localisation parameter, Γ, that includes the temperature dependence (Eq. 2.20). I define a thermal

anomaly parameter *D*, which represents the time-integrated work per unit volume and is proportional to the local increase in temperature if diffusion of heat is neglected (Eq. 2.22). This allows the change in *B* to be given in terms of *D* and Γ (Eq. 2.23). The initial temperature, T_0, defines T_{ref} (Eq. 2.40) which, with the initial value of Γ (Γ_0) and *D*, defines *B* at any point in time (Eq. 2.44). The diffusion of heat away from the region can be approximated by modifying the rate of change of *D* using the diffusion parameter β (Eq. 2.53). I follow Eq. 2.54, 2.55 and 2.56 in non-dimensionlising numbers, which are indicated by prime (e.g. Γ_0').

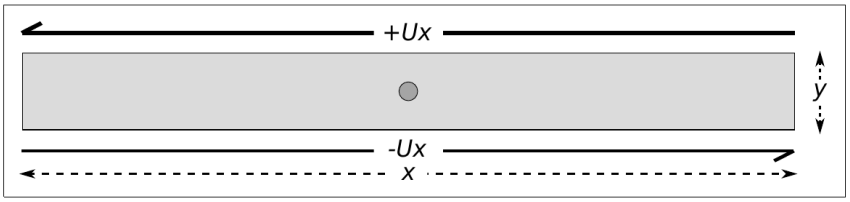

Figure 3.1: The model domain is a rectangular region of length 80r and width 8r in the (x, y) plane with a circular inclusion of radius r *= 1 located centrally. A velocity,* $U_x = \pm 8$ *is applied to the horizontal boundaries such that the background strain rate = 1. The viscosity coefficient* B′ *of the background region is initially set at* $B_0' = 1$ *and the viscosity coefficient of the inclusion is initially weaker than the background region by a factor* Λ.

As an exploration of the general strain localisation problem in two dimensions I now consider a series of numerical experiments on a simplified model of 2D plane-stress deformation of a rectangular region undergoing simple-shear imposed by boundaries moving at a constant rate (Fig. 3.1). I use a rectangular region of length 80 and width 8, with x-direction velocities of ±8 imposed on the y-boundaries so that the background shear strain-rate is $\dot{\varepsilon}_0' = 1$. An initial spatial heterogeneity is required to initiate strain localisation. In reality any spatial heterogeneity can act as a seed for localisation, but

here I describe systematic behaviour in a particularly simple case. I embed small circular inclusion (radius = 1) in the centre of the test region (Fig. 3.1), within which I set the initial rheological factor $B = \Lambda B_0$. I vary n, Λ, Γ_0' and β' . I use the finite element program *basil* to obtain time-dependent solutions of the evolving deformation field by solving for the strain-rate field that satisfies the conditions of stress equilibrium and mass conservation, here amended to allow for temperature-dependent weakening factor Γ and diffusion factor β.For silicates deforming by dislocation creep a strain exponent of n = 3 to 4 is most appropriate. However, strain localisation may require n ~ 10, representing a more plastic deformation, but n may be smaller for a higher strain-weakening component (Γ) (Dayem et al., 2009). I also explore if a Newtonian rheology (n = 1) under strike-slip conditions can promote strain localisation. I thereforefore apply a strain exponent n = 1 to 10.

I set Λ to intially be 0.25, 0.5 or 0.75. The initial dimensionless strength simply relates to the strain exponent, Λ^n. For Λ = 0.75 and for n = 1, 3, 5 or 10 the initial strength will vary between 0.75 to 0.056.Using parameters for olivine (Hirth and Kohlstedt, 2013) and quartz (Hirth et al., 2001; Rutter and Brodie, 1995) and assuming V = 0 (Table 3.1), the dimensional values of Γ (Eq. 2.20) vary between about 6 x 10^{-9} and 3 x 10^{-8} m^3/J for temperatures between about 400 and 1000 K. Due to the strong temperature dependence of the non-dimensionalising factor (Eq. 2.56) the dimensionless Γ' value may vary over orders of magnitude within the lithosphere, though typically in the range 0.01 to 100. In practice the range of interesting behaviour is much more restrictive, and so I focus the experiments focus on values of Γ_0' between 0.4 and 2.0.

Table 3.1: Rheological parameters used in the calculation of the localisation constant. Representative values of T_{ref} *are given for two different temperatures.*

Mineral	**A**	**Q (kJ/ mol)**	**n**	**V (m^3/ mol)**	**Deformation**	**Reference**	**T_{ref}**
							400/ 600 K
Quartz	1E-2.4	242	2.97	-	Dry dislocation	Rutter & Brodie (2004)	0.041/ 0.061
	1E-11.2	135	4	-	Wet dislocation (fugacity exponent = 1.0)	Hirth et al. (2001)	0.099/ 0.148
							400/ 750 K
Plagio-clase (An100)	5.01E12	648	3	-	Dry dislocation	Rybacki & Dresen (2000)	0.015/ 0.029
	3.98E02	356	3	-	Wet dislocation		0.028/ 0.053
							750/ 1000 K
Olivine	1.1E05	530	3.5	14	Dry dislocation	Hirth & Kohlstedt (2013)	0.041/ 0.055
	1600	520	3.5	22	Wet dislocation (fugacity exponent = 1.2)		0.042/ 0.056

As an initial test of the implementation of Eq. 2.44 I set the initial rheological coefficient $B_0' = 1$ everywhere, and $n = 3$, $\Gamma_0' = 1$, $\beta' = 0$, and $T_{ref} = 0$, 0.041 and 0.148 in order to test that the strain-weakening works as expected for an initially homogeneous region under simple-shear boundary conditions, for which the rate of weakening is spatially invariant. The *basil* calculation closely tracks the theoretical relationship (Eq. 2.44) between B' and D' as the strength of the material is reduced by a factor of about 5 in the three tests shown in Fig. 3.2. When $T_{ref} = 0$, Γ is constant during the time integration and the theoretical model predicts exponential decay (a straight line on Fig.

3.2). For these values of T_{ref}, assuming Γ is constant produces slightly faster localisation, though the difference is small relative to the case with T_{ref} = 0.041.

For the same parameters T_{ref} (Eq. 2.40) is typically in the range 0.03 to 0.1 but may be > 0.2 for wet quartz. I use values of 0.041 and 0.148 representative of dry olivine at 1000 K and wet quartz at 600 K respectively in these experiments (Table 3.1).

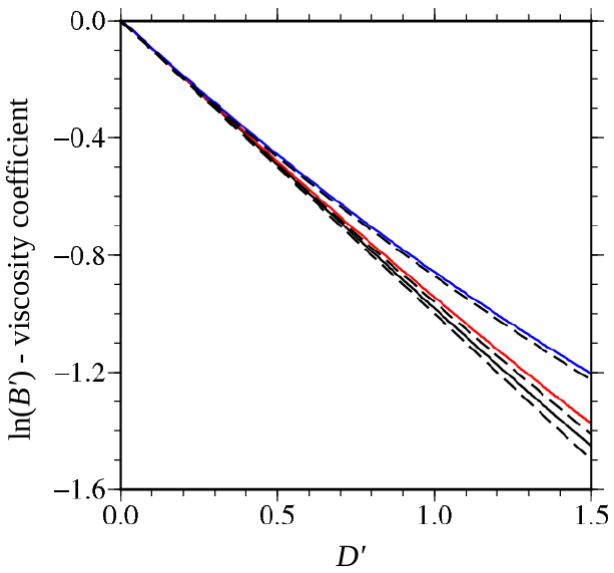

Figure 3.2: Evolution of the strength coefficient B′ *and integrated work* D′ *for an initially homogeneous region with* n = *3 and* Γ_0' = *1.2. Solid lines show evolution calculated by finite element program basil where* T_{ref} *= 0 (black), 0.041 (red) and 0.148 (blue). The black dashed lines show evolution calculated from Eq. 2.44 for corresponding* T_{ref} *values.*

3.3 Results from the simple-shear box model

When a weak inclusion is present (Λ < 1) and strain-weakening is activated (Γ_0' sufficiently large) localised regions of high shear strain rate (relative to the background

value) appear either side of the weak inclusion. These high strain-rate zones extend parallel to the shear direction and diminish in intensity with distance from the inclusion (Fig. 3.3). This strain-rate pattern contrasts with shear zones developed under pure shear, in which typically four high strain regions, aligned at between 35° and 53° to the principal axis develop away from an inclusion (Grujic and Mancktelow, 1998; Kaus and Podladchikov, 2006; Mandal et al., 2004). Depending on the strain-weakening parameters, Γ_0' and T_{ref}, increasing boundary displacement causes the gradient of U_x within these zones to increase as that outside decreases, so that the total velocity contrast across the layer remains consistent with the boundary conditions (Fig. 3.4).

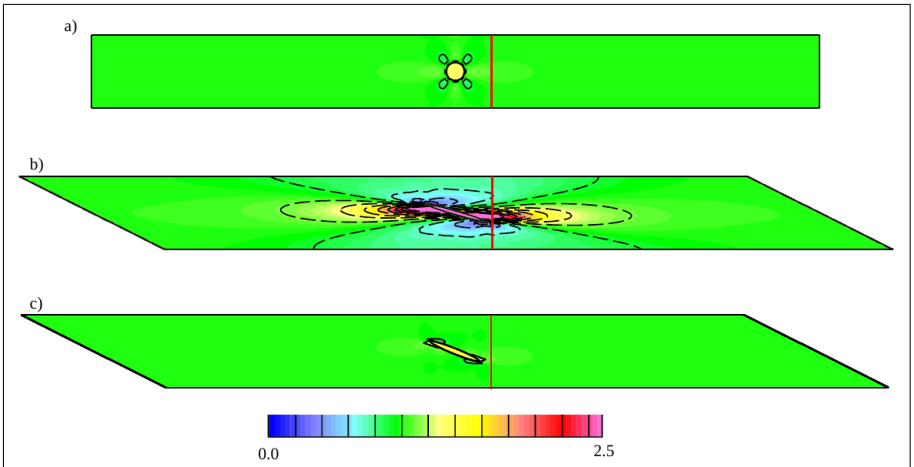

Figure 3.3: The dimensionless maximum shear strain rate in the model at, a) onset of the applied boundary conditions, b) at total strain =1 (with T_{ref} *= 0.041,* Λ *= 0.75,* n *= 3, and* Γ_0' *= 1.0), and c) at total strain = 1 (*Λ *= 0.75,* n *= 3, and* Γ_0' *= 0). Contour intervals at 0.2; colour saturates and contours are not shown for strain-rate > 2.5. Red line shows x' = 4 (location of profiles in Fig. 3.4).*

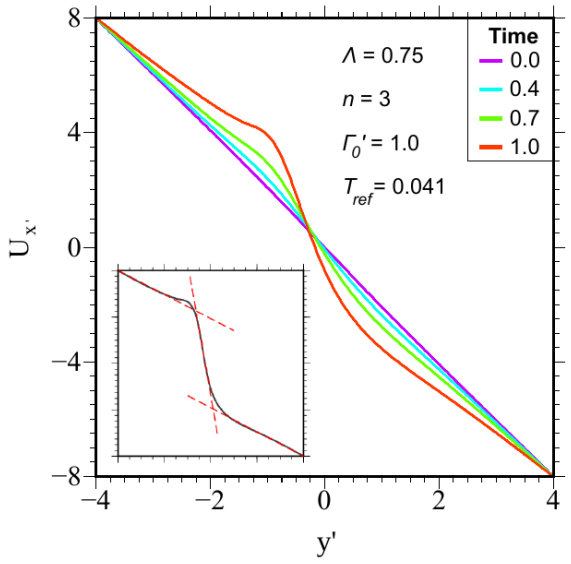

Figure 3.4: Profiles of U_x *across the strain-rate field shown in Fig. 3.3b at* x = 4 *and times as labelled. At* t′ = 0 *the* dU_x/dy *gradient is constant across the line of section. With increasing time (or strain) the gradient in the middle of the region,* $(dU_x/dy)_{sz}$*, increases but the total velocity difference across the region remains unchanged as strain-rates decrease outside the shear zone. The high gradient region corresponds to the developing high strain-rate zones as shown in Fig. 3.3b.*

I quantify strain localisation by measuring the gradient dU_x/dy across the high strain-rate zone. Using this measure I track the development of the shear zone in time and distance from the weak inclusion (Fig. 3.5a, b). For $\beta' = 0$ (no thermal diffusion) the log-linear graph of Fig. 3.5c shows that the shear zone gradient has a growth curve that is faster than exponential, though the early phases of that growth may be approximated as exponential. I therefore investigated whether a power law growth of the form:

$$\left(\frac{dU_x}{dy}\right)_{sz} = a(t_0 - t)^{-p} \qquad \text{Eq. (3.1)}$$

might describe the latter stage of these growth curves. To do so I plot, as a function of time, the measured values of the shear-zone gradient raised to the power -1/*p* (as in Fig.

3.5d) for a range of *p*-values. In general the resulting graph is a straight line for some *p*-value after an initial phase of slow growth, and the projected line intersects the time axis at t_0. I find that the *p*-values decrease systematically with increasing distance from the inclusion, from about 0.8 to about 0.2 (for $n = 3$). The *p*-value increases with *n* and with Γ_0' (Fig. 3.6). The consequence of this type of power-law growth is that, in this idealised model, localisation will collapse to a planar discontinuity (a geological fault) in a finite time t_0, determined by n, Γ_0' , and the properties of the initial heterogeneity (in this case Λ). In a geological scenario thermal diffusion is likely to limit this process well before the theoretical fault discontinuity is achieved, but it can still be inferred that a high degree of localisation is possible for the same values of Γ_0'.

Another way of looking at the increase in strain localisation is to examine the length of the shear zone as a function of increasing overall strain. To compare shear zone development in different experiments I determine the time at which the velocity gradient in the shear zone exceeds 150% of the background velocity gradient. This time is a function of distance from the initial heterogeneity seed, as shown in Fig. 3.7 for three groups of models in which Λ, n or Γ_0' are varied with $T_{ref} = 0.041$ and 0.148 and $\beta' = 0$. In general the length of the zone that exceeds the 150% threshold increases linearly with time. The shear-zone by this definition is initially longer and grows faster for smaller Λ (Fig. 3.7a), for larger n (Fig. 3.7b), and for larger Γ_0' (Fig. 3.7c). For $\Lambda = 0.5$ and 0.25 in Fig. 3.7a, distortion of the finite element mesh prevented the calculations from running further but I propose that the linear relationship of time to the 150% threshold and distance from inclusion persists. Although the shear-zone grows faster where Λ is less, a 50% increase in strain rate is still achieved for $\Lambda = 0.75$ with n = 3 where Γ_0' is sufficiently large (≥ 0.8).

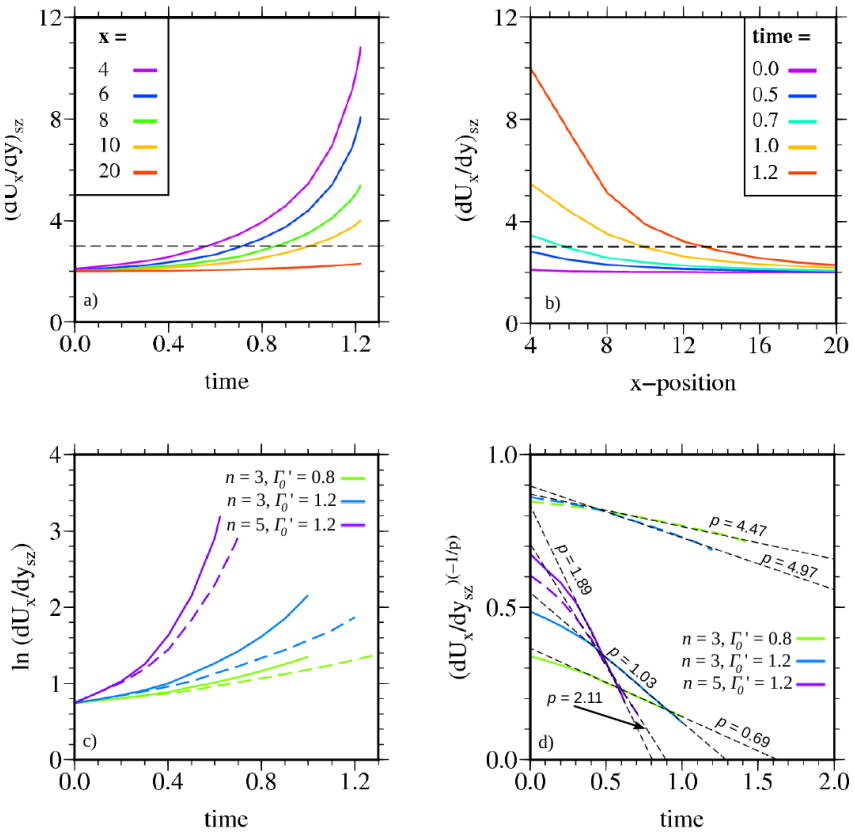

Figure 3.5a: $\Lambda = 0.75$, n = 3, $\Gamma_0' = 1.0$, $\beta' = 0$, $T_{ref} = 0.041$; *velocity gradient dUx/dy in the high-strain rate zone as a function of time for different values of* x; x = 4 *is closest to the inclusion and* x = 20 *is furthest away. b: the same data plotted as a function of x-distance at different times. The dotted lines show when the velocity gradient in the shear zone exceeds 150% of the background velocity gradient. c:* $T_{ref} = 0.041$ *(solid line) and 0.148 (dashed line) and other parameters as for (a); log- linear plot shows that initial shear zone gradient development is approximately exponential, but then increases at a rate greater than exponential, here shown for* x = 4 *but this type of growth curve is observed at all distances from the inclusion. d: the same data as (c) projected to show that shear zone gradient evolves to follow a power law growth (Eq. 3.1).*

In a similar set of experiments with $\beta' > 0$, I investigate the impact of thermal diffusion on the shear zone formation (Fig. 3.8). Following the same approach as before I determine the times at which the values of dU_x/dy in the high strain-rate zone exceed

150% of the background rate. I find that the approximately linear relationship between shear-zone length and time is generally preserved, but an increase in β' reduces the strain localisation and increases the time required to reach the 150% threshold. For T_{ref} = 0.041 and 0.148, sufficiently large values of β' (~ 10 for n = 3 or 5) suppress the thermal localisation of strain. For smaller values of $\beta' > 0$, the initial period of exponential increase in localisation is extended. In such cases it appears that the exponential rate of reduction in the work parameter D associated with $\beta' > 0$ in general is overwhelmed eventually by the power-law (Eq. 2.53) increase caused by viscous heating, if Γ_0' is sufficiently large.

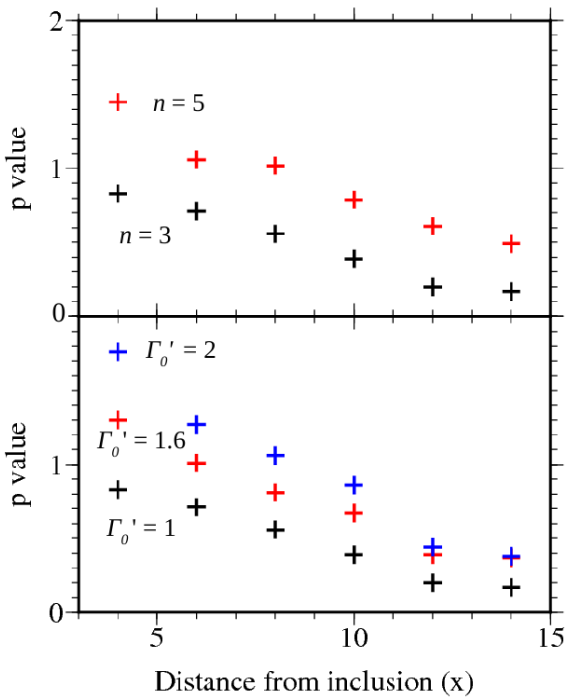

Figure 3.6:For $\Lambda = 0.75$, $T_{ref} = 0.041$ *and* $\Gamma_0' = 1$ *with varying* n *(top) or* n = *3 with varying* Γ_0' *(bottom) the* p*-value from Eq. 3.1 with distance from the centre of the weak inclusion for* $x' \geq 4$. *The* p *values from the line of section that are initially closer to the weak inclusion are not calculated due to the progressively elongated weak inclusion crossing these regions, changing the velocity gradient measurement.*

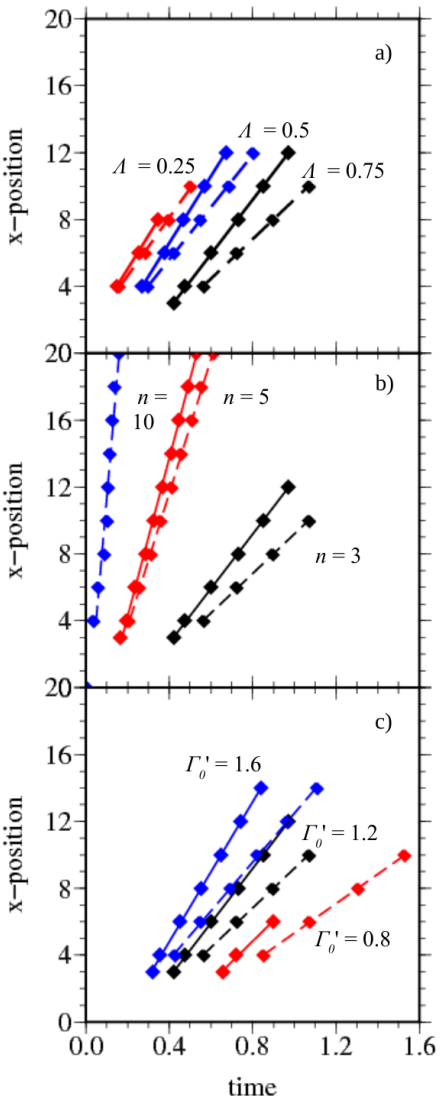

Figure 3.7: Shear-zone extent vs time: for each x-value in an experiment, the time at which dUx/dy in the high strain-rate zone exceeds 150% of the background strain-rate value is plotted for experiments with a) n *= 3,* Γ_0' *= 1.2,* Λ *as labelled; b)* Λ *= 0.75,* Γ_0' *= 1.2,* n *as labelled; c)* Λ *= 0.75, n = 3,* Γ_0' *as labelled. Solid lines are for* T_{ref} *= 0.041, dashed for* T_{ref} *= 0.148; in each case* β' *= 0. The high strain-rate zone does not exceed 150% of the background strain-rate when* n *= 1.*

For n = 1 localised regions of high shear strain rate do not develop, even if Γ_0' is as high as 50 and Λ is as low as 0.25. Consequently in this model for which strain-weakening depends on thermal activation, a non-Newtonian (power-law) rheology appears necessary to the development of significant strain-localisation. Localised deformation is inhibited (i.e. the high-strain regions do not exceed 150% by t' = 1) where $\Gamma_0' \leq 0.3$ for n up to at least 10.

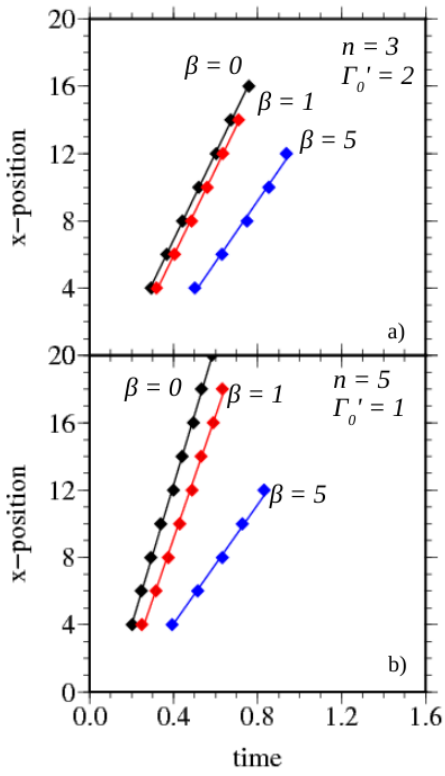

Figure 3.8: Shear zone extent versus time (as defined in Fig. 3.7) for $T_{ref} = 0.041$, $\Lambda = 0.75$ *and values of* β' *as labelled for a)* $n = 3$, $\Gamma_0' = 2$ *and b)* $n = 5$, $\Gamma_0' = 1$. *Increasing* β' *increases the time for strain to become significant or slows the growth of the shear zone. For* $\beta' \geq 10$ *the 150% threshold is not reached for either combination of parameters.*

3.4 Discussion of simple-shear box model results

Kaus & Podladchikov (2006) showed that a visco-elasto-plastic deformation regime was capable of developing regions of reduced viscosity, dependent on a shear-heating efficiency parameter that is analogous to my Γ_0'. My results are broadly consistent with theirs for large values of n (which can be considered an approximation for plastic behaviour) but I find that for any value of $n \geq 2$ strong localisation can develop for a background strain of $\varepsilon_0' = 1$ when Γ_0' exceeds a threshold value. This value depends on n, T_{ref}, Λ, and β'. Values of the time-scale for localisation (t_0' in Eq. 3.1) obtained from my numerical experiments are summarised by the contour plot in the n-Γ_0' parameter space of Fig. 3.9 for two different values of T_{ref}. The value of Γ_0' required for a shear

zone to localise within the time corresponding to a background strain of about 1 ($t_0' = 1$) can then be read from Fig. 3.9 for a given n value. For n = 3 to 4, typical of silicates undergoing dislocation-creep deformation (Table 3.1), $\Gamma_0' > 1.5$ produces localisation on this time-scale for $T_{ref} = 0.041$ (relevant to olivine or dry quartz, Fig. 3.9a). Where $T_{ref} = 0.148$, as for wet quartz, extrapolating the graph to infer that localisation occurs when $\Gamma_0' > 2.5$ (Fig. 3.9b).

For n = 10, used to describe the rheology of the Tibetan lithosphere by Dayem et al. (2009), I find that for $T_{ref} = 0.041$ and 0.148 requires $\Gamma' > 0.1$ for localisation to occur and $\Gamma' \geq 0.2$ for localisation to occur within a time-scale comparable to geological processes (Fig. 3.9). Dayem et al. (2009) find localisation requires a corresponding weakening parameter of $\Gamma' = 0.01$ to 0.3. Their difference in the lower bound may be due to my model permitting Γ' to evolve with temperature change or due to differences in the rate of localisation that originates from a weak region subject to simple-shear, rather than a strong inclusion partially subject to pure shear.

These results demonstrate that for $\Gamma_0' \geq 0.3$ lithospheric silicate minerals are capable of a high degree of localisation if strain is sufficiently rapid that thermal diffusion can be neglected. Where thermal diffusion is significant ($\beta' > 0$), localisation can still occur for a greater value of Γ_0' but, where diffusion is sufficiently high, localisation is suppressed, as Kaus & Podladchikov (2006) showed for 1D viscous deformation models. Although localisation in this idealised model with $\beta' = 0$ I can see the shear-zone collapse into a planar discontinuity conceptually similar to a fault, thermal diffusion will generally prevent that outcome in a real silicate because the decreasing width of the shear zone causes β' to increase as the localisation progresses.

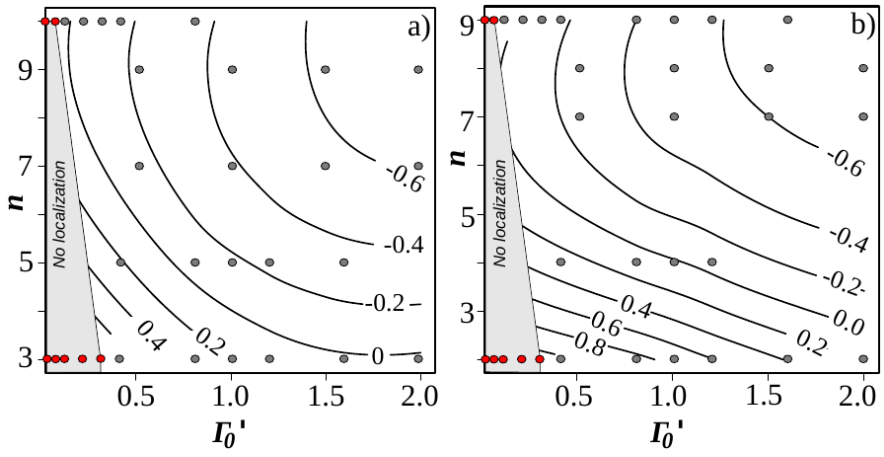

Figure 3.9: Gridded and contoured values of log_{10} (t_0') obtained from the type of analysis shown in Figure 3.5d, using measurements at x *= 4 for experiments with* Λ *= 0.75 and* T_{ref} *= 0.041 (a) or 0.148 (b). Parameter combinations used in the numerical experiments are marked by grey (localisation occurs) and red (no localisation) circles. For* n *= 3 or 4 (most relevant to silicates deforming by dislocation creep) these maps show that* t_0' *< about 1 (i.e. strain is localised within the time interval required for a strain of 1) if* Γ' *> about 1.5 (for* T_{ref} *= 0.041) or about 2.5 (for* T_{ref} *= 0.148). The interval* t_0' *= 1 corresponds to* t_0' *= 3 Myr for a strain rate of* 10^{-14} s^{-1}*. Results for* n *= 1 are not shown here, but in experiments with* Γ_0' *up to 50 no significant localisation was observed.*

It is noteworthy that the shear localisation model described here predicts that the length of the shear zone increases linearly with increasing strain, just as maximum fault displacement increases with length of fault (Cowie and Scholz, 1992). Propagating fault and shear-zone tips may join, resulting in the formation of long composite regions of high strain, which on short time scales may show relatively low displacement. My model has focused on the development of a shear zone from a single point of weakness but it is worth noting that the inclusion of multiple weak seeds, representing the heterogeneous nature of the lithosphere, would enable shear-zone growth through linkage. Shear-zone linkage has been observed at multiple scales, such as in shear zones

< 40 m in length in the southern Alps (Pennacchioni, 2005) and or the 100 km scale Borborema shear zone system in Brazil (Fossen and Cavalcante, 2017). However, the requirements for shear zone localisation remain, i.e. the area around each weak seed requires some sort of strain-weakening. While small scale systems may conceivably maintain the required physical conditions for a strain-weakening mechanism across the region of interest, the inherent variability in large scale systems may be too great and localisation may not occur in the vicinity of some weak seeds. Thus shear-zone linkage may be more prevalent in small scale systems.

3.5 Summary of simple-shear box model experiments

In considering deformation of the continental lithosphere I have shown that a region with a weak inclusion subjected to simple-shear can develop localised zones of high strain-rate near parallel to the direction of shear. A strain-weakening mechanism dependent on the mechanical work done by deformation enhances local strain and promotes further localisation. The work done generates heat that locally raises the temperature of the thermally activated silicate. The strain rate in the shear zone follows a power-law growth curve, whose exponent p is dependent on the inclusion strength (Λ), strain exponent (n), initial strain-weakening parameter (Γ_0') and the rate at which it changes (T_{ref}) with temperature, and the distance from the inclusion. If the strain-rate is sufficiently slow that cooling occurs, the onset of the thermal localisation instability can be delayed or suppressed. In Chapter Four I apply this simplified conceptual model to considering how ductile shear zones localise with depth.

4 Strain localisation with depth by shear heating

4.1 Introduction: strain localisation in the lithosphere

A lithosphere-scale fault zone is typically depicted as a localised fault plane in the upper lithosphere above a ductile shear zone whose width increases with depth in the mid to lower lithosphere (e.g. Burgmann and Dresen, 2008; Moore and Parsons, 2015; Vauchez et al., 1998). Ductile shear zones are capable of localising at depth, as geological evidence can show. Strain estimates from exhumed mylonites of the Alpine Fault infer deformation in the mid to lower crust (20 to 30 km) is accommodated over a relatively narrow width of 1 to 2 km, with thermal weakening a likely localisation mechanism (Norris and Cooper, 2003). Deformation fabrics in mantle xenoliths from the Eastern California Shear Zone indicate the development of strain localisation at the Moho (~ 30 km) (Bernard and Behr, 2017). What controls this maximum localisation depth?

In Chapter Three I considered how localised deformation within a 2D horizontal section of the lithosphere may develop when that section is subject to a simple-shear deformation representative of a strike-slip environment in the lithosphere. I now consider how that development may vary with depth within the lithosphere, recognising that temperature, pressure and lithology vary systematically with depth but that the entire lithospheric section is exposed to the same background strain rate. This approach obviously neglects the interaction between different depths, in order that understanding might be developed without the complexity of a comprehensive 3D thermo-mechanical solution. The lithology, temperature, and pressure enter this analysis because they control the background viscosity coefficient in my 2D deformation experiments. The dimensionless formulation of the problem presented in Chapter Two allows me to

directly interpret that variation of background viscosity as a variation of the dimensionless parameter Γ_0', the initial shear heating weakening component.

I show here that this qualitative understanding of fault-zone structure is consistent with my thermal localisation analysis which predicts that there is a maximum temperature and depth at which a shear zone can localise. This depth is dependent on strain-rate, heat-flow and mineralogy. I then apply the calculations to two major continental strike-slip zones, the San Andreas Fault and North Anatolian Fault, and compare my predicted maximum localisation depths with published seismological images.

4.2 Method for calculating localisation depth

In Chapter Three I showed how deformation around a weak region subject to simple-shear can localise strain when the initial dimensionless strain-weakening parameter (Γ_0') is greater than 1.5 for plagioclase, olivine and dry quartz, and greater than 2.5 for wet quartz. Here I consider how the dimensionless values of Γ_0' may vary with depth within the lithosphere using the formula derived in Chapter Two:

$$\Gamma_0' = \Gamma_0 H_0 \dot{\varepsilon}_0^{1/n} = \left(\frac{2}{3}\right)^{(n+1)/2n} \left(\frac{Q+P_0V}{\rho C_p n R T_0^2}\right) \left[A^{-1} s^m f_{H_2O}^{-r} \dot{\varepsilon}_0\right]^{1/n} \exp\left(\frac{Q+P_0V}{nRT_0}\right) \quad \text{Eq. (4.1)}$$

where $\dot{\varepsilon}_0$ is the background strain-rate, H_0 a physical scale factor for the viscosity coefficient, Γ_0 the initial weakening component, n is the power-law creep exponent, Q and V are activation energy and volume respectively, P is pressure, ρ density, C_p heat capacity, R is the universal gas constant, T temperature in Kelvin, s is the grain size, f_{H2O}

is the fugacity of water, *r* and *m* are experimentally-determined indices, and *A* is an empirical constant determined by experiment.

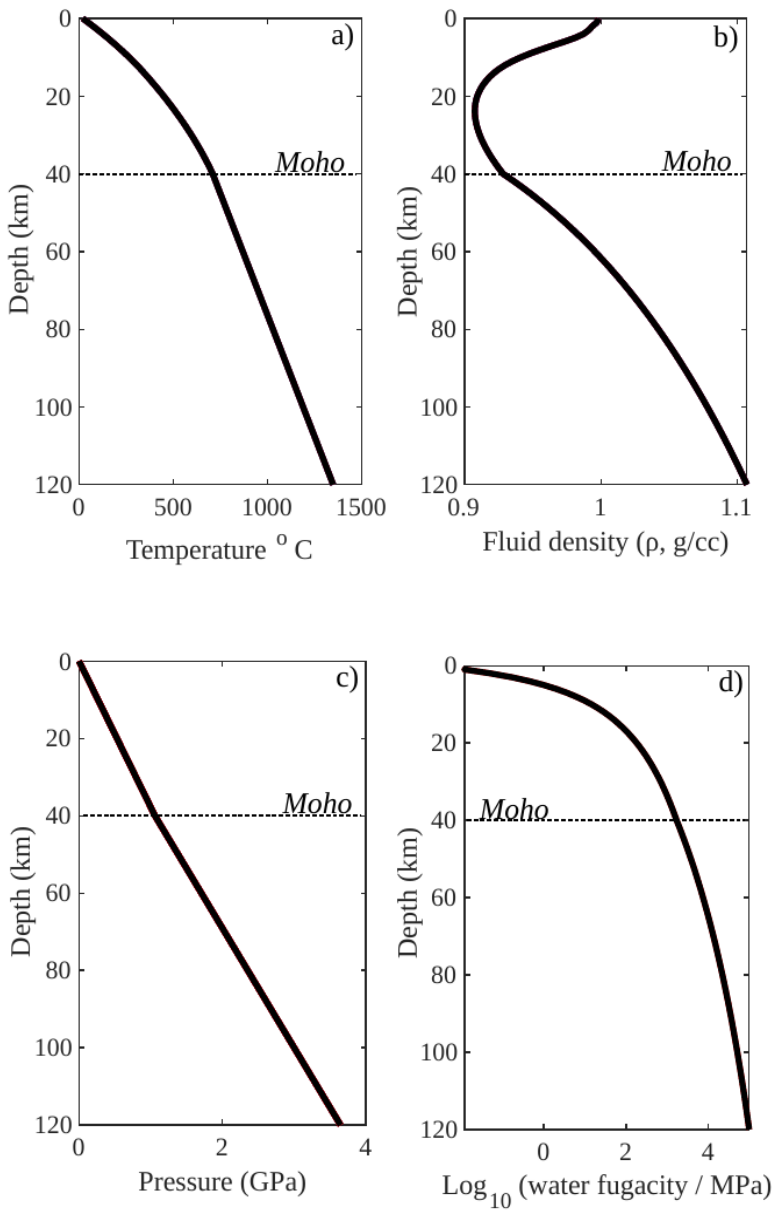

Figure 4.1: a) Geothermal gradient calculated for F *= 70 mW.m^{-2} following the method described in the text. b) Fluid density with depth, which is dependent on temperature and pressure. c) Lithostatic pressure with depth where* ρ *= 2700 kg.m^{-3} for the crust (0 to 40 km) and* ρ *= 3300 km.m^{-3} for the mantle lithosphere (> 40 km). d) Water fugacity with depth, calculated following Pitzer and Sterner (1994) and Sterner and Pitzer (1994).*

To evaluate the relevant dimensionless value of Γ_0' (Eq. 4.1) for a given lithology at a particular depth I require estimates of background strain rate, temperature, pressure, and water fugacity (where relevant). These background values are based on a 1D two-layer model of crust over mantle with a steady-state conductive geothermal in which the top and bottom temperatures are constrained to be 20 ºC and 1350 ºC respectively and I adjust the radioactive heating in the crust to give a prescribed surface heat flow (*F*). In doing so I assume an upper crustal layer to 18 km depth in which the heat production is twice that of a lower crustal layer to 40 km depth and thermal conductivity for crust and mantle of 2.5 and 3.0 $W.m^{-1}K^{-1}$ for crust and mantle respectively.

The calculation of pore-fluid pressure assumes a lithostatic profile with typical crustal and mantle densities of 2700 and 3300 $kg.m^{-3}$, and I calculate fH_2O following the method of Pitzer and Sterner (1994) and Sterner and Pitzer (1994) assuming lithostatic pore fluid pressure (Fig. 4.1):

$$\ln fH_2O = \left[\ln \rho + \frac{A^{res}}{nRT} + \frac{P}{\rho RT} \right]_{P,T} + \ln(RT) - 1 \qquad \text{Eq. (4.2)}$$

Where A^{res} is the residual Helmholtz energy, a measure of the energy obtained from the system[1]. In the lithosphere fluid density (Fig. 4.1b) initially reduces, as the increasing temperature with depth (Fig. 4.1a) counters the increasing pressure (Fig. 4.1c), and the resultant increase in fH_2O is slow. At ~ 20 km the increasing pressure (Fig. 4.1c) dominates, fluid density increases and the increase in fH_2O becomes rapid (Fig. 4.1d).

1 $A = U - TS$ where here *A* is the Helmholtz free energy, *U* is the internal energy, *T* the temperature and *S* the final entropy of the system.

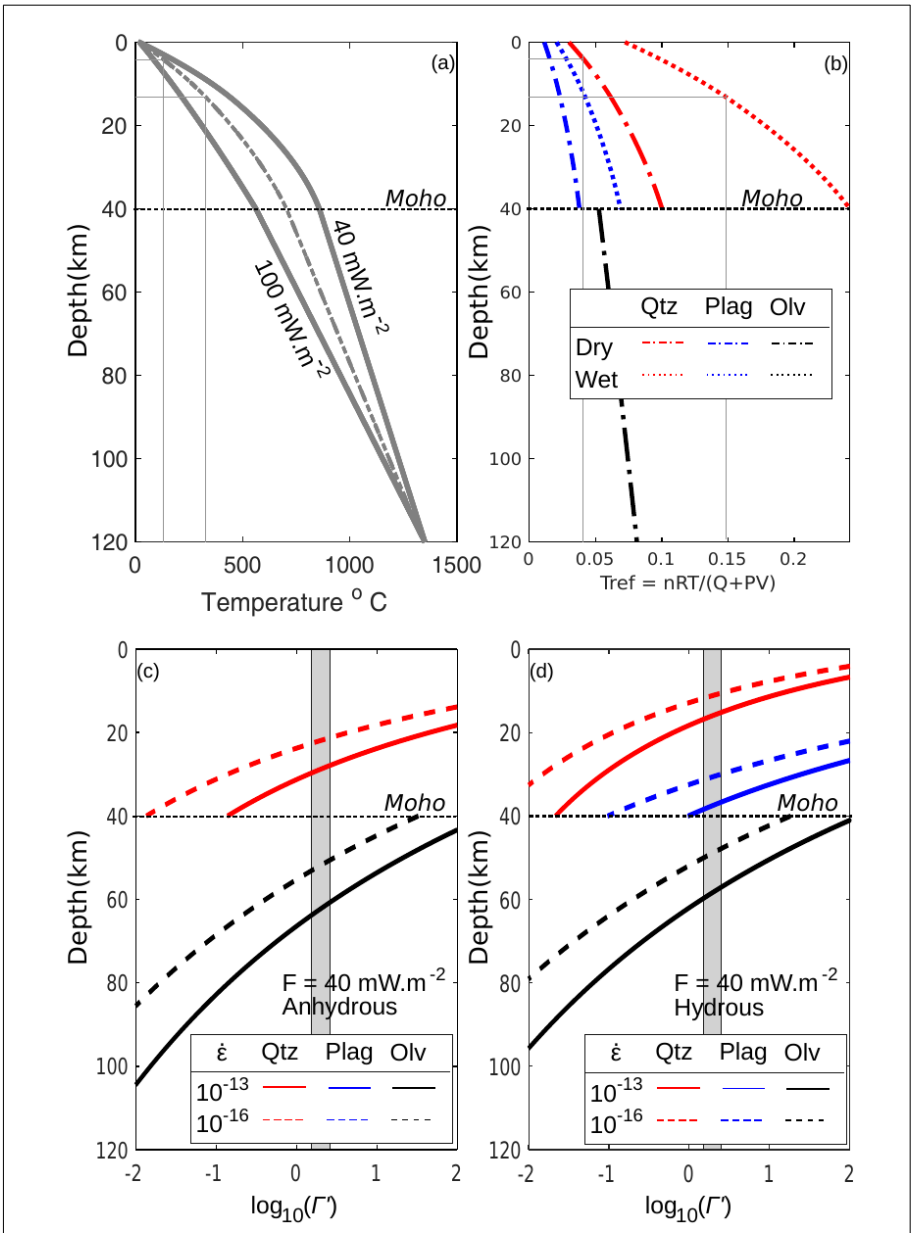

Figure 4.2: continued on next page.

The background strain-rate is assumed constant with depth. Using plausible background tectonic strain-rates in the range 10^{-16} to 10^{-13} s^{-1}, equilibrium geotherms for heat flow in the range 40 to 100 mWm^{-2}, and published rheological constants for quartz, plagioclase and olivine (Hirth et al., 2001; Hirth and Kohlstedt, 2013; Rutter and Brodie, 2004;

Rybacki and Dresen, 2000) (Table 3.1), I calculate how Γ_0' (Eq. 4.1) varies with depth in the lithosphere (Fig. 4.2).

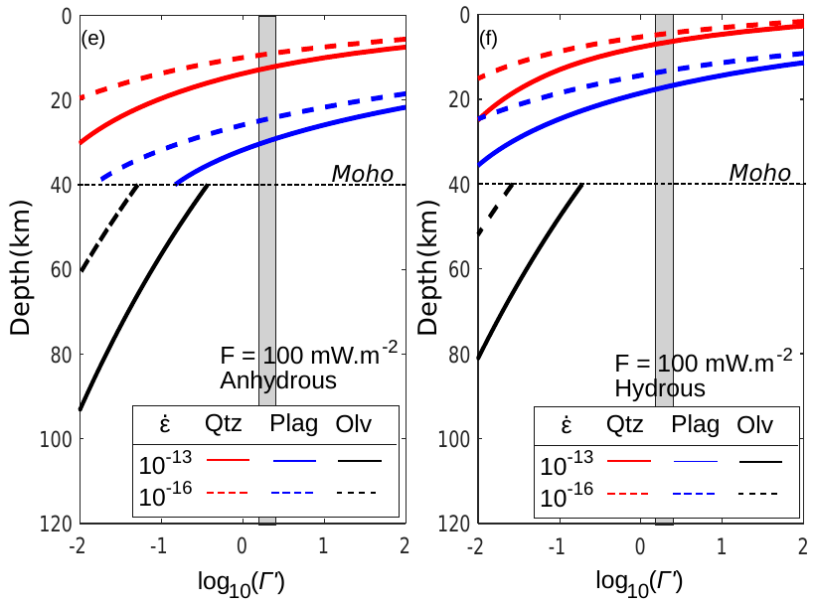

continued.

Figure 4.2 a) Calculated geotherms for surface heat-flow F *= 40, 70 and 100 mWm^{-2}. (b) Values of* T_{ref} *for* F *= 70 mWm^{-2} derived from Eq. 4.1 for dry and wet conditions, with fugacity for quartz and olivine derived for a lithostatic fluid pressure. Representative* T_{ref} *values used in numerical experiments (Table 3.1) are shown here by thin grey lines, with the corresponding temperature for the depth where* F *= 70 mW.m^{-2} shown on Fig. (4.2a). For olivine (black) the* T_{ref} *values are near identical for dry and fugacity dependent rheology. For c), d), e) and f), with* F *as labelled, strain-rate = 10^{-13} s^{-1} (solid lines) and 10^{-16} s^{-1} (dashed), c) and e) show* $log_{10}(\Gamma')$ *vs. depth for dry mineral conditions, and d) and f) show same for fugacity dependant (quartz and olivine) and wet (plagioclase) lithology. The grey band shows the threshold values obtained from Fig. 3.9 for localisation to occur with* $t_0' < 1$*:, i.e.,* $log_{10}(\Gamma') = 0.18$ *for* $T_{ref} = 0.014$ *and* $log_{10}(\Gamma') = 0.40$ *for* $T_{ref} = 0.148$*. For c) the values of* $log_{10}(\Gamma')$ *for plagioclase plot to the right of the graph, so localisation is expected for the entire crustal depth range.*

In Chapter Three I have shown that localisation proceeds very rapidly for values of Γ_0' that are not much greater than 1.5 (for T_{ref} = 0.041, representative of olivine) or 2.5 (for T_{ref} = 0.148, representative of wet quartz), and Fig. 4.2c to f shows that Γ_0' varies by orders of magnitude with depth in the lithosphere, due mainly to a strong dependence of the rheological laws on temperature. The characteristic Γ_0' profiles shown in Fig. 4.2c to f thus imply that localisation is expected to occur at shallower levels in the lithosphere. Furthermore, for any given lithology, there is a depth below which thermal strain localisation cannot occur, even in the absence of thermal diffusion. Although there may be significant uncertainty in the maximum localisation depth due to uncertain mineralogy, water fugacity, surface heat-flow and background strain-rate, the uncertainty arising from the choice of threshold value of Γ_0' is small. In Fig. 4.2 it can be seen that changing the threshold Γ_0' value from 1.5 to 2.5 decreases the maximum localisation depth in olivine by 2 to 3 km.

Deformation in the continental upper crust is often assumed to be represented by the flow law for quartz. In the lower crust the decreasing abundance of quartz with depth suggests that deformation is increasingly accommodated by plagioclase. I therefore show (Fig.4.2c to f) Γ_0' (z) for both of these minerals down to a nominal crustal thickness of 40 km. Within the lithospheric mantle, olivine rheology is assumed to control deformation, so I show Γ_0' (z) for olivine within the mantle layer. In each layer I show Γ_0' (z) for both “dry” and “wet” rheological laws, using parameters in Table 3.1.

Assuming a lithostatic pore-fluid pressure, a quartz-dominated lithology will localise above a depth (Fig. 4.2c to f) that may be as shallow as 5 km (fugacity dependent, F = 100 mW.m^{-2}, $\dot{\varepsilon}$ = 10^{-16} s^{-1}) or as deep as 30 km (dry conditions, F = 40 mW.m^{-2}, $\dot{\varepsilon}$

= 10^{-13} s^{-1}). Plagioclase supports a greater stress at the same strain-rate, and hence localisation can occur at deeper levels in the crust, as shallow as 14 km (hydrous conditions, F = 100 $mW.m^{-2}$, $\dot{\varepsilon}$ = 10^{-16} s^{-1}) and as deep as 60 km (dry conditions, F = 40 $mW.m^{-2}$, $\dot{\varepsilon}$ = 10^{-13} s^{-1}). For typical Moho depths of around 40 km, plagioclase therefore is capable of localising strain throughout the lower crust, but does not do so

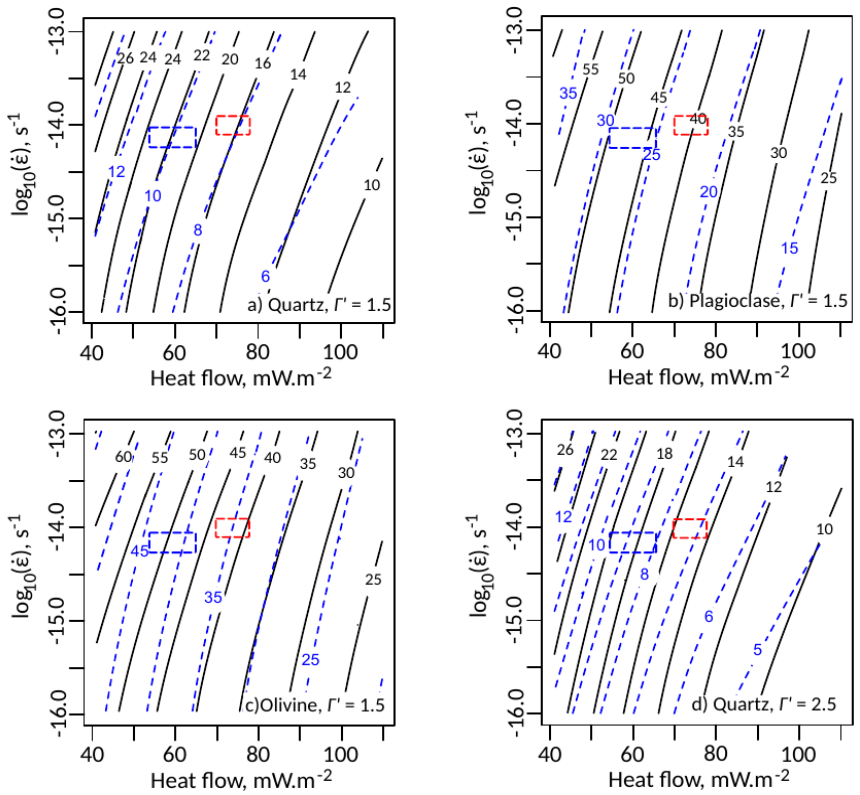

Figure 4.3: Gridded and contoured values for depth (km) at which Γ' = 1.5 (a, b, c) or 2.5 (d) as a function of surface heat flow and strain-rate, based on interpolation of profiles like those shown in Fig. 4.2. Black solid contours indicate dry mineral conditions and blue dashed contours indicate fugacity dependent (quartz, olivine) or wet (plagioclase) minerals. The red and blue boxes show the estimated ranged of surface heat-flow and strain-rate for the SAFZ and NAFZ respectively (refer text), from which a maximum depth of localisation can be inferred for each lithology.

where surface heat flow is relatively high and strain-rate relatively low. Within the mantle lithosphere a similar range of behaviours occurs for an olivine-dominated lithology (Fig. 4.2c to f); at one extreme (fugacity dependent, F = 100 mW.m^{-2}, $\dot{\varepsilon}$ = 10^{-16} s^{-1}) the transition depth for localisation is at 22 km, implying that localisation should not be expected in the upper mantle of normal continental crust. However, localisation depth increases if surface heat flow is decreased or strain-rate is increased, with localisation possible to 64 km depth under dry conditions with F = 40 mW.m^{-2} and $\dot{\varepsilon}$ = 10^{-13} s^{-1}. Strain-localisation in the upper-most part of the continental mantle lithosphere should therefore be expected in regions of lower heat-flow and greater strain-rate, especially in the absence of significant fluid content.

In each lithology that I consider, the maximum depth of localisation deepens with increasing background strain-rate and shallows for increasing surface heat-flow, as summarised in Fig. 4.3. Older, cooler lithosphere may show a greater depth of localisation but the increase in depth may be moderated by slower strain-rates. On the other hand, tectonic environments such as rifts and established orogens typically have a high surface heat flow and the localisation will not be as deep, even allowing for the typically greater strain rates in such regions.

The distribution of aqueous fluids in the lithosphere is likely to be heterogeneous but a broad inference can be made on specific settings. For example, metamorphic rocks that have been exposed to high pressures and temperatures have an insignificant fluid content, but sedimentary basin settings see a high fluid content (Yardley and Bodnar, 2014). Where minerals contain water there is a significant decrease in the depth of localisation (Fig. 4.3). For F = 80 mW.m^{-2} and $\dot{\varepsilon}$ = 10^{-13} s^{-1} a change from dry to 0.07

wt% H_2O in plagioclase moves the maximum depth of localisation from 40 to 23 km, that is a rheology controlled by wet plagioclase does not allow localisation within the lower continental crust. Under the same surface heat-flow and strain-rate conditions, dry olivine will localise below typical Moho depths (~ 46 km). However, if the increase of water fugacity in a hydrous environment is accounted for, the maximum potential localisation depth in olivine is ~ 35 km, shallower than typical Moho depths, thereby suppressing shear localisation in the upper mantle.

Although I neglect thermal diffusion in this simplified analysis ($\beta = 0$), I recognise that the final stages of the localisation instability will be limited in reality by diffusion of heat away from the progressively narrowing shear zone. Where deformation is slow thermal diffusion is likely to inhibit shear zone formation completely.

4.3 Comparison with major strike-slip faults

I now examine geophysical data from two major continental strike-slip shear zones that show differences in surface-heat flow (and hence geothermal gradient) and slip-rate: the San Andreas and North Anatolian Fault zones. I compare the evidence for localisation of deformation at depth within these shear zones with my estimates of maximum shear localisation depth. Evidence of localisation within the crust beneath active strike-slip systems comes primarily from seismology, whether in the occurrence of microseismicity and seismic tremor, or seismic imaging that shows offset structure. Because the activation of localisation occurs over a relatively narrow depth range dependent on the rheological and environmental parameters, evidence for or against

shear localisation at a given depth may place constraints on lithology and water-content in that environment.

For each of these regions published bore-hole data provide estimates of the surface heat-flow, which constrains the geothermal gradient used in the strain localisation calculations. I also require an estimate of the background strain-rate across each of these shear zones. Interseismic geodetic data show in general a well-defined zone of continuous deformation typically 40 or 50 km wide either side of these active strike-slip faults, as summarised by Wright et al. (2013). This is the surface expression of distributed deformation below the seismogenic layer, filtered through the elastic lid, and is often described using the simplified conceptual idea of an elastic plate overlying a buried dislocation on which movement occurs at the plate rate $\dot{s}$ below locking depth d (Savage and Burford, 1973; Segall, 2002). The measured surface deformation actually cannot distinguish between slip on a fault below depth d, and distributed shear across a ductile zone of width πd (Moore, 1999), and in fact the latter is physically more plausible. Thus the same geodetic motion might be indicative of a localised, brittle deformation, or a distributed deformation. I assume, in the absence of more definitive data, that this observed strain-rate:

$$\dot{\varepsilon}_0 = \frac{\dot{s}}{2\pi d} \qquad \text{Eq. (4.3)}$$

is indicative, and plausibly represents a minimum estimate, of the background strain-rate across the deforming region in the ductile layer below the elastic lid. I allow for a 25% uncertainty on my estimate of the background strain-rate in order to show the influence of uncertainty in this parameter. I note however, that strain-rate (raised to the

power of 1/*n*) has less effect on Γ_0' (and hence on the maximum depth of localisation) than mineralogy, presence of fluids or heat-flow, as is evident from Fig. 4.3.

4.3.1 San Andreas Fault Zone

The San Andreas Fault Zone (SAFZ) is a dextral strike-slip system on which the relative motion of the Pacific and North American plates is localised. Geodetic data define a relative strike-slip motion across the central SAFZ of about 38 $mm.yr^{-1}$ (Prescott et al., 2001). Surface deformation is distributed across a near-fault zone that is highly variable in width (Titus et al., 2011). This variability is captured in the locking depth which varies from 6 to about 22 km (Smith-Konter et al., 2011). For a locking depth of 20 km, (e.g. Segall, 2002; Shen et al., 1996) with a nominal 25% uncertainty, the relevant background strain rate is in the range 0.8 to 1.3 x 10^{-14} s^{-1}. Borehole heat-flow measurements of the central SAFZ range from 54 to 92 $mW.m^{-2}$ and the mean measurement is 74 ± 4 $mW.m^{-2}$ (Sass et al., 1997). Given these estimates of strain-rate and heat flow, I can use Fig. 4.3 to infer the expected average maximum depth of shear localisation for typical lithospheric lithologies. To simplify, I again consider my two representative values of T_{ref} (see Chapter Three). For dry quartz, and all plagioclase and olivine T_{ref} = 0.041 is more relevant and maximum localisation depths inferred are 16 km for dry quartz (Fig. 4.3), 23 (wet) to 41 km (dry) for plagioclase (Fig. 4.3) and 35 (wet) to 42 km (dry) for olivine (Fig. 4.3). For wet quartz dominated lithologies at higher temperatures, I infer from the greater value of T_{ref} = 0.148 (Fig. 4.3) a maximum depth of shear localisation of 7 km.

Lower limits on the depth of strain-localisation are clearly indicated by the spatial distribution of microseismicity. A regional study of crustal seismicity in southern California by Nazareth and Hauksson (2004) determined seismogenic thickness varying locally between ~ 10 and ~ 25 km, with an average about 15 km. Other evidence for the extent of localisation depends on the locking depth estimate (as previously mentioned) and structural information derived from seismic imaging. Tomographic inversions for crustal velocity variation in regions that encompass parts of the SAFZ (Allam and Ben-Zion, 2012; Chen et al., 2007; Lin et al., 2007; Thurber et al., 2004) often show a well-defined sharp velocity contrast across the SAFZ that is consistent with localised deformation continuing to a depth of 15 km or more (Thurber et al., 2006) but in general resolution is poor below about 15 km because the tomographic solutions are constrained by local earthquakes that are generally shallower than that depth. Thus the style of deformation in the lower crust is not well constrained by seismological measurements. However, the receiver function method, based on converted waves from teleseismic sources, does provide some important clues about deformation at the Moho. Following Zhu (2000), Yan and Clayton (2007) inferred an increase in Moho depth from 29 to 32 km on the San Gabriel side to 35 to 40 km on the Mojave side of the San Andreas Fault, implying that the SAF cuts right through the crust. Ozakin and Ben-Zion (2015) also found comparably large vertical offsets in the Moho, and associated significant changes in Moho depth with fault complexity in the brittle crust. Although the lateral resolution of the receiver function method is probably no better than 5 or 10 km, the inferred step in the Moho suggests that deformation associated with the SAFZ is localised in the uppermost mantle. The adjacent lowermost crust must have a comparable deformation, but whether localisation is independently maintained through the lower crust is difficult to assess from the available imaging data. At greater depths

there are few constraints, but an S to P receiver function profile across the central (Parkfield) section of the SAFZ by Ford et al. (2014) shows, at ~ 60 to 80 km depth, some variation in the velocity structure occurring over a horizontal distance of ~ 50 km; they interpreted an offset in the lithosphere-asthenosphere boundary related to the fault system. The horizontal resolution of such methods certainly does not preclude the possibility of a localised shear zone reaching depths of 60 or 80 km, but the resolution of the width measurement is also consistent with a low degree of shear localisation at the base of the lithosphere.

The geophysical evidence supports localisation of the SAFZ in the upper crust and at the Moho, consistent with the predictions of my simplified model, but does not clearly constrain the degree of localisation within the lower crust. Localisation throughout the lower crust could be explained by thermal activation of a plagioclase-dominated lithology if water is absent (Fig. 4.3). For a quartz-dominated lithology I do not expect to see thermally-activated localisation deeper than about 16 km under dry conditions, while localisation should be limited to depths < 10 km if water is present. The seismic observations that localisation probably extends to 15 km or more at the SAFZ therefore suggests that either the mid-crust is dry or its rheological law is better represented by that of plagioclase (for which, even if wet, we expect localisation to ~ 23 km) than quartz. The presence of fluid alteration minerals to a depth of 3 km within the San Andreas Fault Observatory at Depth (SAFOD) borehole indicates hydrous conditions within the upper crust (Bradbury et al., 2011; Holdsworth et al., 2011). If hydrous conditions are maintained in the depth range of 10 to 20 km below the SAFZ I infer that a rheological law representative of plagioclase applies in this depth range. If hydrous conditions persist into the lower crust I would not expect shear zone formation to occur

below about 23 km depth. The evidence for localisation in the mantle lithosphere at depths greater than about 50 km is also ambiguous, as the observed lithosphere-asthenosphere boundary offset inferred from S to P receiver functions (Ford et al., 2014) occurs over a region whose width is comparable to the horizontal resolution of the imaging method (~ 50 km). However the apparent structural discontinuity at the Moho, from estimated depth of 30 km to 38 km (Zhu, 2000) is consistent with the thermally activated strain localisation in a dry olivine-dominated lithology, for which our model implies a maximum depth of localisation of 42 km. Acceptance of shear zone localisation in the uppermost mantle therefore can be taken as evidence that the uppermost mantle is dry in this region (Fig. 4.3).

Ultramafic xenoliths from the Calaveras fault (part of the SAFZ) show a dry mineralogy at ~ 40 km (Chatzaras et al., 2015), consistent with the conditions I propose for localisation to occur in the uppermost mantle. Although the grain-sizes of the xenoliths place the deformation mechanism on the boundary between dislocation and diffusion creep, the dry conditions and strong crystallographic preferred orientations of the olivine led Chatzaras et al. (2015) to conclude deformation primarily occurred through dislocation creep. Strain localisation through grain size may occur in the mantle lithosphere (e.g. Drury et al., 1991), but this localisation mechanism takes place in the grain boundary sliding and diffusion creep regime (Karato and Wu, 1993; Warren and Hirth, 2006). The existence of dislocation creep in the upper mantle supports thermally activated strain localisation below the SAFZ.

4.3.2 North Anatolian Fault zone

I now consider the North Anatolian Fault zone (NAFZ), a dextral, strike-slip fault system in northern Turkey that accommodates relative movement of the Eurasian and Anatolian plates and is in many ways comparable to the SAFZ. Geodetic measurements estimate a strike-parallel relative velocity across the NAFZ of 24 $mm.yr^{-1}$ (Hussain et al., 2018; McClusky et al., 2000). Using the same GPS data Yamasaki et al. (2014) showed a profile across the NAFZ at ~ 30.25° E for which a shear zone width of ~ 50 km is apparent, consistent with the locking depths of 16 to 17 km derived by Hussain et al. (2018).

Variation of the shear-zone width along the NAFZ is probably comparable to that along the SAFZ and, although multiple studies have been made of the fault segments that are still affected by after-slip from the 1999 earthquakes at Izmit and Duzce, the pre-seismic strain-rate field is less well constrained by data than is that of the SAFZ. Again assuming a 25% uncertainty I estimate the background strain-rate for the NAFZ between 6 and 10 x 10-15 s^{-1}. This estimate is about 30% less than that for the SAFZ, mainly because the far-field plate-motion rate is ~ 24 $mm.yr^{-1}$ rather than ~ 38 $mm.yr^{-1}$. Terrestrial heat flow in the region cut by the NAFZ is highly variable because of groundwater flow. From borehole data (Pfister et al., 1998) north of 40º N the mean heat flow is 60 ± 5 $mW.m^{-2}$. These measurements constrain only the western end of the NAFZ. In the context of Fig. 4.3, the NAFZ environment is characterised by both lower heat flow and lower strain-rate than that of the SAFZ and when T_{ref} = 0.041 the maximum depth of strain localisation is therefore increased by ~ 5 km for each lithology, to 22 km (Fig. 4.3a) for dry quartz, to 27 (wet) to 48 km (dry) for plagioclase

(Fig. 4.3b), and to 42 (wet) to 49 km (dry) for olivine (Fig. 4.3c). For wet quartz I use T_{ref} = 0.148 (Fig. 4.3d) and infer a maximum depth of shear localisation of 9 km.

Comparable to the SAFZ, a seismogenic depth of ~ 15 km was obtained from the DANA seismic array on a western segment of the NAFZ (Altuncu-Poyraz et al., 2015). However, geophysical images may support a greater depth of strain localisation. Tomographic models based on analysis of local seismic event records show V_p variation beneath the northern branch of the NAFZ (NNAF) (Baris et al., 2005; Salah et al., 2007; Yolsal-Çevikbilen et al., 2012). Yolsal-Çevikbilen et al. (2012) show north-south vertical sections (near perpendicular to the fault) in which positive V_p anomalies extend beneath the NNAF. The geometry of the anomalies varies along strike, likely due to pre-existing crustal heterogeneities, but this method is subject to decreasing resolution in the lower crust. Papaleo et al. (2017), however, used teleseismic events detected by a high density seismic array over the fault segment that ruptured in 1999, and claimed a horizontal and vertical resolution of less than about 15 km (though less well resolved below about 40 km depth). They show a zone of low V_p that extends to about 80 km depth. The width of the low V_p zone is relatively localised in the upper crust (~ 25 km), but it increases to perhaps 50 km in the upper mantle, comparable to the estimate of Ford et al. (2014) for the width of the SAFZ shear zone at the base of the lithosphere. In either case the imaging method would have difficulty in resolving a narrower structure at the lithosphere-asthenosphere boundary. The receiver function method (Kahraman et al., 2015) suggests a localised shear zone below the NNAF at 30 to 30.5° E, where horizontal interfaces in the crust and upper mantle are truncated beneath both strands of the NAF. The lateral resolution of this method at the Moho is about 10 km and increases linearly with depth in the mantle. Their north-south profile across the NAFZ at 30.2° E

shows a positive anomaly horizon at ~ 34 to 39 km depth, interpreted as the Moho. Beneath the NNAF the amplitude of the arrival decreases, suggesting a more gradational velocity contrast across the Moho at this location, without a clear offset of Moho depth. Autocorrelation of ambient seismic noise data by Taylor et al. (2016) shows an absence of *P* wave reflectivity at Moho depths within 7 km of the NNAF, but they interpret distinct offsets of the Moho within about 10 km of the NNAF strand. They attributed the absence of a reflector in the autocorrelagrams below the NNAF to serpentinisation of olivine in the uppermost mantle producing a more gradational velocity variation across the Moho.

The geophysical evidence of localisation occurring throughout the crust in the NAFZ region is consistent with my calculations for a thermally activated regime with a plagioclase dominated lithology in the lower crust. Referring again to Fig. 4.3 for the prevailing strain-rate and thermal conditions relevant to the NAFZ, I predict for a quartz dominated lithology that localisation is limited to depths less than ~ 9 km (wet) or ~ 22 km (dry), contrary to the apparent localisation indicated by discontinuous crustal boundaries in the receiver function sections of Kahraman et al. (2015). For a plagioclase lithology, however, even with fluid present a maximum localisation depth of ~ 27 km is expected. The seismic evidence for localised deformation in the lower crust is not entirely clear but a dry plagioclase lithology would allow localisation of the deformation to extend through the crust. If water is also assumed to be absent in the upper mantle then the olivine dominated lithology in my model would predict a maximum localisation depth of ~ 49 km, consistent with evidence of localised deformation at the Moho. Thus, for both SAFZ and NAFZ I do not expect localisation to extend to the base of the lithosphere. In both regions however, the robustness of these inferences regarding

lithology and role of fluid, would benefit from improved resolution of the seismically imaged shear zones within the lower crust and uppermost mantle.

4.3.3 Limitations in calculating localisation depth

In considering the possibility of a thermal localisation method in a sheared silicate mass I have not dwelt on the relationship between what are evidently faults at near-surface levels and shear-zones of varying width at deeper levels. Faults produced by brittle fracture may propagate downward to form shear zones that extend to deeper levels. Conversely, localised shear at the deeper levels may precede, facilitate and organise faulting at the shallower levels. The two processes are likely interlinked (e.g. Chatzaras et al., 2015), but it is unlikely that shear zones will develop only because of overlying fault systems, unless there is an intrinsic feedback mechanism which progressively weakens the undeformed mass. A numerical approach to strain localisation by Montési and Zuber (2002) found shear heating mechanisms require a pre-existing heterogeneity for localisation to occur. Although they suggested a brittle fault, which could infer that ductile shear localisation originates from an overlaying brittle lid, heterogeneity can arise through a number of factors, as listed at the start of Chapter Three.

It is notable that major strike-slip shear zones, such as the San Andreas and North Anatolian fault zones, extend across 10s of km and typically involve a surface network of anastomosing faults contained within the shear zone (e.g. Şengör et al., 2005). It is also noteworthy that the shear localisation model described here predicts that the length of the shear zone increases linearly with increasing strain, just as maximum fault displacement increases with length of fault (Cowie and Scholz, 1992). The inferences

regarding a maximum depth of localisation are broadly consistent with those of Yuen et al. (1978) in that both approaches show that crustal-scale shear zones are consistent with thermally activated models of lithospheric rheology. Yuen et al. (1978) also established that increasing background temperature suppresses localisation, though they concluded that thermally activated shear zones might be stable to depths of 100 km or more, whereas I do not expect localisation to be stable to depths greater than about 60 km (Fig. 4.2c to f). This difference might be explained by their presupposing that a stable 1D structure is possible, whereas I have approached the question by asking whether a shear zone can grow from a point heterogeneity. The two approaches are complementary ways to view a complex problem.

In calculating the maximum localisation depth I have considered only a shear-heating weakening mechanism. Comparison of these results with seismic data interpretations, suggests that shear-heating can be an important localisation mechanism in the lithosphere. My results do not consider thermal diffusion, and so may over-estimate the depth to which a thermal weakening localisation mechanism is possible. Other strain-weakening mechanisms, such as grain-size reduction, may account for localisation in some circumstances (e.g. Precigout et al., 2007) but, for a sufficiently cool geotherm, grain-size sensitive deformation mechanisms are not thought to be relevant in the crust or upper levels of the mantle-lithosphere (Karato and Wu, 1993).

4.4 Summary of maximum localisation depth calculations

Using published rheological models for the deformation of quartz, plagioclase and olivine, and strain-weakening based on shear heating, I have shown that there is a threshold depth in the lithosphere below which shear does not localise. For these silicates undergoing dislocation-creep with $n = 3$ or 4 a strain-weakening parameter $\Gamma_0' > 1.5$ produces geologically rapid localisation. For a range of representative geotherms, plausible strain-rates, and assumptions of fluid pressure, I calculated how the thermally activated strain-weakening parameter Γ_0' varies with depth in the lithosphere. Lithology is the principal control on localisation depth, with quartz, plagioclase and olivine successively localising to a greater depth. For a given strain rate and geotherm, a dry lithology localises to a greater depth than a hydrous one. Localisation depth increases with strain-rate and shallows for an increase in surface heat-flow, but changes in surface heat flow are the dominant influence. Localisation in olivine to sub-Moho depths is possible, dependent on the crustal thickness, surface heat-flow and strain-rate and appears to be established in the case of two major strike-slip fault zones, both by the model predictions and by the seismic images, but localisation of lithospheric deformation is not predicted to occur at depths greater than about 60 km.

For each of the San Andreas Fault Zone (SAFZ) and North Anatolian Fault Zone (NAFZ) I estimated surface heat-flow measurements and calculated strain-rates from geodetic studies. Under these conditions I do not expect localisation in a hydrous quartz-dominated upper crust below about 10 km. Therefore seismicity to 20 km is more consistent with a dry quartz rheology, but is also possible with a hydrous plagioclase lithology. Localised shear within the lower crust is expected only if a dry

plagioclase lithology applies. Similarly I do not expect well-developed strain localisation in the upper-most mantle for a hydrous olivine lithology whereas a dry olivine lithology can explain the penetration of these major strike-slip shear zones into the uppermost mantle. The inference from seismic images of localised offsets on the Moho therefore implies that the uppermost mantle lithosphere is dry beneath these fault zones.

5 Shear-zone localisation depth in the Tibetan Plateau and implications for long term lithosphere deformation

5.1 Introduction

In the upper crust the amalgamation of cracks in the cold brittle regime can result in fracture and fault displacement. Volume expansion associated with cracking means brittle deformation is typically observed in the upper lithosphere where pressures are lower. With increasing pressure, and hence depth, the volume expansion is suppressed and brittle strength increases, and fault mediated deformation becomes less likely. In a ductile regime the deformation is driven by migration of crystalline point defects, e.g. dislocations and grain boundaries. Due to the weak interactions between defects, deformation typically occurs over a greater region. The corresponding increase in temperature with lithospheric depth enables point defects to move more readily, so ductile strength decreases and ductile deformation becomes more likely. The increasing pressure and temperature with depth in the lithosphere sees a progressive change from slip on faults to ductile deformation.

Shear-zones are regions across which differences in displacement are accommodated (Vauchez et al., 2012). The idealised end point of shear-zone localisation in the brittle regime is fault formation, where in an ideal situation two planar surfaces move past each other. Slip on an existing fault requires less stress than the formation of a new fault. Distributed deformation is more prevalent in the ductile regime, but localised deformation has been observed in exhumed mylonites, e.g. Alpine Fault (Norris, 2004), and inferred in seismic data, e.g. receiver functions of the San Andreas Fault (Yan and

Clayton, 2007). However, power-law rheology, used to describe ductile deformation, can produce relatively modest strain localisation so a mechanism that reduces locally the resistance to deformation is required to move from distributed to localised strain. Such mechanisms have been attributed to the interconnection of weak layers (Jefferies et al., 2006; Montési, 2013), grain-size evolution (Montési and Hirth, 2003; Platt and Behr, 2011a, b; Precigout et al., 2007), shear-heating (Crameri and Kaus, 2010; Regenauer-Lieb and Yuen, 1998) and inherited crystal preferred orientation (Tommasi et al., 2009; Tommasi and Vauchez, 1997).

It has been proposed that the overall lithospheric strength is not controlled by the horizontal rheological layering of the lithosphere but by the relative weakness of plate boundaries and major faults that that penetrate much, or even all, of the lithosphere (e.g. Burgmann and Dresen, 2008; Vauchez et al., 2012). If deformation is principally accommodated along major faults then such faults would be expected to remain relatively localised through the crust and into the mantle; the strength of the lithosphere is then limited by the frictional resistance on the fault zone. Conversely if these faults only localise to a shallow depth it suggests the lithosphere predominately deforms in a continuous manner (England and McKenzie, 1982) and faults are better interpreted as the surface expression of deeper ductile deformation.

The Tibetan Plateau and western China is the largest actively deforming continental region on Earth, and provides an opportunity to examine what controls the depth extent of localised shear zones. Deformation across the region is driven by the subduction of the Indian plate under the Eurasian plate, a process which has been ongoing for ~ 50 Ma (Meng et al., 2012). Over 2000 km of convergence has been accommodated in the

Tibetan Plateau; the region has an average elevation of 4,500 m, and a number of large scale (> 100 km) shear zones (Taylor and Yin, 2009). Across the Tibetan Plateau large-scale strike-slip faults (Fig. 1.3) separate zones of continuous deformation and are a relatively recent response to the increase in gravitational potential from plateau thickening (England and Houseman, 1986; Ge et al., 2015). The extent to which such faults control the present day deformation field is debated. It has been proposed that strike-slip faults accommodate the majority of deformation across Tibet, allowing eastward extrusion of tectonic blocks (Avouac and Tapponnier, 1993; Molnar and Tapponnier, 1975; Tapponnier et al., 1982). InSAR derived inter-seismic strain-rate maps show no major strain-rate concentration over fault regions, inferring deformation is broadly distributed across the Tibetan Plateau (Garthwaite et al., 2013; Wright et al., 2004). The InSAR data provides no direct information on the depth extent of shear-zone localisation, but the broad deformation suggests that localisation is likely confined to the upper part of the lithosphere where faults are evident. What limits the maximum localisation depth of these shear-zones?

In general, the depth extent over which a shear-zone remains relatively localised can be used to infer if deformation is primarily accommodated on faults (Meade, 2007) or through distributed viscous deformation (England and Molnar, 2005). Where localisation does not occur the lithosphere behaves more as a viscous continuum with deformation distributed across the region.

Previously I have shown how, in general, localisation depth is dependent on strain-rate, mineralogy, temperature and water fugacity (Chapter Four). In this chapter I examine how these factors limit localisation depth in two major (> 100 km) strike-slip faults in

the Tibetan Plateau, the Kunlun Fault and the Haiyuan Fault Zone (Figs. 1.3, 5.1). I apply the method developed in Chapter Four for calculating the maximum localisation depth in the lithosphere and compare my results to inferences from geophysical data.

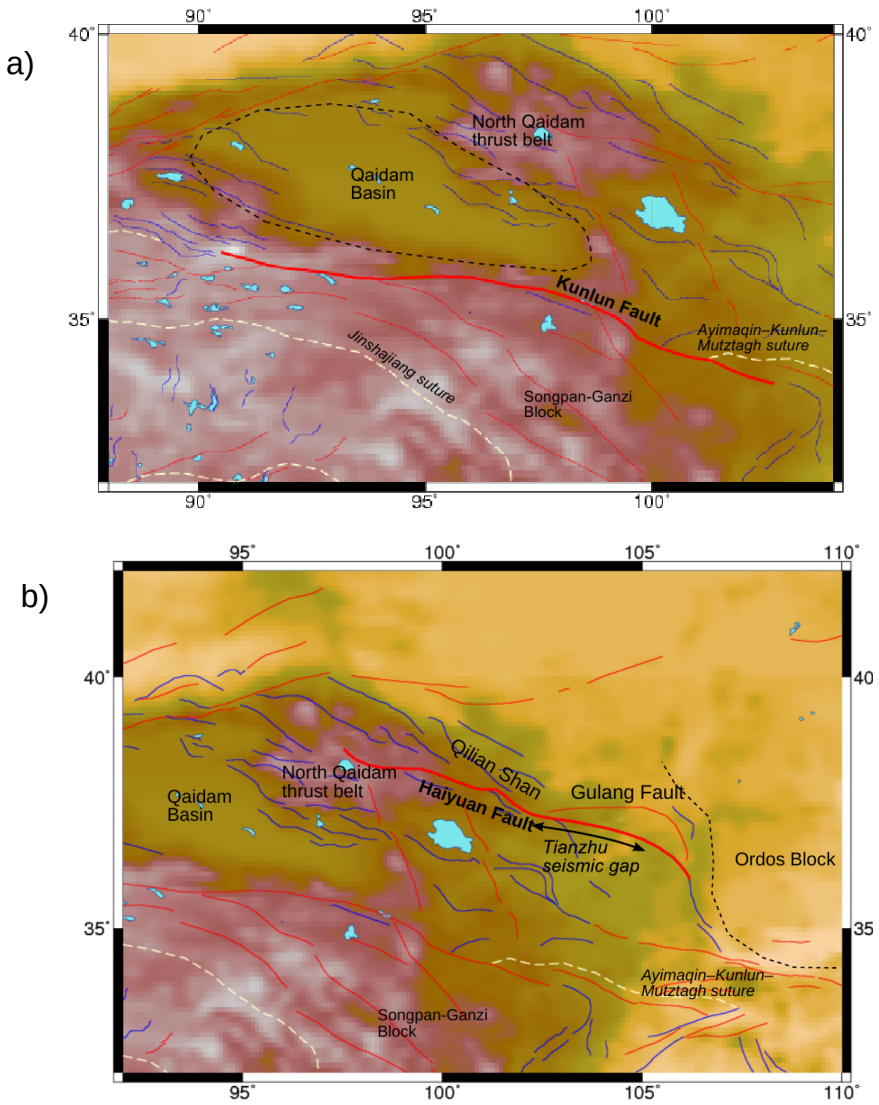

Figure 5.1: a) Surface trace of the Kunlun Fault and the relevant tectonic and suture zones. b) The sinistral Haiyuan fault zone consists of a series of en echelon faults, shown here as a single trace, that mark the north-east boundary of the Tibetan Plateau. The Tianzhu seismic gap marks the region between two >M8 earthquakes that occurred in 1920 and 1927 (Gaudemer et al., 1995). Strike-slip faults, red; normal and thrust faults, blue; suture zones, white dashed. Topography colour scale as Fig. 1.3. Topography data from Amante and Eakins (2009). Fault data after Styron and Okoronkwo, (2010); Taylor and Yin (2009).

The Kunlun Fault (KF) is a ~ 1200 km sinistral strike-slip fault zone in the north-west of the Tibet Plateau that marks the northern boundary of the Songpan-Ganzi terrane (Figs. 1.3, 5.1a). At the western end it follows the Anyimaqin-Kunlun-Muztagh suture and marks the southern boundary of the Qaidam Basin; the curvature of the surface trace suggests the fault dips > 60° to the southwest (Harkins et al., 2010). Along most the fault the deformation can be considered to be accommodated through pure strike-slip movement, except at the major releasing bend at ~ 100° E where long term deformation is equally partioned between dip and strike-slip movement (Harkins et al., 2010). The central and western portion of the KF is seismically active, with large earthquakes occuring in 1937 and 1963, M_w ~ 7.0 (Fitch, 1970); 1971, M_w = 6.4 (Tapponnier and Molnar, 1977); 1997, M_w = 7.6 (Peltzer et al., 1999); 2001, M_w = 7.8 (Lasserre et al., 2005). The last earthquake in the eastern section (~ 101° E and ~ 103° E) is thought to have occured 1,500 ka (Lin and Guo, 2008).

The Haiyuan Fault zone (HFZ) is a 1000 km long group of en echelon sinistral strike-slip faults in the north-east section of the Tibetan Plateau (Figs. 1.3, 5.1b; Gaudemer et al., 1995). The eastern end of the HFZ terminates against the Liupan Shan thrust belt. At the western end of the fault (~ 101 to ~ 102.5° E) approximatly 88% of deformation is accomodated by strike-slip movement, the remainder being accommodated through shortening (Gaudemer et al., 1995). At the junction with the Gulang Fault (Fig. 5.1b) the Haiyuan and Gulang Faults accommodate strike-slip deformation and shortening is accommodated on the Qilan Shan thrusts north of the HFZ (Lasserre et al., 2002). The HFZ is seismically active with major earthquakes occurring in 1920, M = 8.7 and 1927, M = 8 to 8.3 (Gaudemer et al., 1995; Peizhen et al., 1988). The Tianzhu seismic gap is a

~ 260 km along strike region between the epicentre of these earthquakes (Fig. 5.1b; Li et al., 2016).

5.2 Method for calculating shear-zone localisation depth

In Chapter Three I used numerical experiments to show how deformation around an initial single weak heterogeneity embedded in a rectangular region subject to simple-shear can localise strain when a thermal weakening mechanism is active. The governing equations describing deformation are presented in Chapter Two, and I present here a summary.

The numerical experiments use 2D calculations of plane-stress, non-Newtonian, viscous deformation with a work dependent thermal weakening localisation mechanism, interpreted in the horizontal plane with an assumed initially constant background temperature. The strain-rate varies as the n^{th} power of stress scaled by a depth-averaged lithospheric strength coefficient, B, that includes the dependence on temperature, grain-size, fugacity, pressure, and rheological parameters for a specific mineral. In this case of shear zone deformation I assume all mechanical work is converted to heat and that thermal diffusion is sufficiently slow compared to deformation (mechanical work), and so can effectively be ignored.

The change in B can be described using the integrated work done and a shear-heating parameter, Γ, that includes the temperature dependence (Eq. 2.22). Γ_0 changes with

temperature but by defining a reference temperature, T_{ref} (Eq. 2.44) the calculation of the change in B at any point and at any time t can be calculated (Eq. 2.45).

As Γ_0 is a function of temperature (Eq. 2.22) then with increasing depth (and hence temperature) in the lithosphere Γ_0 will reduce. Calculations are carried out using non-dimensional numbers in the finite element model *basil*. Using self-consistent scaling parameters (see section 2.2.6) that depend on externally imposed strain rate and rheological law (Table 3.1) the relation between the dimensional Γ_0 value and its non-dimensional equivalent Γ_0' is:

$$\Gamma_0' = \Gamma_0 H_0 \left(\dot{\varepsilon}_0\right)^{1/n} \qquad \text{Eq. (5.1)}$$
$$= \left(\frac{2}{3}\right)^{(n+1)/2n} \left(\frac{Q+P_0V}{\rho C_p nRT_0^2}\right) \left[A^{-1} s^m f_{H_2O}^{-r} \dot{\varepsilon}_0\right]^{1/n} \exp\left(\frac{Q+P_0V}{nRT_0}\right)$$

where Q and V are the activation energy and volume respectively, P is pressure, T is the temperature in Kelvin, R is the universal gas constant, n is the power-law creep exponent, s is the grain size, f_{H20} is the fugacity of water, r and m are experimentally determined indices, A is an empirical constant determined by experiment, ρ is the density and C_p is the heat capacity. The strong dependence on temperature in Eq. (5.1) means that the dimensionless value of Γ_0' varies by orders of magnitude across the lithosphere and there is a rapid transition from greater depths where strain can not localise under this thermal mechanism to shallow levels where thermal localisation is predicted

Based on experimentally derived rheological parameters and appropriate temperatures, representative values of T_{ref} for quartz and olivine are 0.148 and 0.041 respectively (Table 3.1) are used in the following numerical experiments. These calculations use a

strain exponent of $n = 3$, typical of these silicate minerals. Based on the results of numerical experiments described in Chapter Three, for $T_{ref} = 0.041$, (applicable to olivine) $\Gamma_0' > 1.5$ is sufficient to localise strain into a concentrated shear zone within the time required for a background strain of ~ 1 (Fig. 3.9a). Where $T_{\mathrm{ref}} = 0.148$, (applicable to wet quartz), the results are extrapolated to obtain localisation for $\Gamma_0' > 2.5$ (Fig. 3.9b).

To obtain the temperature to be used in Eq. (5.1) I calculate a lithosphere temperature profile (geotherm) using the approach detailed in section 4.2. This requires constraints on the surface heat-flow and Moho and lithosphere depth. Surface heat-flow values obtained from borehole measurements are absent from the areas of the Tibetan Plateau that are of interest here. I use the heat-flow map of Tao and Shen (2008), that interpolates selected heat-flow measurements across China and the adjacent regions. I assume radioactive heating in the upper crustal layer is twice that of the lower crustal layer, and adjust it to give the prescribed surface heat flow.

To determine a strain-rate to be used in Eq. (5.1) I follow the same approach as section 4.2. For each fault I will use a geodetic derived slip-rate, and take the locking depth (d) as related to the width of the deformation zone, and determine an estimate of background strain-rate

$$\dot{\varepsilon} = \frac{\dot{s}}{2\pi d} \qquad \text{Eq. (5.2)}$$

where $\dot{s}$ is the slip rate and $\dot{\varepsilon}$ is the background strain-rate.

The values for n, A and Q are constant for each mineral, but differ for the dry and wet states (Table 3.1). The experimentally derived rheological laws for quartz and olivine

also include a water-fugacity dependence ($r > 0$). For a dry lithology $r = 0$, so the water-fugacity component can be ignored. For a hydrous lithology I calculate water-fugacity (f_{H_2O}) following the method of Pitzer and Sterner (1994) and Sterner and Pitzer (1994). For this calculation a hydrostatic or lithostatic pore fluid pressure can be considered. A hydrostatic condition is more relevant in the upper (< 20 km) lithosphere where permeability is high but the difference in water-fugacity calculated from hydrostatic and lithostatic pressure is negligible (Fig. 5.2). At deeper levels the permeability decreases, and it is more appropriate to assume lithostatic fluid pressures. In the mid to lower crust (depth > 20 km and above the Moho) I assume deformation is increasingly accommodated on plagioclase. Here, I use the published experimentally derived rheological laws for plagioclase (An_{100}) (Rybacki and Dresen, 2000), which consider only a wet or dry plagioclase. Below the Moho, where olivine is the dominant constituent, the reduction of permeability is such that only lithostatic pressure need be considered. Given the negligible difference in hydrostatic and lithostatic pressure in the upper crust and the absence of a fugacity dependence for plagioclase rheological parameters, I use lithostatic pressure for calculating the quartz and olivine water-fugacity.

In the following section I calculate the maximum thermal localisation depths expected for the Kunlun Fault and the Haiyuan Fault Zone (Fig. 5.1). The localisation depth results based on the thermally activated strain-weakening model are then compared to published seismic data. These comparisons potentially place constraints on lithology and water-content in the lithosphere of these regions.

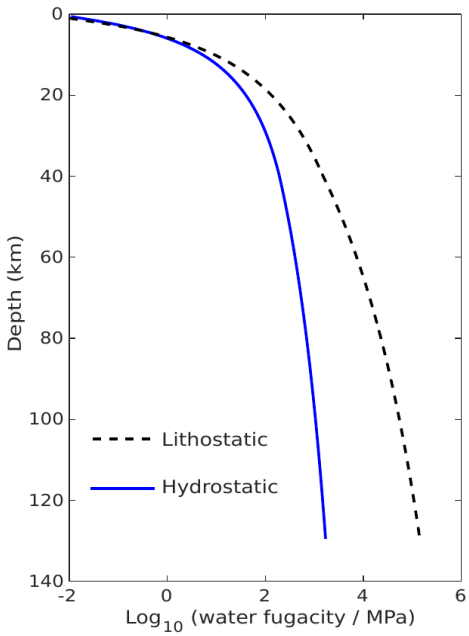

Figure 5.2: The change in water fugacity (f_{H2O}) with lithosphere depth for lithostatic (black dashed) and hydrostatic (blue solid) conditions (after Pitzer and Sterner, 1994).

5.3 Strain localisation with depth for the Kunlun and Haiyuan Fault zones

5.3.1 Kunlun Fault: Moho depth, lithosphere thickness and strain rates

The averaged depth of the lithosphere-asthenosphere boundary (LAB) beneath the Tibetan Plateau decreases northwards (Priestley et al., 2006). P- and S-wave velocity maps, constrained by both body wave arrival times and surface-wave dispersion, show slow velocities at depths of ~ 120 to 140 km below the central part of the KF, interpreted as the LAB (Nunn et al., 2014). From the receiver-function method, S-wave negative anomalies across the KF at 140 km (central) to 120 km (east) depth have been interpreted as the the LAB (Zhang et al., 2012). In a regional study over mainland China

An and Shi (2006) derive an S-wave velocity model from Rayleigh wave dispersion tomography. Here they calculate a velocity-temperature conversion, based on experimentally derived thermo-elastic properties of mantle minerals. They estimate seismic-thermal lithosphere thickness by inverting upper-mantle temperatures, and estimate the LAB depth at ~ 130 km below the KF. These seismic inferences of the LAB depth correlate with lithosphere thickness inferred from peridotite xenoliths from the Qinlang region (34º N, 105º E), ~ 120 km (Su et al., 2010).

The receiver-function method shows a positive anomaly at 50 to 60 km below the KF, interpreted as the Moho (Shi et al., 2009; Vergne et al., 2002; Wang et al., 2018; Xu et al., 2014; Zhu and Helmberger, 1998). A schematic of the lithosphere structure below the KF is shown in Fig. 5.3.

Modelled receiver-function data from across the Qaidam Basin (Fig. 5.1) region of the KF suggest a high-velocity upper crust layer to ~ 18 km and below this depth a low-velocity mid to lower crust (Zhu et al., 1995; Zhu and Helmberger, 1998). The occurrence of a low-velocity zone within the crust may be due to partial melting, (e.g. Jiang et al., 2014; Owens and Zandt, 1997), or differences in crustal composition, (e.g. Vergne et al., 2002). The ratio of P- and S-wave velocities (V_p/V_s — Poisson's ratio) potentially enables discrimination between compositional effects or partial melting as the cause of low velocity. Receiver function data from different profiles acoss the eastern end of the KF shows a north-south change in V_p/V_s. Here, a low V_p/V_s north of the KF implies a felsic composition, average V_p/V_s values below the KF infer a mafic composition, and south of the KF (near the Anyemaqin suture) high values infer either ultramafic and mafic rocks, or the presence of melt (Vergne et al., 2002; Wang et al.,

2018). In contrast to this interpretation, the correlation of mid-crustal (20 to 40 km) anistropy (Xie et al., 2013) with modelled Rayleigh wave dispersion data led Jiang et al. (2014) to suggest the effects were due to mid-crustal flow with partial melting. For my calculations I follow Vergne et al. (2002) and Wang et al. (2018) and assume a mafic lower crust, i.e. deformation is preferentially accommodated on calcium-plagioclase, allowing me to use the experimentally derived rheological laws of Rybacki and Dresen (2000).

Using GPS data strike-slip motion across the KF has been calculated as ~ 4.5 to 10 $mm.yr^{-1}$, where the upper value uses the simple 2D screw dislocation model of Savage and Burford (1973) and the lower value allows for deformation away from the fault (Chen et al., 2004). Other GPS derived slip-rates include those of Zhang et al. (2004) of 10 to 12 $mm.yr^{-1}$ and those calculated by (Zheng et al., 2017a) who estimated along strike variation of 12.8 $mm.yr^{-1}$ ± 1.9 $mm.yr^{-1}$ at the western end (~ 94° E) to 0.7 $mm.yr^{-1}$ ± 2.1 $mm.yr^{-1}$ at 103° E. Assuming a shear zone width of ~ 45 km, the relevant background strain-rate is in the range of 3.5 x 10^{-15} to 2.5 x 10^{-16} s^{-1}.

I calculate a geothermal gradient for the KF using a surface heat flow range of 50 to 70 $mW.m^{-2}$ (Tao and Shen, 2008), an upper crustal thickness of 20 km, a Moho depth of 55 km and a LAB depth of 130 km (Fig. 5.3). I calculate the temperature at the 20 km depth as ~ 400 ºC, and at the Moho as ~ 850 ºC. For this geothermal gradient, a felsic upper crust and intermediate to mafic lower crust would not undergo partial melting.[2]

2. Based on the solidus for felsic magma, 750 ºC to 800 ºC; intermediate magma, 800 ºC to 1000 ºC; mafic, 1000 ºC to 1200 ºC (Best, M G, 2003).

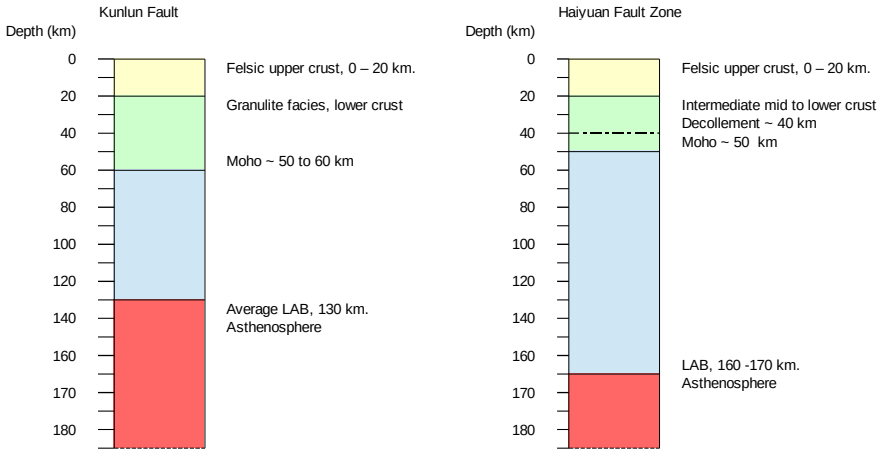

Figure 5.3: Schematic of lithosphere structure below the Kunlun Fault and Haiyuan Fault Zone based on inferences from geophysical data.

5.3.2 Haiyuan Fault Zone: Moho depth, lithosphere thickness and strain rate

The Tianzhu seismic gap in the Haiyuan Fault Zone (HFZ) is a ~ 260 km along strike region between the epicentre of the 1920 and 1927 M > 8 earthquakes (Gaudemer et al., 1995) and has been the focus of multiple seismic (e.g. Lasserre et al., 2001) and remote-sensing studies (Cavalié et al., 2008; Jolivet et al., 2012). I use seismic data from this region to provide constraints on the crust and lithosphere thicknesses below the HFZ. Seismic reflection data within the Tianzhu seismic gap region show a high amplitude reflector at ~ 50 km depth, interpreted as the Moho (Gao et al., 2013; Guo et al., 2016; Wang et al., 2014). This depth is similar to that interpreted from seismic refraction data, where an increase in P- and S-wave velocity at 47 km suggests a change from crust to mantle lithosphere (Liu et al., 2006). Below the HFZ the receiver-function method shows negative amplitudes at depths of 160 to 170 km (Zhang et al., 2012) that are interpreted as the lithosphere-asthenosphere boundary. A schematic of the lithosphere structure below the HFZ is presented in Fig. 5.3.

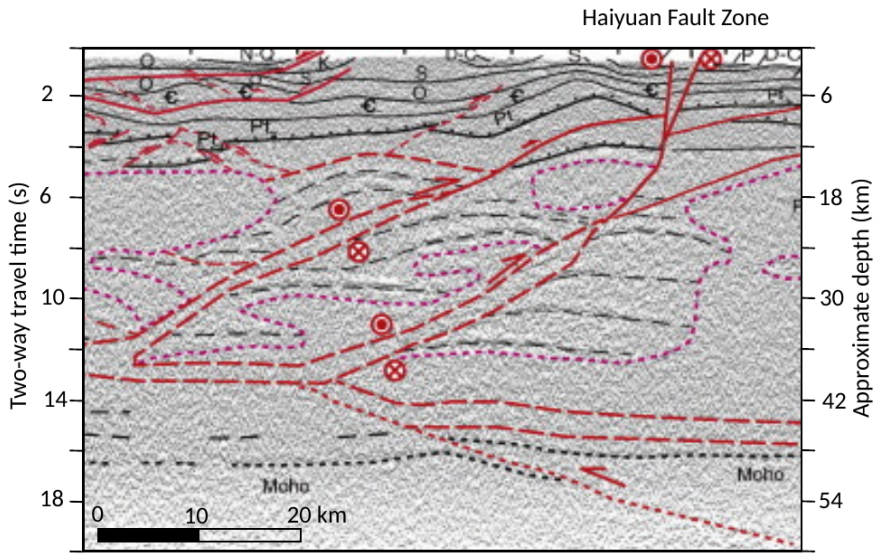

Figure 5.4: Seismic reflection interpretation, (after Wang et al., 2014). Purple dotted lines surround seismically transparent regions. Black dashed lines mark major reflectors. Red lines mark inferred structure of shear-zones, with the surface trace of the HFZ as marked.

Seismic reflection data across the HFZ suggests that the dip of HFZ shallows with depth (Fig. 5.4). Termination of horizontal reflectors implies that the HFZ at the surface dips 60 to 70°, and then two strands develop at ~ 8 to 10 km depth that decrease in dip to 20° to 30° and terminate at a proposed sub-horizontal detachment zone at ~ 40 km (Guo et al., 2016; Wang et al., 2014). An absence of strong seismic reflectors across this detachment zone may be due to the HFZ developing into multiple strands of diffuse deformation rather than being localised (Gao et al., 2013). Unbroken, near flat seismic reflectors at ~ 50 km, indicative of the Moho, suggest that localised shear does not occur at this depth (Gao et al., 2013).

GPS velocity based models indicated averaged slip-rates across the HFZ from 5.2 $mm.yr^{-1}$ for a locking depth of ~ 20 km, derived from kinematic elastic block models (Y. Li et al., 2017), to ~ 8.6 $mm.yr^{-1}$ derived from a rigid block model (Gan et al., 2007). These differences in slip-rate may be due to assumption of focused or more distributed deformation across the HFZ. However, GPS and InSAR derived slip-rates show an along-strike variation; these are proposed to be due to spatial variability in the strain-rate field produced by the India-Asia convergence (Daout et al., 2016). At the western end of the HFZ the convergence in this region is predominately accommodated on the HFZ (8.6 $mm.yr^{-1}$) with significant motion also on the Qilian Shan thrust belt (3.5 $mm.yr^{-1}$). At the eastern end only 5.6 $mm.yr^{-1}$ is accommodated, with the remaining motion accommodated on the Gulang fault which branches ~ 20° to 30° from the HFZ (Fig. 5.1). In a fourth study InSAR data covering the Tianzhu seismic gap region Cavalié et al. (2008) interpreted a depth-dependent dislocation creep model to fit the data. Here they proposed a creep-rate of 11 $mm.yr^{-1}$ in the upper crust (0 to 7 km) and 5 $mm.yr^{-1}$ for > 15 km, with these layers separated by a locked section. For the purpose of my calculations I simplify these multiple findings and assume a slip-rate of 5 to 8 $mm.yr^{-1}$, and a shear zone width of 60 km derived from a locking depth of 22 km (Gan et al., 2007). The corresponding strain-rates are in the range 1.3×10^{-16} to 2.1×10^{-15} s^{-1}.

For the HFZ I calculate the geothermal gradient for a surface heat flow range of 60 to 70 $mW.m^{-2}$ (Tao and Shen, 2008) using an assumed upper crust depth of 20 km, and a Moho and LAB depth of 50 km and 160 km (Fig. 5.3). For this geotherm the base of the lower crust is ~ 400 ºC, and the Moho is ~ 700 ºC. Below the HFZ crustal lithology inferred from seismic refraction data show V_p ~ 6.1 $km.s^{-1}$ for the upper crust (< 20 km), suggesting a felsic composition, and V_p is ~ 6.45 to 6.8 $km.s^{-1}$ for the middle (20 to 40

km) and lower crust (> 40 km), inferring a more intermediate (predominantly amphibole and feldspar) composition (Liu et al., 2006). For my calculated geotherm this crustal composition remains below the solidus.

5.3.3 Results from calculating localisation depths on Kunlun and Haiyuan Fault Zones

Using the relevant calculated strain-rates and geothermal gradient I calculate the change in Γ_0' with depth for hydrous and dry quartz, plagioclase and olivine for the KF and HFZ. For plagioclase, olivine and dry quartz, $T_{ref} = 0.041$ is more relevant, and for $n = 3$ localisation requires a minimum of $\Gamma_0' = 1.5$ (Fig 3.9a). For wet quartz $T_{ref} = 0.148$ is more relevant, and for $n = 3$ localisation requires a minimum of $\Gamma_0' = 2.5$ (Fig 3.9b).

For the KF the maximum localisation depths are quartz 10 (wet) to 22 km (dry), plagioclase 30 (wet) to 50 (dry) km and olivine 44 (wet) to 51 (dry) km. (See Table 5.1 and Fig. 5.5.) For the HFZ the maximum localisation depths are quartz 8 (wet) to 19 (dry) km, plagioclase 27 (wet) to 49 (dry) km and olivine 43 (wet) to 52 (dry) km. (See Table 5.2 and Fig. 5.6)

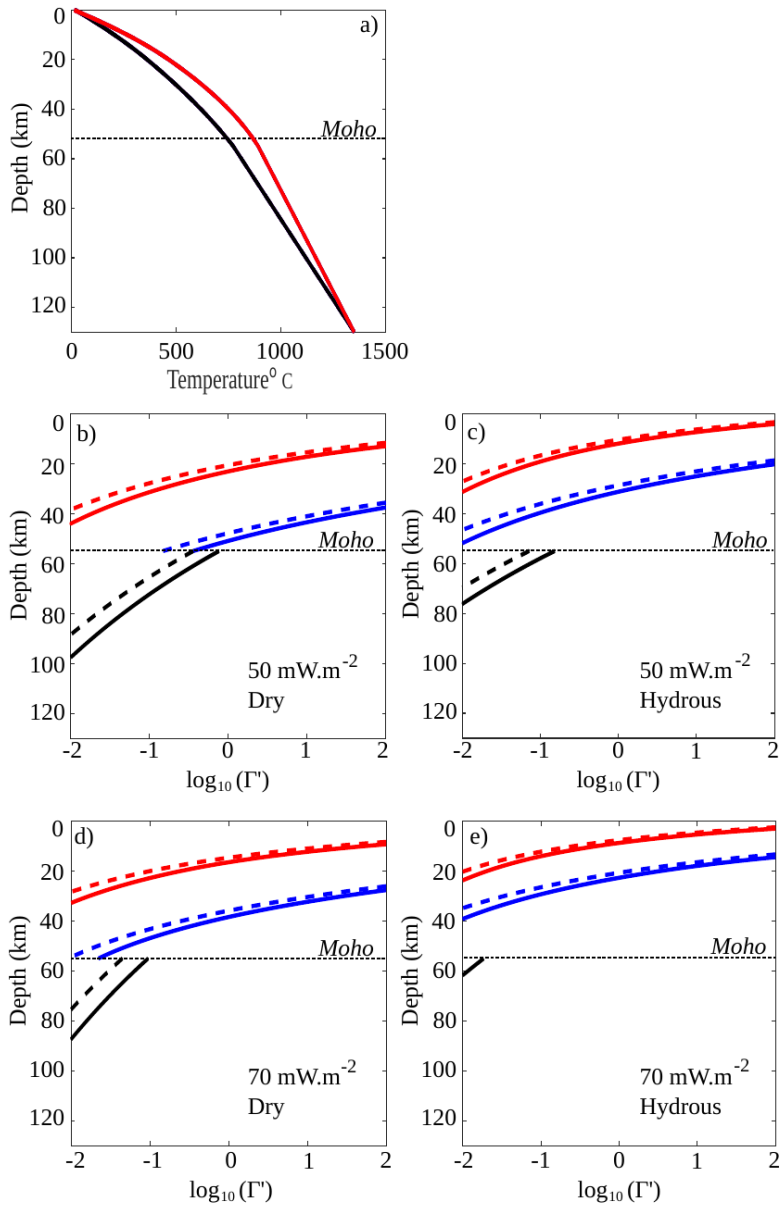

Figure 5.5: For the Kunlun Fault. a) Calculated geothermal gradient for surface heat-flow of 50 (black) and 70 (red) mW.m^{-2}, following the method described in the text. Values of Γ_0' with depth for: b) dry lithology, surface heat flow 50 mW.m^{-2}, c) hydrous lithology, surface heat-flow 50 mW.m^{-2}, d) dry lithology, surface heat flow 70 mW.m^{-2}, c) hydrous lithology, surface heat-flow 70 mW.m^{-2}. red = quartz, blue = plagioclase, black = olivine. Solid line, strain-rate = 3.5 x 10^{-15} s^{-1}; dashed line, strain-rate = 2.5 x 10^{-16} s^{-1}. Maximum localisation depths for plagioclase, olivine and dry quartz are inferred to occur at the depth where Γ_0' < 1.5, and for wet quartz where Γ_0' < 2.5.

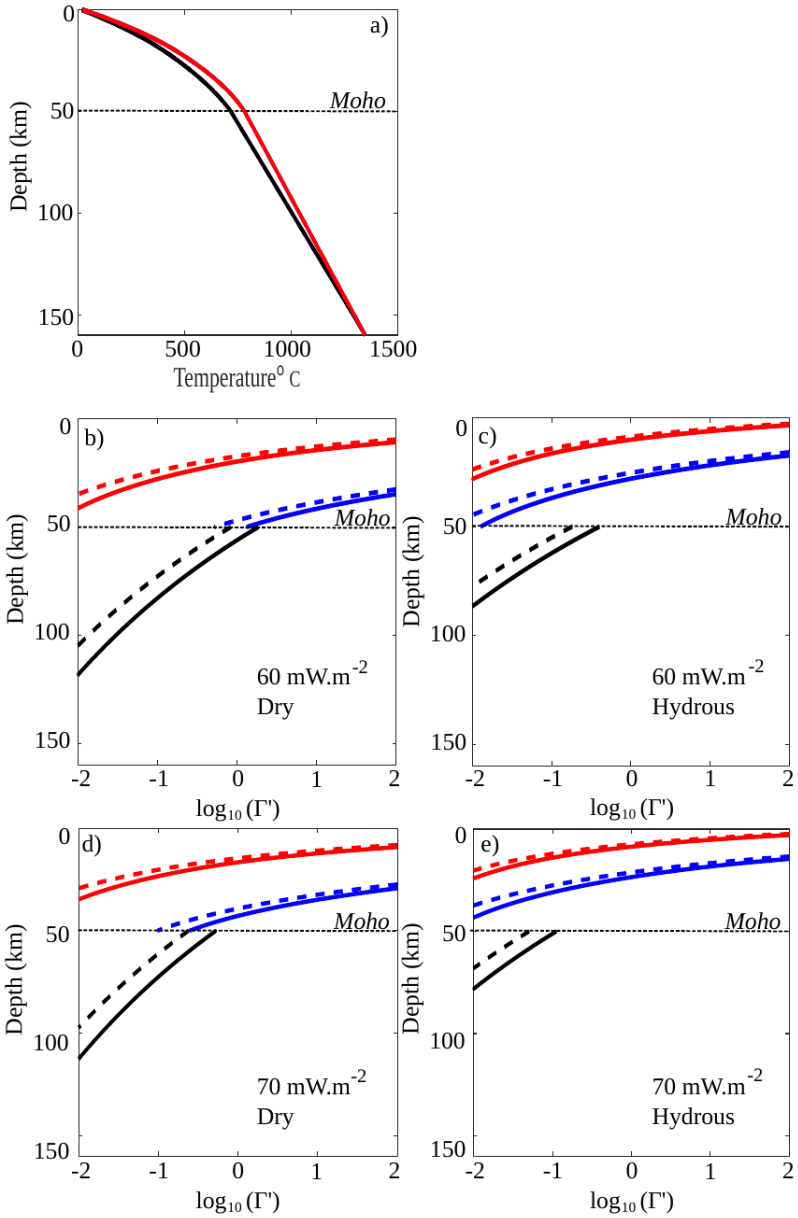

Figure 5.6: For the Haiyuan Fault Zone. a) Calculated geothermal gradient for surface heat-flow of 60 (black) and 70 (red) mW.m^{-2}, following the method described in the text. Values of Γ_0' with depth for: b) dry lithology, surface heat flow 60 mW.m^{-2}, c) hydrous lithology, surface heat-flow 60 mW.m^{-2}, d) dry lithology, surface heat flow 70 mW.m^{-2}, c) hydrous lithology, surface heat-flow 70 mW.m^{-2}. red = quartz, blue = plagioclase, black = olivine. Solid line, strain-rate = 2.1 x 10^{-15} s^{-1}; dashed line, strain-rate = 1.3 x 10^{-16} s^{-1}. Maximum localisation depths for plagioclase, olivine and dry quartz are inferred to occur at the depth where Γ_0' < 1.5, and for wet quartz where Γ_0' < 2.5.

Table 5.1. Maximum supported localisation depths for the Kunlun Fault assuming a lithostatic pressure, upper crust thickness 20 km, Moho depth 55 km and lithosphere thickness 130 km. Wet quartz and olivine are fugacity dependent, wet plagioclase assumes a constant wet fraction.

Strain-rate, s^{-1}		**2.5×10^{-16}**		**3.5×10^{-15}**	
Surface heat flow ($mW.m^{-2}$)		**50**	**70**	**50**	**70**
Max. localisation depth (km)	Quartz, wet (T_{ref} = 0.148)	9	6	10	7
	Quartz, dry (T_{ref} = 0.041)	20	14	22	16
	Plagioclase, wet (T_{ref} = 0.041)	28	20	30	22
	Plagioclase, dry (T_{ref} = 0.041)	47	35	50	37
	Olivine, wet (T_{ref} = 0.041)	42	31	44	33
	Olivine, dry (T_{ref} = 0.041)	47	35	51	38

Table 5.2: Maximum supported localisation depths for the Haiyuan Fault zone assuming a lithostatic pressure, upper crust thickness 20 km, Moho depth 50 km and lithosphere thickness 160 km. Wet quartz and olivine are fugacity dependent, wet plagioclase assumes a constant wet fraction.

Strain-rate, s^{-1}		**1.3×10^{-16}**		**2.1×10^{-15}**	
Surface heat-flow ($mW.m^{-2}$)		**60**	**70**	**60**	**70**
Max. localisation depth (km)	Quartz, wet (T_{ref} = 0.148)	7	6	8	7
	Quartz, dry (T_{ref} = 0.041)	16	14	19	16
	Plagioclase, wet (T_{ref} = 0.041)	24	20	27	22
	Plagioclase, dry (T_{ref} = 0.041)	45	38	49	41
	Olivine, wet (T_{ref} = 0.041)	39	33	43	36
	Olivine, dry (T_{ref} = 0.041)	46	38	52	42

5.4 Discussion: Localisation depth of faults and implications for lithospheric deformation

5.4.1 Comparison of localisation depth calculations with geophysical data

For a thermally activated weakening mechanism the maximum supported localisation depth has a strong dependence on the geothermal gradient. For example, a dry quartz dominated lithology, an increase in strain-rate from 10^{-16} to 10^{-13} s^{-1} will increase the localisation depth by ~ 4 km but a change in surface-heat flow from 80 to 40 $mW.m^{-2}$ will increase localisation depth by ~ 13 km (Fig. 5.7). Plagioclase and olivine exhibit similar dependences.

The maximum localisation depths supported on each lithology for the Kunlun Fault (KF) and Haiyuan Fault Zone (HFZ) are similar. For increases in temperature (and depth) of the surrounding lithosphere, the value of Γ_0' reduces until it becomes sufficiently small ($\Gamma_0' < 1.5$ for plagioclase, olivine and dry quartz, $\Gamma_0' < 2.5$ for wet quartz) that localisation through thermal weakening is no longer supported. For the KF and HFZ the geotherm calculation sets the lithosphere base to the same temperature (1300 ºC) but for the KF the LAB is 30 km shallower than the HFZ, resulting in a steeper gradient overall. The lower range of surface heat-flow over the KF (10 $mW.m^{-2}$ less than the HFZ) results in similar temperatures for the KF and HFZ at a given depth in the crustal lithosphere

Both faults are able to support localisation in the crust, potentially to a depth of 49 to 50 km if dry plagioclase is a dominant mineralogy. While dry olivine can support a greater localisation depth (51 to 52 km) olivine is not a major constituent of the crust. Olivine preferentially accommodates deformation in the mantle lithosphere, where it is one of

the major minerals. Localisation of the KF below the Moho on dry olivine requires a Moho depth of 50 km, as inferred from the receiver-functions (e.g. Zhu and Helmberger, 1998), and the surface heat-flow at the lower limit of 50 $mW.m^{-2}$. Simarly, potential localisation of the HFZ at the top of the mantle lithosphere may occur for a dry olivine lithology.

The seismogenic depth varies along strike of the KF from ~ 20 km (west) to 30 km (east) (Xu et al., 2014), consistent with localisation on a dry quartz lithology in the upper crust (< 20 km), and a plagioclase lithology below 20 km. The absence of offset horizons at the Moho in seismic reflection (Wang et al., 2011), receiver function (Xu et al., 2014) and shear-wave velocity (Li et al., 2013) profiles below the KF suggests the KF does not localise at or below the Moho, consistent with either a wet or dry plagioclase lithology. At 100° E along the KF a low V_s anomaly occurs in the upper mantle, which Li et al. (2013) interpret as partial melting due to delamination of the lithospere and subsequent asthenosphere upwelling. The resultant local increase in mantle-lithosphere temperatures would inhibit localisation at this depth. Based on the geophysical data and my calculations I propose that a thermally activated strain-weakening mechanism is consistent with the lack of evidence for localisation of the KF below the crust.

Wet and dry plagioclase support localisation to depths of 20 to 30 km and 35 to 50 km respectively in the region of KF. Truncation of horizontal reflectors beneath the KF infers the KF reaches ~ 35 km before terminating against a continuous reflector, interpreted as a décollement (Wang et al., 2013). Assuming a plagioclase dominated lithology below 18 km (see section 5.3.1), then for localisation to extend to this depth

suggests the mid to lower crust rheology beneath the KF is best described by a dry plagioclase flow-law.

Earthquakes to depths < 20 km are observed in the HFZ region (e.g. Craig et al., 2012; Lasserre et al., 2001), greater than the calculated maximum localisation depth supported by dry quartz (18 km). A dry or hydrous plagioclase flow-law may support localisation to greater depths (49 or 27 km), but below 20 km any localised region must lack sufficient strength to support earthquake nucleation and deformation be accommodated aseismically. The absence of earthquakes does not imply absence of localised shear strain, but the presence of earthquakes can be interpreted to imply that localisation has occurred in the past.

Geophysical data suggest that the HFZ becomes increasingly listric with depth and terminates against a 40 km deep décollement (Fig. 5.4). The HFZ may have propagated to depths greater than the décollement, with the lower portion being sufficiently displaced that it is no longer within the imaged region. Alternatively the décollement formed prior to the HFZ reaching it, thus inhibiting further development of a shear zone at greater depths. Localisation of strain on the HFZ down to the décollement is supported by a dry plagioclase flow-law, rather than a hydrous one, in the crustal lithosphere.

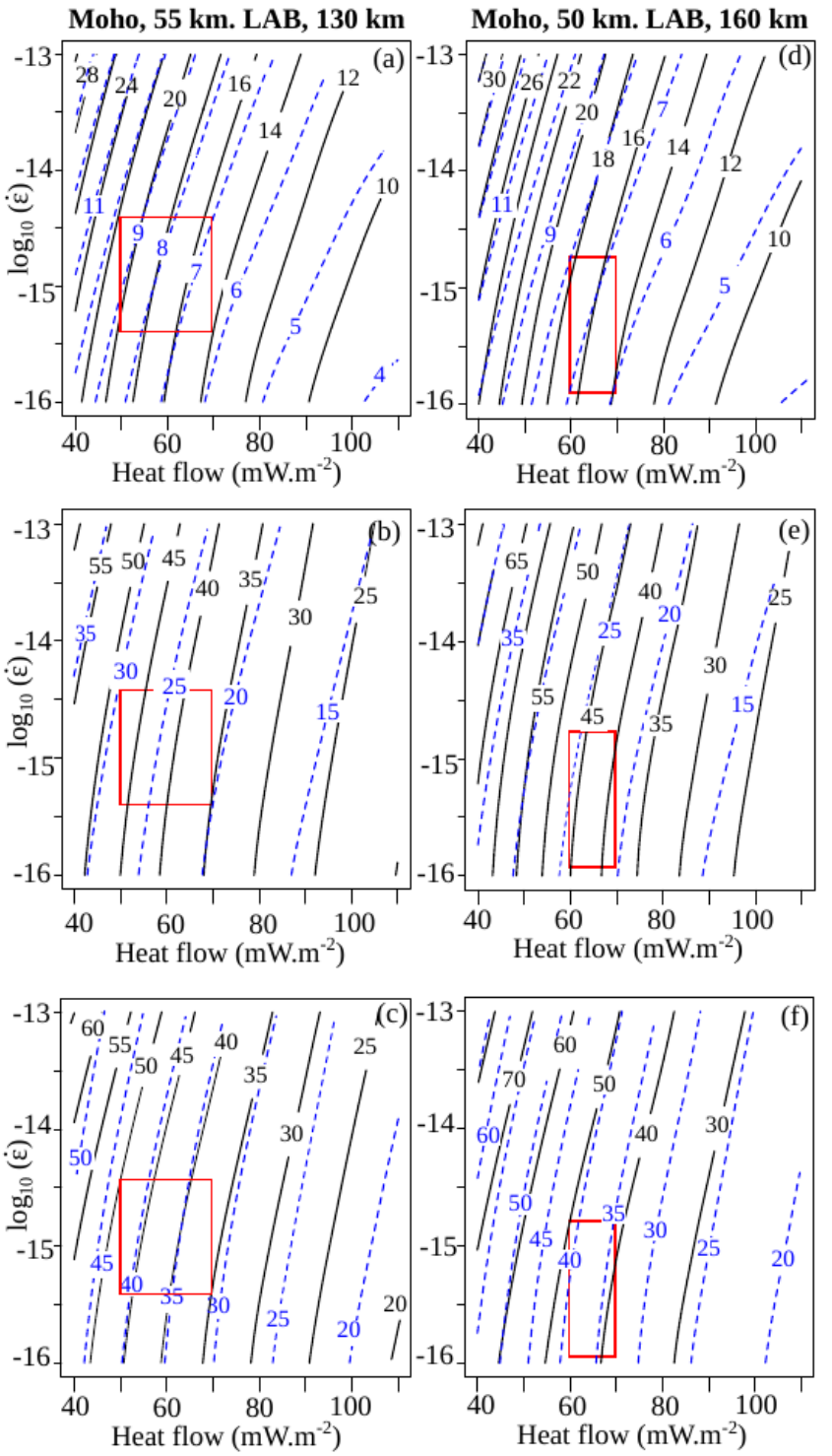

Figure 5.7: Gridded and contoured values for depth (km) at which Γ' = 2.5 (blue dashed lines on a and d) or 1.5 (all other lines) as a function of surface heat flow and strain-rate, based on interpolation of profiles like those shown in Fig. 5.5, 5.6. *Continued on next page.*

cont.

Plots a and d are for quartz, b and e for plagioclase, d and f for olivine. Black solid contours indicate maximum localisation depth for dry mineral conditions (where Γ' *= 1.5) and blue dashed contours indicate maximum localisation depth for fugacity dependent (quartz, olivine) or wet (plagioclase) minerals (where* Γ' *= 2.5). Fig. a to c are for a lithosphere structure typical of the KF, Fig. d to f for the HFZ. The red boxes show the estimated range of surface heat-flow and strain-rate for the KF (a to c) and HFZ (d to f) respectively, from which a maximum depth of localisation can be inferred for each lithology.*

Seismic reflection data from the HFZ (Fig 5.4) show successive vertical offsets that interpreted as the HFZ trace (Gao et al., 2013). At depths > 15 or 21 km (depending on the fault strand) the reflectors terminate against a region of low seismic reflectivity, that increases in width from ~ 2 km at 18 km depth to ~ 5 km at 36 to 40 km depth (Fig. 5.4). This may be interpreted as a change from localised to increasingly distributed deformation, and the change correlates with the seismogenic depth at about 20 km. If localisation is limited to ~ 15 to 21 km then the rheology is best described using either a dry quartz flow-law (maximum supported localisation depth, 14 to 19 km) or a hydrous plagioclase flow-law (maximum supported localisation depth, 22 to 27 km) (Table 5.2).

From comparison of my calculations and geophysical data I propose that the rheology of the mid to lower crust below the HFZ likely follows a hydrous plagioclase flow-law. The maximum localisation depth of the plagioclase (27 km) is greater than the 15 to 20 km suggested from the seismogenic depth and interpreted seismic refraction data. However, viscous heating from the décollement may provide a local contribution to increasing the temperature and decrease the localisation depth on a plagioclase

lithology. With increasing depth deformation becomes increasingly distributed before the HFZ merges with the 40 km ductile décollement.

5.4.2 Limitations to the localisation depth calculations

These calculations are subject to the same limitations as discussed in section 4.3.3 — the use of experimentally derived rheological flow laws for each mineralogy, considering only a shear heating mechanism and negelecting thermal diffusion. For example, localisation depths may be greater where other strain-weakening mechanisms are considered, for example grain-size reduction.

The localisation depth calculations are based on the findings in from the simple-shear box models in Chapter Three, and as such assume deformation is accommodated solely on strike-slip movement. Dip-slip motion effectively increases the crustal thickness and consequently the increase in radioactive heating will raise the temperature of the crust at a given depth. For the western end of the HFZ, where 18% of movement is accommodated by dip-slip movement, the strike-slip assumption will over-estimate the localisation depth.

By combining seismic data and localisation depth inferences can be made on the lithology and hydrous state of the underlying lithosphere. However the experimentally derived flow-laws may represent non-unique solutions and similar flow-laws may be derived for different lithologies and fluid content.

5.4.3 Implications for long term deformation in the Tibetan Plateau

These calculations for a thermally activated strain-weakening mechanism are consistent with inferences from geophysical data that the KF and HFZ are localised only within the crust. These results apparently contrast with those of the San Andreas Fault Zone (SAFZ) and North Anatolian Fault Zone (NAFZ) (Chapter Four) in which localisation is potentially supported to sub-Moho depths. However, the absolute depth that each lithology (quartz, plagioclase or olivine dominated) can support a thermally activated strain-localisation is broadly comparible between these four fault zones (Fig. 4.3, 5.7). While these regions show some differences in surface heat-flow and strain-rates, the important difference lies within the regional variations of the crust and lithosphere thickness, in particular the much greater crustal thickness of Tibet compared to Anatolia and California.

Where the crust is thick (> 40 km), an olivine dominated lithology below the Moho may be too deep (hot) to support localisation, and localisation is supported only in the crust. A thinner crustal lithosphere brings the olivine dominated mantle lithosphere to shallower (cooler) depths, and localisation may be supported at depths greater than the Moho, so that a greater proportion of the lithosphere is subject to localised strain. The lithosphere thickness and thermal structure of the lithosphere are broadly related to tectonic setting. In general, surface heat-flow is high and the lithosphere thin in rift environments and surface heat-flow low and the lithosphere thick in continental cratons. In orogenic settings the thermal structure and lithospheric thickness are dependant on a number of factors that can vary spatially and with time, such as radiogenic heat product, erosion and sedimentation rates (Huerta et al., 1998; Royden, 1993).

If localised shear-zones control the long term strength of the lithosphere (Burgmann and Dresen, 2008) and accommodate deformation across the Tibetan Plateau (e.g. Tapponnier et al., 1982) then such shear-zones should remain relatively localised over a significant proportion of the lithosphere. That the Kunlun and Haiyuan Fault zones only support strain localisation to ~ 30% of the lithosphere thickness is consistent with large-scale continuum deformation models of deformation across the Tibetan Plateau and geodetic strain rates that also infer deformation is broadly distributed across the Plateau (England and McKenzie, 1982; Garthwaite et al., 2013; Wright et al., 2004).

5.5 Summary of shear-zone localisation depth in the Tibetan Plateau

In this chapter I have calculated the maximum supported localisation depth for shear-zones produced by a thermally activated strain-weakening mechanism, and applied it the Kunlun Fault (KF) and Haiyuan Fault Zone (HFZ). The maximum supported localisation depth can be reduced by the presence of fluids or increases in lithosphere temperature, e.g. by delamination of the lower lithosphere and asthenosphere upwelling. Pre-existing structures, such as a décollement or a listric fault structure, e.g. the HFZ, may inhibit the propagation of shear-zones to greater depths.

Knowledge of the seismogenic depth and availability of geophysical interpretations, which in themselves do not provide information on fluid content, can be used with the calculations to provide constraints on the hydrous nature of the lithosphere. Below the KF the localisation in the lower crust (> 20 km) requires a dry plagioclase lithology. For the HFZ a hydrous plagioclase lithology best follows the geophysical interpretations.

Geophysical data can also be used to identify features that cause localisation to terminate at depths shallower than expected. The geophysical evidence suggests that to a first order, and subject to uncertainty about lithology and fluid content, a shear-heating mechanism can explain the maximum depth of strain localisation within the lithosphere.

The absolute depth to which a thermally activated strain-weakening mechanism supports localisation is primarily dependent on lithology and temperature. In general, where the continental lithosphere has a Moho depth > 50 km, an olivine dominated lithology is too hot to support localisation. Where < 30% of the continental lithosphere supports localisation, as with the Kunlun and Haiyuan Fault Zones, then a continuum style of deformation, rather than a fault controlled, is likely to dominate. Fault controlled lithosphere deformation is likely to occur either in regions of relatively thin lithosphere, such as rift settings, or where lower surface heat-flow and/or a dry lithosphere support localisation to greater depths.

6 Development of an India-Asia convergence model

6.1 Motivation for study of strain localisation in Tibet

Lithosphere deformation is predominately localised at plate margins with ~ 15% accommodated in areas that extend away from the plate boundaries, referred to as diffuse plate boundaries (section 1.1). Here I choose to focus on the diffuse India-Asia plate boundary. Deformation is driven by the ongoing subduction of India beneath Asia and is accommodated over a large region (~ 2,500,000 km^2), the Tibetan Plateau, that extends ~ 1,200 km north from the India boundary. The Tibetan Plateau elevation presently averages ~ 5,400 m.

The motion of India relative to a fixed Eurasia is described by an Euler pole, whose position has varied with time (e.g. van Hinsbergen et al., 2011). The Euler pole position is determined from plate-closure calculations, which can be derived from sea-floor spreading rates, GPS and earthquake slip directions and geomagnetic polarity data. At 50 Ma the Euler pole for India was located at 26.44° N, 23.21° E with a rotation rate of ~ 7 $deg.Ma^{-1}$ (van Hinsbergen et al., 2011). The present day Euler pole for India is located 31.7° N, 17.3° E, with a rotation rate of 0.477 $deg.Ma^{-1}$ (DeMets et al., 2010). The decrease in the India-Asia convergence from 50 to 35 Ma (e.g. van Hinsbergen et al., 2011), together with stratigraphic evidence (e.g. Guillot et al., 2003; Zhu et al., 2005) suggest the initial contact of the India and Asia continental margins of India and Asia occurred ~ 50 Ma. The velocity decrease of the Indian Plate has been attributed to orogenic activity in Tibet (Copley et al., 2010).

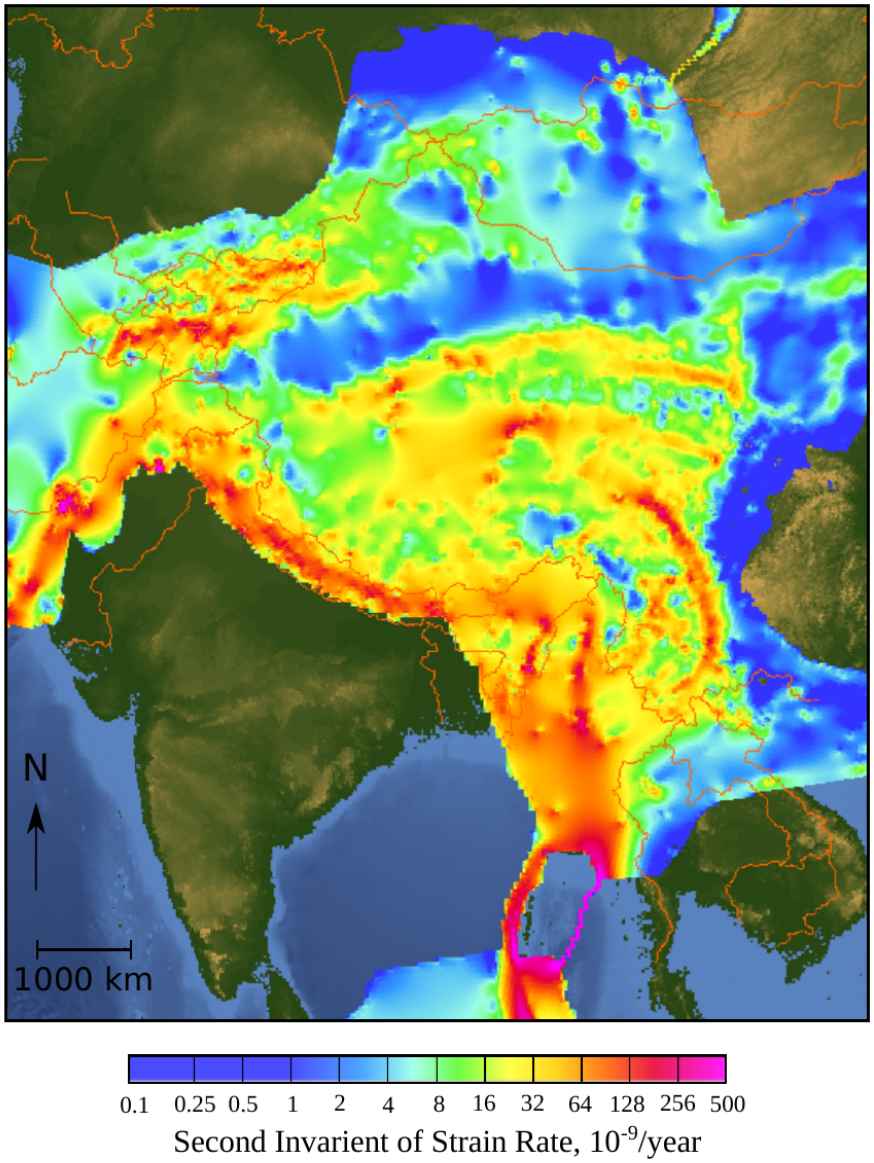

Figure 6.1: Colour scale shows the second invariant of the strain-rate (strain-rate magnitude) derived from GPS measurements across the India-Asia region (after Kreemer et al., 2014). Localised regions of high strain-rate magnitude occur across the Himalayan Front and where major fault systems occur. Landform data from Google Earth, accessed January 2018.

Since the initial contact of the continental margins India has moved ~ 2,000 km north relative to a stable Eurasia (Lin et al., 1988) and a transition from solely north-south compression to partial east-west extension has occurred. Present day focal mechanisms

show a combination of normal and strike-slip faulting over much of the Plateau, with thrust and reverse-slip faulting in the Qaidam basin, south-west Tarim and at the north-east Plateau boundary (Taylor and Yin, 2009). The plate reconstruction of Molnar and Stock (2009) show a further decrease in convergence rate at 20 to 10 Ma. This slow down period coincides with the onset of normal faulting within the Plateau, together with basin subsidence with increased sedimentation into the basins, orogenic growth and rapid (~ 3 km.Ma^{-1}) exhumation of rock along the Main Central Thrust Zone at the edges of the Plateau (see Molnar & Stock, 2009, and references therein). A 1 to 2 km increase in plateau elevation may explain these changes, as further thickening may be resisted and deformation is preferentially accommodated at the edges of the Plateau. The increased elevation may be caused by delamination of cold mantle lithosphere and replacement by hot asthenosphere (England and Houseman, 1989; Molnar and Stock, 2009).

Present day geodetic data show non-uniform gradients of strain across the Tibetan Plateau (Kreemer et al., 2014) (Fig. 6.1). While strain remains relatively distributed across the Plateau, in some areas it is focused in the form of shear-zones that extend 100s km, e.g. Altyn Tagh Fault (~ 1,800 km), Kunlun Fault (~ 1,500 km) (see Chapter Five) and the Longmenshan fault system (~ 400 km).

The Altyn Tagh Fault (ATF) is > 1200 km long, lateral strike-slip fault that marks the boundary of the north-east Tibetan Plateau and Tarim Basin (Fig. 1.3). It has been active since at least the mid Miocene (~ 16 Ma) (Wang, 1997) and from morphological offsets it has been estimated to have 70 to 360 km displacement (Ritts and Biffi, 2000; Wang, 1997). Parts of the ATF are seismically active; earthquake focal mechanisms for events

of M > 5.5 between 1977 and 2008 show strike-slip and normal faulting. Earthquakes of M = 7.2 were recorded in the central section of the ATF in 1924 and 1994 (Yin and Harrison, 2000).

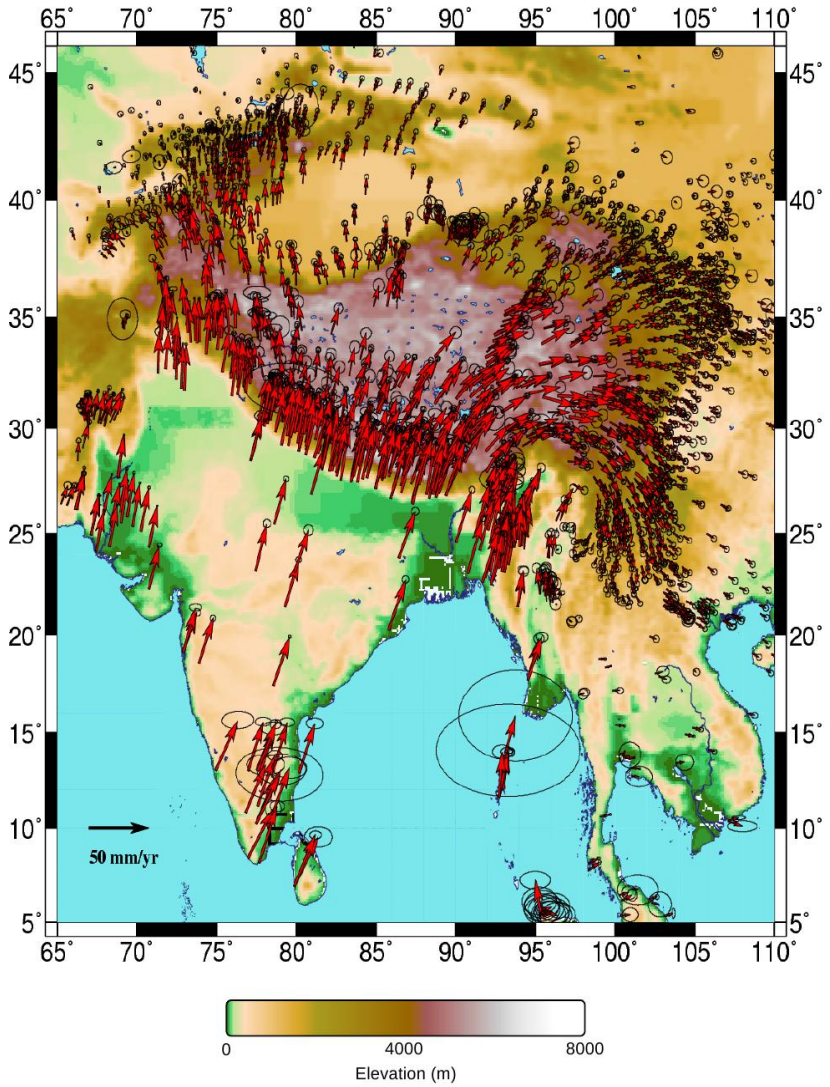

Figure 6.2: Shaded topography (after Amante and Eakins, 2009) and scaled geodetic derived velocities, reference frame Eurasia (after Zheng et al., 2017) where the ellipse marks the 95% confidence level, for present day India and the relevant Asia region.

The Longmen Shan comprises of four major reverse faults over ~ 400 km. It is located on the eastern edge of the Tibetan Plateau and marks an elevation change from 6,500 m in the Tibetan Plateau to 500 m in the Sichuan Basin (Fig. 1.3). Thrust activity occurred ~ 145 Ma, and was reactivated in association with the India-Asia convergence ~ 6 Ma (Chen and Wilson, 1996). Historical records suggest M ≥ 6 earthquakes since 2300 BCE (Z. Li et al., 2017). Recent large earthquakes include the 1970 M_S 6.2 at Dayi, the 2008 M_W 7.9 Wenchuan earthquake, which ruptured two reverse faults in the Longmen Shan, and 2013 M_W 6.6 Lushan earthquakes (Burchfiel et al., 1995; Z. Li et al., 2017).

North-west of the Tibetan Plateau is the Tarim Basin, a relatively undeformed region, with an average elevation of 3100 m (Fig. 1.3). Thin viscous sheet models of the India-Asia convergence show how the inclusion of a relatively strong Tarim Basin significantly influences strain in the surrounding regions. The Tarim Basin can transfer strain to the Tian Shan region, contributing to crustal thickening (Neil and Houseman, 1997). The strength contrast of the Tarim Basin with the weaker Tibetan Plateau focuses deformation in the weaker regions either side and, with the addition of a strain-dependent weakening mechanism, causes strain to localise to a width comparable with the Altyn Tagh shear zone (Dayem et al., 2009).

The Sichuan Basin lies to the east of the Tibetan Plateau (Fig. 1.3). In common with the Tarim Basin it has a low elevation (average 1,700 km), is bordered by mountain ranges (e.g. Longmen Mountains) and is relatively undeformed, inferring it is stronger than the surrounding regions. Paleomagentic studies show that the Sichuan Basin has undergone clockwise rotation since the early Miocene (~ 20 Ma) and it is proposed this controlled the evolution of the Longmenshan and Xianshuihe faults (Tong et al., 2018). Apatite

fission-track thermochronology suggests the relatively strong basement of the Sichuan Basin is focusing lower crustal flow and contributing to plateau uplift in the adjacent region (Enkelmann et al., 2006).

Thin viscous sheet models of the India-Asia convergence have shown how shear-zones develop adjacent to a rheologically strong region (e.g. Dayem et al., 2009) but the development of shear-zones within the Plateau has not been adequately explored. What mechanisms cause the strain to localise and form such shear-zones? Where shear-zones evolve from a low viscosity region (see Chapter Three, Four) how far can they extend across the Tibetan Plateau within the time frame of the India-Asia convergence?

Using the thin viscous sheet model implemented in *basil* I develop a reference model that is configured to resemble the India-Asia convergence from onset of collision ~ 50 Ma to the present day. I compare the topography, velocity and strain-rate fields in the model with present day geographical and geodetic measurements (Fig. 6.2). In the subsequent chapter I use the reference model to show how introduction of a low viscosity region and variations in rheological parameters influence the development of strain localisation across the Tibetan Plateau.

6.2 Development of boundary conditions

6.2.1 Choice of spherical reference frame

Prior thin viscous sheet models of the India-Asia collision simplify the boundary along which India indents Asia either as a trapezoid (Dayem et al., 2009; Houseman and

England, 1986; Neil and Houseman, 1997) or an arc (England and Houseman, 1989, 1986) and apply a fixed velocity boundary condition to represent the convergence history. Evolution of the indenter shape with time and the influence of erosion are ignored. These models typically use a strain rate versus stress exponent between 1 (Newtonian rheology) and 10 (power-law rheology) and are calculated within a Cartesian co-ordinate system which ignores curvature of the spherical shell representing the Asian lithosphere.

The adaptation of the Cartesian thin viscous sheet method used in *basil* to a thin viscous spherical shell was undertaken by G. Houseman and L. Evans (*pers. comm.* G. Houseman). The spherical shell approach has previously been applied to instantaneous deformation problems by Gordon and Houseman (2015), England et al. (2016) and Walters et al. (2017). For this work further adaptation of *basil* allows the velocity of the indenting boundary to be defined by a rotation about an Euler pole, necessitating that the velocity components are re-set at each time level in the integration. The governing equations are described in Chapter Two and are summarised by Gordon and Houseman (2015). Using a sinusoidal equal area projection of the spherical coordinates (longitude and latitude), the stress balance in the horizontal directions is solved and the solution may be readily compared with actual geography.

In common with the Cartesian method the horizontal displacement rates remain invariant with depth, in this case the radial coordinate. The horizontal velocity field is determined from imposed angular velocities or tractions on plate boundaries and may influenced by horizontal gradients of gravitational potential energy within the sheet (England and Molnar, 1997). Stronger regions experience relatively little deformation,

and weaker regions undergo more deformation. The deformation field produced by the India-Asia collision is represented within a dimensionless coordinate system in which distance is scaled using the radius of the sphere, the averaged radius of Earth, 6371 km.

6.2.2 High viscosity regions: India, Tarim and Sichuan Basins

The absence of major deformation in the Indian plate south of the Himalayan Range, compared to the presence of orogens, faults and fold systems in the Asian plate, infers India is relatively strong to resist such major deformation. Therefore for the *basil* model I set an initial high viscosity in the India region. Changes in the shape of the indenting region through the convergence process and changes in lithosphere thickness arising from erosion cannot be adequately constrained. By assuming that this region is strong relative to the Eurasian region further north, and setting a plate-like velocity field on the coastal margins of India the model replicates this behaviour. For simplicity I do not consider the effects of erosion, sediment transport, and deposition in the numerical experiments described here.

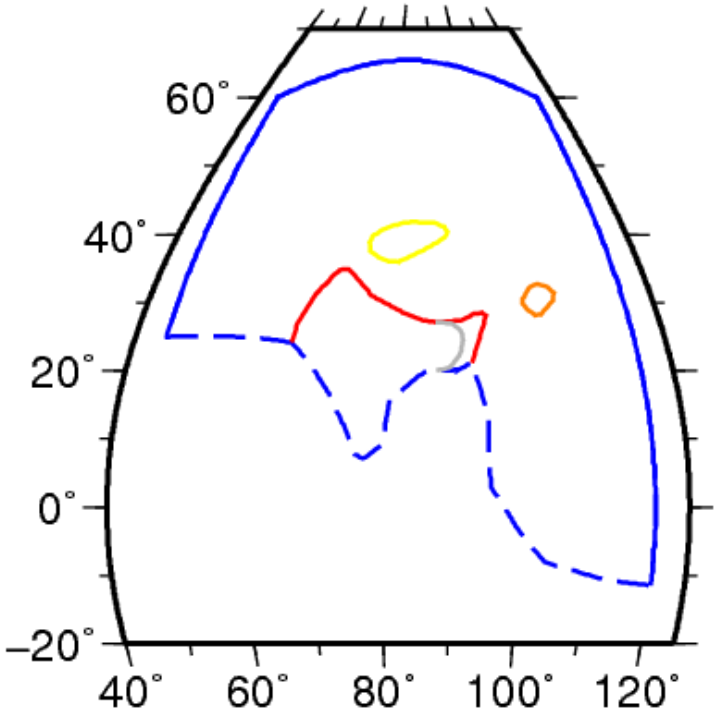

Figure 6.3: Initial India-Asia model on a spherical projection. The points defining the external (blue), Tarim Basin (yellow) and Sichuan Basin (orange) boundaries for the present day configuration of the India-Asia model. The initial Himalayan Front (red) is later modified (grey) to reduce mesh distortion. The external boundary (blue) is either fixed (solid) or has a velocity or traction conditions applied (dashed).

Heterogeneous strain can be initiated through the presence of a strength contrast or by irregular boundary conditions. Indentation of the strong India region will see the development of a high topography region equivalent to the Himalayan Front (England and Houseman, 1986; England and McKenzie, 1982), but India indenting an otherwise homogeneous viscous layer can not develop the sort of strain localisation that is evident across the Tibetan Plateau (Fig. 6.1; e.g. Dayem et al., 2009; England and Houseman, 1986; England and McKenzie, 1982; Neil and Houseman, 1997).

Previous models of the India-Asia convergence have simplified the Tarim Basin as a rigid block (e.g. Dayem et al., 2009; England and Houseman, 1986; Neil and Houseman, 1997). While the Sichuan Basin has not been included in previous thin viscous sheet models cited earlier there is a strong argument for doing so. The average elevation of the Tarim and Sichuan Basins, 1,200 m and < 500 m respectively, is considerably less than that of the bordering Tibetan Plateau, 5,000 m. This suggests that the Basins are strong enough to resist accommodating horizontal shortening through crustal thickening. Deformation is likely accommodated within the bordering orogens and fault systems.

Clark and Royden (2000) propose that a strong Sichuan Basin crust inhibits crustal flow from Tibet, resulting in the present day steep topographic margin. Receiver function data infer a 20 km shallower Moho beneath the Sichuan Basin than eastern Tibet, but a ~ 50 km deeper lithosphere-asthenosphere boundary (Zhang et al., 2010). This thicker Sichuan Basin lithosphere prevents eastward flow of the Tibetan crust, the later which subsequently increases against the Sichuan Basin boundary. Structural deformation evidence obtained from surface outcrops suggests the entire Sichuan Basin rotates counter-clockwise, likely in response to the surrounding crustal flow (Wang et al., 2014).

Beneath the Tarim Basin high-resolution P-wave tomography show a high-velocity zone in the lower crust and upper mantle that continues to 200 to 250 km, suggesting an old rigid lithosphere block (Huang and Zhao, 2006). Regional tomography suggests mantle flow beneath the Tibetan Plateau is effectively blocked by the thickened Tarim lithosphere (Xu et al., 2002).

Within the Tarim Basin sedimentation rates determined from magnetostratigraphy suggest Cenozic basement shortening and uplift in the north and central portion of the basin (Chang et al., 2014). Laborde et al. (2019) used field observations, seismic sections, geological maps, and field and satellite images to construct a structural map and balanced geological transects. They found that Cenozoic compressive deformation of the Tarim Basin is principally (> 94 %) taken up in the surrounding mountain ranges (Western Kunlun, Altyn Tagh, Tian Shan). Up to 7.5% of Cenozoic shortening is accommodated within the Tarim Basin through uplift, notably the Bachu uplift in the western central basin (e.g. Li et al., 2016; Tong et al., 2012), with potential strike-slip faulting at the edge of the uplifts.

Crustal deformaton within the India-Asia collision zone has been quantified using GPS velocity data collected between 1991 to 2015 from 2576 GPS stations, including stations located within the Tarim and Sichuan Basins (Zheng et al., 2017b). Calculated strain-rates are low within the Tarim Basin, but are higher north-west of the basin across the Tian Shan (Fig. 1.3). Caluclated strain-rates are also low in the south-east Plateau, including the Sichuan Basin.

Active deformation adjacent to the north-west Tarim Basin border deformations is indicated by the Jiashi earthquake sequence (1997 to 2003, Mw between 3.5 and 7) (Huang et al., 2017). However, overall earthquake activity within the Tarim and Sichuan Basins is low and generally confined to the western and southern regions repsectively (Taylor and Yin, 2009). Over a 32 year period the number of seismic events > M 5.5 within the Tarim and Sichuan Basins is vastly exceded by those within the Tibetan

Plateau (Figure 2, Taylor and Yin, 2009), further justifying the assumption of rigid basins within the context of modelling the India-Asia convergence.

The potential influence on strain distribution in the Tibetan Plateau warrants the Tarim and Sichuan Basins being defined in the reference model by a distinctly more viscous constitutive law; for simplicity the increased viscosity coefficient (VC) is defined by a multiplicative factor relative to the background viscosity coefficient (Eq. 2.16) that applies elsewhere in the domain. Using Google Earth, I define the present day basin regions using changes in elevation and topography. The number of points required to define each polygonal region is kept to a minimum, but is sufficient to define the basic geometry (Fig. 6.3). Because the model calculation is integrated forward from 47 Ma the location of these stronger regions at the beginning of the calculation must be estimated, as described in section 6.2.6.

6.2.3 Defining the India boundary

I use Google Earth to define the present day boundary for the continental India region. I define the east, south and west boundaries from the extent of the continental shelf. The northern boundary, which indents the weaker Asia region, follows the Himalayan Front. The north-east corner of the India region is smoothed in later models to avoid issues with distortion of the finite element mesh, the changes are shown in Fig. 6.3. Ideally the model simulation should replicate the movement of India relative to Eurasia from the onset of collision through to the present day.

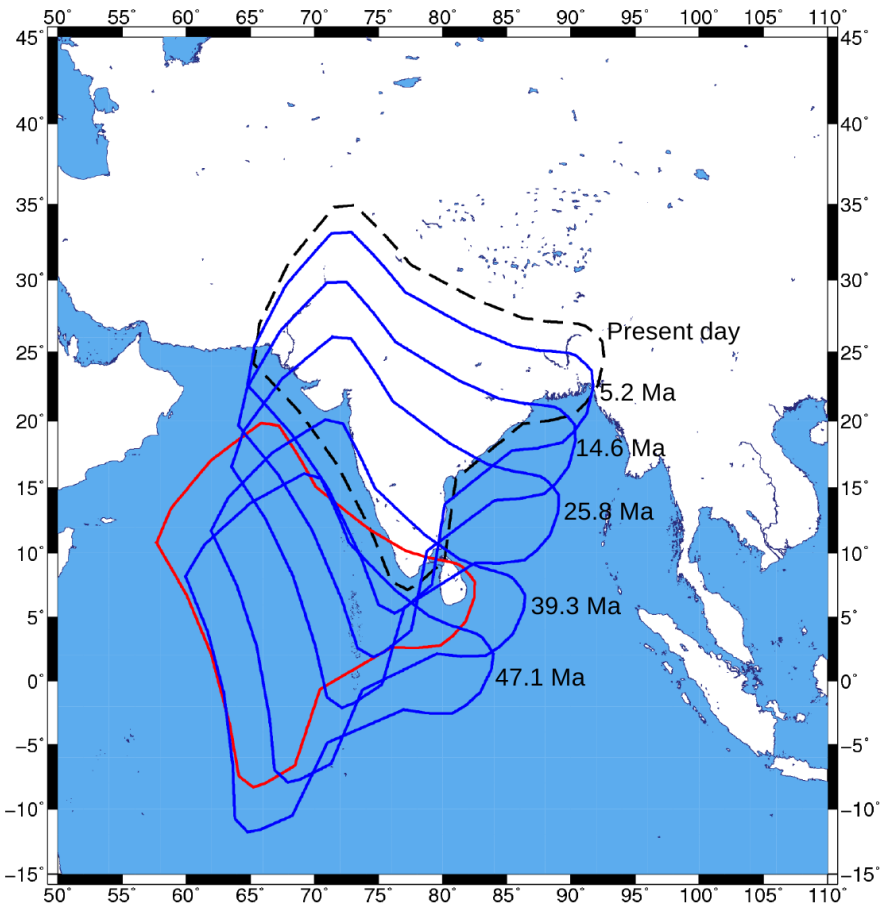

Figure 6.4: Boundary map of India and Asia overlain by the calculated paleo-positions of India. The black dashed line shows the defined present day outline of India for my model which is based on the Himalayan Front and the extent of the continental shelf. This region is rotated about the fixed Euler pole calculated by DeMets et al. (2010) (red) or the age dependent Euler poles calculated by van Hinsbergen et al. (2011) (blue) to 47 Ma. India's position for selected ages are shown for the van Hinsbergen et al. (2011) Euler poles.

The plate rotations determined by van Hinsbergen et al. (2011) use age dependent Euler poles, of which 47.09 Ma is the closest to coincide with the onset of collision. At this time the positions of India determined by van Hinsbergen et al. (2011) is broadly similar to the position obtained by using the present-day Euler pole of DeMets et al. (2010) assumed constant during the same period (Fig. 6.4). In order to simplify further

calculations I therefore use the single Euler pole of DeMets et al. (2010) to define the rotation rate of India since 47 Ma. Using a constant Euler rotation rate pole for the integrated calculation simplifies the calculation and enables direct comparison of strain rate fields at the end of the calculation with observations from geodesy. The setting of the boundary velocity field in the *basil* program was validated by integrating the deformation field backward from the present day and then forward during the 47 Myr period to ensure that the present-day outline was recovered. Given the other uncertainties involved in the calculation, for example the initial topography or the rheology of the continental region now subducted beneath Asia, this choice of a single Euler pole is a reasonable approximation.

6.2.4 Defining the Asia boundary

North of the collision zone, the domain of the solution is limited by north (60º N), east (max 120º E) and west (min 45º E) boundaries that are set sufficiently far from the region of interest (Tibetan Plateau) to minimise boundary affects (Fig. 6.3). To accommodate geodetic data that show a change from a dominant north-east trending velocity to south-east in the south-east region of Tibet and north region of Sundaland (Fig. 6.2) (Taylor and Yin, 2009; Wang et al., 2019), I extend the domain of the solution to include Sundaland. This provides space for potential south-east directed flow that ideally would replicate the present day velocity field.

I set an initial zero traction condition on the Sundaland and east Asia boundaries, and fix the north and west Asia boundaries (Fig. 6.5a, Table 6.1). From these boundary conditions at $t' = 1$ the velocity direction is north-east trending across the modelled

domain (Fig. 6.5b, c). This is in agreement with the present day geodetic velocity across central and north-east Tibet, but differs to that in west and south-east Tibet (Fig. 6.2). At $t' = 1$ the velocity magnitude increases eastwards across the modelled domain, in contrast to present day geodetic data that show velocity magnitude decreases eastwards. This suggests a need to restrict movement of the east Asia boundary, therefore I set a partial traction condition on the Sundaland and east Asia boundaries (Fig. 6.5). However, I find a partial traction condition still promotes an eastward increase in velocity magnitude.

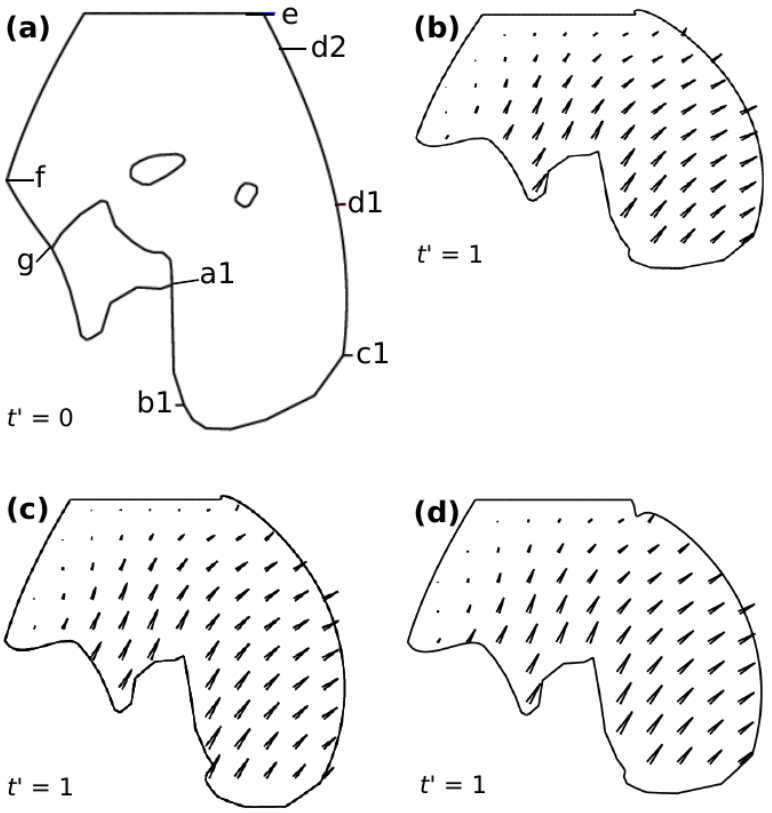

Figure 6.5: Experiment numbers and boundary conditions given in Table 6.1. Black lines mark the internal and external boundaries. I set n *= 1 and* Ar *= 0 for calculating the boundaries at* t′ *= 1. a) Configuration at* t′ *= 0. Experiments b) IA_bnd_08, c) IA_bnd_10, d) IA_bnd_23 at* t′ *= 1. Black arrows show the velocity magnitude and direction.*

Where the boundary condition changes between that set for east Asia (fixed or traction condition) and Sundaland (taper to India rotation pole), then at $t' = 1$ the boundary co-ordinates change abruptly (Fig. 6.5). Varying the initial gradations between changes in the boundary conditions does not resolve this issue (Fig. 6.5b, c, d).

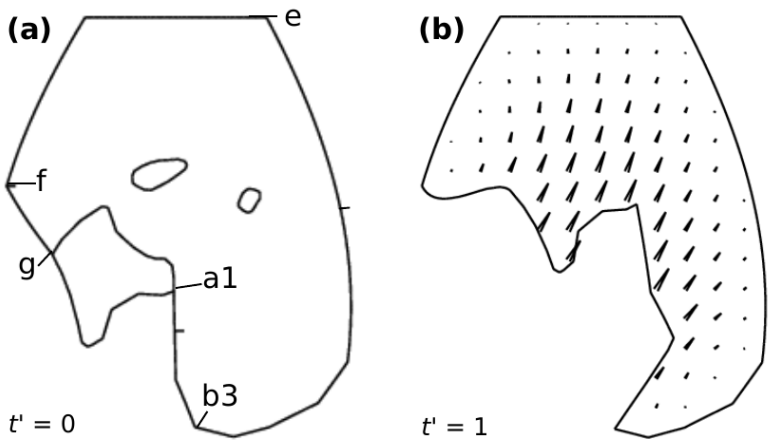

Figure 6.6: Boundary conditions given in Table 6.1. Black lines mark the internal and external boundaries. I set n *= 1 and* Ar *= 0 for calculating the boundaries at* t′ *= 1. a) Configuration at* t′ *= 0. b) Experiment IA_bnd_40 at* t′ *= 1. Black arrows show the velocity magnitude and direction.*

To further explore the Sundaland and Asia boundary conditions I use the initial ($t' = 0$) external boundary co-ordinates, and set a zero velocity condition on the east Asia and south Sundaland boundaries (Fig. 6.6a). At $t' = 1$ (Fig. 6.6b) the velocity magnitude is greatest in central Tibet and decreases to the east and west across the domain. The velocity direction is near north in the west part of the domain, and rotates to the north-east in the east part of the domain. This is broadly comparable to the present day geodetic velocity field, but differs for south-east Tibet where the present day velocity trends south-east. Fixing the Sundaland boundary prevents the Sunda boundary from

restoring to the present day position. The west Sunda boundary forms an approximate curve in the opposite direction to the present day Sunda Trench, formed by subduction of the Australian-Capricorn plates beneath the Eurasian plate.

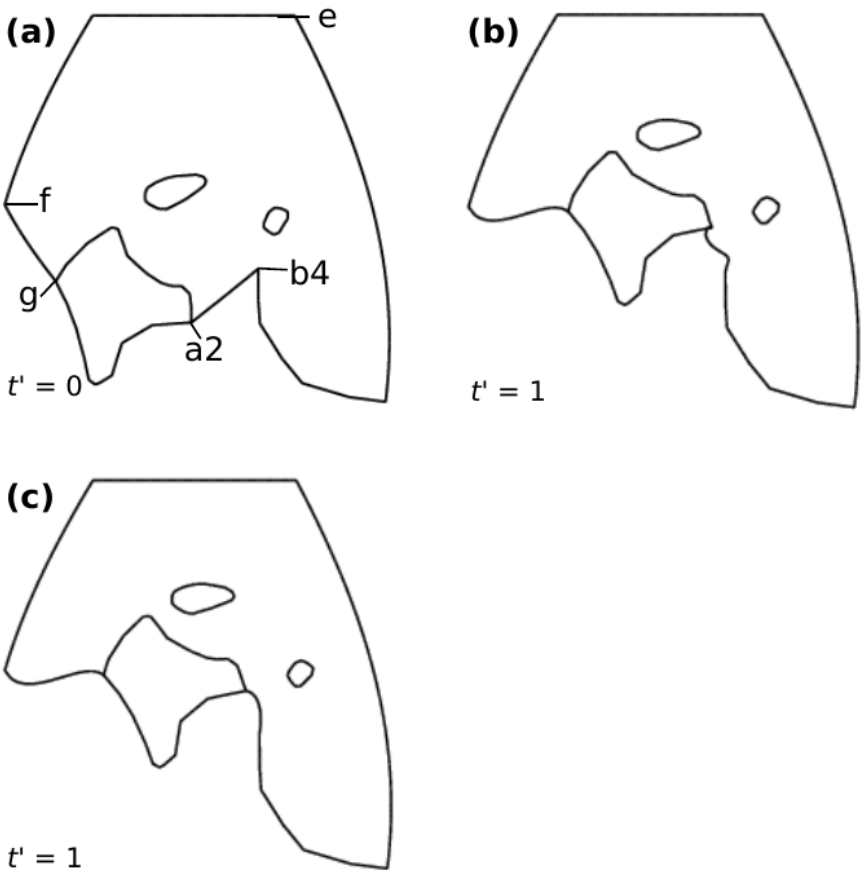

Figure 6.7: Boundary conditions given in Table 6.1. Black lines mark the internal and external boundaries. I set n *= 1 and* Ar *= 0 for calculating the boundaries at* t′ *= 1. a) Configuration at* t′ *= 0. Experiments b) IA_bnd_44, and c) IA_bnd_47 at* t′ *= 1.*

Subduction rollback associated with the Philippine and Pacific plates is likely to promote eastward movement of the east Asia boundary (e.g. Schellart et al., 2019). Potential rollback from the subduction of the Australian plate beneath Sundaland may promote southward movement of Sundaland and contribute towards the rotation of the

velocity direction. In a thin viscous sheet model an applied boundary velocity condition decreases exponentially with distance perpendicular to that boundary (England et al., 1985) (see section 6.3.2), thus limiting exploration of the far-field impact of subduction rollback.

Table 6.1: Boundary conditions applied for different experiments in the India-Asia convergence problem where TX, traction condition in x-direction; TY, traction command in y-direction; fixed, zero velocity condition; Pole 2, Euler pole for India; TP, taper condition where for 1 the taper follows a linear function and for 2 follows a cosine squared function. The x- and y-directions are positive to the east and north respectively. Initially and final boundary positions are shown in Fig. 6.5 (IA_bnd_08, IA_bnd_10, IA_bnd_23), Fig. 6.6 (IA_bnd_40), Fig. 6.7 (IA_bnd_44, IA_bnd_47).

Experiment	**a1 to b1**	**b1 to c**	**c to d1**	**d1 to e**	**e to f**	**f to g**	**g to a1**
IA_bnd_08	TX = 0; TY = 0				Fixed	Fixed to pole 2, TP = 2	Pole 2
IA_bnd_10	TX = -10; TY = -10				Fixed	Fixed to pole 2, TP = 2	Pole 2
Experiment	**a1 to d2**			**d2 to e**	**e to f**	**f to g**	**g to a1**
IA_bnd_23	TX = 0; TY = 0			TX = 0 to -5, TY = 0 to -5, TP = 2	Fixed	Fixed to pole 2, TP = 2	Pole 2
Experiment	**a1 to b3**	**b3 to f**				**f to g**	**g to a1**
IA_bnd_40	Pole 2 to fixed, TP = 2	Fixed				Fixed to pole 2, TP = 2	Pole 2
Experiment	**a2 to b4**	**b4 to f**				**f to g**	**g to a2**
IA_bnd_44	TX = 0; TY = 0	Fixed				Fixed to pole 2, TP = 2	Pole 2
IA_bnd_47	Pole 2 to fixed, TP = 1	Fixed				Fixed to pole 2, TP = 2	Pole 2

I reconfigure the initial modelled geometry of Sundaland such that the west boundary correlates with the present day boundary and set a zero velocity condition (Fig. 6.7). Connection of the west Sundaland boundary to India is discussed in the following

section (6.2.5). The north, east and west boundaries of the Asia domain are also subject to a zero velocity condition. These boundary conditions maintain Sundaland at the present day co-ordinates, and at $t' = 1$ produce an eastward decay in velocity magnitude. Comparison of the modelled and present day velocity field are discussed further in section 6.3.2.

6.2.5 Calculation of the India-Asia connectors

On the boundary segments that connect the fixed parts of the external boundary and the moving Indian peninsula the velocity condition is tapered (following a cosine-squared function) or a zero traction condition applied (Fig. 6.7) to avoid abrupt velocity changes that would otherwise cause local stress concentrations. To explore the boundary locations where India and Asia connect I construct a present day model of the region, defining the India-Asia boundary and Tarim and Sichuan Basin regions as described in the preceding sections (Fig. 6.3, 6.8a). I rotate the external India boundary back to 47 Ma using the reverse of the Euler pole of DeMets et al. (2010), assumed constant. To minimise the calculation time I use a Newtonian rheology ($n = 1$) and omit the buoyancy forces arising from topography contrasts ($Ar = 0$). The reverse model is run from 0 to 47 Ma, with the final boundary positions shown in Fig. 6.8b then serving as an initial estimate for a starting model at 47 Ma, with uniform initial crustal thickness.

I then set the initial boundary and basin regions using those calculating at 47 Ma (shown in Fig. 6.8b), and set India to move in accordance with the Euler pole of DeMets et al. (2010) to the present day position, applying the previous taper conditions to the boundaries connecting India and Asia. The use of the same taper condition as the 0 to 47

Ma model between the fixed Asia boundary and the moving India does not restore the west Sundaland boundary to the present day position, due to the zero traction condition. Retaining the calculated boundary position at 47 Ma but changing the imposed velocity result in further misplacement of the boundary (Fig. 6.7). Instead, a good result can be obtained by simplifying the boundary between India and Sundaland at 47 Ma to a straight line and applying a taper velocity condition (rotating India to fixed Asia) (Fig. 6.7c). This configuration permits the India region to return to its present day position (validating the spherical calculations), prevents mesh distortion that may become high enough to terminate the calculations, and fixes the present day western boundary of Sundaland. While this simplified solution is constructed to comply with the model constraints, in the absence of more precise information on the rotation and deformation of the Sundaland block it is as valid as more complex boundary arrangements.

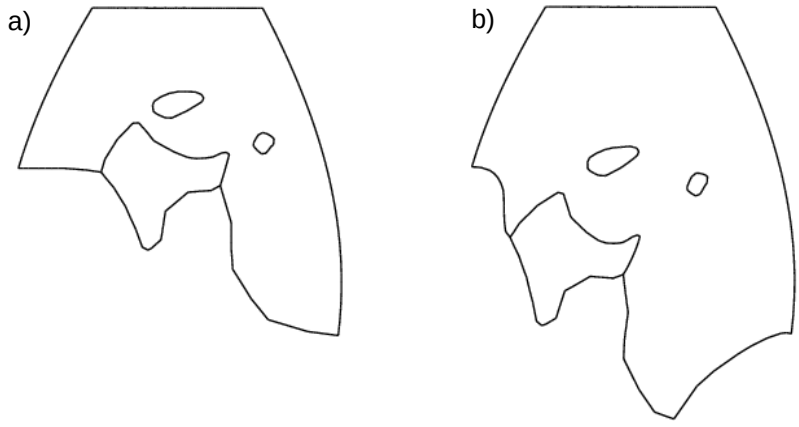

Figure 6.8: a) The present day boundaries for India, Tarim and Sichuan Basins and Asia regions defined for the reverse run (0 to 47 Ma) of the India-Asia model; b) the boundaries at 47 Ma where India has been rotated using the reverse of the DeMets et al. (2010) India-Eurasia Euler Pole (31.7° N, 17.3° E, with a rotation rate of 0.477 deg.Ma^{-1}).

6.2.6 Calculation of basin positions at 47 Ma

Using the geometry and boundary conditions established in the previous section I calculate provisional positions of the modelled Tarim and Sichuan Basins at 47 Ma. The relative strength of the basins to Asia is discussed in section 6.2.2. These interior basins move in response to the resolved velocity field arising primarily from the external boundary conditions. The locations of these basins at 47 Ma are not accurately known, but may be estimated using the reverse model.

Using the co-ordinates determined from the reverse model I then calculate if running a forward model from 47 Ma to 0 Ma restores the Tarim and Sichuan Basins to their present day location. The choice of strain exponent (n) and the balance between vertical and horizontal forces (Ar) influence the velocity field inside the model, and consequently affect the final position of the basins in the forward calculations. I set n = 3, an appropriate value for averaged lithosphere rheology, and Ar = 1 (Chapter Two, Eqs. 2.14, 2.64) to include buoyancy forces and adjust the initial (47 Ma) position of both basins until the forward model moves the basins to their approximate current location (Fig. 6.9d). The adjustment leads to the model moving the Tarim Basin 1150 km northwards during the past 47 Ma, approximately half the distance moved by India (2000 km). The distance agrees with paleomagnetic inclinations that indicate > 1000 km northward movement of the Tarim Basin since 66 Ma (Tan et al., 2003). In the same forward model the Sichuan Basin is moved ~ 450 km northwards.

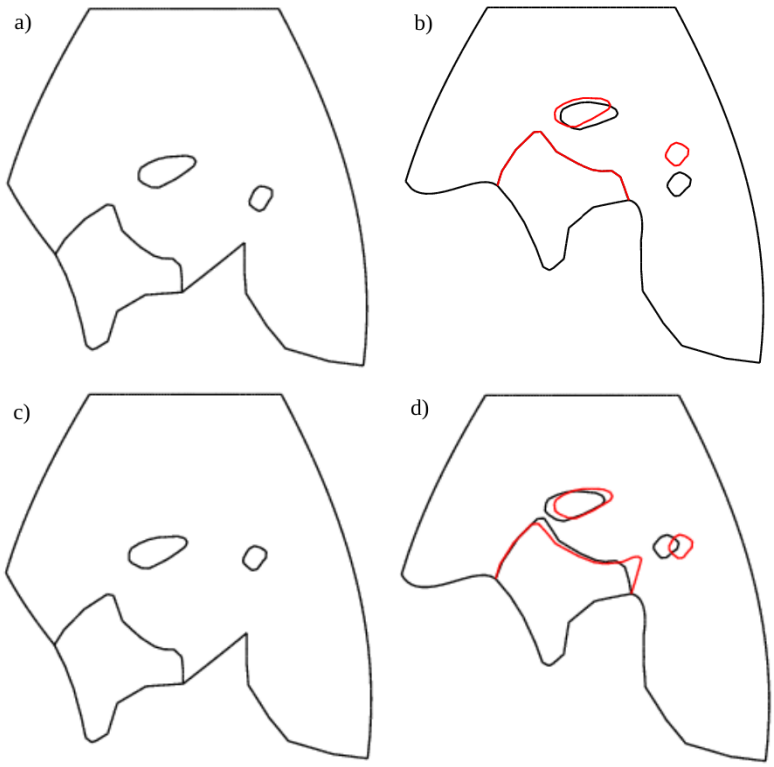

Figure 6.9: a) Initial model configuration at 47 Ma showing the external boundary and India boundary (used in subsequent experiments) and the provisional boundaries of the Tarim and Sichuan Basins calculated using n *= 1,* Ar *= 0. b) Red lines show the present day position of the modified Himalayan Front and the Sichuan and Tarim Basins. Black lines show the boundary configuration at 0 Ma, calculated by solving the thin viscous shell equations with the Indian boundary moved using the Euler pole of DeMets et al. (2010) with* n *= 3 and* Ar *= 1. c) Adjustment of the initial locations of the Tarim and Sichuan Basin based on result of experiment shown in (b). d) after integration of the thin sheet equations with* n *= 3 and* Ar *= 1 and India rotated into it's present day position. The present day position of the Himalayan Front and the Tarim and Sichuan Basins are shown in red.*

For a given model run the final position of the Tarim and Sichuan basins is dependent on the choice of rheological parameters (*n, Ar, Γ*, see Chapter Two, Eqs. 2.14, 2.64, 2.20), the boundary conditions, and the presence of additional rheological contrasts. While the initial position of the basins could be separately determined for any

combination of n, Ar, and Γ, such processes are time consuming and were not considered significant in evaluating the process of strain localisation across the Tibet Plateau. Hence the initial geometry determined for $n = 3$, $Ar = 1$, and $\Gamma = 0$ (Fig. 6.9d) is used throughout subsequent experiments.

6.3 Information from initial model geometry and boundary conditions

I follow Chapter Two (section 2.2.6) in non-dimensionalising time, and set the total rotation of India from its position at 47 Ma to present day to occur at $t' = 1$. Using the model geometry and boundary conditions developed in section 6.2 I initially set dimensionless effective viscosity to 1 across Asia and 10^n (where n is the strain exponent) in India and the Tarim and Sichuan Basins. The crustal thickness is set to an initial uniform value of 30 km. I compare the result at $t' = 1$ (present day configuration) to the present day measurements of the topography (Fig. 6.2), velocity (Fig. 6.2) and strain rate (Fig. 6.1). I consider a Newtonian ($n = 1$, $Ar = 0$) and power-law ($n = 3$, $Ar = 1$) rheology and how the presence of the Tarim and Sichuan Basins influences the development of these fields (Table 6.2).

Table 6.2: Experiments to compare topography, velocity and strain-rate to present day measurements. $\Gamma = 0$ *for all experiments.*

Experiment	**n**	**Ar**	**Sichuan and Tarim Basins present?**	**Notes**
IA_ref_01	1	0	No	
IA_ref_04	1	0	Yes	
IA_ref_05	3	1	No	
IA_ref_08	3	1	Yes	
IA_1908_01	3	0	Yes	
IA_WS_01	3	1	Yes	Low viscosity Sundaland region
IA_WS_02	3	5	Yes	Low viscosity Sundaland region

6.3.1 Comparison of initial experiments and present day elevation

To calculate the elevation across the deforming domain I determine the difference in lithosphere thickness at the required time from the initial uniform thickness and assume an Airy type isostasy with a constant density crust and mantle-lithosphere (2800 $kg.m^{-3}$ and 3300 $kg.m^{-3}$ respectively).

During the rotation of India into Asia the high-viscosity regions of India and the Tarim and Sichuan Basins resist deformation and remain topographically low (average elevation < 500 m). Deformation is instead accommodated in the low-viscosity Asia region. For $n = 1$, $Ar = 0$ and $n = 3$, $Ar = 1$ the indentation of a strong India into a fixed Asia is accommodated by an increase in crustal thickness to an average of ~ 3,000 ($n = 1$) and 4,500 m ($n = 3$) in the Tibetan Plateau area (Fig. 6.10, 6.11). The modelled elevation follows the present day elevation by decreasing outwards from the Tibetan

Plateau and the high viscosity regions remaining topographically low (Fig. 6.11). My experiments show an increase in elevation in the Tian Shan region (north of the Tarim Basin) up to 4,700 m and east of the Sichuan Basin, up to 3,200 m, due to the basin movement in response to the indenting India; the elevation increase does not occur when the basin regions are absent (Fig. 6.12). Elevation is greater in all these areas for $n = 3$ than $n = 1$ (Fig. 6.11).

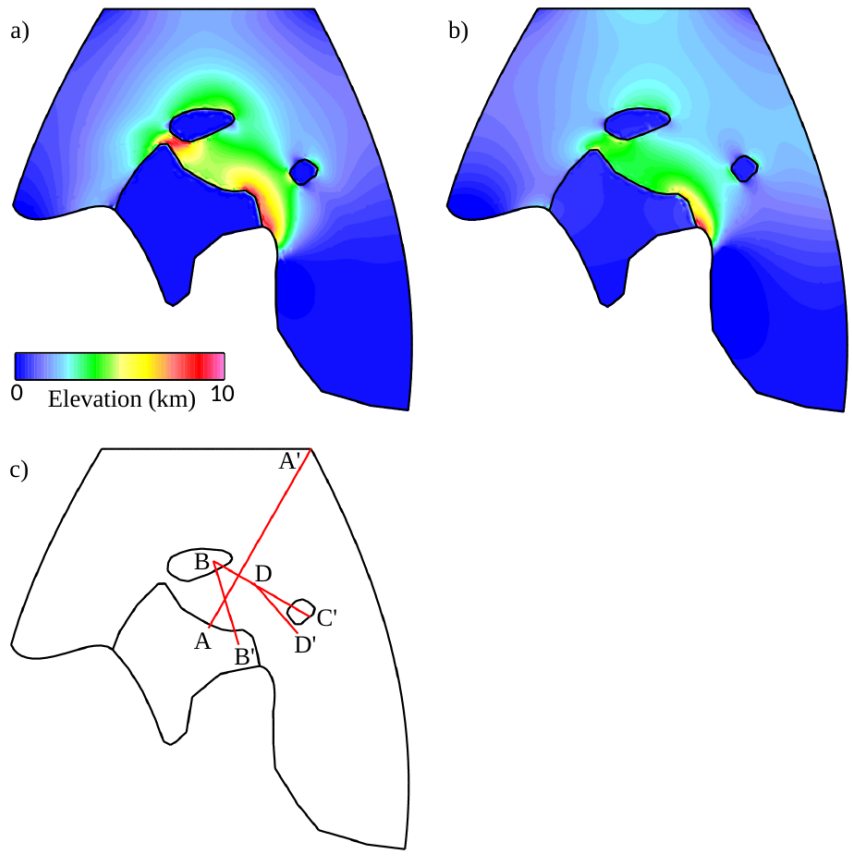

Figure 6.10: Contoured elevation for India-Asia model at t′ *= 1 where a)* n *= 3,* Ar *=1 and b)* n *= 1,* Ar *= 0 where c) shows the profile lines for each model used in Fig. 6.11. (a, experiment IA_ref_08; b, experiment IA_ref_04; see Table 6.2.) The viscosity coefficient for India and the basins regions is set at 10 times that of the Asia region. The extreme topography highs adjacent to the indenter would be removed if erosion were included in the model.*

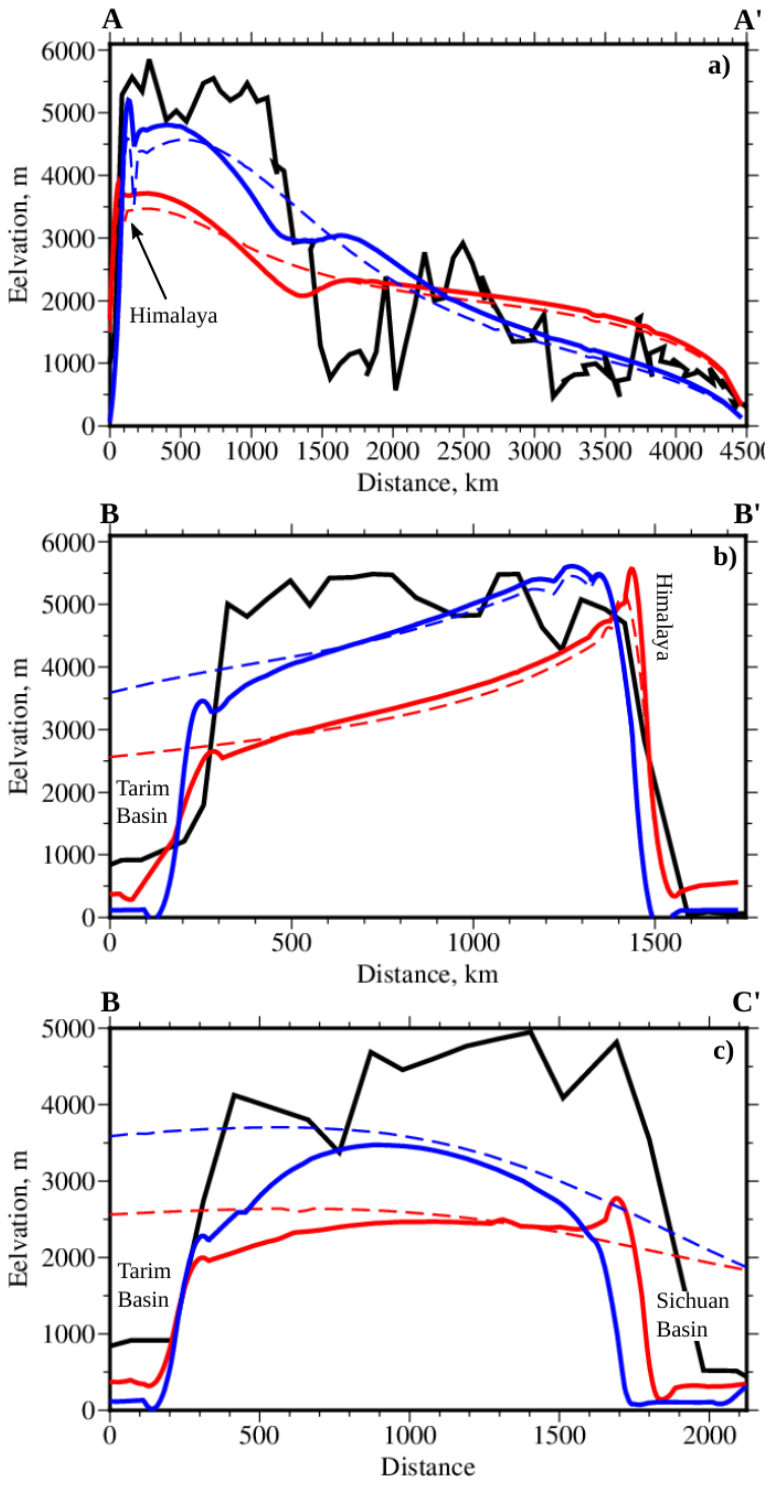

Figure 6.11: At t′ *= 1, elevation for profile a) AA″; b) BB″; c) BC″ (see Fig. 6.10c for profile locations). Red line,* n *= 1,* Ar *= 0; blue line* n *= 3,* Ar *= 1; solid line for models with Tarim and Sichuan Basins, dashed line with no basins. Black line, present day elevation along equivalent profile, data from Amante and Eakins (2009).*

Houseman and England (1986) also observed that increasing *n* in a simplified India-Asia convergence model concentrates deformation closer to the indenting region and increases the Tibetan Plateau thickness. This occurs because the greatest stress differences develop near the indenter and the effective viscosity (η_{eff}) varies as the n^{th} power of stress scaled to the lithospheric strength coefficient, *B*:

$$\eta_{eff} = \frac{B}{2}\dot{E}^{(1-n)/n} \qquad where \qquad \dot{E} = \left(\dot{\varepsilon}_{ij}\,\dot{\varepsilon}_{ij}\right)^{1/2} \qquad \text{Eq. (6.1)}$$

where $\dot{E}$ is a measure of the local strain rate. Eq. 6.1 shows for $n = 1$ the effective viscosity is independent of strain-rate (Newtonian rheology) but for $n > 1$ and where *B* is constant, the effective viscosity decreases with increasing strain rate. Consequently for the $n = 3$ model the effective viscosity decreases with time in front of the indenting India region where the strain-rates are greatest (Fig. 6.13). The temporal change in strain-rate develops as a consequence of the increasing gradients of gravitational potential energy from the crustal thickening and horizontal shortening.

The local strain-rate is modified by the influence of buoyancy forces. For $n = 3$ and $Ar = 0$, that is the buoyancy forces are omitted (Fig. 6.14), the elevation across the Plateau at a given point increases with time and the corresponding strain-rates are higher and the effective viscosity lower than for $Ar = 1$. This is because for $Ar > 0$ the buoyancy forces resist horizontal shortening, limiting the increase in elevation and hence strain-rate.

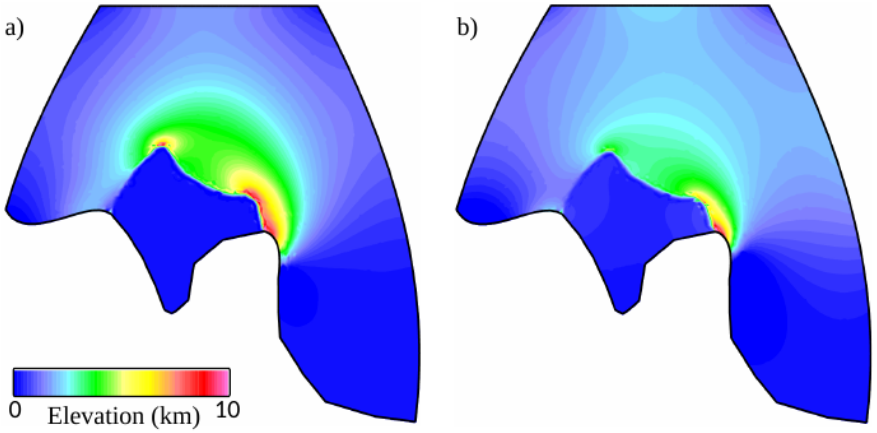

Figure 6.12: India-Asia model at t′ *= 1, without the Tarim and Sichuan Basins. a) Contoured topography for a)* n *= 3,* Ar *=1 and b)* n *= 1,* Ar *= 0. (a, experiment IA_ref_05; b, experiment IA_ref_01; see Table 6.2.) The viscosity coefficient for India is ten times that of the Asia region.*

Where the Tarim and Sichuan basins are present they act as a barrier to limit the outward flow of the viscous sheet from the elevated Tibetan Plateau. The Plateau elevation is at its highest (up to 9,600 m for n =3, Ar = 1 at t' = 1) in the area directly between the Tarim Basin and India, where the outward flow is most limited (Fig. 6.10). Removing the Tarim and Sichuan Basins from the model results in a steady decrease in elevation from the Tibetan Plateau region to Asia, rather than a rapid elevation change (Fig. 6.11, 6.12).

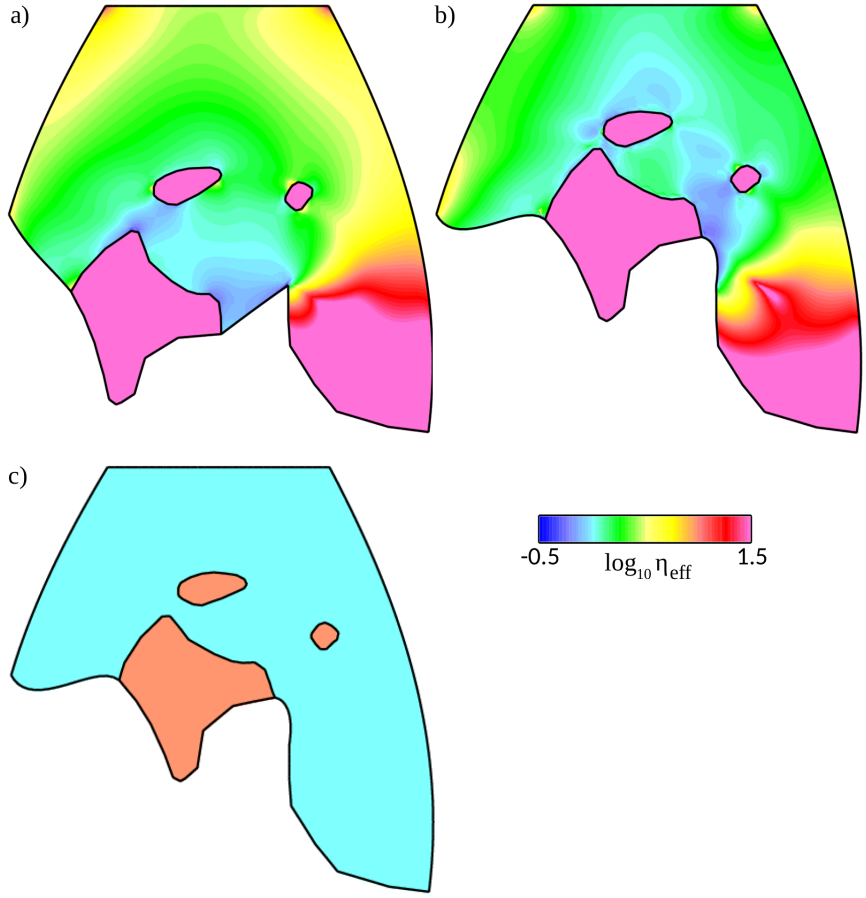

Figure 6.13: India-Asia model showing log_{10} effective viscosity (dimensionless) for a) t′ *= 0.1,* n *= 3, Ar = 1; b)* t′ *= 1,* n *= 3,* Ar *= 1; c)* t′ *= 1,* n *= 1,* Ar *= 0. (a & b, experiment IA_ref_08; c, experiment IA_ref_04; see Table 6.2.) For* n *= 3 the effective viscosity changes in response to the strain-rate. At* t′ *= 0 (47 Ma) the viscosity within the proto-Tibetan region is low relative to the rest of the domain and then increases with time in the Plateau region as strain-rate decreases. For* n *= 1 the effective viscosity remains unchanged between* t′ *= 0 and 1 across the solution domain.*

Broadly the topographic variation in the model at $t' = 1$ for $n = 3$, that includes strong Tarim and Sichuan blocks, follows that of the present day topography (Fig. 6.11). The major difference lies on the west boundaries of the Tarim and Sichuan Basins. Here the

model topography (Fig. 6.10) is not as enhanced as it is across the Altyn Tagh Fault zone of western Tibet and the Longmenshan fold belt of Eastern Tibet (Fig. 6.2).

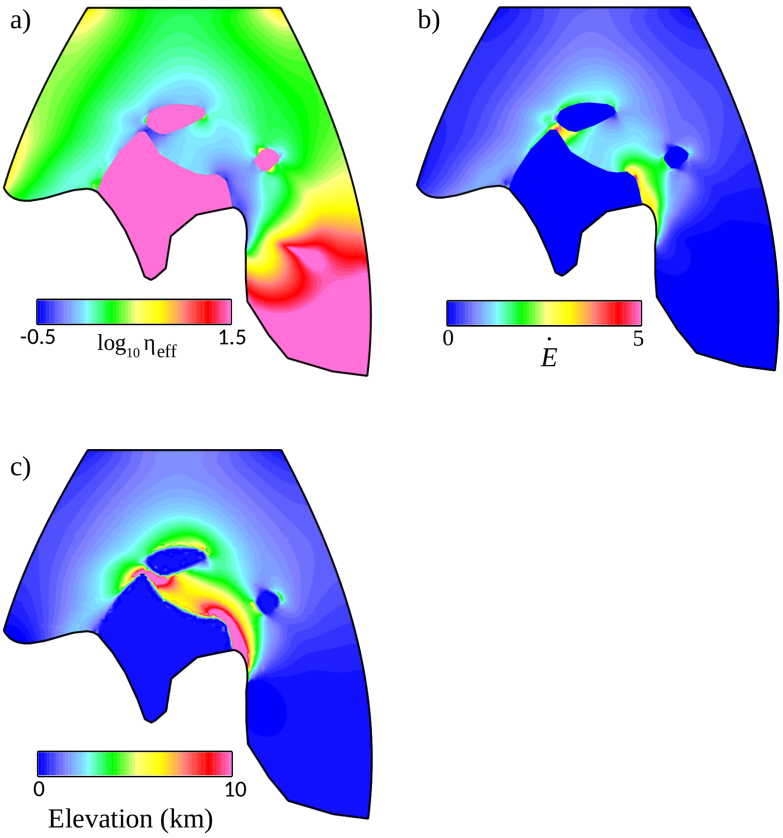

Figure 6.14: India-Asia model at t′ *= 1 for* n *= 3,* Ar *= 0, (experiment IA_1908_01; see Table 6.2). a) Log₁₀ effective viscosity (dimensionless), b) second invariant of the strain-rate (dimensionless) and c) elevation (km). Compare to* $\dot{E}$ *in Fig. 6.10b,* η_{eff} *in 6.13b and elevation in 6.19d for* n *= 3,* Ar *= 1. See text for discussion.*

6.3.2 Comparison of initial experiments and present day velocity field.

At *t′* = 1 (present day) the velocity direction across the modelled domain is similar for *n* = 1, *Ar* =0 or *n* = 3, *Ar* =1, with or without the presence of the Tarim and Sichuan Basins, with a small increase in the velocity magnitude with *n* (Fig. 6.15 & 6.16). This

suggests crustal flow can be described by a Newtonian or power-law rheology. In the strong India region the velocity vectors follow the prescribed Euler pole, rotating anti-clockwise and producing a net velocity with a north-north-east direction. Within the Asia region the velocity magnitude decays away from the indenting India and changes in velocity direction vary smoothly. The west and central portion of Asia maintain the velocity direction imposed by the India rotation. East of the Tibetan Plateau the velocity directions rotates around to the north-east to east direction, likely a consequence of block movement of Tibet and India. The rotation occurs for $Ar = 0$ and 1 (Fig. 6.15) and suggests the presence of Sundaland enables thin viscous sheet flow in this direction. The buoyancy forces exerted when $Ar = 1$ increase the velocity magnitude, inferring a contribution from topographical gradient induced flow.

Where geodetic velocity data is available (Fig. 6.2 & 6.16) comparison with the model shows similar velocity direction and magnitude changes for the central and western region of Asia. For the Eastern Syntaxis and east of the Tibetan Plateau the north component of the geodetic velocity (Fig. 6.16c & g respectively) is rotated up to ~ 90º relative to the model. The rotation can be attributed to a change from a collision driven by north-west shortening to a buoyancy driven east-west extension of the Tibetan region that started ~ 5 Ma (e.g. Copley and McKenzie, 2007).

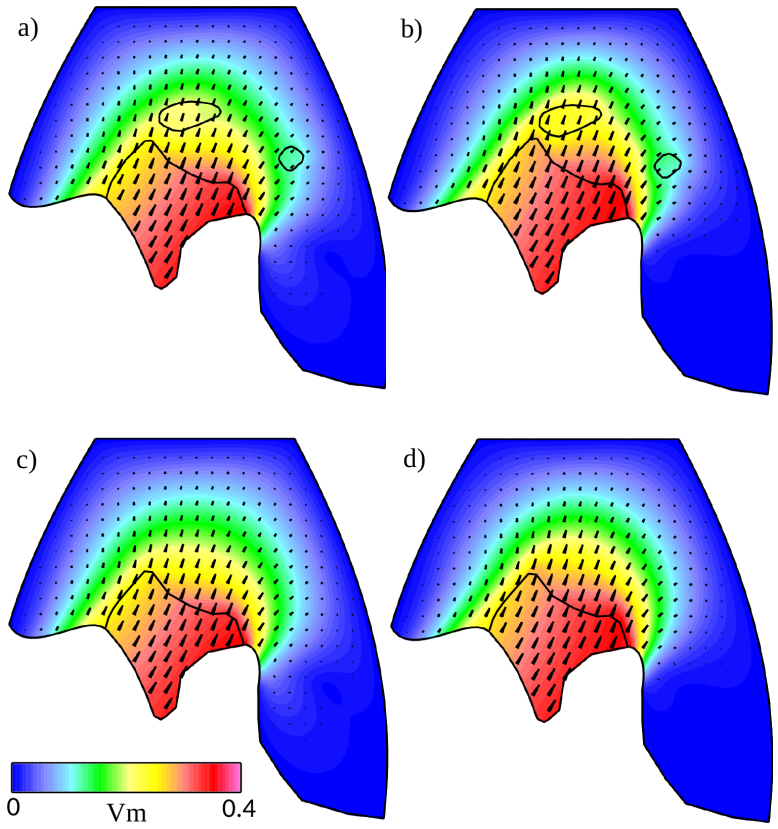

Figure 6.15: India-Asia model run from t′ *= 0 (47 Ma) to* t′ *= 1 (present day) for (a, c)* n *= 1,* Ar *= 0, (b, d)* n *= 3,* Ar *= 1. Contour plots show the dimensionless velocity magnitude and arrows show the velocity direction and relative magnitude. The black lines mark the boundaries between the high-viscosity regions of India and the Tarim and Sichuan Basins, and the low-viscosity region of Asia For (c, d) India is retained and the Tarim and Sichuan Basins are omitted. (a, experiment IA_ref_04; b, experiment IA_ref_08; c, experiment IA_ref_05; b, experiment IA_ref_01; see Table 6.2.)*

England and Houseman (1989) use a thin viscous sheet model to show that the change from a compression to extension dominated regime in the India-Asia convergence is best explained by an increase in gravitational potential energy expected when the lithosphere reaches a critical thickness and experiences accelerated convective heating from the asthenosphere (Houseman et al., 1981). In the thin viscous sheet model *basil* the dynamical effects of convective thinning can be approximated by changing the *Ar*

number locally where the sheet reaches a predetermined thickness. In order to retain a simplified India-Asia reference model I avoid the introduction of an additional variable to the calculations.

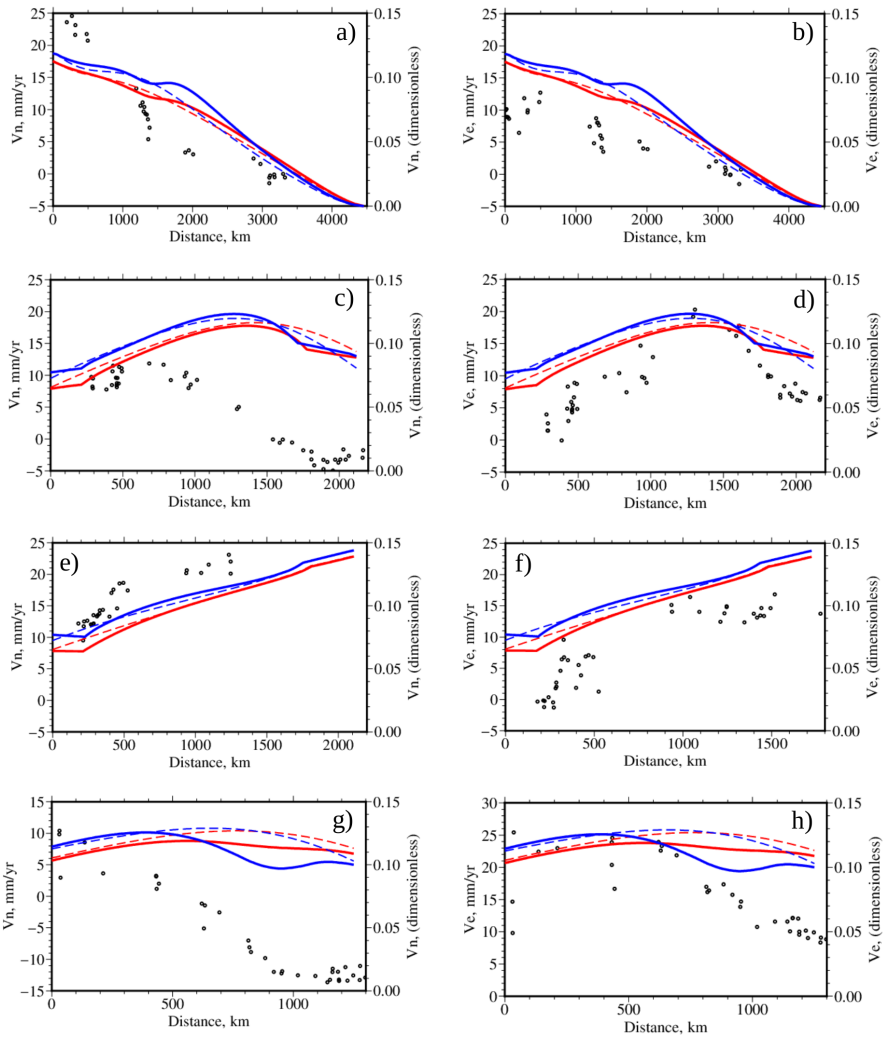

Figure 6.16: North (Vn) and east (Ve) component of the velocity at t′ *= 1 taken from profile locations show in Fig. 6.10. a, b) Profile AA′; c, d) profile BB″; e, f) profile BC″; g, h) profile DD′. Red line,* n *= 1,* Ar *= 0; blue line,* n *= 3,* Ar *=1; solid line, with Tarim and Sichuan basins, dashed line without Tarim and Sichuan Basins. Velocity values for model are dimensionless (right axis). Black circle, present day GPS derived velocity from 50 km wide path along the equivalent profile, values in mm.yr^{-1} (left axis).*

Introduction of an intial topography to the Tibetan Plateau region may result in sufficient bouyancy forces to drive extension without requiring a change in *Ar*. An existing topography of the Plateau prior to continental convergence has been previously suggested (England and Searle, 1986) but in the absence of topography data for Tibet at 47 Ma any initial topography choice for the model would be *ad hoc*.

In an attempt to replicate the present day geodetic velocity I test if the introduction of a low-viscosity region in Sundaland promotes the flow of high elevation into the lower viscosity region (Fig. 6.17). I set VC = 0.5, which for $n = 3$ reduces the viscosity to one-eight that of the remaining Asia region. I set $Ar = 1$ and 5 and apply the same boundary conditions as before. Comparison between this model and the one where the initial viscosity of Asia is uniform at $t' = 1$ show similar velocity magnitudes and directions for $Ar = 1$. For $Ar = 5$ the velocity direction on the east side of the Plateau is rotated ~ 10º clockwise from $Ar = 1$. This suggests the relative strength of Sundaland alone is not a major control on the Tibetan Plateau velocity field, or a considerably weaker lithosphere is required. Combined GPS data show low strain-rate regions immediately north of the Plateau, including the Tarim Basin, and to the south-east of the Plateau, including the Sichuan Basin (Zheng et al., 2017b). These regions may be sufficiently strong to inhibit lithosphere flow outward from the Plateau, focusing deformation towards a less strong Sundaland region. Thus the Sundaland lithosphere may not be weaker than the Tibetan Plateau, but instead weaker than the remaining lithosphere bordering Tibet. Either scenario suggests a greater heterogeneity in the Asian lithosphere than presented in this current set of experiments. Thus I retain the simplest approach with the initial model and assign an initial uniform viscosity across the Asia region that is lower than the regions of India and the Tarim and Sichuan Basins.

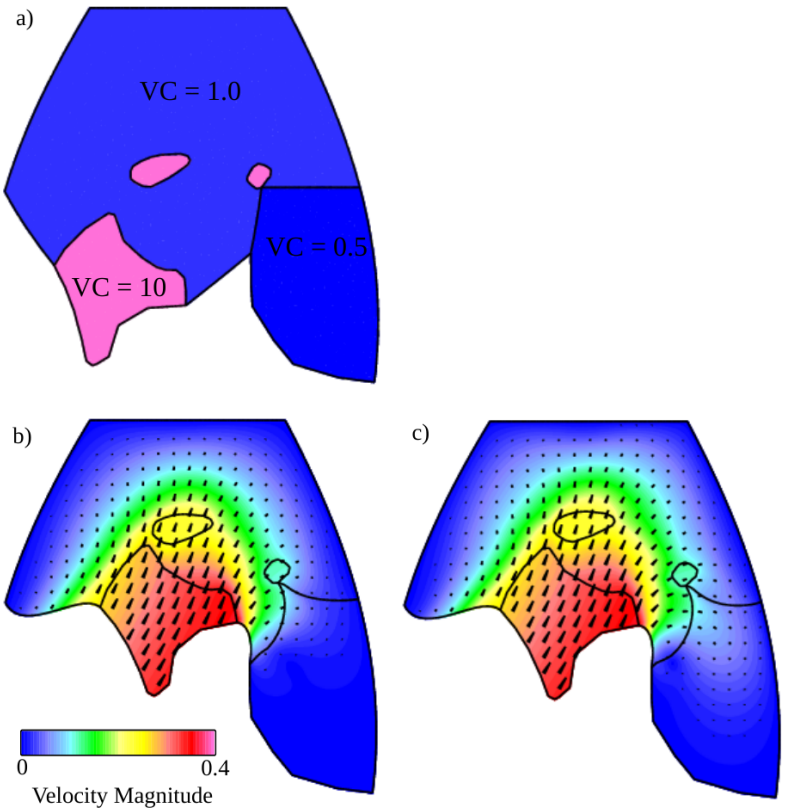

Figure 6.17: a) Initial configuration of the India-Asia model showing the high-viscosity regions of India and the Basins (pink, VC = 10) and a low-viscosity (blue, VC = 0.5) region in the south-east. I set n *= 3 and* Ar *= 1 or 5 and move India from 47 Ma to 0 Ma. b & c) Colour contours and black arrows show the velocity magnitude and direction. The black lines mark the external and internal boundaries.* Ar *= 1 (b) or 5 (c). (b, experiment IA_ws_01; c, experiment IA_ws_02; see Table 6.2.) The weakened Sundaland region does not significantly alter the velocity direction from the model where the initial viscosity of Asia is uniform, but a small clockwise rotation of the vectors on the east side of the Plateau is found when* Ar *= 5.*

In an analogue model of the India-Asia convergence Schellart et al. (2019) show how extension on the Sundaland and east Asia boundary promotes east-west extension in Tibet and eastward continental extrusion, producing a velocity field comparable to present day observations. However, for a thin viscous sheet model any boundary

velocity condition applied to the edge of the sheet will decrease exponentially with distance perpendicular to that boundary (England et al., 1985). For an extensional condition on the east Asia boundary to influence deformation within Tibet, the forces must greatly exceed those arising from an indenting India (England and Houseman, 1989). In contrast the experiments by Schellart et al. (2019) show the total east and Sundaland boundary displacement required (constrained by reconstructions, total extension estimates and seismic tomography) is less than half that of the indenting India. By allowing the eastern boundary to freely deform, instead of applying an extension condition, I found that at $t' = 1$ the velocity magnitude increased west to east across the modelled domain (section 6.2.4). This differs from the present day geodetic velocity in the region of interest. I acknowledge that the static Sundaland and east Asia boundaries as presented in my experiments are a necessary simplification from the limitations of the thin viscous sheet model.

6.3.3 Comparison of initial experiments and present day strain field

In the continental convergence problem the thin viscous sheet approach vertically averages the deviatoric stress and rheological properties. Therefore surface deformation processes that are a result of vertical variation in lithosphere rheology, such as sub-horizontal detachment zones proposed to be active in Tibet (e.g. Royden, 1996), are not specifically represented. Similarly thrust and normal faults are not explicitly shown but may be inferred from changes in sheet thickness, local increases in the 2nd invariant of the strain-rate tensor ($\dot{E}$) and from the ratio of horizontal strain-rates (section 7.6). Development of high strain-rate zones in the model represent depth averaged shear-zone characteristics, such as changes in shear-zone width. Closely spaced individual fault

strands with differing slip-rates that coalesce with depth are indistinguishable for a broader width high strain-rate zone.

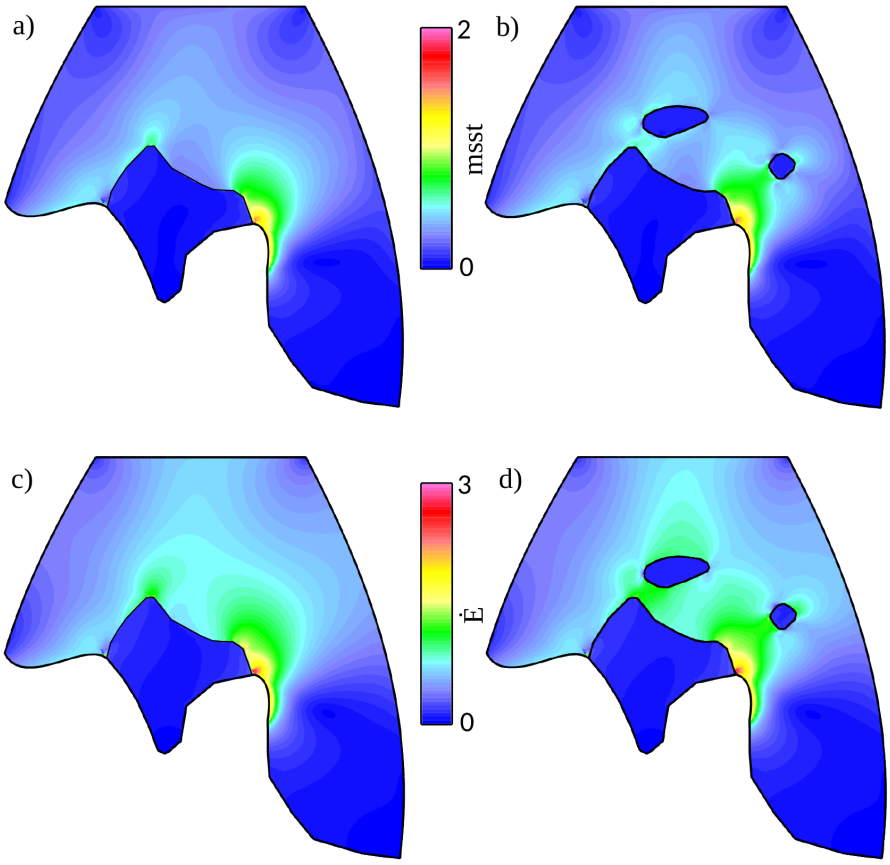

Figure 6.18: Contour plots for msst *(a, b) and* Ė *(c, d) where* n = *1,* Ar = *0. For a & c, Tarim and Sichuan Basins are absent. For b & d, Tarim and Sichuan Basins are present where VC = 10. VC = 1 for Asia, VC = 10 for India. (a & c, experiment IA_ref_01; b & d, experiment IA_ref_04; see Table 6.2.)*

Here I consider the distribution of strain-rate across the model at the present day configuration using two measurements, the 2nd invariant of the strain-rate tensor and the maximum shear strain rate (in the x-y plane). The 2nd invariant of the strain-rate tensor ($\dot{E}$) is a measure of the strain-rate magnitude (Eq. 2.14), where the values are

independent of the orientation of the coordinate system. The maximum shear strain rate (*msst*) is one half the difference of the two horizontal principal strain rates. For the India-Asia problem the *msst* provides an indication of the how much strain is taken up by movement on strike-slip fault systems, as opposed to shortening or extension on dip-slip fault systems. For n = 1 or 3, Ar = 0 or 1, $\dot{E}$ *is* greater than the *msst* values (Figs. 6.18, 6.19, 6.20) due to the movement of India against a fixed Asia region requiring both dip-slip and strike slip styles of deformation (England and Houseman, 1986).

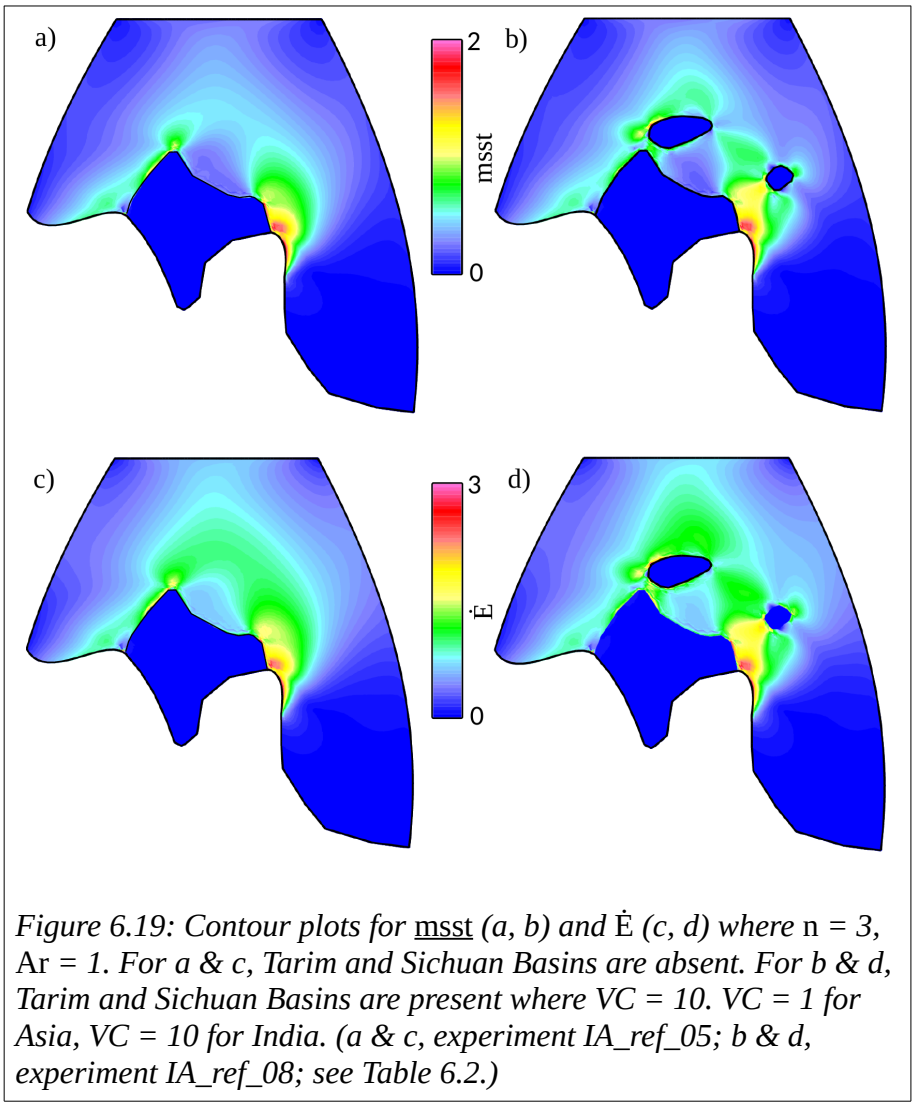

Figure 6.19: Contour plots for msst *(a, b) and* Ė *(c, d) where* n = *3,* Ar = *1. For a & c, Tarim and Sichuan Basins are absent. For b & d, Tarim and Sichuan Basins are present where VC = 10. VC = 1 for Asia, VC = 10 for India. (a & c, experiment IA_ref_05; b & d, experiment IA_ref_08; see Table 6.2.)*

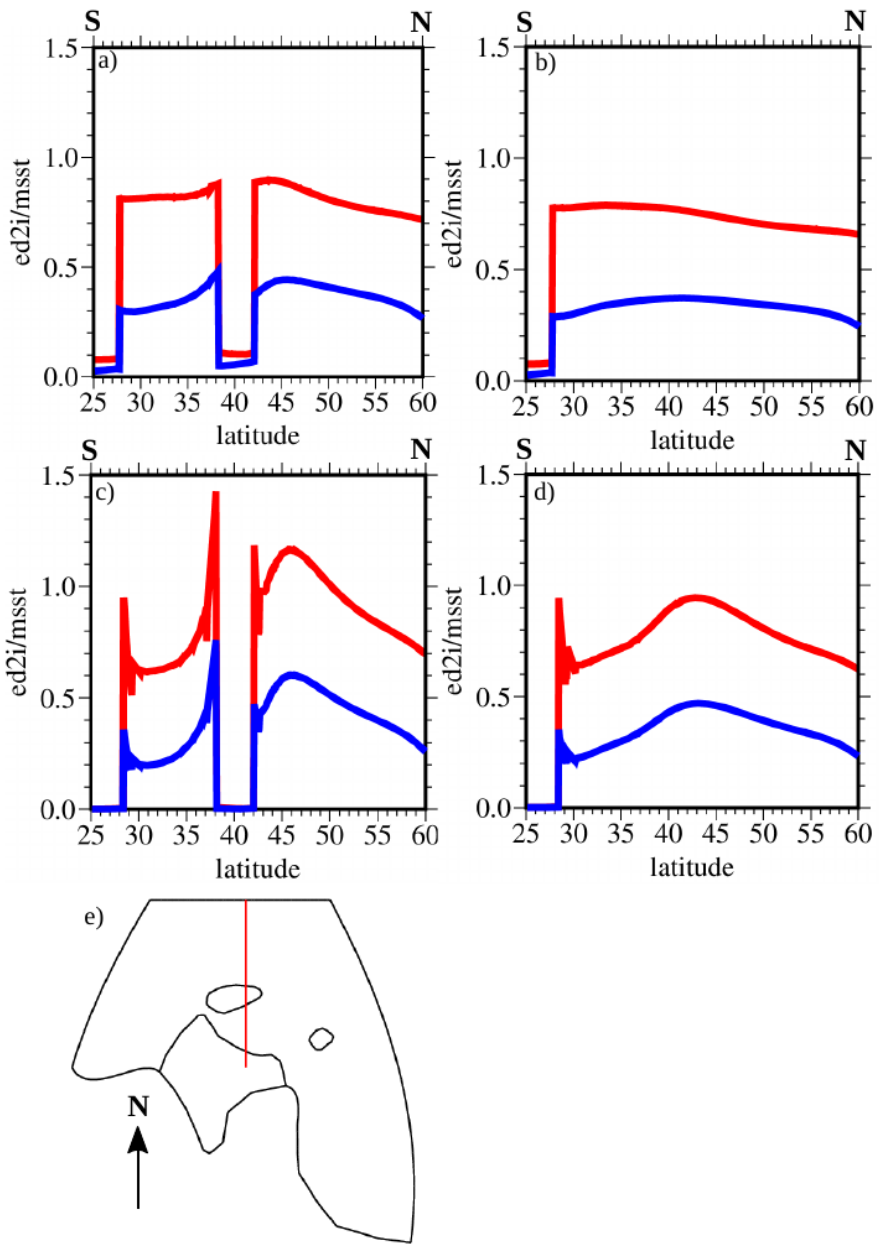

Figure 6.20: Profile of the Ė *(red) and* msst *(blue) at* t′ *= 1 for a)* n *= 1,* Ar *= 0, with Tarim and Sichuan Basins; b)* n *= 1,* Ar *= 0, without Tarim and Sichuan Basins; c)* n *= 3,* Ar *= 1, with Tarim and Sichuan Basins; d)* n *= 3,* Ar *= 1, without Tarim and Sichuan Basins. e) location of the profile line.*

Rotation of India about the Euler pole results in a convergence rate increasing eastward in north-east India (Fig. 6.15) and consequently the highest strain-rates (and hence

lowest viscosities) occur in the region of Tibet adjacent to this boundary. The strong regions (India, Tarim and Sichuan Basins) resist deformation, and strain is preferentially accommodated outside of these strong regions. The strength contrasts focus strain at the boundaries and the strain-rate is higher in the low-viscosity region (Asia) (Figs. 6.18, 6.19). Profiles of $\dot{E}$ and *msst* show that for $n = 3$, $Ar = 1$ relatively narrow zones of high strain-rate develop adjacent to the strong regions, analogous to the Altyn Tagh and Longmen Shan fault systems (Fig. 6.20). For $n = 1$, $Ar = 0$ the variation in strain-rate in the deforming regions is less, i.e. there is a less abrupt change of strain-rate between strong and surrounding weak regions. The changes in effective viscosity cause the zones of high strain-rate. Where the stress difference is:

$$\partial \tau_{ij} = B \dot{\varepsilon}_{ij}^{1/n} \qquad \text{Eq. (6.2)}$$

and B is abruptly increased by a factor Λ then for the stress to remain balanced the strain-rate must decrease by Λ^n.

Where the strong basin regions are absent the strain-rate decreases away from the north India boundary (Himalayan Front) (Fig. 6.20b & d). For $n = 3$, $Ar = 1$ an arc of higher strain rate develops north of the Tibet Plateau (Fig. 6.19d). This is a consequence of the buoyancy forces generated by the increased topography. Consequently when $Ar > 0$ a local increase in gravitational potential energy produces horizontal gradients of stress that resist further thickening.

Geodetically derived strain-rates show linear regions of high strain across the Tibetan Plateau (Fig. 6.1), This contrasts to my experiments where, for $n = 3$, similar high strain

regions are limited to the boundaries of high-viscosity regions (Fig. 6.20). In Chapter Three I demonstrated how strain can localise away from the boundary of a viscosity contrast, where an initial difference in effective viscosity promotes spatial variations in the work done by deformation. This strongly suggests that effective viscosity variations must exist or develop within the proto-Tibetan Plateau during the India-Asia convergence. Such variations may arise from composition, temperature, topography and other factors (see section 3.1). That present day linear regions of high strain extend across the Plateau further suggests that a strain-weakening process (see section 1.5, 3.5) is required to develop strain localisation beyond an immediate effective viscosity contrast.

Given the geological unlikeness of a uniform viscosity across the proto-Tibetain Plateau, and for the model to retain the prescribed boundary conditions and initiate strain-localisation across the Plateau, I will require an initial spatial heterogeneity (section 3.1). Uncertainty in the small scale thermal and topographical evolution of the Plateau means any spatial choice of high- or low-viscosity contrast is ad hoc. Prescribing strength contrasts across the developing Plateau based on present day shear-zones does not permit an exploration of how such shear zones may arise. I maintain a simplified approach and in Chapter Seven I use the India-Asia model developed in this chapter and, following on from Chapter Three and Four, introduce a low viscosity region to observe the temporal and spatial influence on strain.

6.4 Summary of India-Asia model development

The aim of this chapter has been to develop an initial model for the India-Asia collision which I can then use to investigate the conditions required to develop localised shear zones across the Tibetan Plateau. These experiments assume an initial uniform crustal thickness of 30 km. A strong India is rotated about a single Euler pole from its position 47 Ma ($t' = 0$) to that of the present day ($t' = 1$) into a weaker Asia domain.

The topography, velocity and strain-rate fields in the experiments at $t' = 1$ are broadly comparable with present day geographical and geodetic measurements. The present day average elevation of the Tibetan Plateau is ~ 5,400 m. For the experiments $n = 3$, $Ar = 1$ and $n = 1$, $Ar = 0$ the average elevation is ~ 4,500 and 3,000 m respectively, suggesting the former rheology better represents the topography growth. The high elevations at the modelled Himalayan Syntaxes, up to 9,600 for $n = 3$, $Ar = 1$ and 7,000 for $n = 1$, $Ar = 0$, would ordinarily be removed by erosion processes, which I omit from these experiments. Subsequent deposition of material would contribute to Plateau topography, and may, together with isostatic rebound from delamination of the lithosphere, account for some of the difference between the present day and $t' = 1$ elevations. The average elevation of < 500 m at $t' = 1$ for the modelled the Tarim and Sichuan Basins is less than the present day (3,100 and 1,700 m respectively). Again, sediment deposition and isostatic rebound processes may account for some of the difference.

Comparison of the dimensionless modelled velocities at $t' = 1$ with present day GPS derived velocities shows comparable directions and changes in magnitude across west and central Tibet for $n = 3$, $Ar = 1$ and $n = 1$, $Ar = 0$. South-east Tibet and east of the

Tibetan Plateau the GPS derived velocity is rotated up to 90 degrees from that of the model at $t' = 1$. The velocity may be modified by imposing an extensional regime through either convective thinning or setting an initial topography on the proto-Tibetan Plateau, but I omit such processes in order to maintain a simplified model.

For $n = 3$, $Ar = 1$ and $n = 1$, $Ar = 0$ high-strain regions develop with time adjacent to India and, where included, the Tarim and Sichuan Basins. For $n = 3$, $Ar = 1$ narrow regions of high strain-rate develop with time adjacent to the Basins, analogous to the Altyn Tagh and Longmenshan faults. The Global Strain Model shows linear regions of high strain across the Tibetan Plateau. Initiation of these requires a spatial heterogeneity. In Chapter Seven I use the geometry and boundary conditions developed here for $n = 3$, $Ar = 1$ to explore the initiation and development of strain localisation across the Tibetan Plateau.

7 Application of the India-Asia model to determine controls on strain localisation across the Tibetan Plateau

7.1 Introduction

7.1.1 Controls on strain localisation development and purpose of this study

The Tibetan Plateau is an elevated region (~ 2,500,000 km^2) that has formed as a consequence of the ongoing India-Asia convergence, whose onset was ~ 47 Ma (Meng et al., 2012). Strain is distributed across the region (Kreemer et al., 2014) but in some areas localises to form shear zones that extend 100s kms, e.g. Altyn Tagh Fault (~ 1,800 km) and Kunlun Fault (~ 1,500 km) (Fig. 1.3). Thin viscous sheet models of the India-Asia convergence have yet to show how such shear zones might develop across the Tibetan Plateau. Can localised deformation develop within a generally diffuse deformation field?

As a general approach Montési and Zuber (2002) define three ways in which strain localisation can occur. Firstly, through inherited properties, e.g. a strong India and basin regions. Secondly through dynamic localisation, where deformation rates are higher in regions already subject to deformation, that is the rheological properties of the medium evolve with increasing strain. Such behaviour has incorporated in my previous models (Chapters Two, Six) through strain-rate weakening, determined through the strain exponent n (see Eq. 2.14) and through strain-weakening, using the parameter Γ (Eq. 2.20). Montési & Zuber name the third method as imposed localisation which occurs when a homogenous medium has a heterogeneous boundary condition. This may involve differences in the way the boundary moves or is shaped, but ultimately results

in stress concentrations where boundary conditions change rapidly. Stress concentrations due to sudden changes in geometry have been well studied in material science, where such regions are referred to as stress risers. For example, a more uniform stress field in overlapping joins of a material can be induced by rounding the corner, reducing the chance of failure (e.g. Adams and Harris, 1987) or crack propagation may be arrested by the introduction of large holes at the crack tips (e.g. Domazet, 1996; Makabe et al., 2009; Song and Shieh, 2004). In geodynamical models, internal boundaries may be smoothed to minimise such stress concentrations, as per the circular weak region in my shear box model (section 3.2).

In models of the India-Asia convergence the geometry of the indenter (India) controls the morphology of strike-slip faults. Tapponnier and Molnar (1976) and Dayem et al., (2009) found that changing the orientation of the strong region relative to the convergence vector, effectively changing the geometry, influenced the development of a shear zone against it. In the India-Asia model I developed in Chapter Six, the protrusion of the relatively strong India that occurs in the Western Himalaya Syntaxis acts as a significant geometric boundary change and therefore concentrates stress in this region.

While thin viscous sheet models of the India-Asia convergence have shown how shear-zones develop adjacent to a rheologically strong region the development of shear-zones within the Plateau has not been adequately explored. While some prior work assumes that major shear zones are a result of inherited structure, such as former suture zones (e.g. Tapponnier et al., 2001), here I investigate if such shear zones can naturally arise in circumstances where the medium is initially near homogeneous. In Chapter Three, I demonstrated how linear regions of high strain could develop adjacent and away from a

low viscosity inclusion embedded in an otherwise homogenous region subject to simple-shear.

In this Chapter I use a thin viscous sheet model to examine how strain distribution within Tibet during the India-Asia convergence may be influenced by:

a) the presence of a low viscosity region (with potential for inherited localisation);
b) the shape of the indenting boundary, specifically the presence of the Himalayan syntaxes (with potential for imposed localisation).

In doing so I demonstrate how a continuum lithosphere can initiate and maintain localised shear zones across the centre of the Tibetan Plateau, as observed in present day geodetic data. In a wider context this study provides knowledge on how, in a continental collision scenario, the shape of a strong indenter and the presence of spatial heterogeneities can influence strain distribution within the indented region.

7.1.2 Overview of modelling approach

In Chapter Six I developed an initial model configured to approximately represent the India-Asia convergence from onset of collision (~ 47 Ma) through to the present day (Fig. 6.9c). This model contains strong India, Tarim Basin and Sichuan Basin regions within a weaker Asia region, the co-ordinates being defined on a spherical shell. All models are run in the finite element program, *basil*, for which the governing equations are summarised in Chapter Two. India is initially set at the co-ordinates of 47 Ma, the onset of convergence, and then rotated forward in time at a constant rate, around a fixed Euler pole defined by the India-Eurasia pole of DeMets et al. (2010), (31.7° N, 17.3° E, 0.477 deg.Myr^{-1}) to its present day position.

Using the model described in Chapter Six I examine how initial spatial variation in rheological parameters influences the localisation process and consider the contribution of the indenting boundary geometry and presence of the Basins to strain distribution. I introduce an initial circular weak region within the Tibetan Plateau and vary the strain-weakening coefficient (Γ) in the governing equations. I observe the spatial and temporal variation in strain as the deformation is integrated forward in time. For the rheological parameters that promote strain localisation I consider the contribution of the indenting boundary. I modify the Himalayan Front geometry (the north boundary of India), repeat the experiments and compare how the spatial and temporal variation in strain differs between the initial and modified Himalayan Front geometry.

Table 7.1: Comparison of dimensionless time and dimensional age used for the models described in this chapter.

t' (dimensionless)	Ma	t' (dimensionless)	Ma
0	47	0.6	18.8
0.1	42.3	0.7	14.1
0.2	37.6	0.8	9.4
0.3	32.9	0.9	4.7
0.4	28.2	1.0	0
0.5	23.5		

For consistency with the non-dimensional values used in *basil* I non-dimensionalise time. At $t' = 0$ the India is rotated back to its nominal position at 47 Ma. Following integration to dimensionless time $t' = 1$, India has undergone 22.4º rotation and is at its present day location relative to Eurasia. To facilitate interpretation of the dimensionless

calculations a comparison of the non-dimensional and dimensional age are presented in Table 7.1.

7.2 Location of a weak region within the Tibetan Plateau

I explore the rheological parameters and geometric configuration that promotes strain localisation across the Tibetan Plateau using a model which incorporates regions of major strength contrasts (India, Tarim and Sichuan Basins) and rotates India around an Euler pole from onset of collision (47 Ma) to the present day. To initiate strain localisation within the Tibetan Plateau region I require some sort of heterogeneity. Following the example of the simple-shear box experiments (Chapter Three) I use a single circular region whose initial viscosity coefficient is set lower than the surrounding region by a fixed ratio. Due to the spherical co-ordinates used to define the India-Asia region the co-ordinates of this circular region are calculated as follows. I define the centre of the circle as (φ_0, θ'_0) , where φ is the longitude and θ' the latitude. For a radius, Δ, I calculate the points on the circle periphery (φ_1, θ'_1) :

$$\sin\theta'_1 = \sin\theta'_0 \cos\Delta + \cos\theta'_0 \sin\Delta \cos Az \qquad \text{Eq. (7.1)}$$

where *Az* is the azimuth (angular measurement) of (φ_1, θ'_1) from (φ_0, θ'_0) with a value defined by *N* equally separated values between 0 and π, and:

$$\varphi_1 = \varphi_0 \pm \cos^{-1}\left[\frac{\cos\Delta - \sin\theta'_1 \sin\theta'_0}{\cos\theta'_1 \cos\theta'_0}\right] \qquad \text{Eq. (7.2)}$$

where the +/- is used for $\varphi_1 > \varphi_0$ or $\varphi_1 < \varphi_0$.

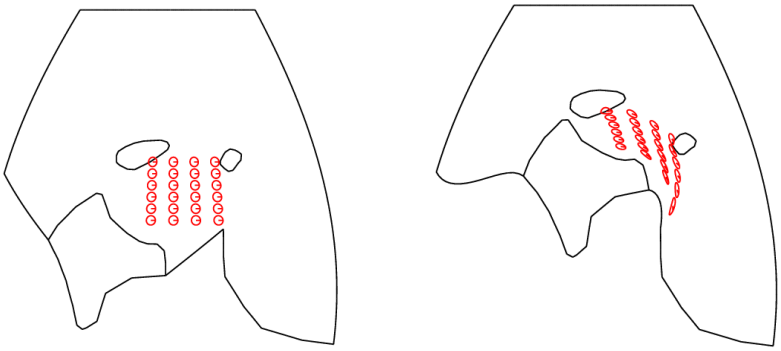

Figure 7.1: Model boundaries and internal regions shown in black, as per the initial model developed in Chapter Six (Fig. 6.9). The strain ellipse markers (red) are passive tracers added that have no dynamic effect, but allow easier visualisation of the deformation. a) At t′ *= 0 (47 Ma), b)* t′ *= 1 (present day). Deformation of the strain ellipse markers show the maximum deformation in the Tibetan Plateau region occurs between the Eastern Syntaxis and the Sichuan Basin.*

The initial model defined in Chapter Six (Fig. 6.9d) covers a large region extending from 45º E to 120º E, and 11.5º S to 60º N. An additional weak region should be small in comparison with the developing Tibetan Plateau region, but not so small that defining it requires a high mesh resolution and results in an unreasonably high computational times. An initial test shows that for a weak region with radius (Δ) ≤ 1º a relatively high mesh resolution is required to define the circle curvature. For Δ = 2º the curvature can be defined with a mesh resolution that minimises computational time. The dimensions of the heterogeneity are arguably arbitrary as it is not representing a specific geographic feature.

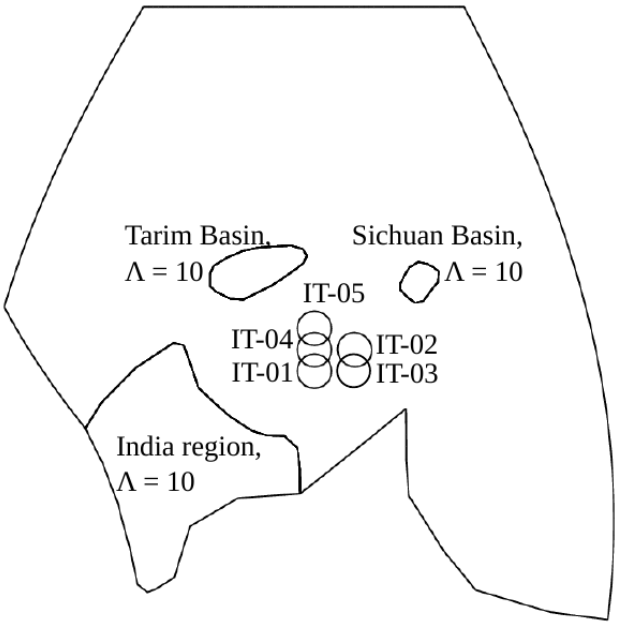

Figure 7.2: India-Asia at t′ *= 0 (47 Ma) for experiments IT-0X showing five different initial positions of the low-viscosity region, defined to have a radius of 2 degrees of latitude, and relative viscosity coefficient (Λ) = 0.5. Co-ordinates for each weak region are given in Table 7.2. Each experiment included only one of the weak regions.*

Table 7.2: Location of tested weak regions. Here n *= 1,* Ar *= 1,* Γ *= 0.5 in all experiments,*

Experiment	**Start lat**	**Start lon**	**Notes**
IT-01	17.5ºN	85ºE	Distortion of the finite element mesh terminates calculations prior to $t' = 1$. (IT-01, $t' = 89$; IT-02, $t' = 0.91$).
IT-02	20ºN	90ºE	
IT-03	17.5ºN	90ºE	At $t' = 1$ the weak region is outside of the Tibetan Plateau.
IT-04	20ºN	85ºE	Calculation completes at $t' = 1$.
IT-05	22.5ºN	85ºE	Calculation completes at $t' = 1$.

Using the initial model at $t' = 1$ (Fig. 6.9d) I identify high strain areas within the Tibetan Plateau region away from the strong regions (Fig. 7.1). In Chapter Three I demonstrated

how strain localisation adjacent to a weak region increases with total strain (section 3.3). Thus to maximise the potential for strain localisation I select five possible locations within the region of highest strain to include a weak region in this model at t' = 0 (47 Ma) (Table 7.2). When integrated forward in time a single weak region may enhance strain rates in the high strain areas such that strain localisation occurs (Fig. 7.2). The ratio of the initial strength of the weak region to that background is given by Λ. Having previously established from the simple-shear box models that a weak inclusion ($\Lambda < 1$) requires $n > 1$ and $\Gamma > 0$ for strain localisation to occur (section 3.3), I initially set $\Lambda = 0.5$ and $\Gamma = 0.5$. Here Γ is set at a value sufficiently high to initiate shear-zone formation, but sufficiently low to prevent excessive mesh distortion by $t' = 1$; Λ is set to a value that permits the weak region to deform but high enough to discourage it from collapsing to a plane by $t' = 1$. I retain the values of $n = 3$ and $Ar = 1$ along with initial and boundary conditions from the initial model (Fig. 6.9).

In an initial test I vary the initial location of a single circular weak region (Table 7.2) and integrate forward in time, keeping all other parameters fixed. The weak region in experiments IT-01 and IT-02 causes sufficient mesh distortion between India and the Sichuan Basin that the calculation is terminated before India reaches the present day position. Experiments IT-03, IT-04 and IT-05 see India restored to the present day position, but for experiment IT-03 the rotation of India into Asia causes the final position of the weak region to be outside of the Tibetan Plateau. In experiments IT-04 and IT-05 minor differences in strain distribution are observed (Fig. 7.3). In the next set of experiments I use model IT-05 (Fig. 7.4) to explore how varying a strain-weakening component influences the temporal and spatial variation of strain.

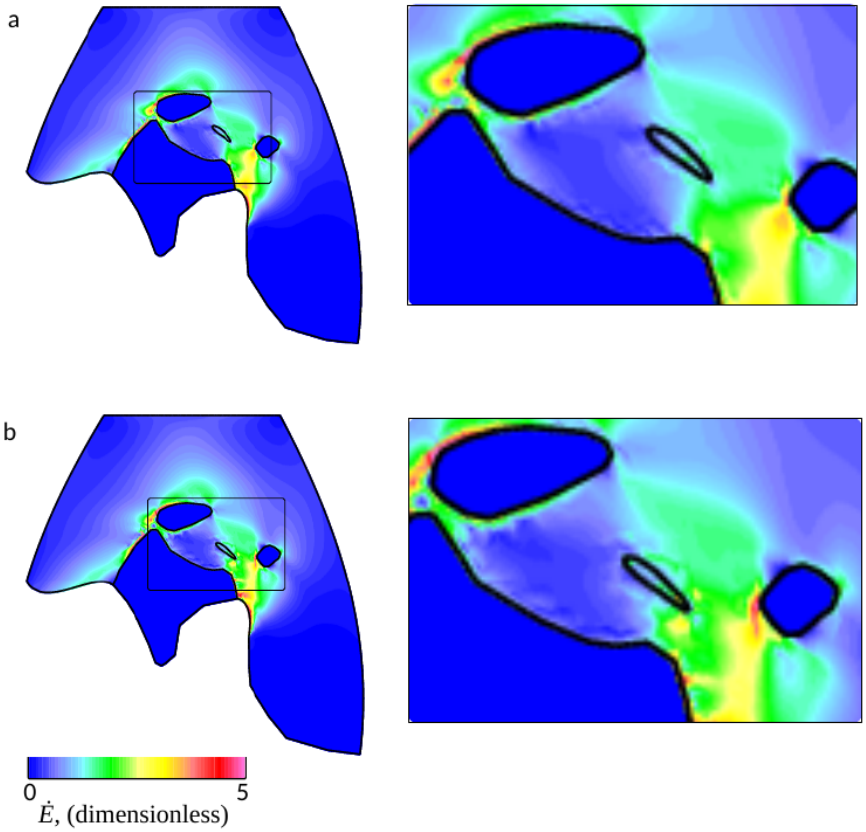

Figure 7.3: Colour contour plots of the dimensionless second invariant of the strain-rate, Ė, *at* t′ *= 1. India has rotated from the initial position at* t′ *= 0 (47 Ma) to the present day position. The weak region is initially circular and the initial location is given in Table 7.2 where a) model IT-05, b) model IT-04;* n *= 3,* Ar *= 1 and* Γ *= 0.5 for both experiments. With increased time the weak region deforms and becomes elliptical, and regions of increased strain develop in and around it. The differences in distribution of strain between a and b are minor, but for model IT-01 and IT-02 (not shown here) high mesh distortion terminates the model prior to* t′ *= 1. Given that the only variable is the initial position of the weak region, the differences in distribution of strain between models IT-01 to 05 suggest that the initial location of the weak region influences the development of strain-rates with time.*

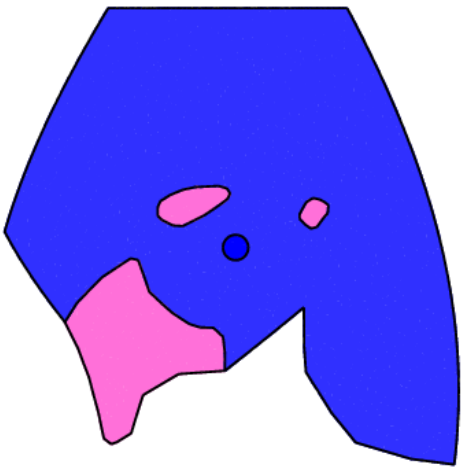

Figure 7.4: The configuration at t′ *= 0 for the next set of experiments in which I explore how varying a strain-weakening component influences the temporal and spatial variation of strain. Here I use the boundaries and boundary conditions defined in Chapter Six (Fig. 6.9) with the addition of a weak region initially located as per model IT-05 (Table 7.2). I set the initial strength of India and the Basins is set to* $\Lambda = 10$ *and that of the weak region is* $\Lambda = 0.5$.

7.3 Mesh dependency check

In order to determine if the discretization of the model with a weak region is adequately resolved I use the initial geometry shown in Fig. 7.4 and repeat the calculation for varying number of elements. I test for a finite element size 0.3, 0.5, 1.0, 1.5 and 2.0 (relative values), for which the number of elements is 22547, 13594, 6801, 4556 and 3425. Using two profiles across the model (Fig. 7.5a) at $t' = 1$ I measure the x- and y-components of the velocity, and at $t' = 0$ and 1 I measure the second invariant of the strain-rate ($\dot{E}$) and compare the results (Fig. 7.5c to j). With increasing mesh resolution the time to calculate to $t' = 1$ increases (Fig. 7.5b).

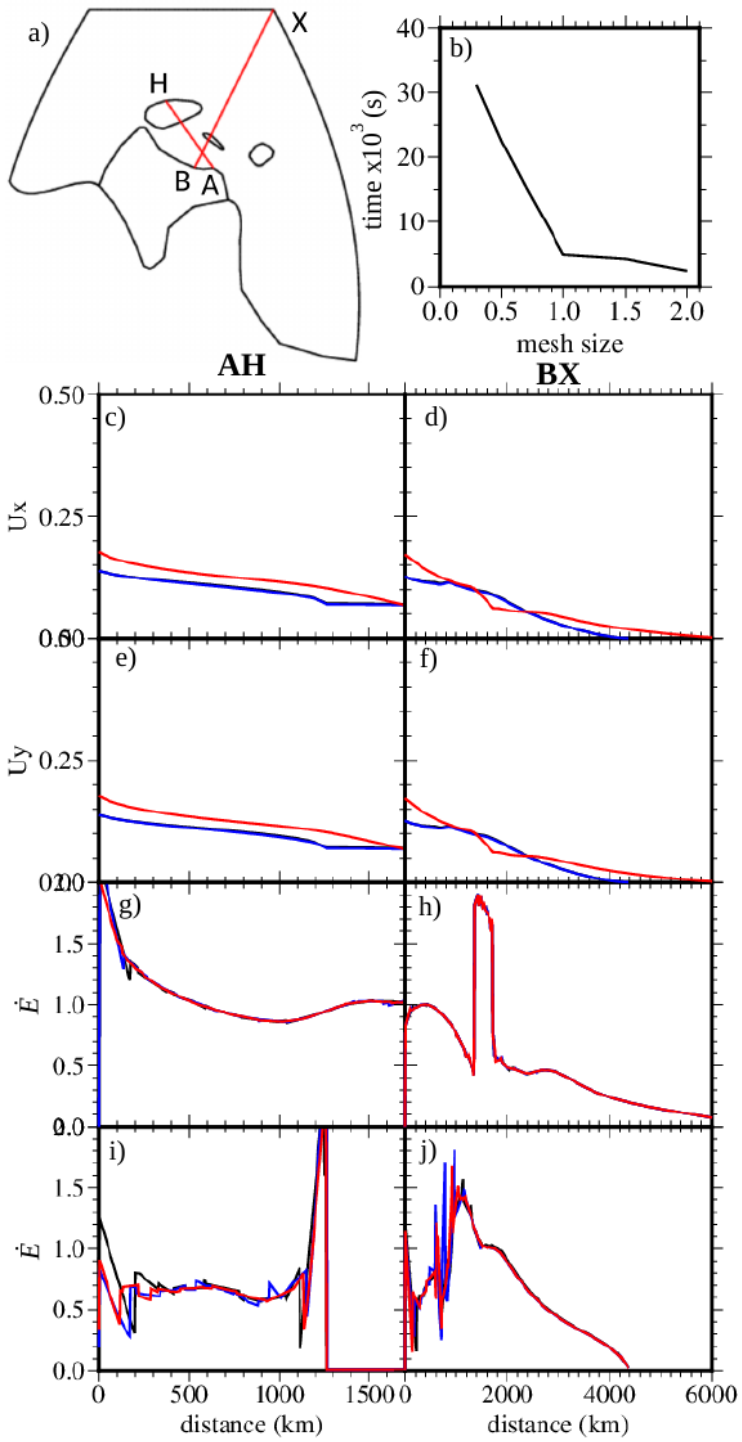

Figure 7.5: a) Location of profiles AH and BX along which Ė *is measured for d to j, using the model with weak region:* n = *3*, Ar *=1*, Γ *=0.5 (IA_iG_03). Caption continued on next page.*

cont.

The same A, H, B and X markers are used for the profiles at t′ *= 0. The calculation step size was set to 1/100 and the remesh command was active. b) mesh size vs. time for calculation to reach* t′ *= 1. c to j) for AH (left column) and BX profiles (right column); c, d) x-component and e, f) y-component of horizontal velocity at* t′ *= 1; g, h)* Ė *at* t′ *= 0; I, j)* Ė *at* t′ *= 1. Mesh sizes shown are 0.7 (black line), 0.5 (blue line) and 0.3 (red line). Where only red and blue lines are visible, mesh size 0.7 has the same results as 0.5. Mesh size 1.5 and 2.0 are omitted for clarity, the results are similar to those shown here but changes at the boundary of viscosity changes are less well resolved. Each profile line plotted comprises of 501 individual data points.*

At $t' = 0$, prior to any integration, $\dot{E}$ is near identical for the different mesh resolutions. At $t' = 1$ the velocity components, which examine the integration in time without the spatial differential, are also near identical. For $\dot{E}$ at $t' = 1$ the longer wavelength is well resolved across all tested mesh resolutions, but the noise increases at the boundary of abrupt viscosity changes.

Overall on the scale of interest there are no major difference in the strain profiles between the different finite element sizes, but an element size < 1.0 would be beneficial for examining high strain regions. Therefore as a compromise between processing time and the level of detail required for future models I set the finite element size to 0.7.

7.4 Influence of changing the strain-weakening parameter, Γ, on Tibetan Plateau shear-zone development

7.4.1 India-Asia model configuration

The simple-shear box experiments (Chapter Three) show that strain-weakening ($\Gamma > 0$) is required in order for shear zone localisation, and the minimum value of Γ is dependent on the value of the strain-rate vs stress exponent, n. I choose here to explore how varying Γ influences shear-zone development in this context of the Indian-Asian continental collision. By maintaining a simply parameterised representation of strain-weakening I avoid the complications that can arise from more complex models. In the experiments that follow, I retain $n = 3$ from the model developed in Chapter Six and include the effect of buoyancy forces acting on crustal thickness variations by setting the Argand number to $Ar = 1$ (Eq. 2.64) and ignore thermal diffusion, $\beta = 0$ (Eq. 2.53). While the box model described in Chapter Three allowed for the evolution of Γ due to temperature changes ($T_{ref} > 0$), here I simplify my approach, averaging the depth dependent properties and consider only a constant value of Γ'. (For ease of reading I omit the prime throughout this chapter, Γ is dimensionless.) Using the model configuration established in section 7.2 (Fig. 7.4) I set Γ to values between 0 and 5.0 and observe the developing strain in the Tibetan Plateau. To assess the contribution of viscous and buoyancy forces I repeat some experiments setting $Ar = 0$. To assess how the weak region influences deformation when $\Gamma > 0.5$, I repeat some experiments without the weak region. A summary of the parameters used in the experiments is presented in Table 7.3).

To compare results in the model I track the movement of selected markers with time. I measure changes in the second invariant of the strain tensor, $\dot{E}$, between pairs of markers (Fig. 7.6). From the profiles between these points regions of localised strain-rate can be identified from peaks on the profiles.

Table 7.3: Summary of experiments and parameters. Where included the viscosity coefficient of the weak region (Λ) = 0.5. For all experiments n = *3. Termination of the calculation prior to* t′ = *1 is due to the distortion of the finite element mesh.*

Number	**Γ**	**Ar**	**Weak region?**	**Comment**
IA_iG_00	0	1	Yes	Completes to $t' = 1$
IA_iG_03	0.5	1	Yes	Completes to $t' = 1$
IA_iG_05	1	1	Yes	Terminates at $t' = 0.895$
IA_iG_06	2	1	Yes	Terminates at $t' = 0.610$
IA_iG_07	3	1	Yes	Terminates at $t' = 0.495$
IA_iG_08	5	1	Yes	Terminates at $t' = 0.243$
IA_A0_06	2	0	Yes	Terminates at $t' = 0.283$
IA_A0_07	3	0	Yes	Terminates at $t' = 0.217$
IA_NI_07	3	1	No	Terminates at $t' = 0.54$
IA_NI_08	5	1	No	Terminates at $t' = 0.3$

7.4.2 Results from varying Γ in the India-Asia model

The development of high strain-rate regions with time in the Tibetan Plateau occurs at the Tarim Basin boundary, within and around the weak region to an area extending down to the west side of Sichuan Basin and adjacent to the Himalayan syntaxes (Fig. 7.6). In general at a given time, increasing Γ increases localisation adjacent to the Tarim Basin and in the high-strain region across the Plateau. Where $\Gamma \geq 1$, high strain-rates distort the finite element mesh and terminate the calculations prior to $t' = 1$.

For all tested values of $\Gamma > 0$, $Ar = 1$ the strain localises over a relatively narrow (< 100 km) region against the southern side of Tarim Basin, corresponding to the Altyn Tagh

Fault system but henceforth referred to as the South Tarim Shear Zone (Fig. 7.6). Measurements of the South Tarim Shear Zone, obtained from measuring $\dot{E}$ along the AH profile of Fig. 7.7, show for $\Gamma \leq 3$ the width decreases with time but for $\Gamma > 3$ the width initially decreases and then increases with time with the development of a shear zone across the Plateau (Fig. 7.7).

From the same AH profile it can be seen that the temporal evolution of the topography and maximum $\dot{E}$ in the South Tarim Shear Zone correlate (Fig. 7.7). For $\Gamma = 0$ to 3 the maximum $\dot{E}$ (and elevation) in the South Tarim Shear Zone increases with time, and at a given time $\dot{E}$ (and elevation) is greater for a higher value of Γ, e.g. at $t' = 1$ (or the last calculated time step where high mesh distortion terminates the calculation) $\dot{E} = 1.7$, 2.4, 4.2 and 5.9 for $\Gamma = 0$, 0.5, 1.0 and 2.0 respectively. For $\Gamma = 3$ the same increase of maximum $\dot{E}$ (and elevation) with time is observed and when the calculation terminates at $t' = 0.5$, $\dot{E} = 1.7$. However, for $\Gamma = 5$ the temporal development of the maximum $\dot{E}$ in the south Tarim shear-zone differs. Initially the strain-rate increases with time but then it decreases. The decrease in $\dot{E}$ (and elevation) corresponds with an increase in strain-rate on a shear zone that crosses the centre of the Plateau (Fig. 7.7).

To determine if the weak region is influencing the localisation on the South Tarim Shear Zone I repeat the experiment for $\Gamma = 3$ and 5 (experiments IA_NI_06, 07; Table 7.3), but omit the weak region (Fig. 7.8). Using the same AH profile co-ordinates as before I examine the maximum $\dot{E}$ and width of the high strain region adjacent to the Tarim basin at each time step. I find changes in the South Tarim Shear Zone width with time follows similar trends with or without the weak region present, but any given time step the width is less when the weak region is present.

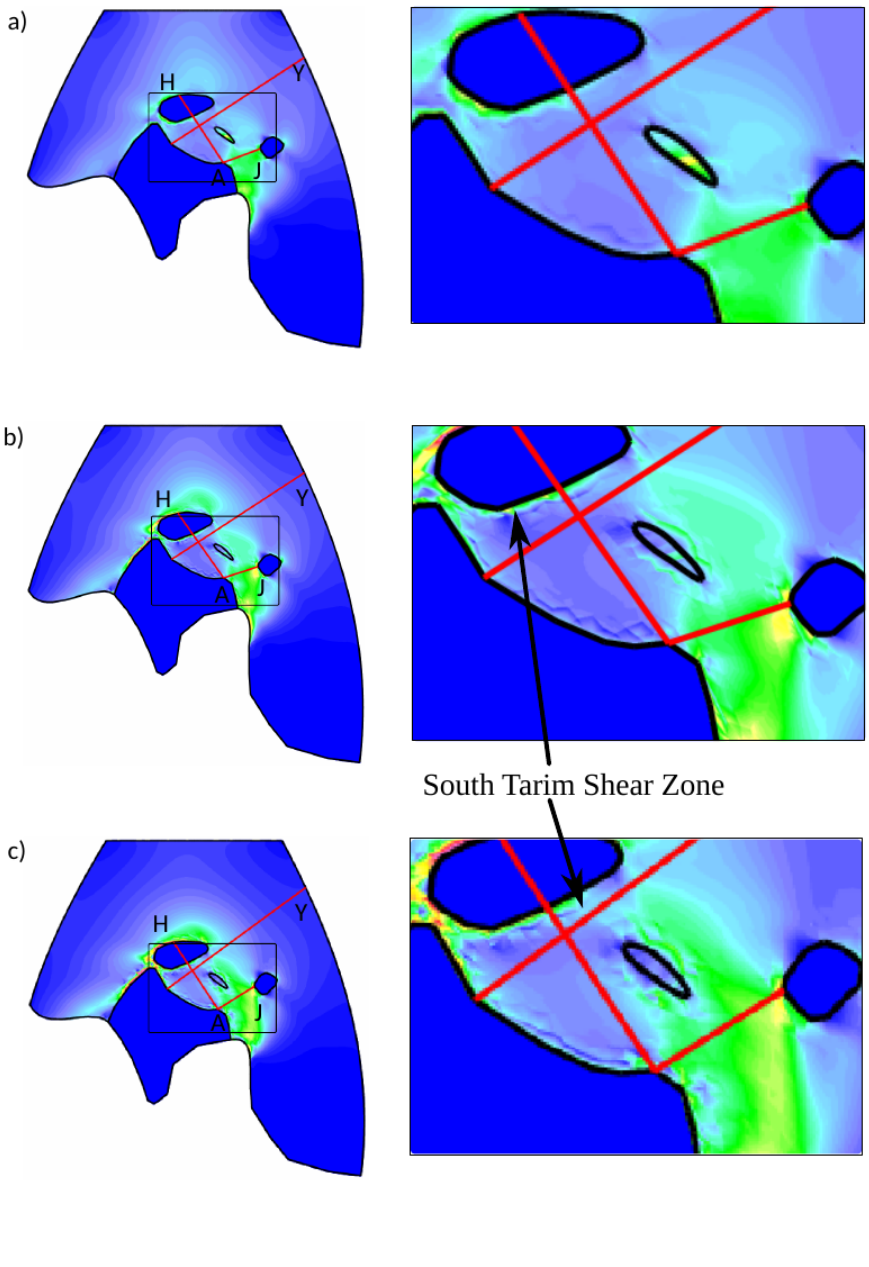

Figure 7.6: continued on next page

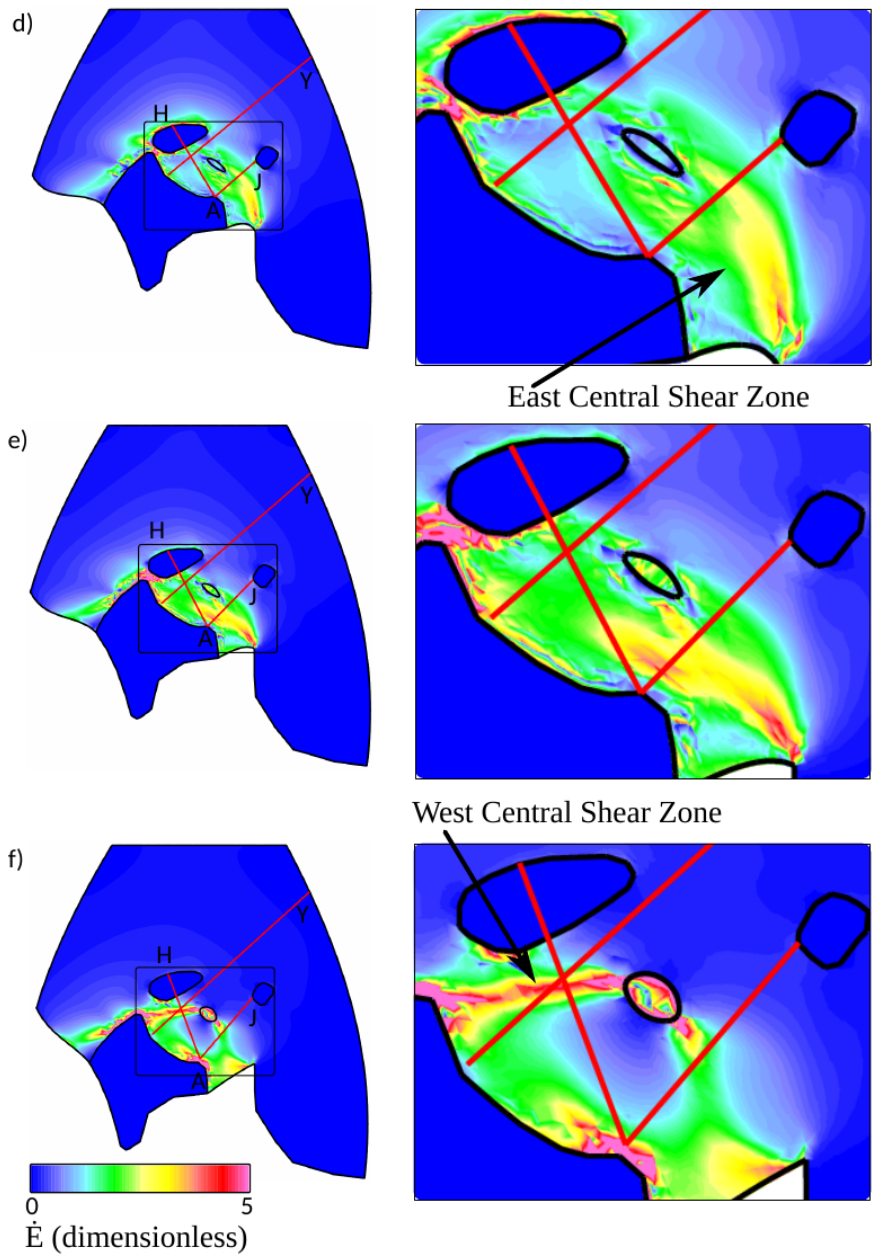

Figure 7.6: For Ar *= 1, with weak region (experiments IA_iG_XX). Colour contour plots of* Ė *for: a)* Γ *= 0 at* t′ *=1; b)* Γ *= 0.5 at* t′ *=1; c)* Γ *= 1 at* t′ *= 0.8; d)* Γ *= 2 at* t′ *= 0.6 ; e)* Γ *= 3 at* t′ *= 0.45; f)* Γ *= 5 at* t′ *= 0.2.* Ar *= 1,* n *= 3 for all figures. Red lines mark the profile lines used to measure* Ė *and elevation. See text for full description.*

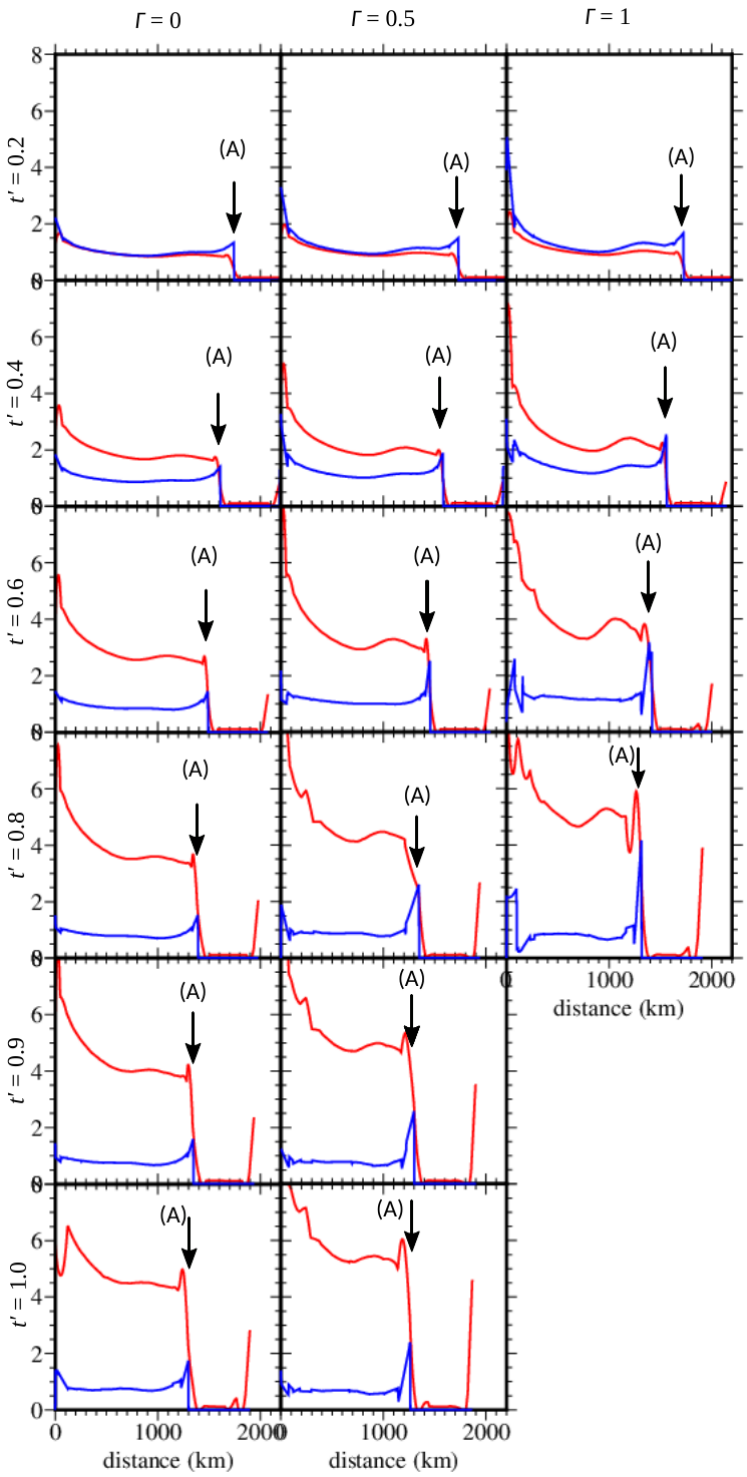

Figure 7.7: continued on next page.

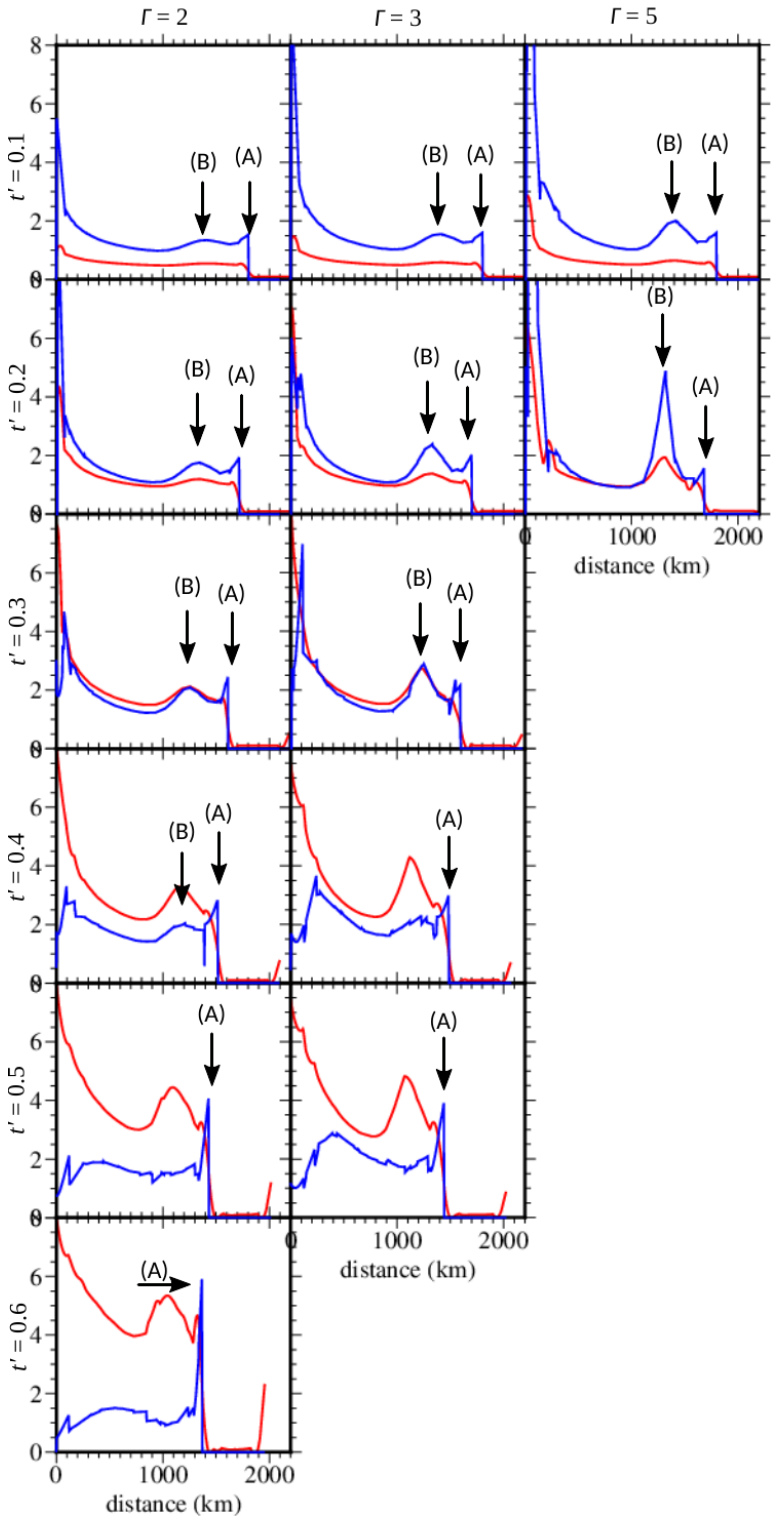

Figure 7.7: For n = *3,* Ar = *1, with weak region (experiments IA_iG_XX). Measurements obtained along the AH profile (Fig. 7.6) for* Ė *(blue) and scaled elevation (red in km) (see section 6.3.1 for isostatic and density assumptions).*

Fig. 7.7 continued. Arrow A marks the South Tarim Shear Zone, arrow B marks the western end of the Central Shear Zone. The elevation between the South Tarim Shear Zone and the Himalayan Front (at 0 km on the profile) increases with time. From the measurements of Ė *the width of the South Tarim Shear Zone decreases with time. The west Central Shear Zone develops only when* $\Gamma \geq 2$. *See text for further discussion.*

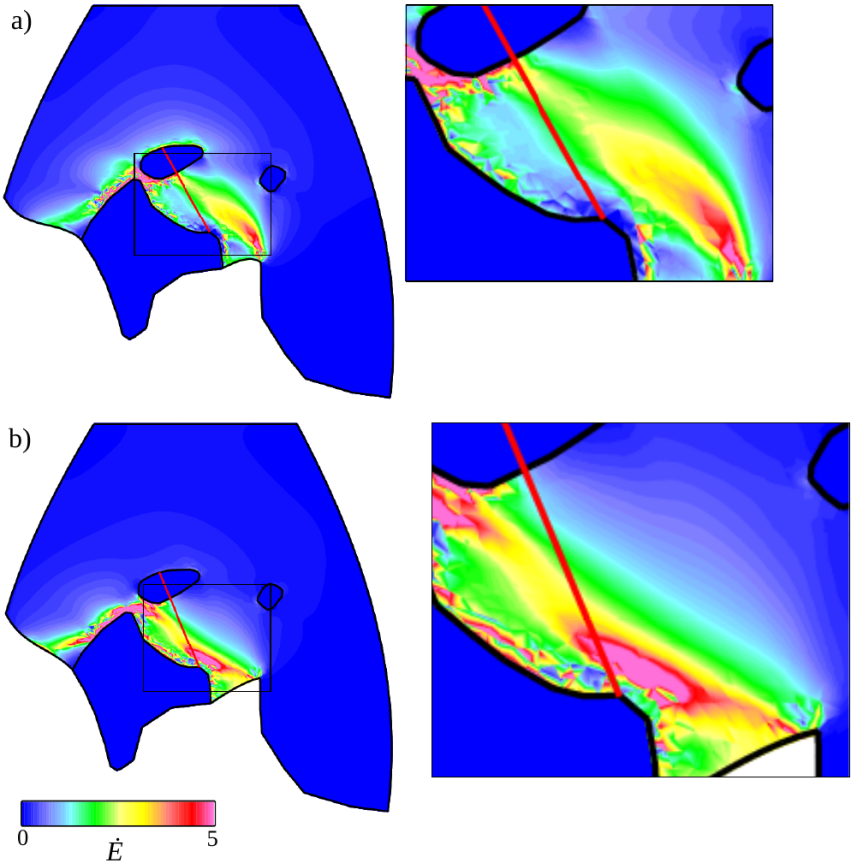

Figure 7.8: For n = *3,* Ar = *1, without weak region (experiments IA_NI_XX). Colour contour plots of* Ė *for a)* Γ = *3 at* t′ = *0.5, b)* Γ = *5 at* t′ = *0.3 The red line marks the AH profile used in Fig. 7.9.*

7.6). For Γ = 0.5 or 1.0 the strain increase is predominately focused north and east of the weak region over a relatively broad area (~ 500 km wide) (Fig. 7.11). For Γ = 2, 3 or 5 linear bands of strain initiate at the weak region and develop with time across the

Tibetan Plateau, forming a high strain-rate region, henceforth referred to as the Central Shear Zone.

The development of the Central Shear Zone differs east and west of the inclusion. Initial development (increased $\dot{E}$) is to the east of the weak region (Fig. 7.10). Here, for $\Gamma \geq 2$, the Central Shear Zone grows in length with time and links at the boundary where India and Asia join (for example, see Fig. 7.12). The east Central Shear Zone width decreases with time and this decrease is greater when Γ is higher (Fig. 7.10). With increasing time a localised west Central Shear Zone initially develops for Γ = 2 or 3 (Fig. 7.7) but then $\dot{E}$ in the shear-zone reduces ($t' > 0.3$). For Γ = 5 the west Central Shear Zone persists through time, and links with the Western Syntaxis (Fig. 7.6). However, extreme distortion of the finite element mesh presents the Γ = 5 model running beyond t' = 0.213.

Within the weak inclusion $\dot{E}$ initially increases and then decreases with time, which is most clearly observed for Γ = 2 or 3 (Fig. 7.11). To test if the buoyancy forces (from changes in layer thickness) are resisting horizontal shortening I repeat experiments IA_iG_06 and IA_iG_07 but set Ar = 0 (buoyancy forces are neglected). I find for Ar = 0 (experiments IA_GA0_06 & 07), $\dot{E}$ continues to increase with time in the weak region (Fig. 7.14).

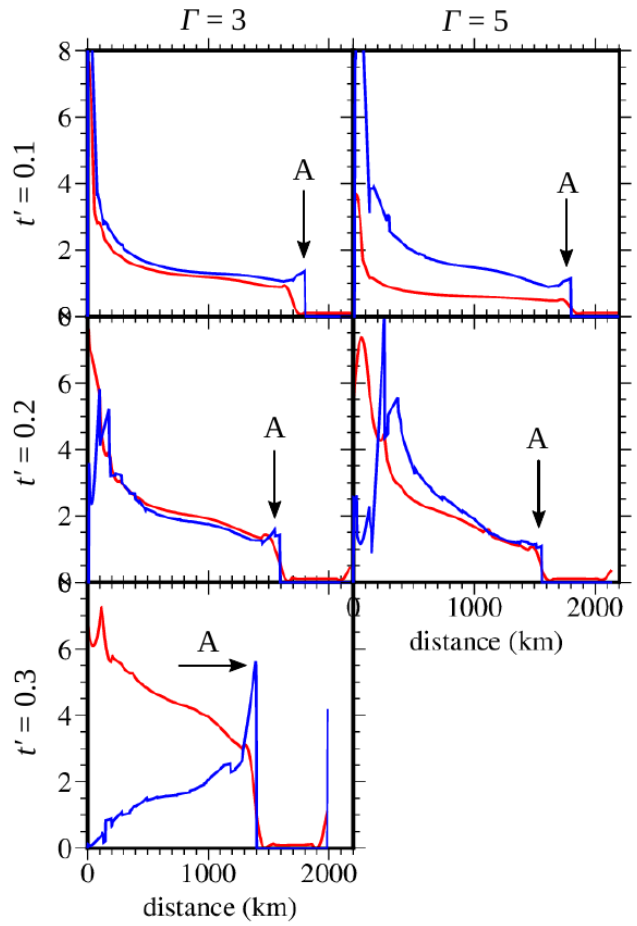

Figure 7.9: For n = *3,* Ar = *1, without weak region (experiments IA_NI_XX). Measurements obtained along the AH profile (Fig. 7.6) for* Ė *(blue) and dimensionless elevation (red) for* Γ = *3 and 5. Arrow A marks the South Tarim Shear Zone.*

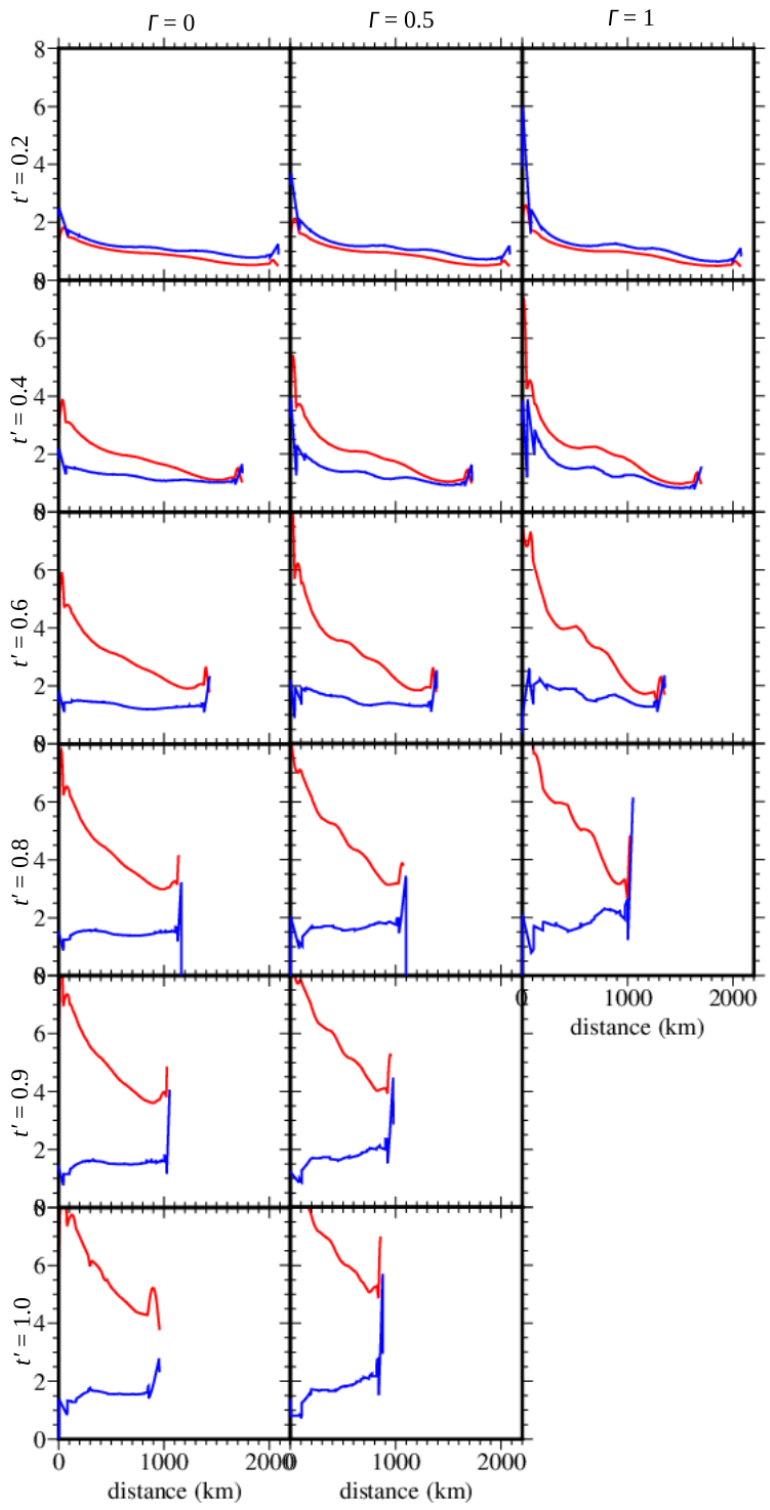

Figure 7.10: continued on next page.

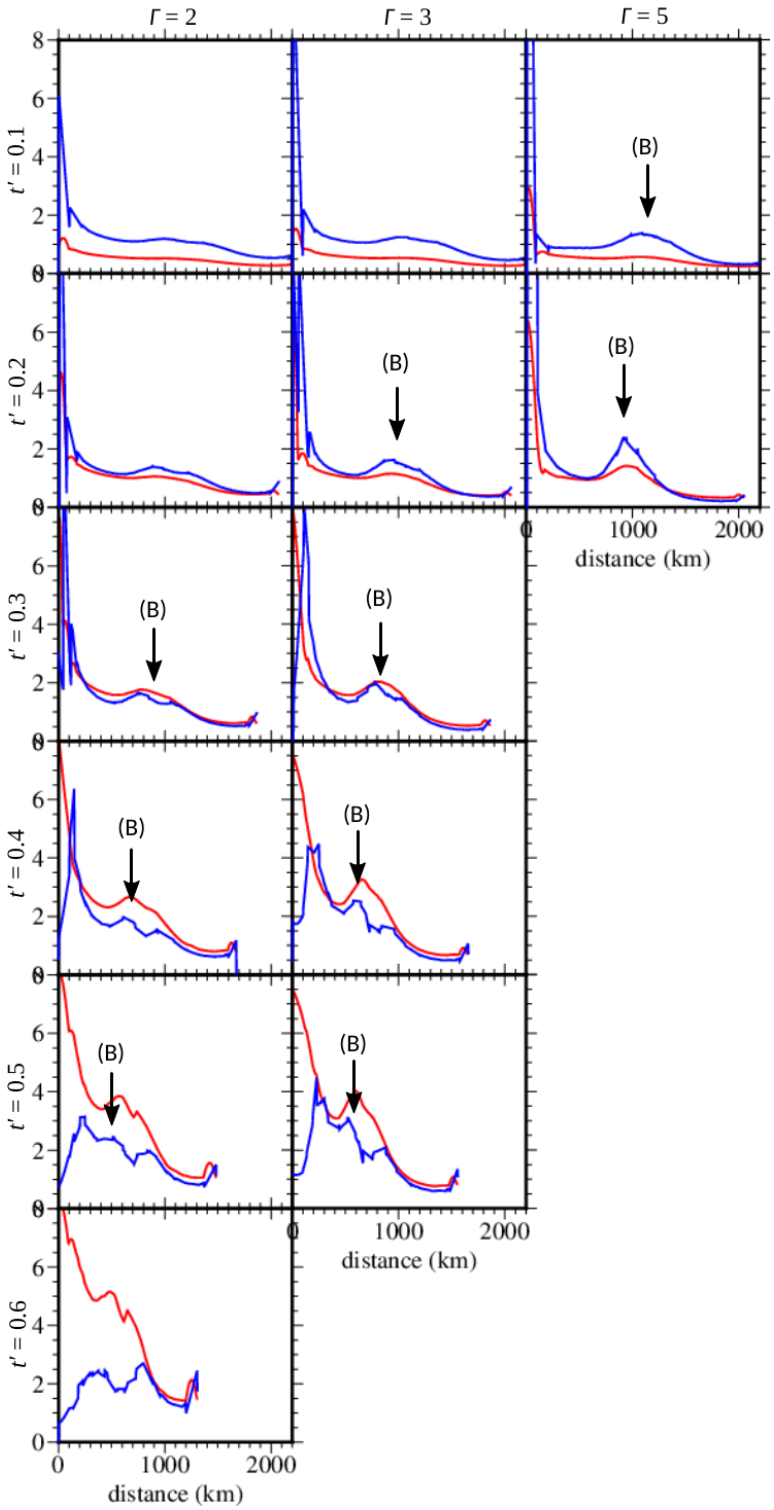

Figure 7.10: For n = *3,* Ar = *1, with weak region (experiments IA_iG_XX), profiles of* Ė *(dimensionless, blue) and elevation (km, red) along the AJ profile of the experiments shown in Fig. 7.6. Arrow B marks the eastern end of the Central Shear Zone that develops only when* Γ ≥ *2. Measurements of* Ė *show a decrease in the Central Shear Zone width with time.*

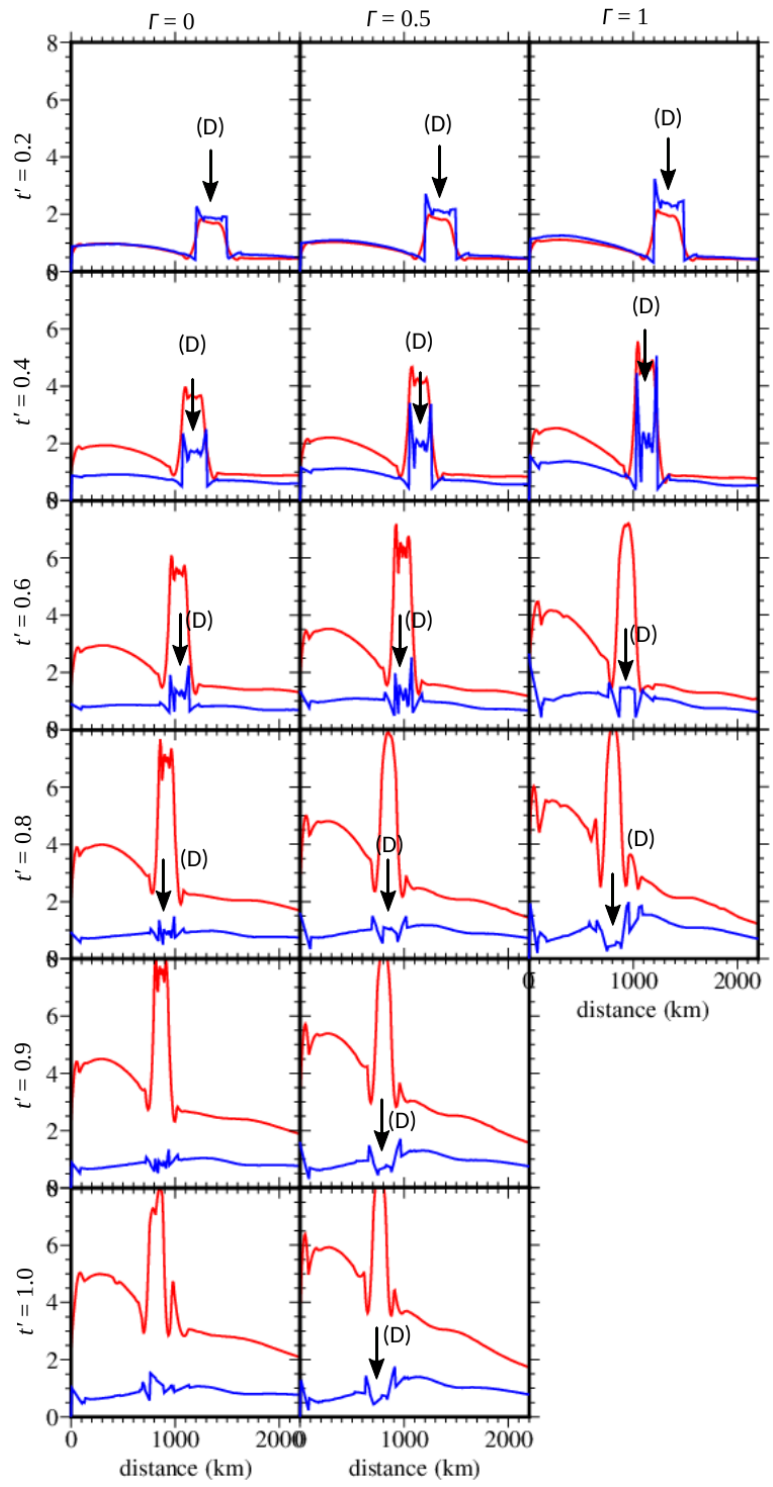

Figure 7.11: continued on next page.

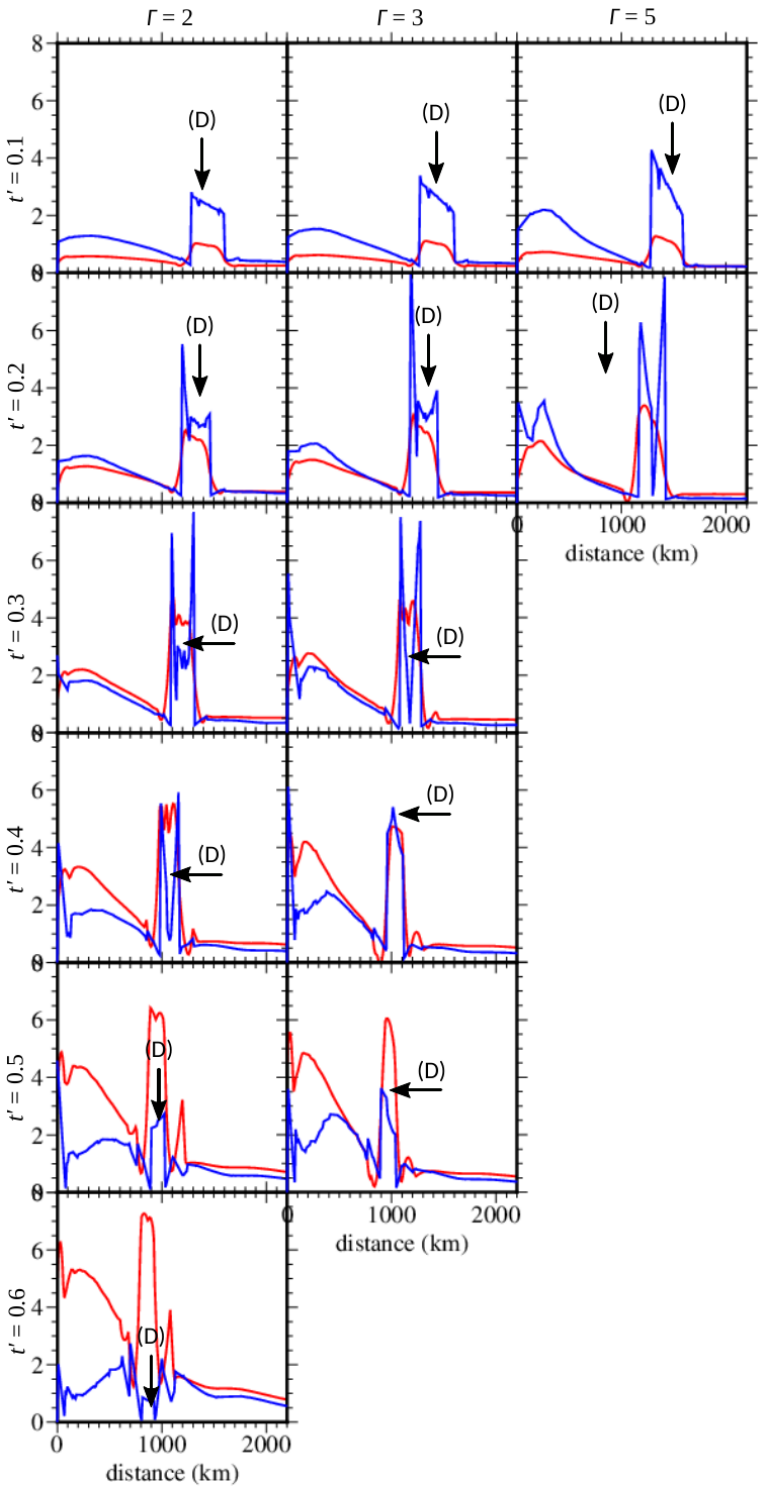

Figure 7.11: For n = *3,* Ar = *1, with weak region (experiments IA_iG_XX). Measurements obtained along the BX profile (Fig. 7.6) for* Ė *(dimensionless, blue) and elevation (km, red). Arrow D marks the location of the weak region.*

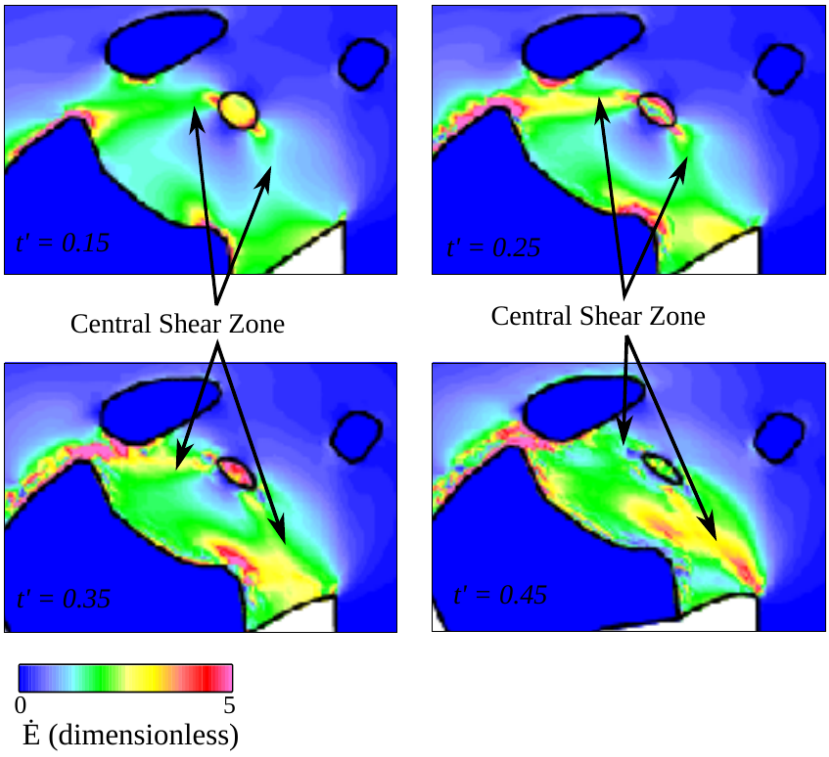

Figure 7.12: For Ar *= 1,* Γ *= 3, with weak region (experiment IA_iG_07).* Ė *colour contour plots at increasing time intervals showing the development of the Central Shear Zone. With increasing time the east end links with the high-strain region at the boundary of India-Asia, and the west end links with the high-strain region between the Western Syntaxis and the Tarim Basin. At* t′ *= 0.45 increased buoyancy forces resist the horizontal deformation and* Ė *reduces in the west Central Shear Zone.*

7.4.3 Discussion: strain-weakening and shear-zone formation on the Tibetan Plateau

Variations in elevation growth with time influences the location of shear-zones. Gravitational potential energy increases with elevation (sheet thickness). For $Ar > 0$ in any thin viscous sheet model (and here, in these experiments $Ar = 1$) topography growth will slow with time when the crustal buoyancy acts to locally resist further crustal thickening. Hence, when a critical crustal thickness is reached (dependent on the n, Γ and the viscosity coefficient) strain-rates will reduce with increasing elevation. Where

elevation gradients occur the crustal thickening rates increase outside the region of high topography, assuming both regions are a similar viscosity. Lower elevation regions of a high viscosity may resist deformation, for example in these experiments the strong Tarim Basin region does not deform despite the increase in elevation adjacent to it.

Accommodation of the India-Asia convergence by increased layer thickness preferentially occurs in and around the weak region. Here the elevation increase with time extends out from the weak region and across the Tibetan Plateau (Fig. 7.7). For $\Gamma > 0$ the work-dependent strain-weakening decreases the viscosity between the India boundary and Tarim Basin, accentuating this topography development which at a given time increases with Γ. For $\Gamma \geq 2$ the strain localises to form the Central Shear Zone (Fig. 7.6d, e, marked with arrow B; 7.12). Overall the Tibetan Plateau elevation increases with time but the Tarim Basin elevation remains lower and near constant. Strain-rates locally increase with time as a consequence of the increasing gradients of gravitational potential energy. The increasing Plateau elevation and the high-viscosity, low elevation Tarim Basin enhances the rate of decrease of the South Tarim Shear Zone width and the increase in maximum $\dot{E}$. Elevation changes adjacent to the Tarim Basin follow maximum $\dot{E}$ changes in the South Tarim Shear Zone.

For $\Gamma > 3$ the strain-weakening is sufficiently high that the lithosphere within the Central Shear Zone becomes locally very weak within a relatively short time. From this point the continuing convergence is preferentially accommodated on the Central Shear Zone such that the Central Shear Zone evolves with time faster than the South Tarim Shear Zone.

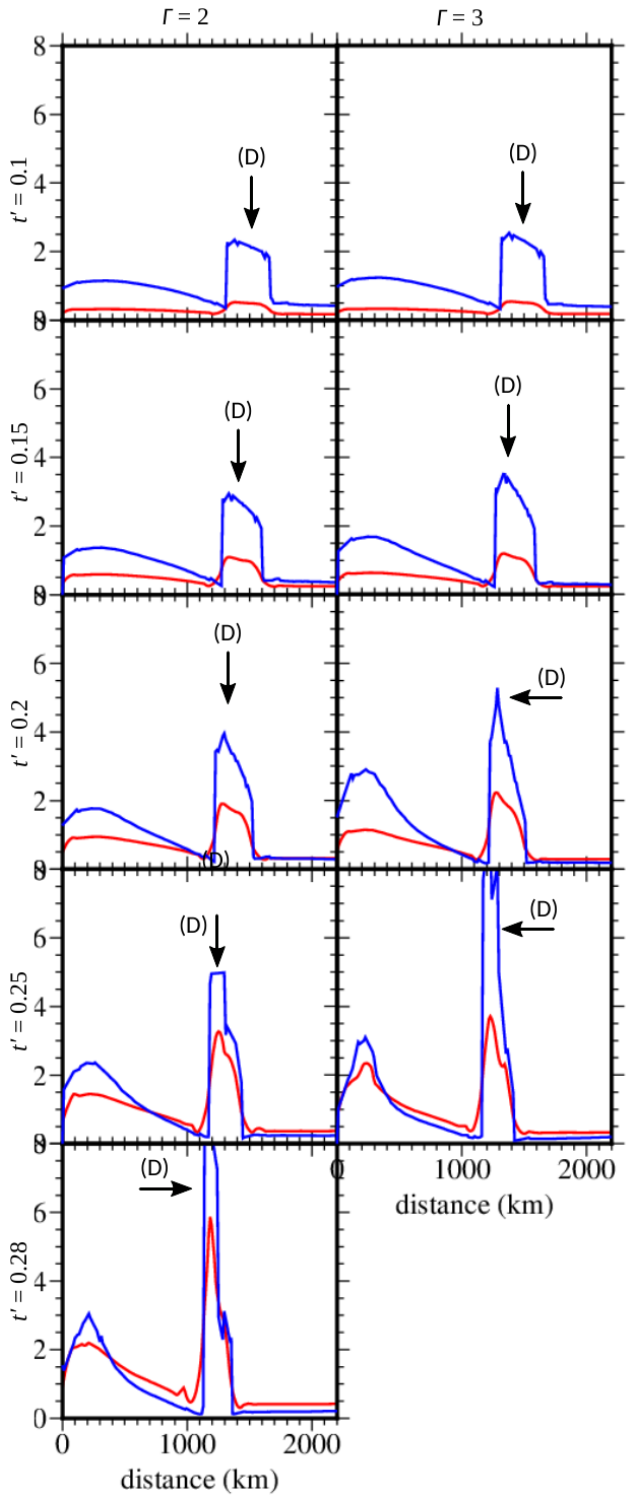

Figure 7.13: For Ar *= 0, with weak region (experiments IA_A0_XX). Measurements obtained along the BX profile (Fig. 7.6) for dimensionless* Ė *(blue) and elevation (red). Arrow D marks the location of the weak region.*

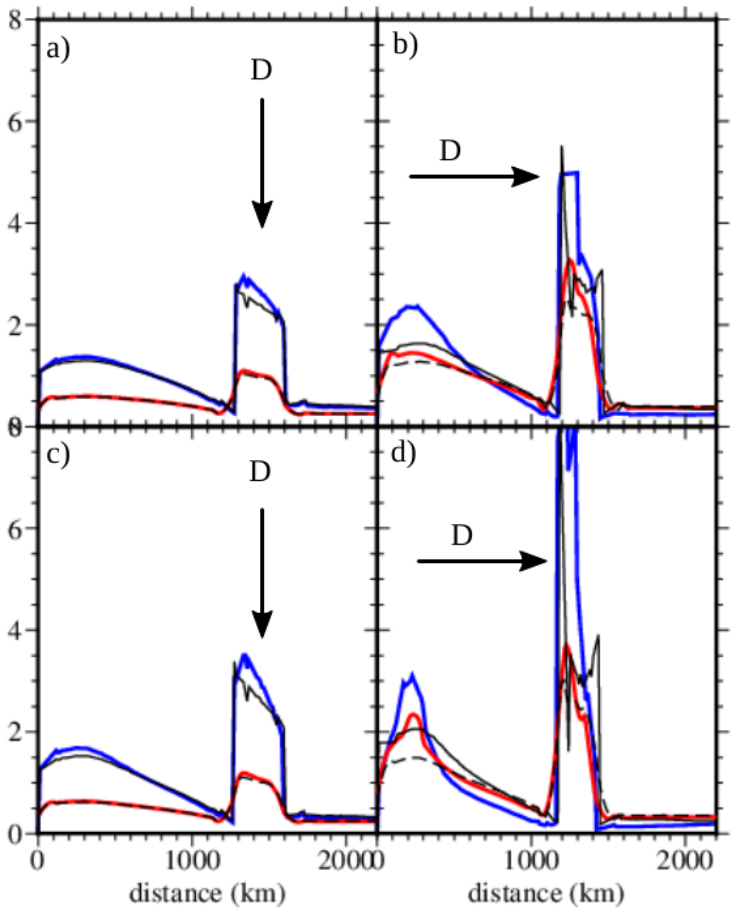

Figure 7.14: Measurements obtained along the BX profile (Fig. 7.6) for dimensionless Ė *(blue) and elevation, km (red). These for* Ar *= 0 (experiments IA_A0_XX)., where a)* Γ *= 2,* t′ *= 0.1; b)* Γ *= 2,* t′ *= 0.2; c)* Γ *= 3,* t′ *= 0.1; b)* Γ *= 3,* t′ *= 0.2. Calculation terminates at* t′ *= 0.22 due to high mesh distortion of the finite element mesh. Arrow D marks the location of the weak region. Black lines show* Ė *(solid) and elevation (dashed) for* Ar *= 1 at equivalent* Γ *and time steps. Despite the short time of the model it can be seen that for* Ar *= 0, the maximum* Ė *continues to increase with time across the weak region.*

For *Ar* = 0 (experiments IA_GA0_06 & 07) $\dot{E}$ increases with time in the weak region (Fig. 7.13). For *Ar* = 1 (e.g. IA_iG_06 & 07) $\dot{E}$ increases and then decreases (Fig. 7.11). At a given time $\dot{E}$ is less in the weak region for *Ar* = 1 than for *Ar* = 0 (Fig. 7.14). This is because for *Ar* > 0 buoyancy forces resist horizontal shortening when a critical

(dependent on Γ) layer thickness is reached. The same effects of buoyancy force resistance are also observed in the west Central Shear Zone. For Ar =1 and Γ = 2 or 3 the shear-zone elevation increases with time, corresponding with a net decrease in strain-rate in the west Central Shear Zone (Fig. 7.7). High mesh distortion terminates the calculations at t' = 0.243 for Ar = 1, Γ = 5 (IA_iG_08), so I am unable to observe if the same net reduction in strain-rate with time occurs. However, comparison of strain-rates in the west Central Shear Zone at t' = 0.2 for Γ = 3 and Γ = 5 shows for Γ = 5 the strain-rates double with only a 65% increase in elevation. High strain-weakening (here, Γ = 5) reduces the viscosity decrease and hence the sheet thickness that can be supported. Therefore buoyancy forces may not increase to the point where horizontal shortening is resisted. This infers for Γ = 5 the presence of the west Central Shear Zone will persist to t' = 1.

For experiments IA_iG_XX, where $\Gamma > 0$ the increased localisation of the east Central Shear Zone with time is likely a partial artefact of the boundary conditions. An abrupt change in boundary geometry where India and Asia connect acts to focus strain. With increasing time the initial east Central Shear Zone associated with the weak region links to high-strain region at the boundary, and subsequently strain-rates are enhanced in the coalesced regions.

In their simplified India-Asia model Dayem et al. (2009) found that a high strain zone developed adjacent to a strong region (analogous to the Tarim Basin) for n = 10, Ar =3 and Γ = 0.01 to 0.3. The 75 to 100 km width of this high strain zone was comparable to that of the Altyn Tagh fault. My experiments show that, for n = 3 and Ar =1, a South Tarim Shear Zone of comparable width (~ 113 km) is achieved after 47 Ma of

convergence for $\Gamma = 0.5$. However, for $\Gamma = 0.5$ the maximum $\dot{E}$ in the South Tarim Shear Zone is only ~ 2.5 times the average across the Tibetan Plateau, but for $\Gamma = 1$ or 2 the maximum $\dot{E}$ is ~ 6 times the average. For $\Gamma = 1$ or 2 a shear-zone width < 100 km is achieved by $t' = 0.4$ and 0.5. This suggests that for the South Tarim Shear Zone to evolve and increasingly focus deformation then for a depth-averaged lithospheric rheology with a strain exponent of $n = 3$, a strain-weakening coefficient of $\Gamma = 1$ to 2 is required.

In the simple-shear box model I described in Chapter Three, the development of localised shear bands for $n = 3$ required a strain-weakening component of $\Gamma \sim 1.2$ to 2. In this India-Asia model a greater strain-weakening component, $\Gamma = 5$, is required for the development of a comparable linear region of high strain that propagates away from the weak region. This difference may be due to the deformation regimes - the box model is subject to simple-shear, the India-Asia model is subject to a combination of pure- and simple-shear.

7.5 Influence of the Himalaya Syntaxes on localisation across the Tibetan Plateau

7.5.1 Motivation for changing the Western Himalaya Syntaxis geometry

Analogue models containing multiple strong or weak inclusions show that with increasing compressive stress, shear zones nucleate against the inclusions and then develop and link with each other (Mandal et al., 2004; Misra and Mandal, 2007). Given the general view that fault and shear-zone displacement is proportional to length (e.g. Cowie and Scholz, 1992; Fossen and Cavalcante, 2017) then shear-zone linkage will

enhance the strain-rate within coalesced shear-zones. Fault and shear-zone linkage has been observed in extension, compression and strike-slip settings (e.g. Aydin and Schultz, 1990; Fossen and Rotevatn, 2016; Peacock and Sanderson, 1991; Walsh et al., 1999).

Table 7.4: Parameters for the modified Himalayan Front experiments, where Ar = *1,* n = *3 for all. I retain the viscosity coefficients of 0.5 for the weak region and 10 for India and the Tarim and Sichuan Basins.*

Experiment	***Γ***	**Comments**
IA_HF2_03	0.5	Terminates at $t' = 1$
IA_HF2_05	1	Terminates at $t' = 0.93$ (finite element mesh distortion)
IA_HF2_06	2	Terminates at $t' = 0.98$ (finite element mesh distortion)
IA_HF2_07	3	Terminates at $t' = 0.84$ (finite element mesh distortion)
IA_HF2_08	5	Terminates at $t' = 0.94$ (finite element mesh distortion)

In section 7.4 I show how for $\Gamma = 5$ a weak region in the Tibetan Plateau initiates the growth with time of a localised shear zone (named the Central Shear Zone) across the Tibetan Plateau. With increased time strain-rates also increase along the indenting boundary (India). By $t' = 0.2$ the west branch of the Central Shear Zone links with the Western Himalaya Syntaxis. I propose this linkage enhances strain-rates in the west Central Shear Zone. To test this I modify the Himalayan Front boundary to remove the curvature associated with the present day Western Syntaxis and repeat my numerical experiments with the weak region for $n = 3$, $Ar = 1$ and $\Gamma = 0.5$, 1.0, 2.0, 3.0 or 5.0 (Fig. 7.15). These experiments and associated parameters are given in Table 7.4. Whilst acknowledging the original Himalayan Front geometry at 47 Ma is unknown, this modification allows me to also examine in more detail the processes happening on the north-east side of the Plateau without the deformation on the north-west side halting the calculation.

7.5.2 Results from experiments with the modified Himalayan Front

There are two major differences in distribution of strain between the modified and original Himalayan Front experiments. Firstly, these experiments (IA_HF2_XX) lack the persistent Central Shear Zone associated with the weak region, as seen in the original Himalayan Front experiment for $\Gamma = 5$ (IA_iG_08; Fig. 7.6e). Secondly, for $\Gamma \geq 2$ these experiments (IA_HF2_XX) show temporal development of a shear zone (which I name the North Plateau Shear Zone) that appears to initiate at the south-west Sichuan Basin boundary and then links with the weak region (Fig. 7.15). Where $\Gamma = 3$ or 5 the North Plateau Shear Zone initially intercepts the weak region, but with increasing time moves further north and links with a high strain-rate region north of the Tarim Basin (Fig. 7.15d, e). Using measurements along profile AJ I observe how the North Plateau Shear Zone width and maximum $\dot{E}$ change with time (Fig. 7.16). In common with the Central Shear Zone for the original Himalayan Front configuration (experiments IA_iG_XX) at a given time the shear zone width decreases and the maximum $\dot{E}$ increases with increasing Γ.

These experiments with the modified Himalayan Front (IA_HF2_XX) follow those of the original Himalayan Front (IA_iG_XX) in the development of the South Tarim Shear Zone with time (Fig. 7.17). For $\Gamma \geq 2$ (IA_iG_06, 07, 08) maximum $\dot{E}$ in the shear zone increases and then decreases with time.

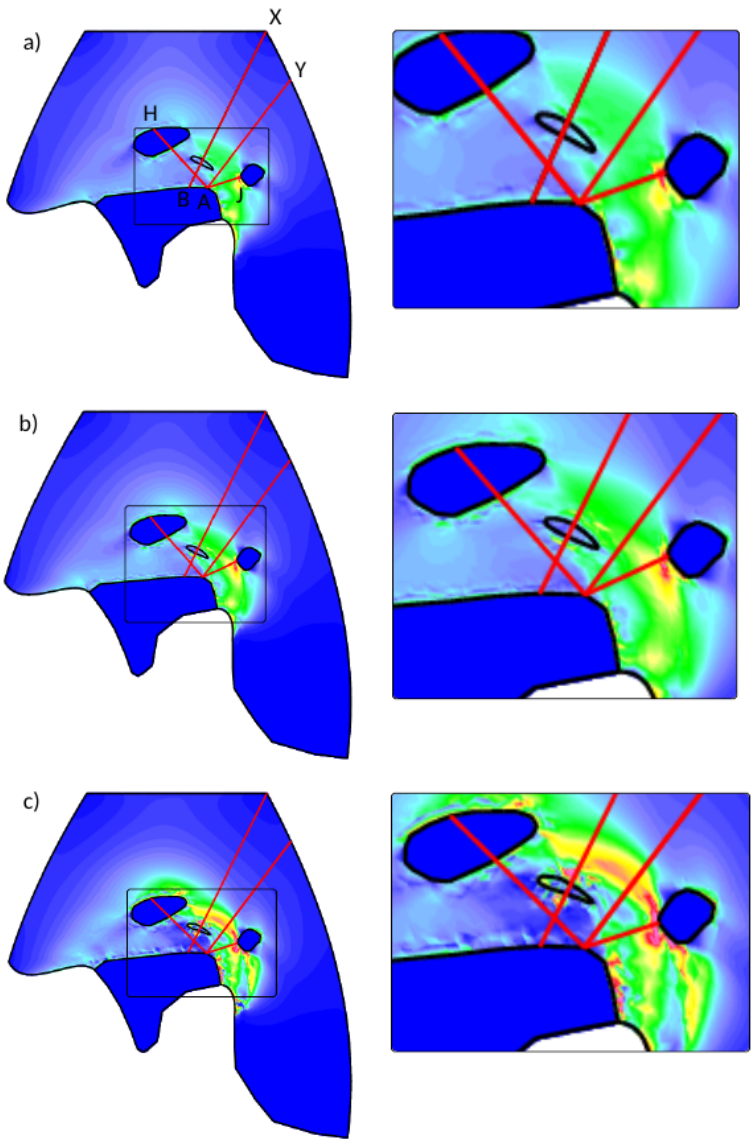

Figure 7.15: continued on next page.

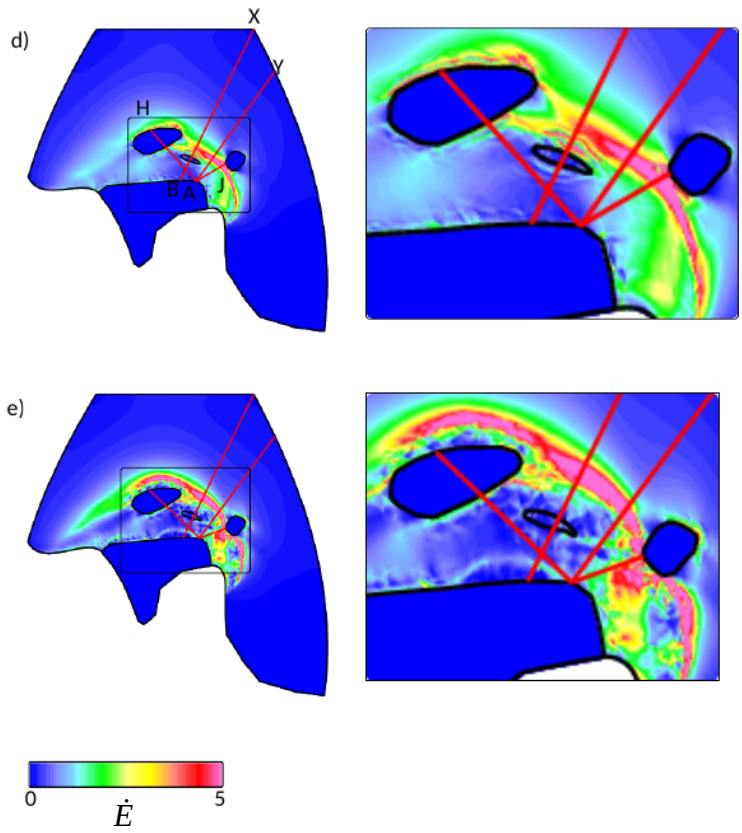

Figure 7.15: For modified Himalayan Front experiments, Ar *= 1,* n *= 3 (IA_HF2_XX). Colour contour plots of* Ė *for: a)* Γ *= 0.5 at* t′ *=1; b)* Γ *= 1 at* t′ *= 0.9; c)* Γ *= 2 at* t′ *= 0.9 ; d)* Γ *= 3 at* t′ *= 0.8; e)* Γ *= 5 at* t′ *= 0.9. Red lines mark the profile lines used to measure* Ė *and elevation.*

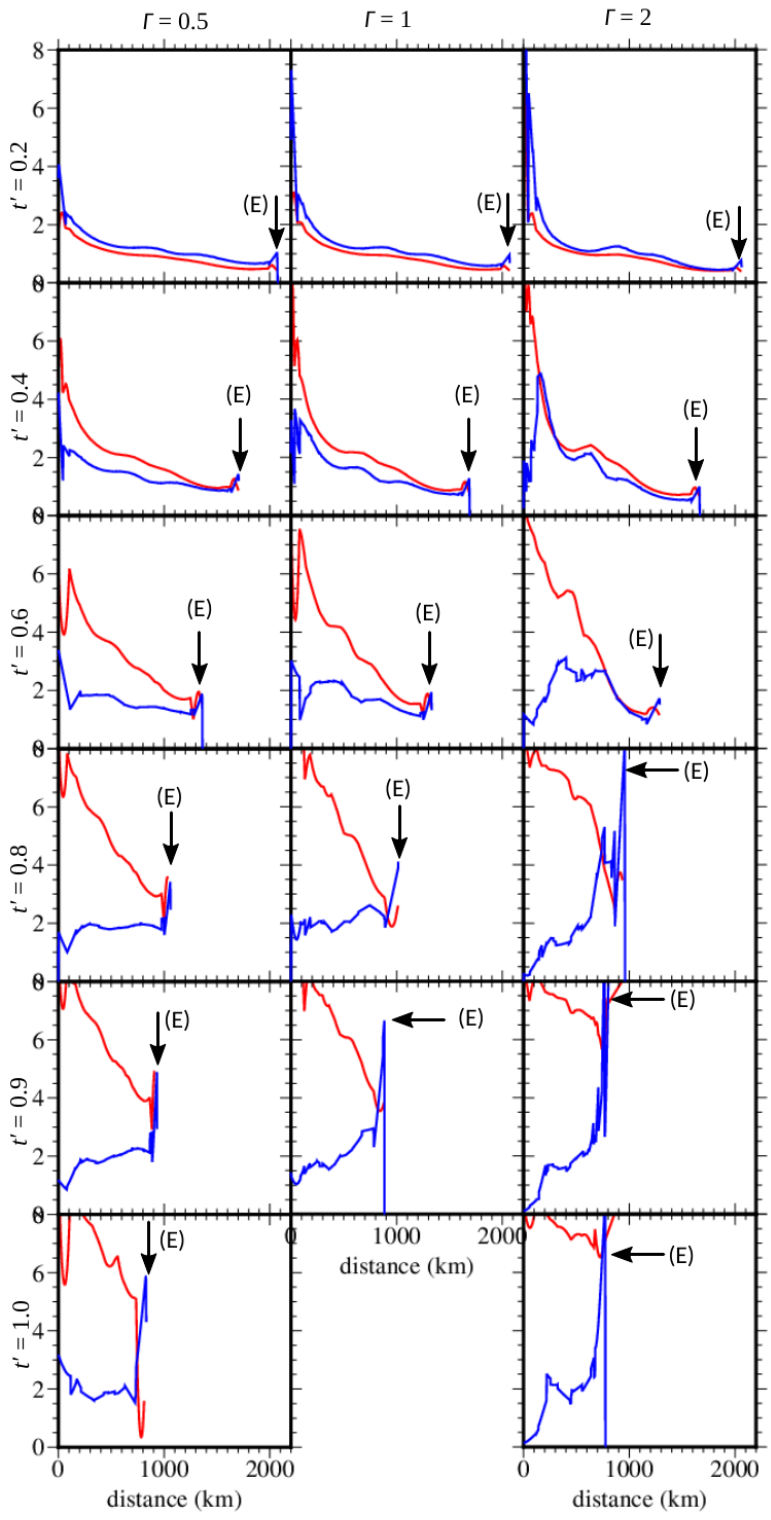

Figure 7.16: continued on next page.

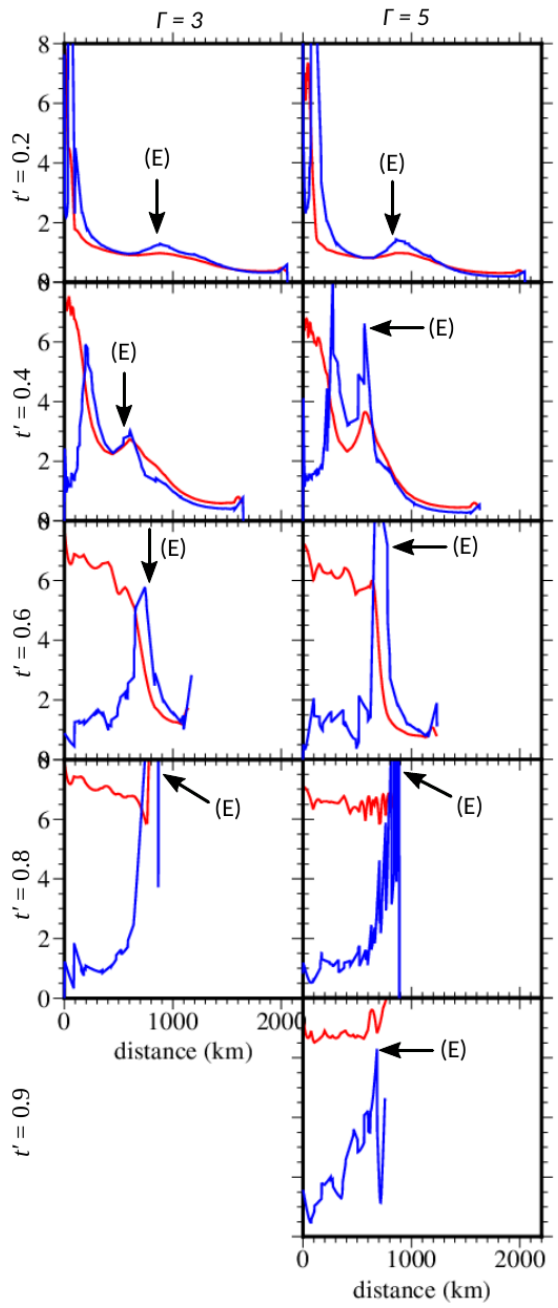

Figure 7.16: For modified Himalayan Front experiments, Ar *= 1,* n*= 3 (IA_HF2_XX). Measurements of topography (km, red) and* Ė *(dimensionless, blue) measured along the AJ profile at different time intervals. Arrow E indicates the high strain region that develops adjacent to the Sichuan Basin (North Plateau Shear Zone). At a given time with increasing* Γ *the maximum* Ė *in the North Plateau Shear Zone increases and the distance across which* Ė *is higher than the background strain-rate decreases, i.e. increasing* Γ *increases localisation on the North Plateau Shear Zone.*

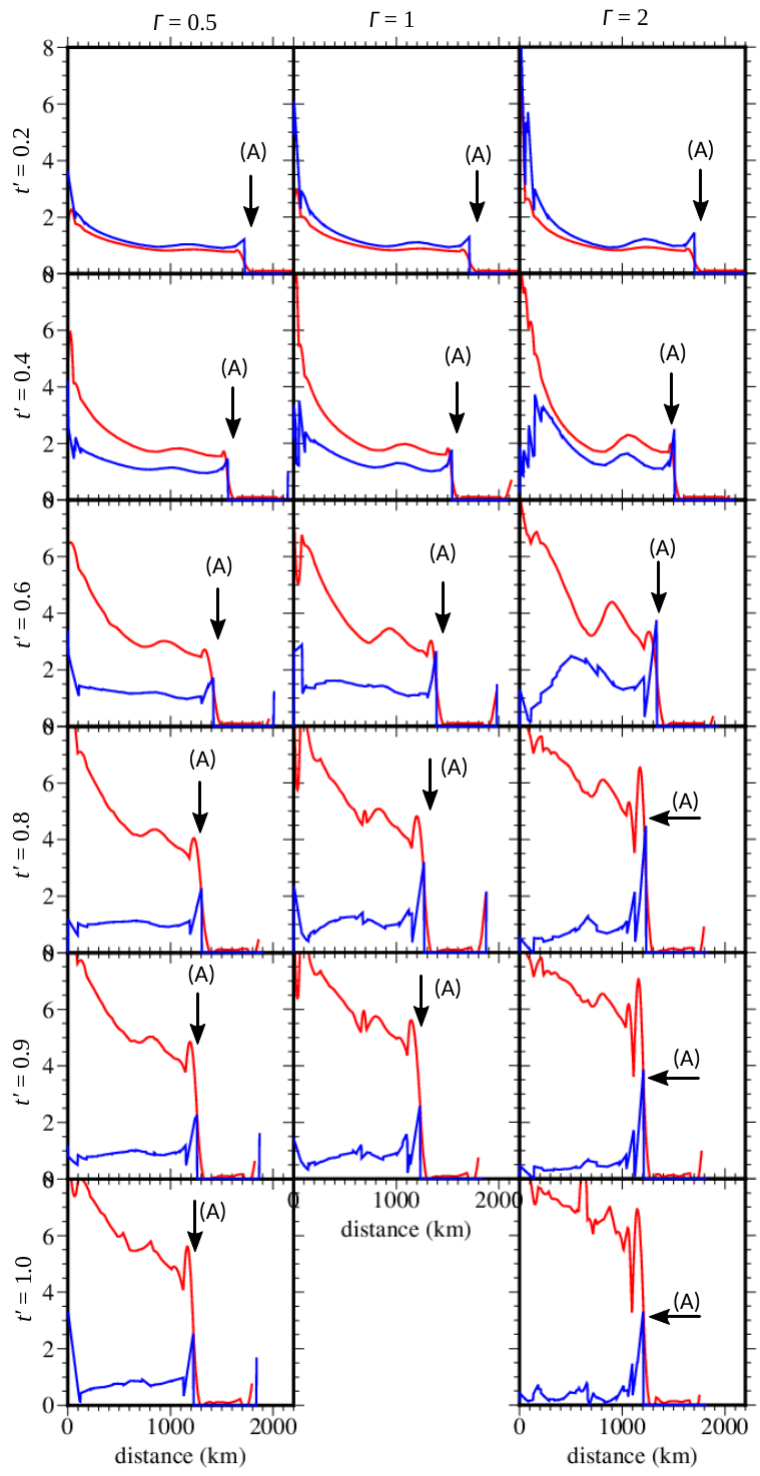

Figure 7.17: continued on next page.

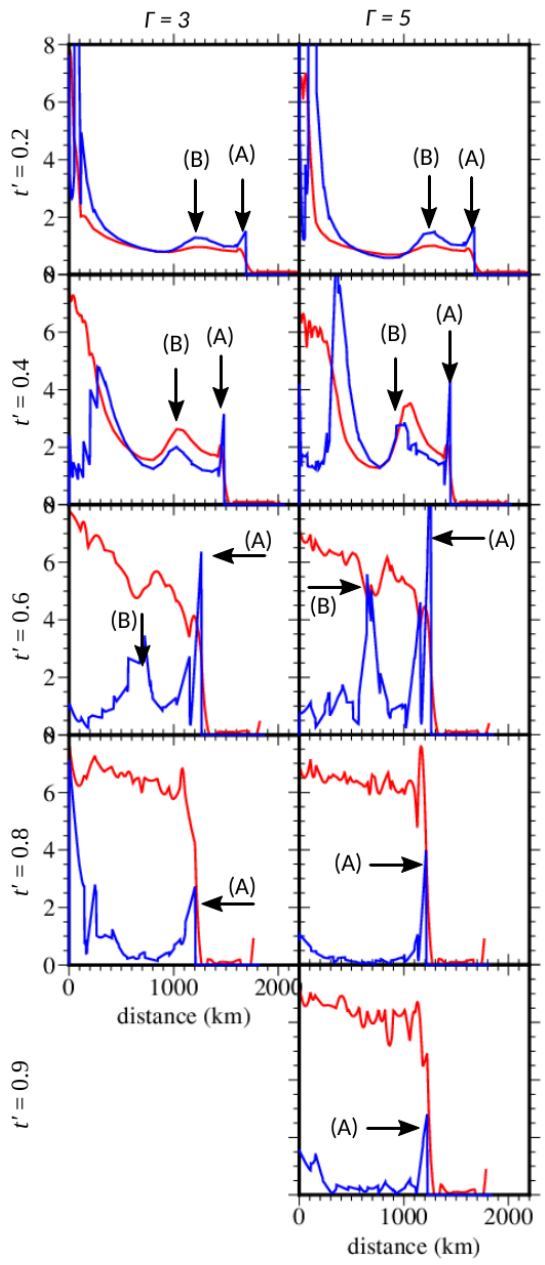

Figure 7.17: For modified Himalayan Front experiments, n = *3,* Ar *= 1 (IA_HF2_0X). Measurements of topography (km, red) and* Ė *(dimensionless, blue) measured along the AH profile at different time intervals. Arrow A indicates the high strain region that develops adjacent to the Tarim Basin (South Tarim Shear Zone). Localisation follows the North Plateau Shear Zone (see Fig. 7.16) - increasing* Γ *increases localisation on the South Tarim Shear Zone. Arrow B shows the transient high-strain region (equivalent to the Central Shear Zone in Fig. 7.7) that develops in response to the topography difference. With time the topography equalisation reduces the strain-rate in this area.*

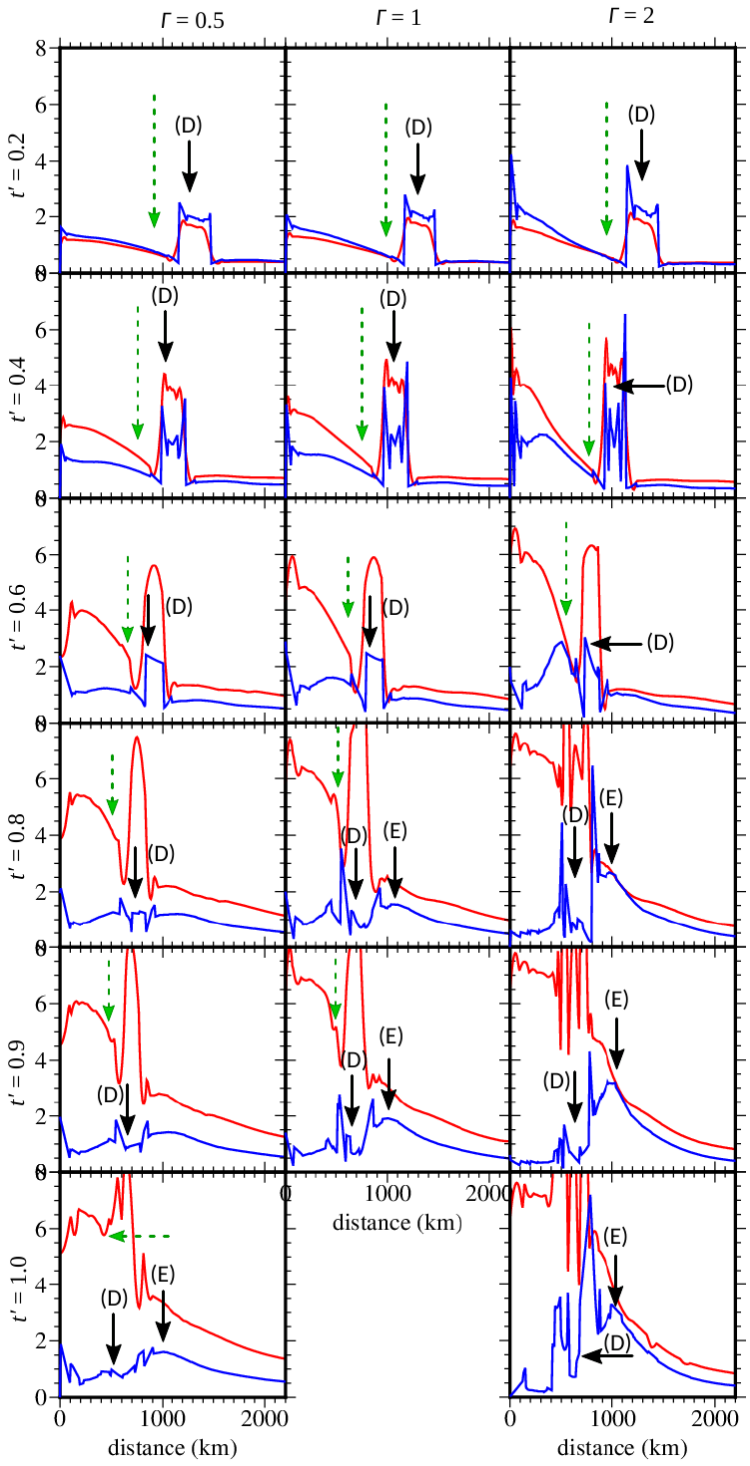

Figure 7.18: continued on next page.

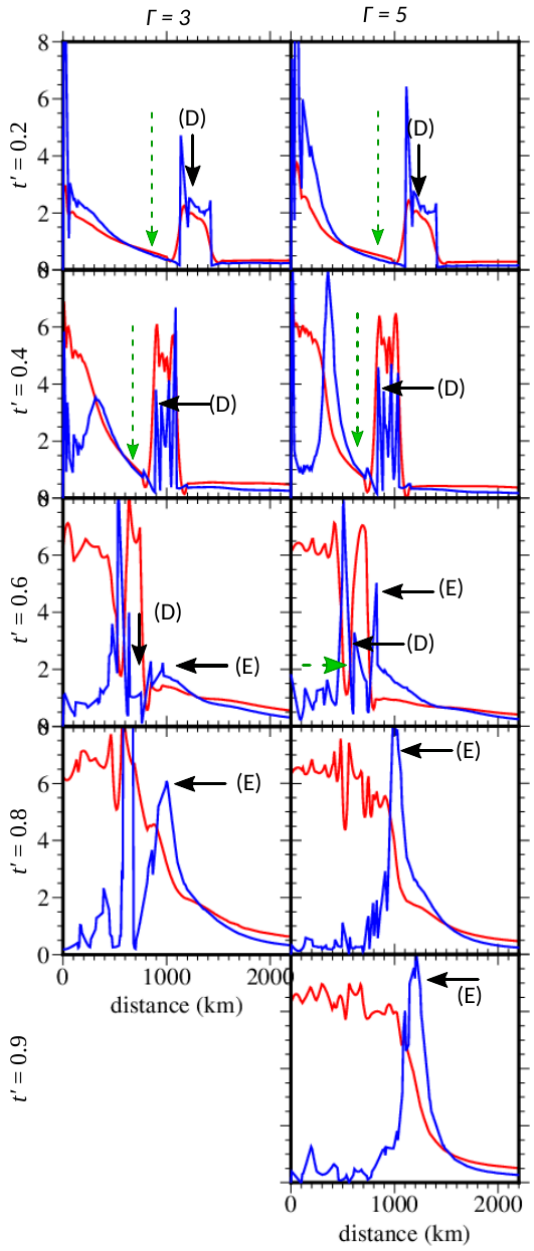

Figure 7.18: For modified Himalayan Front experiments, n = *3,* Ar *=1 (IA_HF2_XX). Dimensionless measurements of topography (red) and* Ė *(blue) measured along the BX profile (see Fig. 7.15 for location) at different time intervals. Arrow D indicates the weak region and a transient high-strain regions that develop adjacent to it. The gradient in topography between the Himalayan Front and the weak region is gradually reduced (green dashed arrow). Arrow E indicates the developing North Plateau Shear Zone that occurs adjacent to the elevated Plateau.*

7.5.3 Discussion on how modified the Himalayan Front alters the shear zone distribution

The removal of the Western Syntaxis (experiments IA_HF2_XX) increases the area between India and the Tarim Basin over which the convergence is accommodated. Consequently in this region the elevation growth with time is distributed over a greater area and the elevation (and hence buoyancy forces) at a given point are less from when the Western Syntaxis is present. For $\Gamma \geq 2$ the rate of elevation growth with time across the Tibetan Plateau levels off after initial growth (Fig.7.17, 7.18). The continued rotation of India into Asia maintains the Plateau topography.

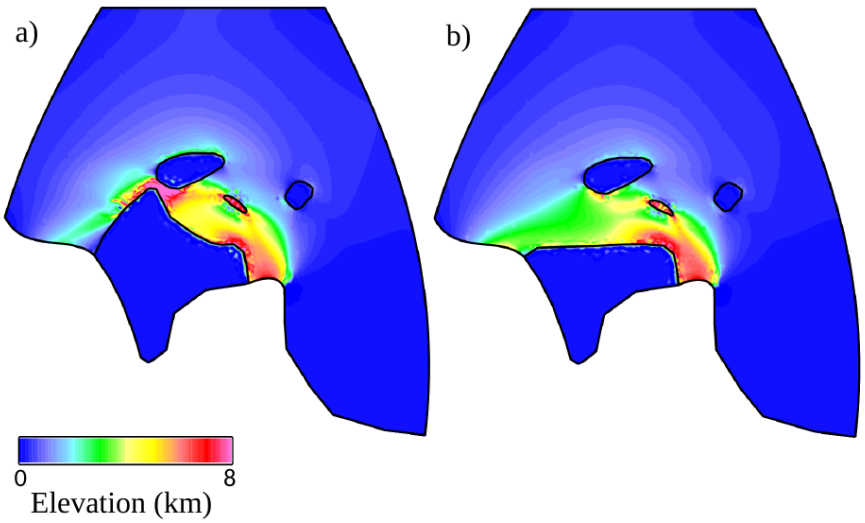

Figure 7.19: Contoured topography for $\Gamma = 2.0$ *at* $t' = 0.6$. *a) For original Himalayan Front and b) modified Himalayan Front. For the original Himalayan Front experiment the calculation terminates at* $t' = 0.6$, *due to distortion of the finite element mesh. Hence the modified Himalayan Front experiment is compared at the same time step.*

In these experiments (IA_HF2_XX) the principal stress concentration occurs between the Eastern Syntaxis and the Sichuan Basin (Fig. 7.15). Here the topography smoothly reduces west and north of the Eastern Syntaxis, in contrast to the topography variations across the Plateau when the Western Syntaxis is present (Fig. 7.19). Between the topographically high Plateau and low Asia, steep elevation gradients occur at the north-east and east side the Plateau (Fig. 7.18). The resultant increase in crustal thickening rates outside the region of high topography forms the North Plateau Shear Zone.

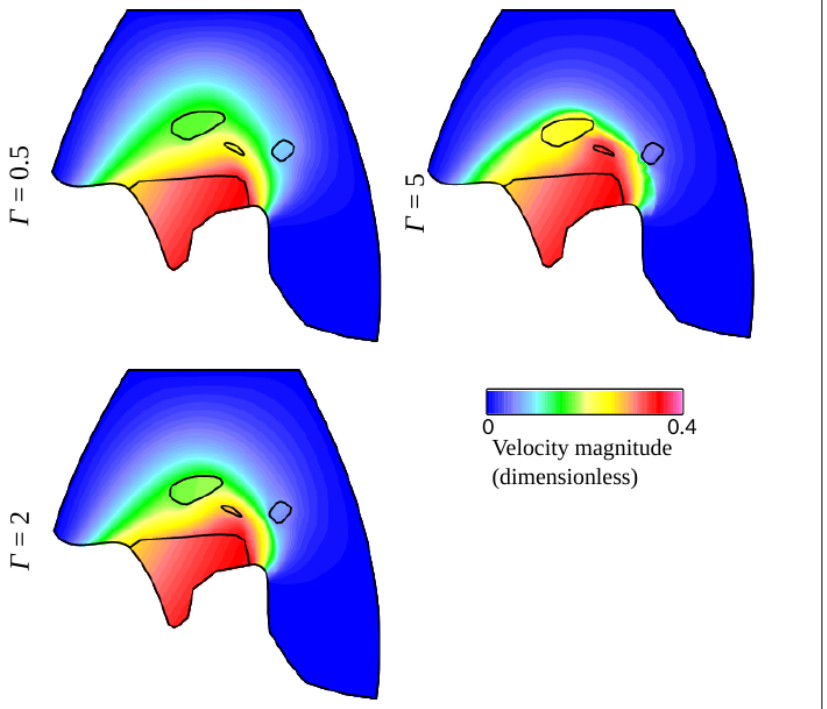

Figure 7.20: For modified Himalayan Front experiments (IA_HF2_XX) at t′ = 0.8. With increasing Γ (shown here for Γ = 0.5, 2 and 5 but applicable for all tested values of Γ) the magnitude of the of the horizontal velocity across the Tibetan Plateau elevation increases.

At a given time the effective viscosity reduces across the Plateau with increasing Γ (Fig. 7.21; Eqs. 2.16, 2.21); with increasing time the elevation and horizontal velocity is

greater where the effective viscosity is less (Fig. 7.20, 7.21). The movement of the elevated Plateau outwards, constrained by India and the Tarim and Sichuan Basins, moves the North Plateau Shear Zone.

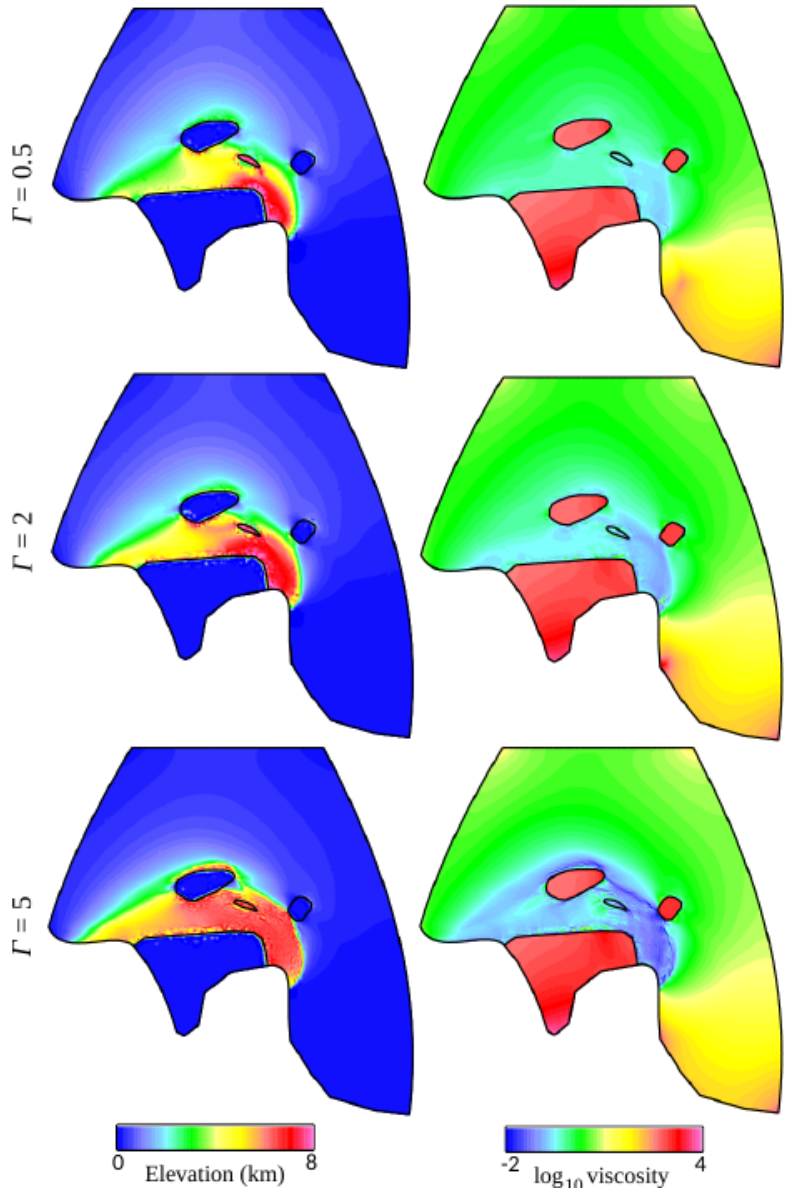

Figure 7.21: For modified Himalayan Front experiments (IA_HF2_XX) at t′ = 0.8. With increasing Γ (shown here for Γ = 0.5, 2 and 5, but applicable for all tested values of Γ) at a given time the Tibetan Plateau elevation increases and the effective viscosity reduces.

The 400 km Longmen Shan Fault system is located along the western edge of the Sichuan Basin and marks the elevation change from 6,500 m in the Tibetan Plateau to 500 m in the Sichuan Basin (Fig. 1.3). In these experiments (IA_HF_XX) strain localises against the south-west side of the Sichuan Basin (Fig. 7.15), comparable to the Longmen Shan Fault system. Here, the east side of the topographically high Tibetan Plateau extends as far the south-west side of the Sichuan Basin, but the west side of the Sichuan Basin is bordered by the lower elevation of Asia (Fig. 7.21). Differences between the actual and modelled Tibetan Plateau elevation may be due to choice of geometry or rheological parameters. For $\Gamma = 2$ at $t' = 0.6$ the similarity in the north-east and east extent of the elevated Tibetan Plateau for both Himalayan Front configurations suggests the geometry of indenting boundary is not the principal control on the extent of the Tibetan Plateau (Fig. 7.19). In exploring strain localisation against the Tarim Basin Dayem et al. (2009) suggest the deformation is best described by $n > 10$. Increasing n in my experiments would reduce effective viscosity (Eq. 2.16), increase the horizontal velocity and move the Plateau edge outwards. The limitations of the model mean a high n would result in distortion of the finite element mesh and termination of the calculation before a comparison between the present day and modelled elevation could be made.

Copley and McKenzie (2007) suggest the Eastern Syntaxis geometry is a consequence of crustal flow from the bordering Himalaya and Indo-Burma ranges, and that a similar process may have formed the Western Syntaxis. Gahalaut and Kundu (2012) propose that the geometry of the Eastern and Western Himalayan syntaxes is influenced by the subduction of two north-south trending ridges, the Chagos-Laccadive-Deccan ridge and a ridge at 90 ºE in the Indian Ocean. In either scenario the present Syntaxes geometry

has evolved from an original shape at 47 Ma, with the evolution of the shape through time unknown.

In these experiments the stress concentrations at the Eastern and Western Syntaxes, and hence development of the North Plateau or Central Shear Zones, occurs because of the initial geometry. There is insufficient evidence to say when this geometry first evolved. However, these experiments show localised shear-zones develop prior to the full rotation of India; those associated with the Western Syntaxis develop by $t' = 0.2$ (for $\Gamma = 5$) and with the Eastern Syntaxis by $t' = 0.6$ (for $\Gamma \geq 2$). When scaled this gives 9.4 and 20.2 Ma respectively (Table 7.1), indicating formation of the present day Himalaya Syntaxes geometry by 21 Ma would permit associated shear zone development. Stress concentrations at a given time are likely to be higher where the present day Eastern Syntaxis geometry is used, rather than the simplified geometry used throughout this chapter (see section 6.2). The associated strain localisation could therefore develop in a shorter (< 21 Ma) time frame.

Changes in the Himalayan arc geometry with time could result in changes in stress and strain distribution within the Tibetan Plateau. Consequently the location of topography growth and high strain-rate regions may vary with time. In my original Himalayan Front experiments (IA_iG_XX) at a given time (dependent on Γ) strain was transferred between the Central and South Tarim Shear-Zones. Similarly, changes in the Himalayan arc geometry could result in strain being accommodated across one shear zone giving way to preferential displacement on a new shear zone .

7.6 Inferred contribution of thrust, strike-slip and normal faulting

In comparing these experiments with earthquake focal mechanisms in Tibet I am mindful that the present day spatial distribution of shear-zones does not correlate with that developed in my experiments. Tibet is seismically active and earthquake focal mechanisms indicate that faulting mostly occurs in the upper ~ 10 km of crust (e.g. Taylor and Yin, 2009). Analysis of earthquake focal mechanisms for events M > 5.5 (Taylor and Yin, 2009) shows normal faulting below regions of high elevation (> 5 km) in south and central Tibet, with combined strike-slip and normal faulting at lower elevations. In central Tibet there is a change to a dominant strike-slip component. Thrust faulting is largely confined to the Himalayan Front, north-east Plateau boundaries and north of the Plateau.

In the thin viscous sheet model the strain-rate tensor is assumed to be invariant across lithosphere layers, but can vary horizontally. The overlaying brittle crust deforms as a passive response to the underlying viscous lithosphere. To explore the relative contribution of dip-slip and strike-slip faulting in the brittle layer in my experiments I follow Houseman and England (1986) and Gordon and Houseman (2015) in considering the ratio of principal horizontal strain-rates, $\dot{\varepsilon}_1$ and $\dot{\varepsilon}_2$. A graph of these strain-rates (Fig. 7.22) defines an angle, which is mapped to the the parameter *q*:

$$q = \left(\frac{3}{4} + \frac{1}{\pi} \tan^{-1} \left(\frac{\dot{\varepsilon}_2}{\dot{\varepsilon}_1} \right) \right) \qquad \text{Eq. (7.3)}$$

The value of *q* (between 0 and 1) indicates the inferred style of faulting in the brittle layer, where:

a) thrust only on orthogonal planes, $0 \leq q \leq 0.25$;

b) combination of thrust > strike-slip, $0.25 < q < 0.325$;

c) combination of strike-slip > thrust, $0.325 < q < 0.5$;

d) strike-slip only, $q = 0.5$;

e) combination of strike-slip > normal, $0.5 < q < 0.625$;

f) combination of normal > strike slip, $0.625 < q < 0.75$;

g) normal only on orthogonal planes, $0.75 \leq q \leq 1$.

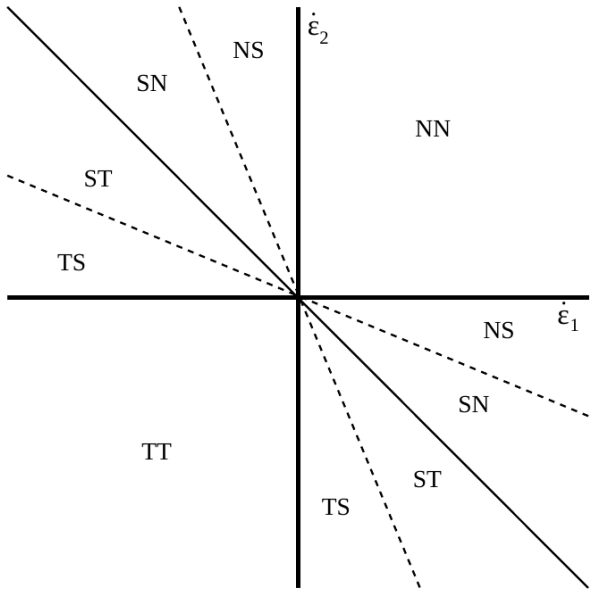

Figure 7.22: Ratio of principal horizontal strain-rates, $\dot{\varepsilon}_1$ and $\dot{\varepsilon}_2$ modified from England and Houseman (1989). Letters show permutations of the two permissible styles of deformation: S, strike-slip; T, thrust; N, normal. The dashed lines separate fields in which strike-slip (ST and SN), reverse (TT and TS) and normal (NN and NS) failure dominate deformation. Solid line where strike-slip only occurs.

For $\Gamma = 5$, with the experiment using the present day Himalayan Front (experiment IA_iG_08, Table 7.3), at $t' = 0.2$ a contour plot of $\dot{E}$ (Fig. 7.23a) shows deformation is

principally accommodated in the Tibetan Plateau region, and around the Himalayan syntaxes. A linear region of high strain develops away from the low viscosity region (Central Shear Zone, Fig. 7.15). Contour plots of q (Fig. 7.23b, c) show that within the Tibetan Plateau $q < 0.5$, inferring the presence of thrust faulting and the absence of normal faulting. Within the same region, positive values on the z-component of the strain-rate tensor (Fig. 7.23d) indicate an increase in sheet thickness, consistent with thrust faulting (normal faulting would require negative values). Across most of the Plateau $q < 0.25$, inferring faulting is solely accommodated on thrust faults on orthogonal planes. In the Central Shear Zone, $0.25 < q < 0.325$, inferring a component of strike-slip deformation, but that thrust faulting remains the dominant mechanism.

Experiment IA_iG_08 ($\Gamma = 5$) terminates at $t' = 0.2$, due to distortion of the finite element mesh. To explore if the inferred style of faulting persists through time I examine results from experiment IA_iG_05 (see Table 7.4), where $\Gamma = 1$ and calculations continue until $t' = 0.8$ (Fig. 7.24). I find within most of the Tibetan Plateau that $q < 0.5$ (Fig. 7.24a, b) and that the z-component of the strain-rate tensor retains positive values of(Fig. 7.24c), inferring a similar dominance of thrust faulting. South of the Tarim Basin $0.25 < q < 0.325$, infers a component of strike-slip faulting that is less than thrust faulting. This is in contrast to the present day Altyn Tagh Fault (Fig. 3.1) where deformation is principally accommodated through strike-slip movement. In the area north of the eastern syntaxis $0.325 < q < 0.5$, suggesting a greater proportion of strike-slip over thrust faulting. This is in agreement with earthquake focal mechanism in this region (Taylor and Yin, 2009). That the modelled $\dot{E}$ is greater around the east syntaxis than elsewhere in the Plateau further suggests that within this region the India convergence is principally accommodated through strike-slip faulting at $t' = 0.8$.

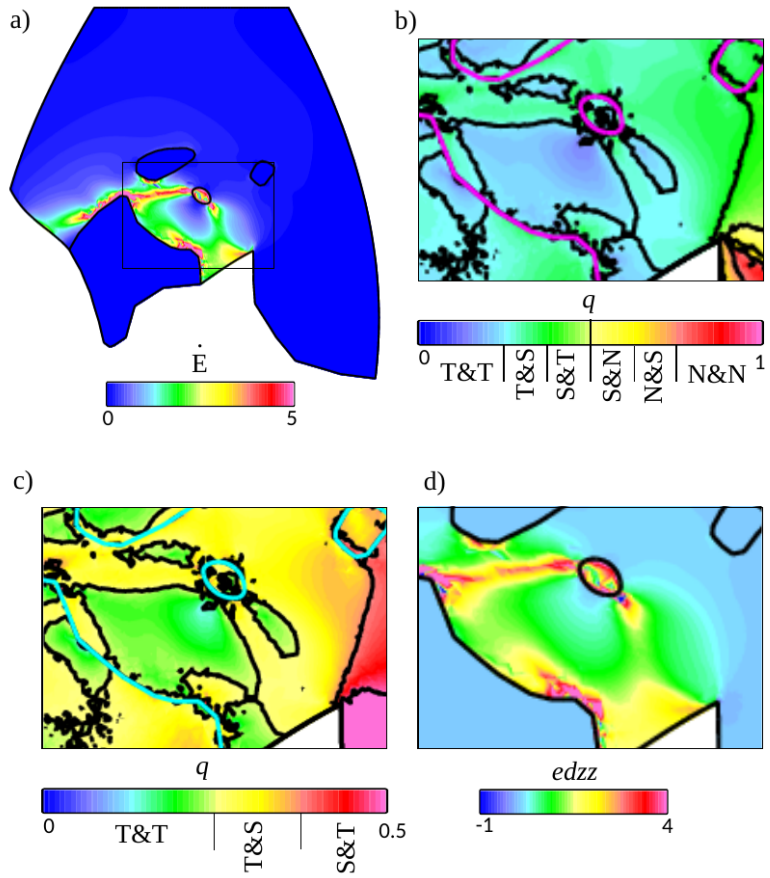

Figure 7.23: For Γ *= 5,* n *= 3,* Ar *= 1 at* t′ *= 0.2 (experiment IA_iG_08, Table 7.3). a) Colour contour plot of* Ė*. Black rectangle shows location of the following figures. b, c) Colour contours of* q *(Eq. 7.3) used to infer style of faulting in the overlaying brittle crust. Coloured lines mark the internal boundaries; c is rescaled to better identify proportion of thrust and strike-slip faulting in the Plateau. See Fig. 7.22 for letter key. d)* $\dot{\varepsilon}_{zz}$ *colour contour plot; black lines mark the external and internal boundaries.*

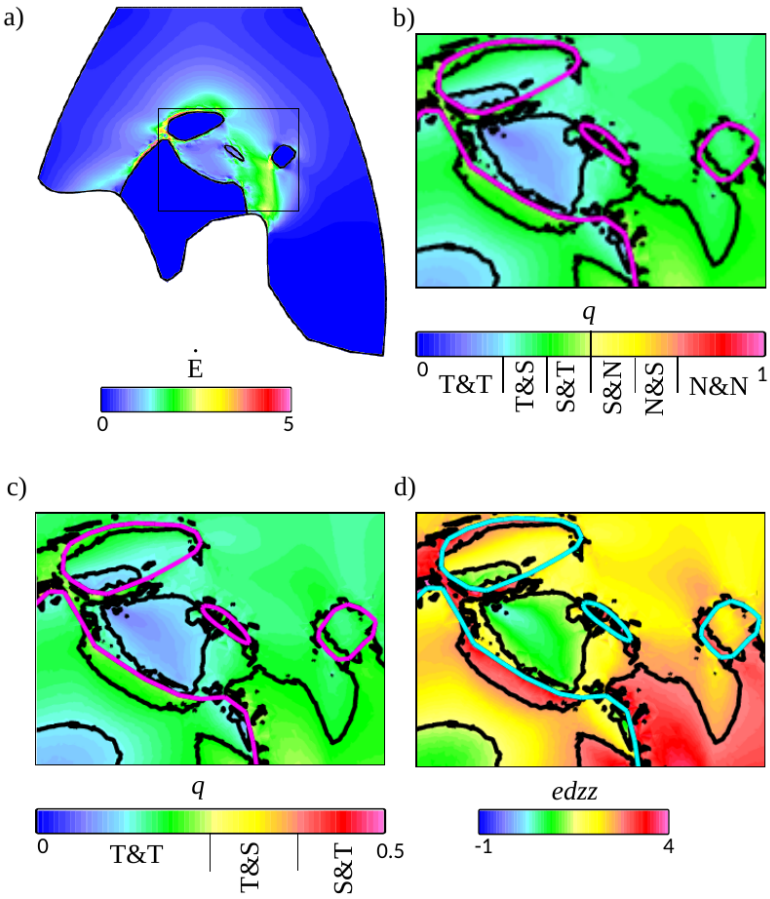

Figure 7.24: For Γ = *1,* n = *3,* Ar = *1 at* t′ = *0.9 (experiment IA_iG_05, Table 7.3). a) Colour contour plot of* Ė. *Black rectangle shows location of the following figures. b, c) Colour contours of* q *(Eq. 7.3) used to infer style of faulting in the overlaying brittle crust. Coloured lines mark the internal boundaries; c is rescaled to better identify proportion of thrust and strike-slip faulting in the Plateau. See Fig. 7.22 for letter key. d)* $\dot{\varepsilon}_{zz}$ *colour contour plot; black lines mark the external and internal boundaries.*

The absence of inferred normal faulting in experiments IA_iG_05 (Γ = 1) and IA_iG_08 (Γ = 5) contrasts with the present day observations. Extension and associated normal faulting in a region subject to continued continental convergence has been attributed to gravitational collapse once the Himalayan orogen has achieved a critical elevation

(Burchfiel and Royden, 1985; Molnar and Tapponnier, 1978). A solution to this has been proposed that requires a rapid change in gravitational potential energy linked to the thermal evolution of the thickened lithosphere (Copley and McKenzie, 2007; England and Houseman, 1989; Molnar et al., 1993). Including this process here goes beyond the scope of the present study (see section 1.3.4). In my experiments, at the final time-step before the calculation terminates due to mesh distortion, the average elevation across the Tibetan Plateau away from the boundary of indenting India is ~ 5.5 km for $\Gamma = 1$ ($t' = 0.2$) and ~ 5.5 km for $\Gamma = 1$ ($t' = 0.8$).

For my experiments with the modified Himalayan Front (IA_HF2_xx, see Table 7.4) reduced mesh distortion enables calculations to complete a greater number of time-steps. Consequently when the calculations terminate, the average elevation of the Tibetan Plateau region is higher. For $\Gamma = 5$ (experiment IA_HF2_08) at $t' = 0.2$ the q values infer thrust dominated faulting across the Plateau (Fig. 7.25a, b), and, omitting the region immediately adjacent to the indenting India, the average elevation of the Tibetan Plateau is ~ 1.5 km (see Fig. 7.16). At $t' = 0.9$ the q values infer components of normal faulting across the Tibetan Plateau region (Fig. 7.25c, d), with the average elevation now ~ 8 km. Spatial differences between the inferred and present day normal faulting in Tibet are likely a consequence of the modified Himalayan Front.

My experiments follow that of present day behaviour — the lithosphere supports a maximum topographical load that is limited through crustal extension. That my experiments require a higher elevation than present day Tibet to initiate normal faulting suggests either the modelled regional viscosity is too high, or that the ratio of gravitational forces to boundary driven forces is insufficient (Ar needs to increase).

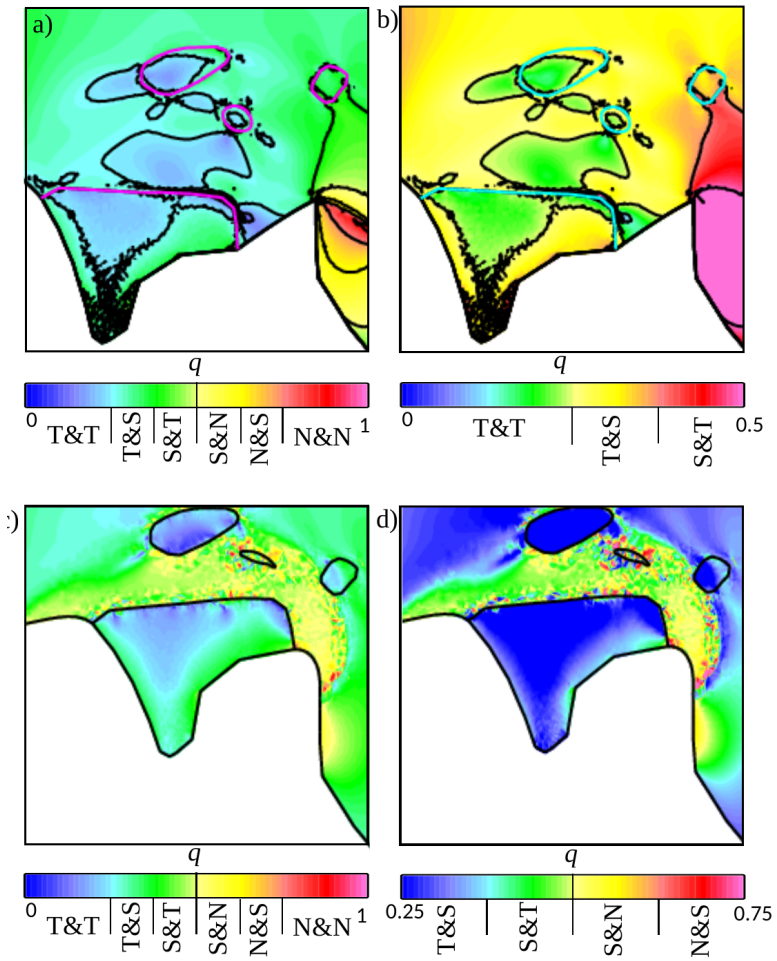

Figure 7.25: For Γ *= 5,* n *= 3,* Ar *=1 with modified Himalayan Front (see Table 7.4 experiment IA_HF2_08), showing India, Tarim and Sichuan Basins and Tibetan Plateau. a, b). Contour plot of of* q *(Eq. 7.3) values at t′ = 0.2. Internal black lines show contours, coloured lines show internal boundaries. c, d). Colour contour plot of* q *values at* t′ *= 0.9. Contour lines omitted for clarity, black lines show internal and external boundaries. See Fig. 7.22 for letter key.*

7.7 Implications for the geological make-up, setting and rheological feedbacks within the Tibetan Plateau

In these India-Asia experiments spatial variations in strain-rate, in association with regions of contrasting strength, develop with the continued indentation of India into Asia. My experiments show strain-rates at strength boundaries are higher in the weaker region. Localised strain can still develop within the stronger region, e.g. the Central Shear Zone (Fig.7.6), where strain localises in an initially stronger Asia region (where VC = 1 at $t' = 0$) surrounding the weak inclusion (where VC = 0.5 at $t' = 0$), but not within the India and Basin regions (where VC = 10 at $t' = 0$). This suggests that variations in present day strain-rates across the Tibetan Plateau (Kreemer et al., 2014) could be attributed to spatial variations in strength in the proto-Plateau region. Thus modelling the proto-Tibetan Plateau as a number of weak regions in a strong matrix is likely to be a gross simplification. Such inferences are in agreement with present day variation in lithology (e.g. Royden et al., 2008), but differences in temperature and fluid content through time may also contribute to local strength variation. Consequently inherited localisation (Montési and Zuber, 2002) may be the principal means by which strain localisation is initiated.

In contrast to previous thin viscous sheet models of the India-Asia convergence, that have suggested strain localisation requires large values of n (~ 10, representing plastic deformation, Dayem et al., 2009), I have shown that strain localisation can occur for n = 3, provided a strain-weakening mechanism is active. This suggests that strain localisation requires a decrease in lithosphere strength through time, i.e. a form of weakening is required. Thus strain localisation across the Tibetan Plateau could initiate

and grow for a strain ($\Gamma > 0$) or strain-rate ($n > 1$) weakening mechanism, or a combination of both.

In all India-Asia experiments I set an initial ($t' = 0$) uniform elevation of 0 km across the domain. With increasing time the elevation increase is greater in weaker regions and, in general, the final elevation of India and the Basins < Tibetan Plateau < weak inclusion. Furthermore in regions where viscosity reduces with time the topography growth increases. This implies that topography growth is linked to relative lithosphere strength. The present day average elevations of the Tarim Basin, Sichuan Basin, Tibetan Plateau and Himalaya are ~ 3,100 m, ~ 1,700 m, ~ 5,000 m, and ~ 6,100 m respectively. This suggests that the Tibetan Plateau and Himalayas were either relatively weak at the onset of deformation, or have become weaker with time through a strain-weakening mechanism. For a work dependent strain-weakening the deformation contributing to orogenic growth may result in viscosity reduction that further enhances the height of the orogen. However, the maximum supported topographical load relates to the lithosphere viscosity (England and McKenzie, 1982). Therefore a final elevation will depend on the balance between a sufficiently weak lithosphere to permit elevation increase and a sufficiently strong lithosphere to limit orogenic collapse.

In either group of experiments (original and modified Himalayan Front, IA_iG_xxx and IA_HF2_xxx, Table 7.3, 7.4) the reduction in area between the basins and India is accommodated by an increase in elevation (section 6.3.1). That the elevation growth is less when the modelled basins are absent (experiments IA_ref_01, IA_ref_05, Table 6.1) suggests that Tibetan lithosphere flow away from the indenting India is restricted by the basins. Consequently, stronger regions around the Tibetan Plateau act not only to

focus localised deformation, but are critical for elevation growth of the Tibetan Plateau. Similarly others have proposed that high topography in eastern Tibet can be explained by lower crustal flow obstructed by a strong Sichuan Basin (Clark et al., 2005).

In experiments for $Ar > 0$ differences in elevation are associated with enhanced shear-zone development ($\dot{E}$ increases). This suggests that, in addition to boundary forces, topographical gradients contribute to deformation. Consequently orogenic activity (e.g. Himalaya and Kunlun Mountains, Fig. 1.3), already a region of high strain, may further contribute to variation in strain-rates across the Tibetan Plateau. Such arguments have previously been presented regarding the relationship between elevation and the development of an extensional and associated normal faulting regime (e.g. Burchfiel and Royden, 1985; Molnar and Tapponnier, 1978). However, given for most of my India-Asia experiments inferred thrust faulting dominates in the overlaying brittle layer (section 7.6) then I suggest topographical gradients may also contribute to thrust faulting.

The India-Asia experiments show how an initial increase and decrease of strain-rates in one area can be accompanied by a concurrent zero to increase in strain-rates in another area (section 7.4.3). Strain transfer between different surface structures has been proposed for regions within the Tibetan Plateau (e.g. Burchfiel et al., 1989; Li et al., 2018) and inferred in other tectonic settings, such as the strike-slip San Andreas Fault system (Walker et al., 2005) and the Afar rift region (Manighetti et al., 2001). Here I have demonstrated how, for a continental convergence problem, strain transfer does not require pre-existing shear-zone structures. Within a continuously deforming lithosphere lateral variation in strain-rates can occur, but the spatial distribution of the highest

strain-rates may vary through time. Such behaviour would explain apparent contradictions in characteristics of the Karakorum Fault (KKF, Fig. 1.3). Here geologically inferred offsets of up to 555 km (Replumaz and Tapponnier, 2003), have been taken to support block deformation of Tibet (Klemperer et al., 2013; Replumaz and Tapponnier, 2003). In contrast, present day zero to low geodetic slip-rates (0 to 6 mm. yr^{-1}, Wang and Wright, 2012) are used to argue for continuous deformation of Tibet. My experiments show that a continuum model of continental convergence can support the growth and later abandonment of shear-zones, thus explaining how a shear zone may have large offsets with a present day low slip-rate.

7.8 Summary of results from India-Asia model

Using the initial model developed in Chapter Six with the addition of a circular weak region I explored how varying the strain-weakening parameter (Γ) and Himalayan Front geometry initiates and maintains localised shear zones across and adjacent to the Tibetan Plateau. I find that shear-zone development occurs in an initially near homogeneous region, and is linked to topography growth (dynamic localisation), the strain-weakening parameter (dynamic localisation), and stress concentrations associated with the weak region (inherited properties) and the Himalayan Syntaxes (inherited properties and imposed localisation).

Increases in topography gradients causes a corresponding increase in crustal thickening rates (and strain-rates) in the lower elevation region. The topography gradient between the Tibetan Plateau and the lower elevation Tarim Basin forms the South Tarim Shear

Zone. Preferential deformation on the weak region initiates the Central Shear Zone. The elevation growth associated with the Central Shear Zone further increases the topography gradient between the Plateau and the Tarim Basin, and enhances localisation of the South Tarim Shear Zone.

For zones of localised shear to form across the Plateau the strain-weakening parameter, Γ, must be at least 2. At a given time the maximum strain-rate in any shear zone is greater and the shear-zone width less with increasing Γ. For $\Gamma > 3$ the lithosphere weakening within the Central Shear Zone is such that deformation is preferentially accommodated here rather than on the South Tarim Shear Zone.

Increased buoyancy forces can resist horizontal deformation, and reduce strain-rates in high elevation regions. For $\Gamma = 2$ and 3, the increase in buoyancy forces with time becomes sufficient that horizontal deformation is resisted and with further time the high strain-rates associated with the west Central Shear Zone reduce. With increasing Γ the reduction in averaged lithosphere viscosity with time reduces the crustal elevation that can be supported. For $\Gamma = 5$ the limitation on elevation growth prevents buoyancy forces becoming sufficiently high to resist the horizontal forces, and the west Central Shear Zone develops with time.

Linkage of stress concentrations at the Western Himalaya Syntaxis and the weak region enhances deformation in the Central Shear Zone. In the absence of the Western Syntaxis the largest stress concentration occurs at the Eastern Syntaxis. This links with stress concentrations at the Sichuan Basin. For $\Gamma \geq 2$ with increasing time the North Plateau Shear Zone grows along the east and north side of the Plateau, where the topography

gradient is high. With increasing Γ the reduction in the Tibetan Plateau viscosity causes outward growth of the high elevation Plateau and the North Plateau Shear Zone.

8 Conclusions

8.1 Purpose of this study

This thesis has shown how a low-viscosity domain embedded in a region subject to simple-shear that includes a strain-weakening mechanism influences the temporal and spatial distribution of strain. Strain-rate in a shear-zone is quantified using a power-law growth. The same model, representing a horizontal section of the lithosphere, is used to calculate the maximum depth to which a thermally activated strain-weakening mechanism can produce shear-zone localisation in the lithosphere. This thesis has also shown how a strain-weakening mechanism within a model of the India-Asia convergence from 47 Ma to the present day can promote strain localisation across the Tibetan Plateau away from the boundary of high- or low-viscosity domains.

8.2 Summary of the main research findings into strain localisation

For a circular low-viscosity domain embedded in a region subject to simple-shear where strain-weakening is active, zones of shear develop either side of the weak domain parallel to the direction of shear. The temporal and spatial evolution of the shear zones is dependent on the relative viscosity of the weak domain (Λ), strain exponent (n), strain-weakening parameter (Γ_0') and a recovery parameter (β). Here Γ_0' and β represent shear-heating and thermal diffusion respectively. Strain localisation requires a power-law rheology ($n \geq 2$) and a rate of strain-weakening ($\Gamma_0' \geq 0.3$) that is dependent on Λ, n, and β. For the ideal case of no thermal diffusion ($\beta = 0$) thermally activated shear-zone localisation grows faster than exponential and after a finite time, dependent on n and Γ_0', the shear zone collapses to a planar discontinuity, the equivalent of a geological fault.

Including a large thermal diffusion component ($\beta \sim 10$ for $n = 3$ or 5) suppresses strain localisation, but lower values of β extend the time it takes for localisation to develop.

I used results from this two-dimensional model together with published constitutive laws based on deformation experiments for quartz, plagioclase and olivine to show there is a maximum depth to which a thermally activated strain-weakening mechanism supports localisation in the lithosphere. The localisation depth is dependent on mineralogy, temperature and water fugacity and, to a lesser extent, strain-rate. Quartz, plagioclase and olivine successively support greater localisation depths. The maximum depth of localisation deepens with increasing background strain-rate and shallows for increasing surface heat-flow. For a given lithology and temperature the presence of pore-fluid pressure decreases the maximum localisation depth.

Comparison of my calculations with geophysical data from four major continental strike-slip faults is generally consistent with predicted maximum localisation depth and allows inferences to made on the hydrous state of the lithosphere. For the San Andreas Fault Zone (SAFZ) and North Anatolian Fault Zone (NAFZ) receiver function data suggests localisation affects the uppermost mantle. My calculations support localisation below the Moho to 42 (SAFZ) and 49 km (NAFZ) for a dry olivine lithology. Localisation of the SAFZ or NAF to the base of the lithosphere is not supported by the calculations or the geophysical data. I looked at two fault zones within the Tibetan Plateau, the Kunlun Fault (KF) and Haiyuan Fault Zone (HFZ). Seismic reflection data suggest the KF reaches 35 km before terminating against a décollement. Localisation to these depths requires a lower crust with rheology comparable to dry plagioclase.

Seismic reflection data infer the HFZ is localised to 15 to 21 km, is listric with depth, and terminates at a 40 km deep décollement. From my calculations a lower crust hydrous plagioclase lithology best matches the inferred localisation depth. My calculations do not support localisation of the KF and HFZ below the 55 km and 50 km Moho.

Strain localisation within the Tibetan Plateau occurs on a number of large (> 100 km) shear zones. To explore how such shear zones form, I developed a thin viscous sheet model representing the India-Asia convergence from 47 Ma ($t' = 0$) to the present day ($t' = 1$). The model included the Tarim and Sichuan Basins as regions that are more resistant to deformation. This is the first study to use time-dependent spherical shell calculations with plate boundary conditions defined by Euler poles in the finite element program *basil*. At $t' = 1$ the model approximately represents the current elevation of the Tibetan Plateau where a non-Newtonian rheology applies and $n = 3$. The Tarim and Sichuan Basins inhibit flow away from the Plateau contributing to the high elevation of the Plateau. At $t' = 1$ the modelled dimensionless velocity field in the west and central Tibetan Plateau is comparable to that derived from geodetic measurements; in the east Plateau the clockwise rotation of modelled velocity does not adequately represent the observed geodetic velocity. Inclusion of a low-viscosity domain within the Tibetan Plateau allows a linear region of high shear strain to develop across the Plateau, linking the weak region and the Western Himalaya Syntaxis. This requires a high strain-weakening rate ($\Gamma' > 2$).

8.3 Significance of the findings in the context of lithosphere deformation

These numerical experiments show how, for a thin viscous sheet approximation of long term lithosphere deformation, a low-viscosity domain can localise strain away from domain boundaries when subject to either simple-shear or a combination of simple- and pure-shear. Strain localisation requires an initial strength heterogeneity, a non-Newtonian rheology (strain exponent, $n > 1$) and a viscous coefficient which decreases with strain, at a rate which is dependent on n. Within the Tibetan Plateau strain localisation away from domain boundaries occurs on a number of shear zones, whose location may correspond with geodetically derived high strain-rates. Micro-plate models assume the pre-existence of such high strain regions but I have shown how a continuum model can initiate and grow localised deformation within a region of generally diffuse deformation.

For an overall increase in strain with time any shear zone deformation may be influenced by other shear-zones, either through transfer of preferential deformation or by linkage enhancing strain localisation. This suggests that multiple shear-zone growth cannot be viewed as a set of independent events, but a set of processes that potentially feedback to each other.

This study provides a basis for the quantification of strain-localisation in thin viscous sheet models. When considering a horizontal section of the lithosphere the change in strain rate as a shear zone localises follows a power-law dependence which is primarily dependent on the strain exponent (n) and initial strain-weakening parameter (Γ_0'). The finite depth to which a thermally activated strain-weakening mechanism supports strain

localisation in the continental lithosphere is primarily dependent on mineralogy, hydrous state and temperature.

I have shown how comparable localisation depths are obtained from inferences of seismic data and calculations using differing parameters for an experimentally derived flow law. This suggests that as a first order an appropriate experimentally derived flow law can represent the lithosphere rheology. Parameters for such flow laws are typically obtained for a single mineral, generally quartz, feldspar or olivine which are sufficiently abundant in the upper crust, lower crust or upper mantle respectively, and weak enough to preferentially accommodate deformation. Tectonic setting influences lithosphere thickness (and hence the depths at which mineralogy changes), the geothermal gradient, and the presence of fluids. Increased temperature and fluid content will decrease the depth of the brittle-ductile transition, i.e. the depth at which frictional strength is limited by sufficient decrease in viscous strength (section 1.2). Inferences on mineralogy and fluid content derived from tectonic environment, seismic data and geological samples will influence the choice of parameters used in the flow-law. That a localisation depth for a given geothermal gradient can be calculated using experimentally derived parameters for a flow law does not implicitly state where a mineralogy is dominant. Rather I have shown how in different tectonic environments the rheology at different depths can be described using a quartz, plagioclase or olivine flow law for a wet or dry mineralogy.

Crustal thickness is the principal determinant of whether localisation is limited to the lower crust (e.g. Kunlun and Haiyuan Fault Zones) or extends deeper than the Moho (e.g. San Andreas and North Anatolia Fault Zones). Where only a small (< 30%)

proportion of lithosphere thickness supports localisation it suggests that the long term deformation of the lithosphere is consistent with a continuum model. Localisation to ~ 50% lithosphere thickness requires a dry olivine lithology and a relatively low surface-heat flow for the relevant lithosphere thickness (e.g. 40 $mW.m^{-2}$ where the lithosphere is 120 km thick, Fig.4.2c). That tectonic setting is a major influence on crustal thickness (e.g. generally considerably thinner at rift than convergent margins) further suggests that the tectonic environment is a contributing factor to the proportion of localised versus diffuse deformation.

8.4 Limitations of this study

Throughout this thesis I have used a thin viscous sheet approximation in which the horizontal gradients of strain are invariant with depth. Consequently differences in upper and lower crustal flow, which may be occurring beneath Tibet, are excluded from the model. Time-dependent three-dimensional models are computationally expensive and the use of a two-dimensional approximation has enabled a wider exploration of the parameter space.

In calculating the maximum localisation depth I have considered only a thermal weakening mechanism. By neglecting other strain-weakening mechanisms, such as grain size changes that may support localisation within the mantle lithosphere, I may have underestimated the maximum supported localisation depth. On the other hand by disregarding recovery mechanisms, such as thermal diffusion, I may have over-estimated the depth to which a thermal weakening localisation mechanism is supported. However, my calculations of maximum localisation depth for continental strike-slip

faults broadly agree with seismic data interpretations, suggesting shear-heating could be an important localisation mechanism and it is not suppressed by thermal diffusion in the high strain rate zones of these major fault systems.

Application of alternative strain-weakening mechanisms must consider the conditions under which they are active. Grain size sensitive (GSS) diffusion creep dominates below a threshold grain size, and grain size changes are themselves dependent on pressure and temperature (e.g. Braun et al., 1999). A strain-weakening mechanism representing grain size changes in the diffusion creep regime may require an initial reduction in grain size before GSS creep is active. Recovery is linked to grain growth and once the threshold grain size is exceeded then GSS creep no longer acts as a weakening mechanism. Depending on the initial assumptions of grain size, pressure and temperature a greater total strain could be needed prior to onset of strain localisation.

Strain-weakening through fabric development may only be significant in some mineralogies (e.g. Escartín et al., 2001; Holyoke and Tullis, 2006a) and, given lithological variation with depth, in certain portions of the lithosphere. Strain-weakening is enhanced when grain rotation leads to alignment of weaker crystal planes with the principal stress direction (e.g. Holyoake and Tullis, 2006b). Mineral dependence of fabric development will vary the rate of growth of strain localisation with depth. For an averaged lithosphere rheology the proportion of lithosphere for which strain-weakening through fabric development is active must be considered. For a constant stress regime a recovery mechanism is not needed. Significant changes in principal stresses may act to reset fabric development.

In calculating the maximum localisation depth I considered the lithosphere as a series of two-dimensional horizontal layers. This simplified approach does not consider the interaction between horizontal layers. In the India-Asia experiments I showed how linkage of stress concentrations enhanced localisation, and a similar process may occur between horizontal layers.

In using an Argand number (*Ar*) (the ratio between the boundary forces to deform the domain at a nominal strain rate and the vertically averaged deviatoric stress arising from crustal thickness contrasts) in the continental convergence problem I consider topographical changes only in relation to changes in crustal thickness. I neglect any contribution from the under-thrusting Indian Plate that may act to dynamically maintain topography (e.g. Owens and Zandt, 1997) or contribute to rotation of the Tarim Basin (Craig et al., 2012). The resultant increased gradients of topography would enhance local strain-rates. By assuming instantaneous isostatic equilibrium any transient strain during isostatic adjustment is ignored, but quantification of deformation arising from isostatic adjustment within the 47 Ma convergence process is uncertain. In assuming zero basal traction the contribution of basal drag from the subducting slab (see Pusok and Kaus, 2015) to viscous wedge formation is neglected.

8.5 Recommendations arising from this study for further research in lithosphere deformation

A natural progression of this work is to explore the impact that multiple low-viscosity domains may have on the temporal and spatial distribution of strain in a continuum

model. Would resultant shear zones link? Or would they develop into independent shear zones? How is the localisation depth influenced by contact with layers above and below that I have treated in isolation?

Further research on localisation depth could explore different strain-weakening mechanisms, notably grain-size changes in the diffusion creep regime. Do other weakening mechanisms allow localisation to occur at greater depths than are possible with a thermal weakening process? Are we able to distinguish which weakening mechanism is enabling localisation in the lithosphere? Additional modelling work could quantify how the juxtaposition of different temperature materials caused by dip-slip in shear zones influences localisation depth

In showing how localised strain might develop in a generally diffuse deformation field I have taken steps towards quantifying the relative contributions of localised versus diffuse deformation in regions like the Tibetan Plateau. Further work could quantify these types of deformation and assess their relative importance in lithosphere deformation.

References

Adams, R.D., Harris, J.A., 1987. The influence of local geometry on the strength of adhesive joints. International Journal of Adhesion and Adhesives 7, 69–80. https://doi.org/10.1016/0143-7496(87)90092-3

Allam, A.A., Ben-Zion, Y., 2012. Seismic velocity structures in the southern California plate-boundary environment from double-difference tomography. Geophys. J. Int. 190, 1181–1196. https://doi.org/10.1111/j.1365-246X.2012.05544.x

Altuncu-Poyraz, S., Teoman, M.U., Türkelli, N., Kahraman, M., Cambaz, D., Mutlu, A., Rost, S., Houseman, G.A., Thompson, D.A., Cornwell, D., Utkucu, M., Gülen, L., 2015. New constraints on micro-seismicity and stress state in the western part of the North Anatolian Fault Zone: Observations from a dense seismic array. Tectonophysics 656, 190–201. https://doi.org/10.1016/j.tecto.2015.06.022

Amante, C., Eakins, B.W., 2009. ETOPO1 1 Arc-Minute Global Relief Model: Procedures, Data Sources and Analysis. National Geophysical Data Center. https://doi.org/10.7289/V5C8276M

An, M., Shi, Y., 2006. Lithospheric thickness of the Chinese continent. Physics of the Earth and Planetary Interiors 159, 257–266. https://doi.org/10.1016/j.pepi.2006.08.002

Avouac, J.-P., Tapponnier, P., 1993. Kinematic model of active deformation in central Asia. Geophysical Research Letters 20, 895–898. https://doi.org/10.1029/93GL00128

Aydin, A., Schultz, R.A., 1990. Effect of mechanical interaction on the development of strike-slip faults with echelon patterns. Journal of Structural Geology 12, 123–129. https://doi.org/10.1016/0191-8141(90)90053-2

Baris, S., Nakajima, J., Hasegawa, A., Honkura, Y., Ito, A., Ucer, B., 2005. Three-dimensional structure of Vp, Vs and Vp/Vs in the upper crust of the Marmara region, NW Turkey. Earth Planets Space 57, 1019–1038. https://doi.org/10.1186/BF03351882

Beaumont, C., Muñoz, J.A., Hamilton, J., Fullsack, P., 2000. Factors controlling the Alpine evolution of the central Pyrenees inferred from a comparison of observations and geodynamical models. J. Geophys. Res. Solid Earth 105, 8121–8145. https://doi.org/10.1029/1999JB900390

Ben-Zion, Y., Sammis, C.G., 2013. Shear heating during distributed fracturing and pulverization of rocks. Geology 41, 139–142.

Bercovici, D., Ricard, Y., 2012. Mechanisms for the generation of plate tectonics by two-phase grain-damage and pinning. Physics of the Earth and Planetary Interiors 202–203, 27–55. https://doi.org/10.1016/j.pepi.2012.05.003

Bernard, R.E., Behr, W.M., 2017. Fabric heterogeneity in the Mojave lower crust and lithospheric mantle in Southern California. Journal of Geophysical Research: Solid Earth 122, 5000–5025. https://doi.org/10.1002/2017JB014280

Best, M G, 2003. Igneous and metamorphic petrology. Blackwell Science.

Bird, P., 2003. An updated digital model of plate boundaries. Geochemistry, Geophysics, Geosystems 4. https://doi.org/10.1029/2001GC000252

Bird, P., Piper, K., 1980. Plane-stress finite-element models of tectonic flow in southern California. Physics of the Earth and Planetary Interiors 21, 158–175. https://doi.org/10.1016/0031-9201(80)90067-9

Brace, W.F., Kohlstedt, D.L., 1980. Limits on lithospheric stress imposed by laboratory experiments. J. Geophys. Res. 85, 6248–6252. https://doi.org/10.1029/jb085ib11p06248

Bradbury, K.K., Evans, J.P., Chester, J.S., Chester, F.M., Kirschner, D.L., 2011. Lithology and internal structure of the San Andreas fault at depth based on characterization of Phase 3 whole-rock core in the San Andreas Fault Observatory at Depth (SAFOD) borehole. Earth Planet. Sci. Lett. 310, 131–144. https://doi.org/10.1016/j.epsl.2011.07.020

Braun, J., Chéry, J., Poliakov, A., Mainprice, D., Vauchez, A., Tomassi, A., Daignières, M., 1999. A simple parameterization of strain localization in the ductile regime due to grain size reduction: A case study for olivine. J. Geophys. Res. 104, 25167–25181. https://doi.org/10.1029/1999jb900214

Brun, J.-P., 2002. Deformation of the continental lithosphere: Insights from brittle-ductile models. Geol. Soc. Spec. Publ. 200, 355–370. https://doi.org/10.1144/GSL.SP.2001.200.01.20

Brun, J.P., Cobbold, P.R., 1980. Strain heating and thermal softening in continental shear zones: a review. J. Struct. Geol. 2, 149–158. http://dx.doi.org/10.1016/0191-8141(80)90045-0

Burchfiel, B.C., Quidong, D., Molnar, P., Royden, L., Yipeng, W., Peizhen, Z., Weiqi, Z., 1989. Intracrustal detachment within zones of continental deformation. Geology 17, 748–752. https://doi.org/10.1130/0091-7613(1989)017<0448:IDWZOC>2.3.CO;2

Burchfiel, B.C., Royden, L.H., 1985. North-south extension within the convergent Himalayan region. Geology 13, 679–682. https://doi.org/10.1130/0091-7613(1985)13<679:NEWTCH>2.0.CO;2

Burchfiel, B.C., Zhiliang, C., Yupinc, L., Royden, L.H., 1995. Tectonics of the Longmen Shan and Adjacent Regions, Central China. International Geology Review 37, 661–735. https://doi.org/10.1080/00206819509465424

Burg, J.-P., Schmalholz, S.M., 2008. Viscous heating allows thrusting to overcome crustal-scale buckling: Numerical investigation with application to the Himalayan syntaxes. Earth Planet. Sci. Lett. 274, 189–203. https://doi.org/10.1016/j.epsl.2008.07.022

Burgmann, R., Dresen, G., 2008. Rheology of the Lower Crust and Upper Mantle: Evidence from Rock Mechanics, Geodesy, and Field Observations. Annu. Rev. Earth Planet. Sci. 36, 531–67. https://doi.org/10.1146/annurev.earth.36.031207.124326

Burov, E.B., Diament, M., 1995. The effective elastic thickness (T e) of continental lithosphere: What does it really mean? J. Geophys. Res. 100, 3905–3927. https://doi.org/10.1029/94jb02770

Byerlee, J., 1978. Friction of rocks. Pure Appl. Geophys 116, 615–26.

Calais, E., Dong, L., Wang, M., Shen, Z., Vergnolle, M., 2006. Continental deformation in Asia from a combined GPS solution. Geophys. Res. Lett. 33.

Calignano, E., Sokoutis, D., Willingshofer, E., Gueydan, F., Cloetingh, S., 2015a. Strain localization at the margins of strong lithospheric domains: Insights from analog models. Tectonics 34, 396–412. http://dx.doi.org/10.1002/2014TC003756

Calignano, E., Sokoutis, D., Willingshofer, E., Gueydan, F., Cloetingh, S., 2015b. Asymmetric vs. symmetric deep lithospheric architecture of intra-plate continental orogens. Earth and Planetary Science Letters 424, 38–50. http://dx.doi.org/10.1016/j.epsl.2015.05.022

Cavalié, O., Lasserre, C., Doin, M.-P., Peltzer, G., Sun, J., Xu, X., Shen, Z.-K., 2008. Measurement of interseismic strain across the Haiyuan fault (Gansu, China), by InSAR. Earth and Planetary Science Letters 275, 246–257. https://doi.org/10.1016/j.epsl.2008.07.057

Cerca, M., Ferrari, L., Bonini, M., Corti, G., Manetti, P., 2004. The role of crustal heterogeneity in controlling vertical coupling during Laramide shortening and the development of the Caribbean-North America transform boundary in southern Mexico: insights from analogue models. Geol. Soc. Spec. Publ. 227, 117–139. https://doi.org/10.1144/GSL.SP.2004.227.01.07

Chang, H., An, Z., Liu, W., Ao, H., Qiang, X., Song, Y., Lai, Z., 2014. Quaternary structural partitioning within the rigid Tarim plate inferred from magnetostratigraphy and sedimentation rate in the eastern Tarim Basin in China. Quaternary Research 81, 424–432. https://doi.org/10.1016/j.yqres.2013.10.018

Chatzaras, V., Tikoff, B., Newman, J., Withers, A.C., Drury, M.R., 2015. Mantle strength of the San Andreas fault system and the role of mantle-crust feedbacks. Geology 43, 891–894. https://doi.org/10.1130/G36752.1

Chen, P., Zhao, L., Jordan, T.H., 2007. Full 3D Tomography for the Crustal Structure of the Los Angeles Region. BSSA 97, 1094. https://doi.org/10.1785/0120060222

Chen, Q., Freymueller, J.T., Wang, Q., Yang, Z., Xu, C., Liu, J., 2004. A deforming block model for the present-day tectonics of Tibet. Journal of Geophysical Research: Solid Earth 109, B01403. http://dx.doi.org/10.1029/2002JB002151

Chen, S.F., Wilson, C.J.L., 1996. Emplacement of the Longmen Shan Thrust Nappe Belt along the eastern margin of the Tibetan Plateau. Journal of Structural Geology 18, 413–430. https://doi.org/10.1016/0191-8141(95)00096-V

Chen, W.-P., Molnar, P., 1983. Focal depths of intracontinental and intraplate earthquakes and their implications for the thermal and mechanical properties of the lithosphere. J. Geophys. Res. 88, 4183–4214. https://doi.org/10.1029/jb088ib05p04183

Chu, D., Gordon, R.G., 1999. Evidence for motion between Nubia and Somalia along the Southwest Indian ridge. Nature 398, 64–67.

Clark, M.K., Bush, J.W.M., Royden, L.H., 2005. Dynamic topography produced by lower crustal flow against rheological strength heterogeneities bordering the Tibetan Plateau. Geophysical Journal International 162, 575–590. https://doi.org/10.1111/j.1365-246x.2005.02580.x

Clark, M.K., Royden, L.H., 2000. Topographic ooze: Building the eastern margin of Tibet by lower crustal flow. Geology 28, 703. https://doi.org/10.1130/0091-7613(2000)28<703:TOBTEM>2.0.CO;2

Cloetingh, S., Wees, J.D. van, Ziegler, P.A., Lenkey, L., Beekman, F., Tesauro, M., Förster, A., Norden, B., Kaban, M., Hardebol, N., Bonté, D., Genter, A., Guillou-Frottier, L., Voorde, M.T., Sokoutis, D., Willingshofer, E., Cornu, T., Worum, G., 2010. Lithosphere tectonics and thermo-mechanical properties: An integrated modelling approach for Enhanced Geothermal Systems exploration in Europe. Earth Sci. Rev. 102, 159–206. https://doi.org/10.1016/j.earscirev.2010.05.003

Cook, K.L., Royden, L.H., 2008. The role of crustal strength variations in shaping orogenic plateaus, with application to Tibet. Journal of Geophysical Research 113. https://doi.org/10.1029/2007jb005457

Copley, A., Avouac, J.-P., Royer, J.-Y., 2010. India-Asia collision and the Cenozoic slowdown of the Indian plate: Implications for the forces driving plate motions. Journal of Geophysical Research: Solid Earth 115. https://doi.org/10.1029/2009JB006634

Copley, A., McKenzie, D., 2007. Models of crustal flow in the India-Asia collision zone. Geophysical Journal International 169, 683–698. https://doi.org/10.1111/j.1365-246X.2007.03343.x

Corti, G., Bonini, M., Mazzarini, F., Boccaletti, M., Innocenti, F., Manetti, P., Mulugeta, G., Sokoutis, D., 2002. Magma-induced strain localization in centrifuge models of transfer zones. Tectonophysics 348, 205–218. http://dx.doi.org/10.1016/S0040-1951(02)00063-X

Cowgill, E., Gold, R.D., Xuanhua, C., Xiao-Feng, W., Arrowsmith, J.R., Southon, J., 2009. Low Quaternary slip rate reconciles geodetic and geologic rates along the Altyn Tagh fault, northwestern Tibet. Geology 37, 647–650. https://doi.org/10.1130/G25623A.1

Cowie, P.A., Scholz, C.H., 1992. Physical explanation for the displacement-length relationship of faults using a post-yield fracture mechanics model. J. Struct. Geol. 14, 1133–1148. https://doi.org/10.1016/0191-8141(92)90065-5

Craig, T.J., Copley, A., Jackson, J., 2012. Thermal and tectonic consequences of India underthrusting Tibet. Earth and Planetary Science Letters 353–354, 231–239. https://doi.org/10.1016/j.epsl.2012.07.010

Crameri, F., Kaus, B.J.P., 2010. Parameters that control lithospheric-scale thermal localization on terrestrial planets. Geophysical Research Letters 37. https://doi.org/10.1029/2010GL042921

Dalmayrac, B., Molnar, P., 1981. Parallel thrust and normal faulting in Peru and constraints on the state of stress. Earth and Planetary Science Letters 55, 473–481. https://doi.org/10.1016/0012-821X(81)90174-6

Daout, S., Jolivet, R., Lasserre, C., Doin, M.-P., Barbot, S., Tapponnier, P., Peltzer, G., Sun, J., 2016. Along-strike variations of the partitioning of convergence across the Haiyuan fault system detected by InSAR. Geophysical Journal International 205, 536–547. https://dx.doi.org/10.1093/gji/ggw028

Dayem, K.E., Houseman, G.A., Molnar, P., 2009. Localization of shear along a lithospheric strength discontinuity: Application of a continuous deformation model to the boundary between Tibet and the Tarim Basin. Tectonics 28, TC3002. https://doi.org/10.1029/2008TC002264

Dell'Angelo, L.N., Tullis, J., 1996. Textural and mechanical evolution with progressive strain in experimentally deformed aplite. Tectonophysics 256, 57–82.

DeMets, C., Gordon, R.G., Argus, D.F., 2010. Geologically current plate motions. Geophysical Journal International 181, 1–80. https://doi.org/10.1111/j.1365-246X.2009.04491.x

Domazet, Z., 1996. Comparison of fatigue crack retardation methods. Engineering Failure Analysis 3, 137–147. https://doi.org/10.1016/1350-6307(96)00006-4

Drury, M.R., Vissers, R.L.M., Van der Wal, D., Hoogerduijn Strating, E.H., 1991. Shear localisation in upper mantle peridotites. pure and applied geophysics 137, 439–460. https://doi.org/10.1007/BF00879044

Elliott, J.R., Biggs, J., Parsons, B., Wright, T.J., 2008. InSAR slip rate determination on the Altyn Tagh Fault, northern Tibet, in the presence of topographically correlated atmospheric delays. Geophysical Research Letters 35. https://doi.org/10.1029/2008GL033659

England, P., Houseman, G., 1989. Extension during continental convergence, with application to the Tibetan Plateau. J. Geophys. Res. 94, 17561–17579.

England, P., Houseman, G., 1986. Finite Strain Calculations of Continental Deformation 2. Comparison With the India-Asia Collision Zone. Journal of Geophysical Research 91, 3664–3676. https://doi.org/10.1029/JB091iB03p03664

England, P., Houseman, G., 1985. Role of lithospheric strength heterogeneities in the tectonics of Tibet and neighbouring regions. Nature 315, 297.

England, P., Houseman, G., Nocquet, J.-M., 2016. Constraints from GPS measurements on the dynamics of deformation in Anatolia and the Aegean. J. Geophys. Res. Solid Earth 121, 8888–8916. https://doi.org/10.1002/2016JB013382

England, P., Houseman, G., Sonder, L., 1985. Length scales for continental deformation in convergent, divergent, and strike slip Environments: Analytical and approximate solutions for a thin viscous sheet model. J. Geophys. Res. 90, 3551–3557. https://doi.org/10.1029/JB090iB05p03551

England, P., McKenzie, D., 1982. A thin viscous sheet model for continental deformation. Geophys J. R. astr. Soc. 70, 295–321. https://doi.org/10.1111/j.1365-246X.1982.tb04969.x

England, P., Molnar, P., 2005. Late Quaternary to decadal velocity fields in Asia. J. Geophys. Res. Solid Earth 110. https://doi.org/10.1029/2004JB003541

England, P., Molnar, P., 1997. Active Deformation of Asia: From Kinematics to Dynamics. Science 278, 647–650. https://doi.org/10.1126/science.278.5338.647

England, P., Searle, M., 1986. The Cretaceous-tertiary deformation of the Lhasa Block and its implications for crustal thickening in Tibet. Tectonics 5, 1–14. https://doi.org/10.1029/TC005i001p00001

England, P.C., 1987. Tectonic settings of regional metamorphism - Diffuse continental deformation: length scales, rates and metamorphic evolution. Philosophical Transactions of the Royal Society of London A: Mathematical, Physical and Engineering Sciences 321, 3–22. https://doi.org/10.1098/rsta.1987.0001

Enkelmann, E., Ratschbacher, L., Jonckheere, R., Nestler, R., Fleischer, M., Gloaguen, R., Hacker, B.R., Zhang, Y.Q., Ma, Y.-S., 2006. Cenozoic exhumation and deformation of northeastern Tibet and the Qinling: Is Tibetan lower crustal flow

diverging around the Sichuan Basin? GSA Bulletin 118, 651–671. https://doi.org/10.1130/B25805.1

Escartín, J., Hirth, G., Evans, B., 2001. Strength of slightly serpentinized peridotites: Implications for the tectonics of oceanic lithosphere. Geology 29, 1023–1026. https://doi.org/10.1130/0091-7613(2001)029<1023:SOSSPI>2.0.CO;2

Evans, B., Goetze, C., 1979. The temperature variation of hardness of olivine and its implication for polycrystalline yield stress. J. Geophys. Res. 84, 5505–5524. https://doi.org/10.1029/JB084iB10p05505

Fitch, T.J., 1970. Earthquake mechanisms in the Himalayan, Burmese, and Andaman Regions and continental tectonics in central Asia. Journal of Geophysical Research (1896-1977) 75, 2699–2709. https://doi.org/10.1029/JB075i014p02699

Ford, H.A., Fischer, K.M., Lekic, V., 2014. Localized shear in the deep lithosphere beneath the San Andreas fault system. Geology 42, 295. http://dx.doi.org/10.1130/G35128.1

Fossen, H., Cavalcante, G.C.G., 2017. Shear zones - A review. Earth-Science Reviews 171, 434–455. https://doi.org/10.1016/j.earscirev.2017.05.002

Fossen, H., Rotevatn, A., 2016. Fault linkage and relay structures in extensional settings: A review. Earth-Science Reviews 154, 14–28. https://doi.org/10.1016/j.earscirev.2015.11.014

Gahalaut, V.K., Kundu, B., 2012. Possible influence of subducting ridges on the Himalayan arc and on the ruptures of great and major Himalayan earthquakes. Gondwana Research 21, 1080–1088. https://doi.org/10.1016/j.gr.2011.07.021

Gan, W., Zhang, P., Shen, Z.-K., Niu, Z., Wang, M., Wan, Y., Zhou, D., Cheng, J., 2007. Present-day crustal motion within the Tibetan Plateau inferred from GPS

measurements. J. Geophys. Res. Solid Earth 112, B08416. http://dx.doi.org/10.1029/2005JB004120

Gao, R., Wang, H., Yin, A., Dong, S., Kuang, Z., Zuza, A.V., Li, W., Xiong, X., 2013. Tectonic development of the northeastern Tibetan Plateau as constrained by high-resolution deep seismic-reflection data. Lithosphere 5, 555. http://dx.doi.org/10.1130/L293.1

Gardner, R., Piazolo, S., Evans, L., Daczko, N., 2017. Patterns of strain localization in heterogeneous, polycrystalline rocks - a numerical perspective. Earth and Planetary Science Letters 463, 253–265. https://doi.org/10.1016/j.epsl.2017.01.039

Garthwaite, M.C., Houseman, G.A., 2011. Validity of the thin viscous sheet approximation in models of continental collision. J. Geophys. Res. 116. https://doi.org/10.1029/2010jb007770

Garthwaite, M.C., Wang, H., Wright, T.J., 2013. Broadscale interseismic deformation and fault slip rates in the central Tibetan Plateau observed using InSAR. J. Geophys. Res. Solid Earth 118, 5071–5083. https://doi.org/10.1002/jgrb.50348

Gaudemer, Y., Tapponnier, P., Meyer, B., Peltzer, G., Shunmin, G., Zhitai, C., Huagung, D., Cifuentes, I., 1995. Partitioning of crustal slip between linked, active faults in the eastern Qilian Shan, and evidence for a major seismic gap, the ‘Tianzhu gap’, on the western Haiyuan Fault, Gansu (China). Geophysical Journal International 120, 599–645. https://doi.org/10.1111/j.1365-246X.1995.tb01842.x

Ge, W.-P., Molnar, P., Shen, Z.-K., Li, Q., 2015. Present-day crustal thinning in the southern and northern Tibetan Plateau revealed by GPS measurements. Geophys. Res. Lett. 42, 5227–5235.

Goetze, C., Evans, B., 1979. Stress and temperature in the bending lithosphere as constrained by experimental rock mechanics. Geophysical Journal of the Royal Astronomical Society 59, 463–478. https://doi.org/10.1111/j.1365-246x.1979.tb02567.x

Gordon, R.G., 1998. The Plate Tectonic Approximation: Plate Nonrigidity, Diffuse Plate Boundaries, and Global Plate Reconstructions. Annual Review of Earth and Planetary Sciences 26, 615–642. https://doi.org/10.1146/annurev.earth.26.1.615

Gordon, R.G., DeMets, C., Argus, D.F., 1990. Kinematic constraints on distributed lithospheric deformation in the equatorial Indian Ocean from present motion between the Australian and Indian Plates. Tectonics 9, 409–422. http://dx.doi.org/10.1029/TC009i003p00409

Gordon, R.G., Houseman, G.A., 2015. Deformation of Indian Ocean lithosphere: Evidence for a highly nonlinear rheological law. Journal of Geophysical Research: Solid Earth 120, 4434–4449. https://doi.org/10.1002/2015JB011993

Grujic, D., Mancktelow, N.S., 1998. Melt-bearing shear zones: analogue experiments and comparison with examples from southern Madagascar. J. Struct. Geol. 20, 673–680. http://dx.doi.org/10.1016/S0191-8141(98)00006-6

Gueydan, F., Précigout, J., Montési, L.G.J., 2014. Strain weakening enables continental plate tectonics. Tectonophysics 631, 189–196. https://doi.org/10.1016/j.tecto.2014.02.005

Guillot, S., Garzanti, E., Baratoux, D., Marquer, D., Mahéo, G., de Sigoyer, J., 2003. Reconstructing the total shortening history of the NW Himalaya. Geochemistry, Geophysics, Geosystems 4. https://doi.org/10.1029/2002GC000484

Guo, X., Gao, R., Li, S., Xu, X., Huang, X., Wang, H., Li, W., Zhao, S., Li, X., 2016. Lithospheric architecture and deformation of NE Tibet: New insights on the

interplay of regional tectonic processes. Earth and Planetary Science Letters 449, 89–95. https://doi.org/10.1016/j.epsl.2016.05.045

Harkins, N., Kirby, E., Shi, X., Wang, E., Burbank, D., Chun, F., 2010. Millennial slip rates along the eastern Kunlun fault: Implications for the dynamics of intracontinental deformation in Asia. Lithosphere 2, 247. https://doi.org/10.1130/L85.1

Hirth, G., Kohlstedt, D., 2013. Rheology of the Upper Mantle and the Mantle Wedge: A View from the Experimentalists, in: Eiler, J. (Ed.), Inside the Subduction Factory. American Geophysical Union, pp. 83–05. https://doi.org/10.1029/138GM06

Hirth, G., Kohlstedt, D.L., 1995. Experimental constraints on the dynamics of the partially molten upper mantle: 2. Deformation in the dislocation creep regime. J. Geophys. Res. 100, 15441–15449.

Hirth, G., Teyssier, C., Dunlap, W.J., 2001. An evaluation of quartzite flow laws based on comparisons between experimentally and naturally deformed rocks. International Journal of Earth Sciences 90, 77–87. https://doi.org/10.1007/s005310000152

Holdsworth, R.E., Diggelen, E.W.E. van, Spiers, C.J., Bresser, J.H.P. de, Walker, R.J., Bowen, L., 2011. Fault rocks from the SAFOD core samples: Implications for weakening at shallow depths along the San Andreas Fault, California. J. Struct. Geol. 33, 132–144. https://doi.org/10.1016/j.jsg.2010.11.010

Holyoke III, Caleb W., Tullis, J., 2006a. The interaction between reaction and deformation: an experimental study using a biotite-plagioclase-quartz gneiss. Journal of Metamorphic Geology 24, 743–762. https://doi.org/10.1111/j.1525-1314.2006.00666.x

Holyoke III, Caleb W., Tullis, J., 2006b. Formation and maintenance of shear zones. Geology 34, 105–108.

Horner-Johnson, B.C., Gordon, R.G., Argus, D.F., 2007. Plate kinematic evidence for the existence of a distinct plate between the Nubian and Somalian plates along the Southwest Indian Ridge. J. Geophys. Res. 112. https://doi.org/10.1029/2006JB004519

Houseman, G., England, P., 1993. Crustal thickening versus lateral expulsion in the Indian-Asian continental collision. Journal of Geophysical Research: Solid Earth 98, 12233–12249. https://doi.org/10.1029/93JB00443

Houseman, G., England, P., 1986. Finite Strain Calculations of Continental Deformation 1. Method and General Results for Convergent Zones. Journal of Geophysical Research 91, 3651–3663. https://doi.org/10.1029/JB091iB03p03651

Houseman, G.A., McKenzie, D.P., Molnar, P., 1981. Convective instability of a thickened boundary layer and its relevance for the thermal evolution of continental convergent belts. J. Geophys. Res. 86, 6115–6132. https://doi.org/10.1029/JB086iB07p06115

Huang, G.D., Roecker, S.W., Levin, V., Wang, H., Li, Z., 2017. Dynamics of intracontinental convergence between the western Tarim basin and central Tien Shan constrained by centroid moment tensors of regional earthquakes. Geophysical 208, 561–576.

Huang, J., Zhao, D., 2006. High-resolution mantle tomography of China and surrounding regions. J. Geophys. Res. 111. https://doi.org/10.1029/2005jb004066

Huerta, A.D., Royden, L.H., Hodges, K.V., 1998. The thermal structure of collisional orogens as a response to accretion, erosion, and radiogenic heating. Journal of

Geophysical Research: Solid Earth 103, 15287–15302. https://doi.org/10.1029/98JB00593

Hussain, E., Hooper, A., Wright, T.J., Walters, R.J., Bekaert, D.P.S., 2016. Interseismic strain accumulation across the central North Anatolian Fault from iteratively unwrapped InSAR measurements. J. Geophys. Res. Solid Earth 121, 9000–9019. http://dx.doi.org/10.1002/2016JB013108

Hussain, E., Wright, T.J., Walters, R.J., Bekaert, D.P.S., Lloyd, R., Hooper, A., 2018. Constant strain accumulation rate between major earthquakes on the North Anatolian Fault. Nat. Commun. 9, 1392.

Jackson, J., 2002. Strength of the continental lithosphere: Time to abandon the jelly sandwich? GSA Today 12, 4–10. https://doi.org/10.1130/1052-5173(2002)012<0004:sotclt>2.0.co;2

Jefferies, S.P., Holdsworth, R.E., Wibberley, C.A.J., Shimamoto, T., Spiers, C.J., Niemeijer, A.R., Lloyd, G.E., 2006. The nature and importance of phyllonite development in crustal-scale fault cores: an example from the Median Tectonic Line, Japan. Journal of Structural Geology 28, 220–235. https://doi.org/10.1016/j.jsg.2005.10.008

Jiang, C., Yang, Y., Zheng, Y., 2014. Penetration of mid-crustal low velocity zone across the Kunlun Fault in the NE Tibetan Plateau revealed by ambient noise tomography. Earth and Planetary Science Letters 406, 81–92. https://doi.org/10.1016/j.epsl.2014.08.040

Jolivet, R., Lasserre, C., Doin, M.-P., Guillaso, S., Peltzer, G., Dailu, R., Sun, J., Shen, Z.-K., Xu, X., 2012. Shallow creep on the Haiyuan Fault (Gansu, China) revealed by SAR Interferometry. Journal of Geophysical Research: Solid Earth 117. https://doi.org/10.1029/2011JB008732

Jourdon, A., Le Pourhiet, L.L., Mouthereau, Frédéric, Masini, E., 2019. Role of rift maturity on the architecture and shortening distribution in mountain belts. Earth and Planetary Science Letters 512, 89–99. https://doi.org/10.1016/j.epsl.2019.01.057

Kahraman, M., Cornwell, D.G., Thompson, D.A., Rost, S., Houseman, G.A., Türkelli, N., Teoman, U., Poyraz, S.A., Utkucu, M., Gülen, L., 2015. Crustal-scale shear zones and heterogeneous structure beneath the North Anatolian Fault Zone, Turkey, revealed by a high-density seismometer array. Earth Planet. Sci. Lett. 430, 129–139. https://doi.org/10.1016/j.epsl.2015.08.014

Kameyama, M., Yuen, D.A., Fujimoto, H., 1997. The interaction of viscous heating with grain-size dependent rheology in the formation of localized slip zones. Geophysical Research Letters 24, 2523–2526. https://doi.org/10.1029/97GL02648

Karato, S., 2006. Remote Sensing of Hydrogen in Earth's Mantle. Reviews in Mineralogy and Geochemistry 62, 343–375. https://doi.org/10.2138/rmg.2006.62.15

Karato, S., Wu, P., 1993. Rheology of the Upper Mantle: A Synthesis. Science 260, 771–778. https://doi.org/10.1126/science.260.5109.771

Karato, S.-I., 1984. Grain-size distribution and rheology of the upper mantle. Tectonophysics 104, 155–176. https://doi.org/10.1016/0040-1951(84)90108-2

Karato, S.-I., Paterson, M.S., FitzGerald, J.D., 1986. Rheology of synthetic olivine aggregates: Influence of grain size and water. Journal of Geophysical Research: Solid Earth 91, 8151–8176. http://dx.doi.org/10.1029/JB091iB08p08151

Kaus, B.J.P., Podladchikov, Y.Y., 2006. Initiation of localized shear zones in viscoelastoplastic rocks. J. Geophys. Res. 111.

Keep, M., 2000. Models of lithospheric-scale deformation during plate collision: effects of indentor shape and lithospheric thickness. Tectonophysics 326, 203–216. http://dx.doi.org/10.1016/S0040-1951(00)00123-2

Klemperer, S.L., Kennedy, B.M., Sastry, S.R., Makovsky, Y., Harinarayana, T., Leech, M.L., 2013. Mantle fluids in the Karakoram fault: Helium isotope evidence. Earth and Planetary Science Letters 366, 59–70. https://doi.org/10.1016/j.epsl.2013.01.013

Kohlstedt, D.L., Goetze, C., 1974. Low-stress high-temperature creep in olivine single crystals. J. Geophys. Res. 79, 2045–2051. https://doi.org/10.1029/JB079i014p02045

Krabbendam, M., Urai, J.L., Vliet, L.J. van, 2003. Grain size stabilisation by dispersed graphite in a high-grade quartz mylonite: an example from Naxos (Greece). Journal of Structural Geology 25, 855–866. https://doi.org/10.1016/S0191-8141(02)00086-X

Kreemer, C., Blewitt, G., Klein, E.C., 2014. A geodetic plate motion and Global Strain Rate Model. Geochem. Geophys. Geosyst. 15, 3849–3889. https://doi.org/10.1002/2014GC005407

Laborde, A., Barrier, L., Simoes, M., Li, H., Coudroy, T., Woerd, J.V. der, Tapponnier, P., 2019. Cenozoic deformation of the Tarim Basin and surrounding ranges (Xinjiang, China): A regional overview. Earth-Science Reviews 197, 102891. https://doi.org/10.1016/j.earscirev.2019.102891

Langstaff, M.A., Meade, B.J., 2013. Edge-driven mechanical microplate models of strike-slip faulting in the Tibetan plateau. Journal of Geophysical Research: Solid Earth 118, 3809–3819. http://dx.doi.org/10.1002/jgrb.50272

Lasserre, C., Bukchin, B., Bernard, P., Tapponnier, P., Gaudemer, Y., Mostinsky, A., Dailu, R., 2001. Source parameters and tectonic origin of the 1996 June 1 Tianzhu (Mw=5.2) and 1995 July 21 Yongden (Mw=5.6) earthquakes near the Haiyuan fault (Gansu, China). Geophysical Journal International 144, 206–220. https://doi.org/10.1046/j.1365-246x.2001.00313.x

Lasserre, C., Gaudemer, Y., Tapponnier, P., Mériaux, A.-S., Van der Woerd, J., Daoyang, Y., Ryerson, F.J., Finkel, R.C., Caffee, M.W., 2002. Fast late Pleistocene slip rate on the Leng Long Ling segment of the Haiyuan fault, Qinghai, China. Journal of Geophysical Research: Solid Earth 107, ETG 4-1. https://doi.org/10.1029/2000JB000060

Lasserre, C., Peltzer, G., Crampé, F., Klinger, Y., Van der Woerd, J., Tapponnier, P., 2005. Coseismic deformation of the 2001 Mw = 7.8 Kokoxili earthquake in Tibet, measured by synthetic aperture radar interferometry. Journal of Geophysical Research: Solid Earth 110. https://doi.org/10.1029/2004JB003500

Le Pourhiet, L., Huet, B., May, D.A., Labrousse, L., Jolivet, L., 2012. Kinematic interpretation of the 3D shapes of metamorphic core complexes. Geochem. Geophys. Geosyst. 13. https://doi.org/10.1029/2012GC00427

Lechmann, S.M., May, D.A., Kaus, B.J.P., Schmalholz, S.M., 2011. Comparing thin-sheet models with 3-D multilayer models for continental collision. Geophysical Journal International 187, 10–33. https://doi.org/10.1111/j.1365-246X.2011.05164.x

Lechmann, S.M., Schmalholz, S.M., Hetényi, G., May, D.A., Kaus, B.J.P., 2014. Quantifying the impact of mechanical layering and underthrusting on the dynamics of the modern India-Asia collisional system with 3-D numerical

models. J. Geophys. Res. Solid Earth 119, 616–644. https://doi.org/10.1002/2012jb009748

Leloup, P.H., Ricard, Y., Battaglia, J., Lacassin, R., 1999. Shear heating in continental strike-slip shear zones:model and field examples. Geophysical Journal International 136, 19–40. https://doi.org/10.1046/j.1365-246X.1999.00683.x

Li, L., Li, A., Murphy, M.A., Fu, Y.V., 2016. Radial anisotropy beneath northeast Tibet, implications for lithosphere deformation at a restraining bend in the Kunlun fault and its vicinity. Geochem. Geophys. Geosyst. 17, 3674–3690.

Li, L., Li, A., Shen, Y., Sandvol, E.A., Shi, D., Li, H., Li, X., 2013. Shear wave structure in the northeastern Tibetan Plateau from Rayleigh wave tomography. J. Geophys. Res. Solid Earth 118, 4170–4183.

Li, Y., Liu, M., Wang, Q., Cui, D., 2018. Present-day crustal deformation and strain transfer in northeastern Tibetan Plateau. Earth and Planetary Science Letters 487, 179–189. https://doi.org/10.1016/j.epsl.2018.01.024

Li, Y., Shan, X., Qu, C., Zhang, Y., Song, X., Jiang, Y., Zhang, G., Nocquet, J.-M., Gong, W., Gan, W., Wang, C., 2017. Elastic block and strain modeling of GPS data around the Haiyuan-Liupanshan fault, northeastern Tibetan Plateau. Journal of Asian Earth Sciences 150, 87–97. https://doi.org/10.1016/j.jseaes.2017.10.010

Li, Z., Liu-Zeng, J., Almeida, R., Hubbard, J., Sun, C., Yi, G., 2017. Re-evaluating seismic hazard along the southern Longmen Shan, China: Insights from the 1970 Dayi and 2013 Lushan earthquakes. Tectonophysics 717, 519–530. https://doi.org/10.1016/j.tecto.2017.09.001

Lin, A., Guo, J., 2008. Nonuniform Slip Rate and Millennial Recurrence Interval of Large Earthquakes along the Eastern Segment of the Kunlun Fault, Northern

Tibet. Bulletin of the Seismological Society of America 98, 2866–2878. https://doi.org/10.1785/0120070193

Lin, G., Shearer, P.M., Hauksson, E., 2007. Applying a three-dimensional velocity model, waveform cross correlation, and cluster analysis to locate southern California seismicity from 1981 to 2005. J. Geophys. Res. Solid Earth 112. https://doi.org/10.1029/2007JB004986

Lin, J., Watts, D.R., Shackleton, R.M., Dewey, J.F., Windley, B.F., 1988. Palaeomagnetic constraints on Himalayan-Tibetan tectonic evolution. Philosophical Transactions of the Royal Society of London. Series A, Mathematical and Physical Sciences 326, 177–188. https://doi.org/10.1098/rsta.1988.0084

Liu, M., Mooney, W.D., Li, S., Okaya, N., Detweiler, S., 2006. Crustal structure of the northeastern margin of the Tibetan plateau from the Songpan-Ganzi terrane to the Ordos basin. Tectonophysics 420, 253–266. https://doi.org/10.1016/j.tecto.2006.01.025

Loveless, J.P., Meade, B.J., 2011. Partitioning of localized and diffuse deformation in the Tibetan Plateau from joint inversions of geologic and geodetic observations. Earth and Planetary Science Letters 303, 11–24. https://doi.org/10.1016/j.epsl.2010.12.014

Maggi, A., Jackson, J.A., McKenzie, D., Priestley, K., 2000a. Earthquake focal depths, effective elastic thickness, and the strength of the continental lithosphere. geology 28, 495–498.

Maggi, A., Jackson, J.A., Priestley, K., Baker, C., 2000b. A re-assessment of focal depth distributions in southern Iran, theÂ Tien Shan and northern India: do

earthquakes really occur in the continental mantle? Geophysical Journal International 143, 629–661. https://doi.org/10.1046/j.1365-246x.2000.00254.x

Makabe, C., Murdani, A., Kuniyoshi, K., Irei, Y., Saimoto, A., 2009. Crack-growth arrest by redirecting crack growth by drilling stop holes and inserting pins into them. Engineering Failure Analysis 16, 475–483. https://doi.org/10.1016/j.engfailanal.2008.06.009

Mandal, N., Misra, S., Samanta, S.K., 2004. Role of weak flaws in nucleation of shear zones: an experimental and theoretical study. J. Struct. Geol. 26, 1391–1400. http://dx.doi.org/10.1016/j.jsg.2004.01.001

Manighetti, I., Tapponnier, P., Courtillot, V., Gallet, Y., Jacques, E., Gillot, P.-Y., 2001. Strain transfer between disconnected, propagating rifts in Afar. Journal of Geophysical Research: Solid Earth 106, 13613–13665. https://doi.org/10.1029/2000JB900454

McClusky, S., Balassanian, S., Barka, A., Demir, C., Ergintav, S., Georgiev, I., Gurkan, O., Hamburger, M., Hurst, K., Kahle, H., Kastens, K., Kekelidze, G., King, R., Kotzev, V., Lenk, O., Mahmoud, S., Mishin, A., Nadariya, M., Ouzounis, A., Paradissis, D., Peter, Y., Prilepin, M., Reilinger, R., Sanli, I., Seeger, H., Tealeb, A., Toksöz, M.N., Veis, G., 2000. Global Positioning System constraints on plate kinematics and dynamics in the eastern Mediterranean and Caucasus. J. Geophys. Res. Solid Earth 105, 5695–5719. https://doi.org/10.1029/1999JB900351

McKenzie, D., Fairhead, D., 1997. Estimates of the effective elastic thickness of the continental lithosphere from Bouguer and free air gravity anomalies. J. Geophys. Res. 102, 27523–27552. https://doi.org/10.1029/97jb02481

McKenzie, D., Nimmo, F., Jackson, J.A., Gans, P.B., Miller, E.L., 2000. Characteristics and consequences of flow in the lower crust. J. Geophys. Res. 105, 11029–11046. https://doi.org/10.1029/1999jb900446

McKenzie, D.P., Parker, R.L., 1967. The North Pacific: an Example of Tectonics on a Sphere. Nature 216, 1276–1280. http://dx.doi.org/10.1038/2161276a0

Meade, B.J., 2007. Present-day kinematics at the India-Asia collision zone. Geology 35, 81–84. https://doi.org/10.1130/G22924A.1

Medvedev, S.E., Podladchikov, Y.Yu., 1999. New extended thin-sheet approximation for geodynamic applications - I. Model formulation. Geophysical Journal International 136, 567–585. https://doi.org/10.1046/j.1365-246x.1999.00734.x

Meng, J., Wang, C., Zhao, X., Coe, R., Li, Y., Finn, D., 2012. India-Asia collision was at 24 N and 50 Ma: palaeomagnetic proof from southernmost Asia. Scientific Reports 925, DOI:10.1038/srep0092.

Minster, J.B., Jordan, T.H., 1978. Present-day plate motions. J. Geophys. Res. 83, 5331–5354. https://doi.org/10.1029/JB083iB11p05331

Misra, S., Mandal, N., 2007. Localization of plastic zones in rocks around rigid inclusions: Insights from experimental and theoretical models. Journal of Geophysical Research: Solid Earth 112, B09206. https://doi.org/10.1029/2006JB004328

Misra, S., Mandal, N., Dasgupta, S., 2015. Role of pressure and temperature in inclusion-induced shear localization: An analogue experimental approach. J. Struct. Geol. 81, 78–88. http://dx.doi.org/10.1016/j.jsg.2015.10.004

Molnar, P., 1988. Continental tectonics in the aftermath of plate tectonics. Nature 335, 131–137. http://dx.doi.org/10.1038/335131a0

Molnar, P., England, P., Martinod, J., 1993. Mantle dynamics, uplift of the Tibetan Plateau, and the Indian Monsoon. Reviews of Geophysics 31, 357–396. https://doi.org/10.1029/93RG02030

Molnar, P., Stock, J.M., 2009. Slowing of India's convergence with Eurasia since 20 Ma and its implications for Tibetan mantle dynamics. Tectonics 28. https://doi.org/10.1029/2008TC002271

Molnar, P., Tapponnier, P., 1978. Active tectonics of Tibet. J. Geophys. Res. Solid Earth 83, 5361–5375. http://dx.doi.org/10.1029/JB083iB11p05361

Molnar, P., Tapponnier, P., 1975. Cenozoic Tectonics of Asia: Effects of a Continental Collision. Science 4201, 419–426. https://doi.org/10.1126/science.189.4201.419

Montési, L.G.J., 2013. Fabric development as the key for forming ductile shear zones and enabling plate tectonics. Journal of Structural Geology 50, 254–266. https://doi.org/10.1016/j.jsg.2012.12.011

Montési, L.G.J., Hirth, G., 2003. Grain size evolution and the rheology of ductile shear zones: from laboratory experiments to postseismic creep. Earth and Planetary Science Letters 211, 97–110. https://doi.org/10.1016/S0012-821X(03)00196-1

Montési, L.G.J., Zuber, M.T., 2002. A unified description of localization for application to large-scale tectonics. J. Geophys. Res. Solid Earth 107, 1–21. https://doi.org/10.1029/2001JB000465

Moore, J.D.P., Parsons, B., 2015. Scaling of viscous shear zones with depth-dependent viscosity and power-law stress–strain-rate dependence. Geophys. J. Int. 202, 242–260. http://dx.doi.org/10.1093/gji/ggv143

Moore, M.A., 1999. Crustal deformation in the southern New Zealand region. (PhD Thesis). University of Oxford.

Munteanu, I., Willingshofer, E., Sokoutis, D., Matenco, L., Dinu, C., Cloetingh, S., 2013. Transfer of deformation in back-arc basins with a laterally variable rheology: Constraints from analogue modelling of the Balkanides–Western Black Sea inversion. Tectonophysics 602, 223–236. http://dx.doi.org/10.1016/j.tecto.2013.03.009

Nabelek, P.I., Whittington, A.G., Hofmeister, A.M., 2010. Strain heating as a mechanism for partial melting and ultrahigh temperature metamorphism in convergent orogens: Implications of temperature-dependent thermal diffusivity and rheology. J. Geophys. Res. 115. https://doi.org/10.1029/2010JB007727

Nazareth, J.J., Hauksson, E., 2004. The Seismogenic Thickness of the Southern California Crust. BSSA 94, 940. https://doi.org/10.1785/0120020129

Neil, E., Houseman, G., 1997. Geodynamics of the Tarim Basin and the Tian Shan in central Asia. Tectonics 16, 571–584. https://doi.org/10.1029/97TC01413

Nicolas, A., Bouchez, J.L., Blaise, J., Poirier, J.P., 1977. Geological aspects of deformation in continental shear zones. Tectonophysics 42, 55–73. http://dx.doi.org/10.1016/0040-1951(77)90017-8

Norris, R.J., 2004. Strain localisation within ductile shear zones beneath active faults: The Alpine Fault contrasted with the adjacent Otago fault system, New Zealand. Earth, Planets and Space 56, 1095–1101.

Norris, R.J., Cooper, A.F., 2003. Very high strains recorded in mylonites along the Alpine Fault, New Zealand: implications for the deep structure of plate boundary faults. Journal of Structural Geology 25, 2141–2157.

Nunn, C., Roecker, S.W., Tilmann, F.J., Priestley, K.F., Heyburn, R., Sandvol, E.A., Ni, J.F., Chen, Y.J., Zhao, W., Team, the I., IV, 2014. Imaging the lithosphere beneath NE Tibet: teleseismic P and S body wave tomography incorporating

surface wave starting models. Geophysical Journal International 196, 1724–1741. https://doi.org/10.1093/gji/ggt476

Okada, Y., 1992. Internal deformation due to shear and tensile faults in a half-space. Bulletin of the Seismological Society of America 82, 1018–1040.

Owens, T.J., Zandt, G., 1997. Implications of crustal property variations for models of Tibetan plateau evolution. Nature 387, 37–43.

Ozakin, Y., Ben-Zion, Y., 2015. Systematic Receiver Function Analysis of the Moho Geometry in the Southern California Plate-Boundary Region. Pure Appl. Geophys. 172, 1167–1184. http://dx.doi.org/10.1007/s00024-014-0924-6

Papaleo, E., Cornwell, D.G., Rawlinson, N., 2017. Seismic tomography of the North Anatolian Fault: New insights into structural heterogeneity along a continental strike-slip fault. Geophys. Res. Lett. 44, 2186–2193. https://doi.org/10.1002/2017GL072726

Peacock, D.C.P., Sanderson, D.J., 1991. Displacements, segment linkage and relay ramps in normal fault zones. Journal of Structural Geology 13, 721–733. https://doi.org/10.1016/0191-8141(91)90033-F

Peizhen, Z., Molnar, P., Weigi, Z., Qidong, D., Yipeng, W., Burchfiel, B.C., Fangmin, S., Royden, L., Decheng, J., 1988. Bounds on the Average Recurrence Interval of Major Earthquakes Along the Haiyuan Fault In North-Central China. Seismological Research Letters 59, 81–89. https://doi.org/10.1785/gssrl.59.3.81

Peltzer, G., Crampé, F., King, G., 1999. Evidence of Nonlinear Elasticity of the Crust from the Mw7.6 Manyi (Tibet) Earthquake. Science 286, 272–276. https://doi.org/10.1126/science.286.5438.272

Peltzer, G., Saucier, F., 1996. Present-day kinematics of Asia derived from geologic fault rates. Journal of Geophysical Research: Solid Earth 101, 27943–27956. http://dx.doi.org/10.1029/96JB02698

Pennacchioni, G., 2005. Control of the geometry of precursor brittle structures on the type of ductile shear zone in the Adamello tonalites, Southern Alps (Italy). Journal of Structural Geology 27, 627–644. https://doi.org/10.1016/j.jsg.2004.11.008

Pfister, M., Rybach, L., Simsek, S., 1998. Geothermal reconnaissance of the Marmara Sea region (NW Turkey): surface heat flow density in an area of active continental extension. Tectonophysics 291, 77–89. https://doi.org/10.1016/S0040-1951(98)00032-8

Pitzer, K.S., Sterner, S.M., 1994. Equations of state valid continuously from zero to extreme pressures with H2O and CO2 as examples. International Journal of Thermophysics 16, 511–518. https://doi.org/10.1007/BF01441917

Platt, J.P., 2015. Influence of shear heating on microstructurally defined plate boundary shear zones. Journal of Structural Geology 79, 80–89. https://doi.org/10.1016/j.jsg.2015.07.009

Platt, J. P., Behr, W.M., 2011. Grainsize evolution in ductile shear zones: Implications for strain localization and the strength of the lithosphere. Journal of Structural Geology 33, 537–550. https://doi.org/10.1016/j.jsg.2011.01.018

Platt, J.P., Behr, W.M., 2011. Lithospheric shear zones as constant stress experiments. Geology 39, 127. https://doi.org/10.1130/G31561.1

Precigout, J., Gueydan, F., 2009. Mantle weakening and strain localization: Implications for the long-term strength of the continental lithosphere. Geology 37, 147–150. https://dx.doi.org/10.1130/G25239A.1

Precigout, J., Gueydan, F., Gapais, D., Garrido, C.J., Essaifi, A., 2007. Strain localisation in the subcontinental mantle - a ductile alternative to the brittle mantle. Tectonophysics 445, 318–336. https://doi.org/10.1016/j.tecto.2007.09.002

Prescott, W.H., Savage, J.C., Svarc, J.L., Manaker, D., 2001. Deformation across the Pacific-North America plate boundary near San Francisco, California. J. Geophys. Res. 106, 6673–6682.

Priestley, K., Debayle, E., McKenzie, D., Pilidou, S., 2006. Upper mantle structure of eastern Asia from multimode surface waveform tomography. J. Geophys. Res. 111.

Pusok, A.E., Kaus, B.J.P., 2015. Development of topography in 3-D continental-collision models. Geochemistry, Geophysics, Geosystems 16, 1378–1400. https://doi.org/10.1002/2015GC005732

Regenauer-Lieb, K., Rosenbaum, G., Lyakhovsky, V., Liu, J., Weinberg, R., Segev, A., Weinstein, Y., 2015. Melt instabilities in an intraplate lithosphere and implications for volcanism in the Harrat Ash-Shaam volcanic field (NW Arabia). J. Geophys. Res. Solid Earth 120, 1543–1558. http://dx.doi.org/10.1002/2014JB011403

Regenauer-Lieb, K., Yuen, D., 1998. Rapid conversion of elastic energy into plastic shear heating during incipient necking of the lithosphere. Geophysical Research Letters 25, 2737–2740.

Reinen, L.A., Weeks, J.D., Tullis, T.E., 1991. The frictional behavior of serpentinite: Implications for aseismic creep on shallow crustal faults. Geophysical Research Letters 18, 1921–1924. https://doi.org/10.1029/91GL02367

Replumaz, A., Tapponnier, P., 2003. Reconstruction of the deformed collision zone Between India and Asia by backward motion of lithospheric blocks. J. Geophys. Res. 108.

Ritts, B.D., Biffi, U., 2000. Magnitude of post–Middle Jurassic (Bajocian) displacement on the central Altyn Tagh fault system, northwest China. GSA Bulletin 112, 61–74. https://doi.org/10.1130/0016-7606(2000)112<61:MOPJBD>2.0.CO;2

Royden, L., 1996. Coupling and decoupling of crust and mantle in convergent orogens: Implications for strain partitioning in the crust. Journal of Geophysical Research: Solid Earth 101, 17679–17705. https://doi.org/10.1029/96JB00951

Royden, L.H., 1993. The steady state thermal structure of eroding orogenic belts and accretionary prisms. Journal of Geophysical Research: Solid Earth 98, 4487–4507. https://doi.org/10.1029/92JB01954

Royden, L.H., Burchfiel, B.C., King, R.W., Wang, E., Chen, Z., Shen, F., Liu, Y., 1997. Surface Deformation and Lower Crustal Flow in Eastern Tibet. Science 276, 788–790. https://doi.org/10.1126/science.276.5313.788

Royden, L.H., Burchfiel, B.C., van der Hilst, R.D., 2008. The Geological Evolution of the Tibetan Plateau. Science 321, 1054. https://doi.org/10.1126/science.1155371

Rutter, E.H., Brodie, K.H., 2004. Experimental grain size-sensitive flow of hot-pressed Brazilian quartz aggregates. J. Struct. Geol. 26, 2011–2023. https://doi.org/10.1016/j.jsg.2004.04.006

Rutter, E.H., Brodie, K.H., 1995. Mechanistic interactions between deformation and metamorphism. Geol. J. 30, 227–240. https://doi.org/10.1002/gj.3350300304

Rybacki, E., Dresen, G., 2000. Dislocation and diffusion creep of synthetic anorthite aggregates. J. Geophys. Res. 105, 26017–26036. https://doi.org/10.1029/2000JB900223

Salah, M.K., Sahin, S., Kaplan, M., 2007. Seismic Velocity Structure along the Western Segment of the North Anatolian Fault Zone Imaged by Seismic Tomography. Bulletin of the Earthquake Research Institute 82, 209–223.

Sass, J.H., Williams, C.F., Lachenbruch, A.H., Galanis, S.P., Grubb, F.V., 1997. Thermal regime of the San Andreas Fault near Parkfield, California. J. Geophys. Res. Solid Earth 102, 27575–27585. https://doi.org/10.1029/JB102iB12p27575

Savage, J.C., 1983. A dislocation model of strain accumulation and release at a subduction zone. J. Geophys. Res. 88, 4984–4996. https://doi.org/10.1029/jb088ib06p04984

Savage, J.C., Burford, R.O., 1973. Geodetic Determination of Relative Plate Motion in Central California. J. Geophys. Res. 78, 832–845.

Schellart, W.P., Chen, Z., Strak, V., Duarte, J.C., Rosas, F.M., 2019. Pacific subduction control on Asian continental deformation including Tibetan extension and eastward extrusion tectonics. Nature Communications 10, 4480.

Segall, P., 2002. Integrating Geologic and Geodetic Estimates of Slip Rate on the San Andreas Fault System. International Geology Review 44, 62–82. https://doi.org/10.2747/0020-6814.44.1.62

Selway, K., 2013. On the Causes of Electrical Conductivity Anomalies in Tectonically Stable Lithosphere. Surv Geophys 35, 219–257. https://doi.org/10.1007/s10712-013-9235-1

Şengör, A.M.C., Tüysüz, O., İmren, C., Sakınç, M., Eyidoğan, H., Görür, N., Pichon, X.L., Rangin, C., 2005. The North Anatolian Fault: A new look. Annual Review of Earth and Planetary Sciences 33, 37–112. https://doi.org/10.1146/annurev.earth.32.101802.120415

Shen, Z.-K., Jackson, D.D., Ge, B.X., 1996. Crustal deformation across and beyond the Los Angeles basin from geodetic measurements. J. Geophys. Res. 101, 27957–27980. https://doi.org/10.1029/96JB02544

Shen, Z.-K., Jiangning, L., Wang, M., Bürgmann, R., 2005. Contemporary crustal deformation around the southeast borderland of the Tibetan Plateau. J. Geophys. Res. 110. https://doi.org/10.1029/2004jb003421

Shi, D., Shen, Y., Zhao, W., Li, A., 2009. Seismic evidence for a Moho offset and south-directed thrust at the easternmost Qaidam–Kunlun boundary in the Northeast Tibetan plateau. Earth and Planetary Science Letters 288, 329–334. https://doi.org/10.1016/j.epsl.2009.09.036

Smith-Konter, B.R., Sandwell, D.T., Shearer, P., 2011. Locking depths estimated from geodesy and seismology along the San Andreas Fault System: Implications for seismic moment release. J. Geophys. Res. Solid Earth 116. http://dx.doi.org/10.1029/2010JB008117

Sokoutis, D., Burg, J.-P., Bonini, M., Corti, G., Cloetingh, S., 2005. Lithospheric-scale structures from the perspective of analogue continental collision. Tectonophysics 406, 1–15. http://dx.doi.org/10.1016/j.tecto.2005.05.025

Sonder, L.J., England, P., 1986. Vertical averages of rheology of the continental lithosphere: relation to thin sheet parameters. Earth and Planetary Science Letters 77, 81–90. https://doi.org/10.1016/0012-821X(86)90134-2

Song, P.S., Shieh, Y.L., 2004. Stop drilling procedure for fatigue life improvement. International Journal of Fatigue 26, 1333–1339. https://doi.org/10.1016/j.ijfatigue.2004.04.009

Stamps, D.S., Calais, E., Saria, E., Hartnady, C., Nocquet, J.-M., Ebinger, C.J., Fernandes, R.M., 2008. A kinematic model for the East African Rift. Geophys. Res. Lett. 35. https://doi.org/10.1029/2007GL032781

Stein, S., Okal, E.A., 1978. Seismicity and tectonics of the Ninetyeast Ridge Area: Evidence for internal deformation of the Indian Plate. J. Geophys. Res. 83, 2233–2245. https://doi.org/10.1029/JB083iB05p02233

Sterner, S.M., Pitzer, K.S., 1994. An equation of state for carbon dioxide valid from zero to extreme pressures. Contrib. Mineral. Petrol 117, 362–374. https://doi.org/10.1007/BF00307271

Stewart, M., Holdsworth, R.E., Strachan, R.A., 2000. Deformation processes and weakening mechanisms within the frictional-viscous transition zone of major crustal-scale faults: insights from the Great Glen Fault Zone, Scotland. Journal of Structural Geology 22, 543–560. https://doi.org/10.1016/S0191-8141(99)00164-9

Styron, R.,. Taylor, M., Okoronkwo, K., 2010. HimaTibetMap-1.0: new ‘web-2.0’ online database of active structures from the Indo-Asian collision. Eos 91.

Su, B., Zhang, H., Sakyi, P.A., Qin, K., Liu, P., Ying, J., Tang, Y., Malaviarachchi, S.P.K., Xiao, Y., Zhao, X., Mao, Q., Ma, Y., 2010. Formation of melt pocket in mantle peridotite xenolith from western Qinling, Central China: Partial melting and metasomatism. Journal of Earth Science 21, 641–668. https://doi.org/10.1007/s12583-010-0116-y

Tan, X., Kodama, K.P., Chen, H., Fang, D., Sun, D., Li, Y., 2003. Paleomagnetism and magnetic anisotropy of Cretaceous red beds from the Tarim basin, northwest China: Evidence for a rock magnetic cause of anomalously shallow

paleomagnetic inclinations from central Asia. J. Geophys. Res. 108. https://doi.org/10.1029/2001JB001608

Tao, W., Shen, Z., 2008. Heat flow distribution in Chinese continent and its adjacent areas. Progress in Natural Science 18, 843–849. https://doi.org/10.1016/j.pnsc.2008.01.018

Tapponnier, P., Molnar, P., 1977. Active faulting and tectonics in China. Journal of Geophysical Research 82 (20), 2905–2930. https://doi.org/10.1029/JB082i020p02905

Tapponnier, P., Molnar, P., 1976. Slip-line field theory and large-scale continental tectonics. Nature 264, 319–324.

Tapponnier, P., Peltzer, G., Le Dain, A.Y., Armijo, R., Cobbold, P., 1982. Propagating extrusion tectonics in Asia: New insights from simple experiments with plasticine. Geology 10, 611–616.

Tapponnier, P., Zhiqin, X., Roger, F., Meyer, B., Arnaud, N., Wittlinger, G., Jingsui, Y., 2001. Oblique Stepwise Rise and Growth of the Tibet Plateau. Science 294, 1671–1677. https://doi.org/10.1126/science.105978

Taylor, G., Rost, S., Houseman, G., 2016. Crustal imaging across the North Anatolian Fault Zone from the autocorrelation of ambient seismic noise. Geophys. Res. Lett. 43, 2502–2509. https://doi.org/10.1002/2016GL067715

Taylor, M., Yin, A., 2009. Active structures of the Himalayan-Tibetan orogen and their relationships to earthquake distribution, contemporary strain field, and Cenozoic volcanismActive structures on the Tibetan plateau and surrounding regions. Geosphere 5, 199. https://doi.org/10.1130/GES00217.1

Thatcher, W., 2009. How the Continents Deform: The Evidence From Tectonic Geodesy. Annual Review of Earth and Planetary Sciences 37, 237–262. https://doi.org/10.1146/annurev.earth.031208.100035

Thielmann, M., Kaus, B.J.P., 2012. Shear heating induced lithospheric-scale localization: Does it result in subduction? Earth Planet. Sci. Lett. 359–360, 1–13. https://doi.org/10.1016/j.epsl.2012.10.002

Thurber, C., Roecker, S., Zhang, H., Baher, S., Ellsworth, W., 2004. Fine scale structure of the San Andreas fault zone and location of the SAFOD target earthquakes. Geophys. Res. Lett. 31. https://doi.org/10.1029/2003GL019398

Thurber, C., Zhang, H., Waldhauser, F., Hardebeck, J., Michael, A., Eberhart-Phillips, D., 2006. Three-Dimensional Compressional Wavespeed Model, Earthquake Relocations, and Focal Mechanisms for the Parkfield, California, Region. BSSA 96, S38. http://dx.doi.org/10.1785/0120050825

Titus, S.J., Dyson, M., DeMets, C., Tikoff, B., Rolandone, F., Bürgmann, R., 2011. Geologic versus geodetic deformation adjacent to the San Andreas fault, central California. Geol. Soc. Am. Bull. 123, 794. http://dx.doi.org/10.1130/B30150.1

Tommasi, A., Knoll, M., Vauchez, A., Signorelli, J.W., Thoraval, C., Logé, R., 2009. Structural reactivation in plate tectonics controlled by olivine crystal anisotropy. Nature Geoscience 2, 423–427. https://doi.org/10.1038/ngeo528

Tommasi, A., Vauchez, A., 1997. Continental-scale rheological heterogeneities and complex intraplate tectono-metamorphic patterns: insights from a case-study and numerical models. Tectonophysics 279, 327–350. http://dx.doi.org/10.1016/S0040-1951(97)00117-0

Tommasi, A., Vauchez, A., Daudre, B., 1995. Initiation and propagation of shear zones in a heterogeneous continental lithosphere. J. Geophys. Res. 100, 22083–22101. https://doi.org/10.1029/95JB02042

Tong, D., Zhang, J., Yang, H., Hu, D., Ren, J., 2012. Fault system, deformation style and development mechanism of the Bachu uplift, Tarim basin. Journal of Earth Science 23, 529–541. https://doi.org/10.1007/s12583-012-0273-2

Tong, Y., Sun, Y., Wu, Z., Mao, C., Pei, J., Yang, Z., Pu, Z., Zhao, Y., Xu, H., 2018. Passive crustal clockwise rotational deformation of the Sichuan Basin since the Miocene and its relationship with the tectonic evolution of the fault systems on the eastern edge of the Tibetan Plateau. GSA Bulletin 131, 175–190. https://doi.org/10.1130/B31965.1

Tullis, J., Yund, R.A., 1985. Dynamic recrystallization of feldspar: A mechanism for ductile shear zone formation. geology 13, 238–241.

Turcotte, D.L., Schubert, G., 2014. Geodynamics, Third. ed. Cambridge University Press.

Urai, J.L., Feenstra, A., 2001. Weakening associated with the diaspore–corundum dehydration reaction in metabauxites: an example from Naxos (Greece). Journal of Structural Geology 23, 941–950. https://doi.org/10.1016/S0191-8141(00)00165-6

van Hinsbergen, D.J.J., Steinberger, B., Doubrovine, P.V., Gassmöller, R., 2011. Acceleration and deceleration of India-Asia convergence since the Cretaceous: Roles of mantle plumes and continental collision. J. Geophys. Res. 116. https://doi.org/10.1029/2010JB008051

Vauchez, A., Tommasi, A., Barruol, G., 1998. Rheological heterogeneity, mechanical anisotropy and deformation of the continental lithosphere. Tectonophysics 296, 61–86. https://doi.org/10.1016/S0040-1951(98)00137-1

Vauchez, A., Tommasi, A., Mainprice, D., 2012. Faults (shear zones) in the Earth's mantle. Tectonophysics 558–559, 1–27. https://doi.org/10.1016/j.tecto.2012.06.006

Vergne, J., Wittlinger, G., Hui, Q., Tapponnier, P., Poupinet, G., Mei, J., Herquel, G., Paul, A., 2002. Seismic evidence for stepwise thickening of the crust across the NE Tibetan plateau. Earth and Planetary Science Letters 203, 25–33. https://doi.org/10.1016/S0012-821X(02)00853-1

Vilotte, J.P., Daignieres, M., Madariaga, R., Zienkiewicz, O.C., 1984. The role of a heterogeneous inclusion during continental collision. Physics of the Earth and Planetary Interiors 36, 236–259. http://dx.doi.org/10.1016/0031-9201(84)90049-9

Walker, J.D., Kirby, E., Andrew, J.E., 2005. Strain transfer and partitioning between the Panamint Valley, Searles Valley, and Ash Hill fault zones, California. Geosphere 1, 111–118. https://doi.org/10.1130/GES00014.1

Walsh, J.J., Watterson, J., Bailey, W.R., Childs, C., 1999. Fault relays, bends and branch-lines. Journal of Structural Geology 21, 1019–1026. https://doi.org/10.1016/S0191-8141(99)00026-7

Walters, R.J., England, P.C., Houseman, G.A., 2017. Constraints from GPS measurements on the dynamics of the zone of convergence between Arabia and Eurasia. J. Geophys. Res. Solid Earth 122, 1470–1495. https://doi.org/10.1002/2016JB013370

Wang, C., Gao, R., Yin, A., Wang, H., Zhang, Y., Guo, T., Li, Q., Li, Y., 2011. A mid-crustal strain-transfer model for continental deformation: A new perspective from high-resolution deep seismic-reflection profiling across NE Tibet. Earth and Planetary Science Letters 306, 279–288. https://doi.org/10.1016/j.epsl.2011.04.010

Wang, E., 1997. Displacement and timing along the northern strand of the Altyn Tagh fault zone, Northern Tibet. Earth and Planetary Science Letters 150, 55–64. http://dx.doi.org/10.1016/S0012-821X(97)00085-X

Wang, E., Meng, K., Su, Z., Meng, Q., Chu, J.J., Chen, Z., Wang, G., Shi, Xuhua., Liang, X., 2014. Block rotation: Tectonic response of the Sichuan basin to the southeastward growth of the Tibetan Plateau along the Xianshuihe-Xiaojiang fault. Tectonics 33, 686–718. https://doi.org/10.1002/2013tc003337

Wang, H., Wright, T.J., 2012. Satellite geodetic imaging reveals internal deformation of western Tibet. Geophysical Research Letters 39. https://doi.org/10.1029/2012GL051222

Wang, H., Wright, T.J., Liu-Zeng, J., Peng, L., 2019. Strain Rate Distribution in South-Central Tibet From Two Decades of InSAR and GPS. Geophysical Research Letters 46, 5170– 5179. https://doi.org/10.1029/2019GL081916

Wang, W., Qiao, X., Yang, S., Wang, D., 2017. Present-day velocity field and block kinematics of Tibetan Plateau from GPS measurements. Geophysical Journal International 208, 1088–1102. https://doi.org/10.1093/gji/ggw445

Wang, X., Chen, L., Ai, Y., Xu, T., Jiang, M., Ling, Y., Gao, Y., 2018. Crustal structure and deformation beneath eastern and northeastern Tibet revealed by P-wave receiver functions. Earth and Planetary Science Letters 497, 69–79. https://doi.org/10.1016/j.epsl.2018.06.007

Wang, Y., Wang, M., Shen, Z.-K., Ge, W., Wang, K., Wang, F., Sun, J., 2013. Inter-seismic deformation field of the Ganzi-Yushu fault before the 2010 Mw 6.9 Yushu earthquake. Tectonophysics 584, 138–143. https://doi.org/10.1016/j.tecto.2012.03.026

Wang-Ping, C., Grimison, N.L., 1989. Earthquakes associated with diffuse zones of deformation in the oceanic lithosphere: some examples. Tectonophysics 166, 133–150. https://doi.org/10.1016/0040-1951(89)90209-6

Warren, J.M., Hirth, G., 2006. Grain size sensitive deformation mechanisms in naturally deformed peridotites. Earth and Planetary Science Letters 248, 438–450. https://doi.org/10.1016/j.epsl.2006.06.006

Wiens, D.A., DeMets, C., Gordon, R.G., Stein, S., Argus, D., Engeln, J.F., Lundgren, P., Quible, D., Stein, C., Weinstein, S., Woods, D.F., 1985. A diffuse plate boundary model for Indian Ocean tectonics. Geophys. Res. Lett. 12, 429–432. http://dx.doi.org/10.1029/GL012i007p00429

Willingshofer, E., Sokoutis, D., Burg, J.-P., 2005. Lithospheric-scale analogue modelling of collision zones with a pre-existing weak zone. Geol. Soc. Spec. Publ. 243, 277–294. http://dx.doi.org/10.1144/GSL.SP.2005.243.01.18

Wright, T.J., Elliott, J.R., Wang, H., Ryder, I., 2013. Earthquake cycle deformation and the Moho: Implications for the rheology of continental lithosphere. Tectonophysics 609, 504–523. https://doi.org/10.1016/j.tecto.2013.07.029

Wright, T.J., Parsons, B., England, P.C., Fielding, E.J., 2004. InSAR Observations of Low Slip Rates on the Major Faults of Western Tibet. Science 305, 236–239. https://doi.org/10.1126/science.1096388

Xie, J., Ritzwoller, M.H., Shen, W., Yang, Y., Zheng, Y., Zhou, L., 2013. Crustal radial anisotropy across Eastern Tibet and the Western Yangtze Craton. J. Geophys. Res. Solid Earth 118, 4226–4252.

Xu, T., Wu, Z., Zhang, Z., Tian, X., Deng, Y., Wu, C., Teng, J., 2014. Crustal structure across the Kunlun fault from passive source seismic profiling in East Tibet. Tectonophysics 627, 98–107. https://doi.org/10.1016/j.tecto.2013.11.010

Xu, Y., Liu, F., Liu, J., Chen, H., 2002. Crust and upper mantle structure beneath western China from P wave travel time tomography. J. Geophys. Res. 107, ESE 4-1–ESE 4-15. https://doi.org/10.1029/2001jb000402

Yamasaki, T., Wright, T.J., Houseman, G.A., 2014. Weak ductile shear zone beneath a major strike slip fault: Inferences from earthquake cycle model constrained by geodetic observations of the western North Anatolian Fault Zone. J. Geophys. Res. Solid Earth 119, 3678–3699. https://doi.org/10.1002/2013JB010347

Yan, Z., Clayton, R.W., 2007. Regional mapping of the crustal structure in southern California from receiver functions. J. Geophys. Res. Solid Earth 112. https://doi.org/10.1029/2006JB004622

Yardley, B.W.D., Bodnar, R.J., 2014. Fluids in the Continental Crust. Geochem. Perspect. 3, 1–127. https://doi.org/10.7185/geochempersp.3.1

Yin, A., Harrison, T.M., 2000. Geologic Evolution of the Himalayan-Tibetan Orogen. Annual Review of Earth and Planetary Sciences 28, 211–280. https://doi.org/10.1146/annurev.earth.28.1.211

Yolsal-Çevikbilen, S., Biryol, C.B., Beck, S., Zandt, G., Taymaz, T., Adiyaman, H.E., Özacar, A.A., 2012. 3-D crustal structure along the North Anatolian Fault Zone in north-central Anatolia revealed by local earthquake tomography. Geophys. J. Int. 188, 819–849. http://dx.doi.org/10.1111/j.1365-246X.2011.05313.x

Yuen, D.A., Schubert, G., Fleitout, L., Froidevaux, C., 1978. Shear deformation zones along major transform faults and subducting slabs. Geophys. J. Int. 54, 93–119. https://dx.doi.org/10.1111/j.1365-246X.1978.tb06758.x

Zhang, H., Teng, J., Tian, X., Zhang, Z., Gao, R., Liu, J., 2012. Lithospheric thickness and upper-mantle deformation beneath the NE Tibetan Plateau inferred from S receiver functions and SKS splitting measurements. Geophysical Journal International 191, 1285–1294. https://doi.org/10.1111/j.1365-246X.2012.05667.x

Zhang, P.-Z., Molnar, P., Xu, X., 2007. Late Quaternary and present-day rates of slip along the Altyn Tagh Fault, northern margin of the Tibetan Plateau. Tectonics 26, n/a–n/a. https://doi.org/10.1029/2006TC002014

Zhang, P.-Z., Shen, Z., Wang, M., Gan, W., Bürgmann, R., Molnar, P., Wang, Q., Niu, Z., Sun, J., Wu, J., Hanrong, S., Xinzhao, Y., 2004. Continuous deformation of the Tibetan Plateau from global positioning system data. Geology 32, 809. https://doi.org/10.1130/G20554.1

Zhang, Z., Yuan, X., Chen, Y., Tian, X., Kind, R., Li, X., Teng, J., 2010. Seismic signature of the collision between the east Tibetan escape flow and the Sichuan Basin. Earth and Planetary Science Letters 292, 254–264. https://doi.org/10.1016/j.epsl.2010.01.046

Zheng, G., Wang, H., Wright, T.J., Lou, Y., Zhang, R., Zhang, W., Shi, C., Huang, J., Wei, N., 2017a. Crustal Deformation in the India-Eurasia Collision Zone From 25Â Years of GPS Measurements. J. Geophys. Res. Solid Earth 122, 9290–9312.

Zheng, G., Wang, H., Wright, T.J., Lou, Y., Zhang, R., Zhang, W., Shi, C., Huang, J., Wei, N., 2017b. Crustal deformation in the India-Eurasia collision zone from 25

years of GPS measurements. Journal of Geophysical Research: Solid Earth 122, 9290–9312. http://dx.doi.org/10.1002/2017JB014465

Zhu, B., Kidd, W.S.F., Rowley, D.B., Currie, B.S., Shafique, N., 2005. Age of Initiation of the India-Asia Collision in the East-Central Himalaya. The Journal of Geology 113, 265–285. https://doi.org/10.1086/428805

Zhu, L., 2000. Crustal structure across the San Andreas Fault, southern California from teleseismic converted waves. Earth Planet. Sci. Lett. 179, 183–190. https://doi.org/10.1016/S0012-821X(00)00101-1

Zhu, L., Helmberger, D.V., 1998. Moho Offset Across the Northern Margin of the Tibetan Plateau. Science 281, 1170–1172. https://doi.org/10.1126/science.281.5380.1170

Zhu, L., Owens, T.J., Randall, G.E., 1995. Lateral variation in crustal structure of the northern Tibetan Plateau inferred from teleseismic receiver functions. Bulletin of the Seismological Society of America 85, 1531–1540.

Zoback, M.D., Zoback, M.L., Mount, V.S., Suppe, J., Eaton, J.P., Healy, J.H., Oppenheimer, D., Reasenberg, P., Jones, L., Raleigh, C.B., Wong, I.G., Scotti, O., Wentworth, C., 1987. New Evidence on the State of Stress of the San Andreas Fault System. Science 238, 1105–1111. https://doi.org/10.1126/science.238.4830.1105